CORA Cork Open Research Archive
Cartlann Taighde Oscailte Chorcaí

Title	Unveiling transport, optical and spin-scattering mechanisms in GeSn alloys through first-principles calculations
Authors	Sewell, Kevin
Publication date	2025
Original Citation	Sewell, K. 2025. Unveiling transport, optical and spin-scattering mechanisms in GeSn alloys through first-principles calculations. PhD Thesis, University College Cork.
Type of publication	Doctoral thesis
Rights	© 2025, Kevin Sewell. - https://creativecommons.org/licenses/by/4.0/
Download date	2026-10-13 07:31:40
Item downloaded from	https://hdl.handle.net/10468/18405

UCC
University College Cork, Ireland
Coláiste na hOllscoile Corcaigh

Unveiling Transport, Optical and Spin-Scattering Mechanisms in GeSn Alloys Through First-Principles Calculations

Kevin Sewell
PhD
121103407

NATIONAL UNIVERSITY OF IRELAND, CORK

School of Science

Department of Physics

Thesis submitted for the degree of Doctor of Philosophy

June 2025

Head of Department: Prof. Paul Callanan

Supervisors: Dr. Felipe Murphy-Armando

Research supported by Research Ireland

Contents

List of Figures iv
List of Tables vii
List of Acronyms xi
Publication List xii
Acknowledgements xiv
Abstract xv

I Background 1

1 Introduction 2
1.1 Energy Consumption in Electronics 2
1.2 Electron Spin - A New Logic Variable 3
1.2.1 Spintronic Applications and Devices 4
1.2.1.1 GMR-based Devices 4
1.2.1.2 Spin-based Transistors 5
1.2.1.3 Opto-spintronics 6
1.2.1.4 Quantum Devices 7
1.2.2 Challenges - Finding a Candidate Material 8
1.3 GeSn - A New Semiconductor 10
1.3.1 Applications of GeSn 13
1.3.1.1 Transport Applications 13
1.3.1.2 Optoelectronic Applications 13
1.3.1.3 Integration with Si-technologies 14
1.3.1.4 Spintronic Applications 15
1.3.2 Experimental Challenges 16
1.4 Thesis Overview 19

2 Electron Spin: Theoretical Foundations 21
2.1 The Origin of Electron Spin 21
2.2 The Quantum Mechanics of Spin 22
2.3 Spin-Orbit Coupling 25
2.4 Spin Relaxation 27
2.4.1 Spin Relaxation Mechanisms - Elliott-Yafet 28
2.4.1.1 The Elliott and Yafet Processes 28
2.4.1.2 Relaxation Rates/Times 30
2.4.1.3 Developments of the EY Mechanism 32

II Theory 35

3 Band Structure Methods 36
3.1 Density Functional Theory 36
3.1.1 Local Density Approximation 39
3.1.2 Structural Relaxation 41

3.1.3 Plane Waves . . . 41
3.1.4 Pseudopotentials . . . 43
3.1.5 ABINIT . . . 44
3.1.5.1 Convergence Testing in ABINIT . . . 44
3.2 GW Method . . . 45
3.3 Virtual Crystal Approximation . . . 46
3.4 Kane Model . . . 47
3.5 k.p Theory . . . 48

4 Band Structure of GeSn **50**
4.1 Band structures of Ge and Sn . . . 50
4.2 Achieving a Direct Gap in GeSn . . . 52
4.2.1 Direct Gap through Addition of Sn . . . 52
4.2.2 Direct Gap through Strain . . . 54
4.3 Effective Masses . . . 56
4.4 Scattering in GeSn . . . 57

5 Scattering Theory **60**
5.1 Electron Scattering . . . 60
5.1.1 Derivation of the Alloy Scattering Matrix . . . 61
5.1.1.1 T-matrix Formalism . . . 62
5.1.1.2 Alloy Scattering Matrix Elements . . . 63
5.1.1.3 Alloy Scattering Rate . . . 65
5.1.2 Electron-Phonon Scattering . . . 65
5.1.2.1 Frozen Phonon Method . . . 65
5.1.2.2 Electron-Phonon Scattering Rate . . . 66
5.2 Mobility from the Boltzmann Transport Equation . . . 68
5.2.1 The Boltzmann Transport Equation . . . 68
5.2.2 The Relaxation Time Approximation . . . 69
5.2.3 Mobility from the BTE and the RTA . . . 70
5.2.4 Carrier Mobility for Parabolic Bands . . . 71
5.3 Optical Properties: Absorption and Emission Mechanisms . . . 72
5.3.1 Direct Transitions . . . 74
5.3.2 Indirect Transitions . . . 75
5.3.3 Transitions into Quasi-Degenerate Bands . . . 76

III Results **79**

6 Transport Properties of GeSn **80**
6.1 Alloy Scattering Parameters of GeSn . . . 82
6.1.1 Theoretical Framework . . . 82
6.1.2 Results . . . 84
6.2 Electron Mobility . . . 85
6.2.1 Theoretical Framework . . . 86
6.2.2 Results . . . 89
6.2.2.1 Room Temperature Mobility of unstrained GeSn 89

6.2.2.2 Room Temperature Mobility of biaxially tensile strained GeSn . . . 92
6.2.2.3 Low Temperature Mobility (15K) of (strained) GeSn . . . 93
6.2.2.4 The Effect of Temperature on the Mobility of (strained) GeSn . . . 94
6.3 Conclusions . . . 95

7 Spin Relaxation in GeSn 98
7.1 Theoretical Framework . . . 98
7.1.1 Spin-Alloy Scattering . . . 99
7.1.2 Electron Spin-Phonon Scattering . . . 101
7.2 Results . . . 103
7.2.1 Spin-Alloy Scattering Parameters . . . 103
7.2.2 Electron Spin-Phonon Scattering Parameters . . . 109
7.2.3 Spin Relaxation of unstrained GeSn . . . 110
7.2.4 The Effect of Strain . . . 113
7.2.5 Spin Diffusion Length . . . 114
7.2.6 Spin-Alloy Scattering in SiGe . . . 115
7.3 Conclusions . . . 118

8 Optical Properties of GeSn 120
8.1 Theoretical Framework . . . 122
8.2 Results . . . 123
8.2.1 Absorption Coefficient of GeSn . . . 123
8.2.2 Photoluminescence of GeSn . . . 127
8.3 Conclusions . . . 131

IV Summary, Conclusions and Outlook 133

9 Summary, Conclusions and Outlook 134
9.1 Summary and Conclusions . . . 134
9.2 Outlook . . . 136

V Bibliography 137

List of Figures

1.1 A typical GMR structure, where the spacer layer is a non-magnetic material for a spin-valve, or an insulating layer for a MTJ. . . . 5
1.2 Schematic of a spin FET (left), with arrows indicating the magnetisation direction of the source and drain contacts, and an N-P-N Spin Bipolar Junction Transistor (right), with a ferromagnetic base. 6
1.3 Schematic of a spin-laser, where the resonant cavity is formed by two mirrors made of distributed Bragg reflectors (DBRs) and the active region is typically composed of quantum wells/dots. The upper spacer is p-type while the lower spacer is n-type. 7
1.4 Schematic cross section of a quantum bus device. 8
1.5 Diamond FCC crystallographic structure; the structure for Group IV materials Si, Ge and Sn. 12
1.6 Phase Diagram of GeSn under equilibrium conditions. 17
1.7 GeSn manuscript evolution in the scientific community in the past 20 years (2004-2024). 18

2.1 Experimental arrangement of the Stern-Gerlach apparatus. . . . 22

4.1 Electronic band structure of Ge in eV. 51
4.2 Electronic band structure for Sn in eV. 52
4.3 Calculated energy (eV) of Γ (red) and L (black) valleys in GeSn against Sn concentration at $300K$. 53
4.4 Calculated energy (eV) of Γ (red) and L (black) valleys in GeSn against Sn concentration at $0K$. 54
4.5 Calculated energy (eV) of Γ (red) and L (black) valleys in Ge against strain percentage at $300K$. 55
4.6 Schematics of the intervalley g-type and f-type scattering between the six equivalent Δ points, and the intervalley LL scattering between the four equivalent L points. 59

5.1 Schematic of the Hamiltonian matrix describing electron–phonon and alloy interactions between conduction band states near the band edge, specifically the Γ and the L valleys. 77

6.1 Calculated intravalley and intervalley scattering matrix elements for $Ge_{1-x}Sn_x$ with relaxed and unrelaxed atomic positions around the perturbing atom. All parameters are calculated using a 64-atom supercell, with Ge as the host atom and a single Sn impurity. 85
6.2 Room-temperature intrinsic n-type electron mobility of unstrained GeSn as a function of Sn concentration and difference in bandgaps $E_{L\Gamma} = E_L - E_\Gamma$ (in eV). The second scale is better representative of the behaviour of the electron mobility, since the mobility only begins to rise after $E_{L\Gamma}$ becomes positive, and Sn concentration may not correspond to $E_{L\Gamma}$ directly due to clustering. 90

6.3 Thermal average of the group velocity at Γ of GeSn in m/s as a function of Sn concentration. 91
6.4 Thermal average of DOS of the Γ valley as a function of Sn concentration. 91
6.5 Room temperature mobility with alloy scattering (black), without intervalley alloy scattering (red) and without alloy scattering (blue) contributions, as a function of Sn concentration. 92
6.6 Room-temperature intrinsic n-type electron mobility of unstrained GeSn (black) and 1% biaxially tensile strained GeSn (red), as a function of Sn concentration and difference in bandgaps $E_{L\Gamma} = E_L - E_\Gamma$ (in eV). 93
6.7 Low-temperature (15K) intrinsic n-type electron mobility and carrier concentration ratios at L and Γ as a function of Sn concentration and difference in bandgaps. 94
6.8 Intrinsic n-type electron mobility of Ge and $Ge_{0.9}Sn_{0.1}$ as a function of temperature (K). 95

7.1 Schematic of the long 4-atom supercell used to calculate the intervalley electron spin-phonon scattering parameters of GeSn between the L and Γ valleys, showing the Cartesian coordinates of each atom. 103
7.2 Intervalley spin-alloy scattering parameters between the L valleys of GeSn (in meV) with spin-polarisation in the z-direction. . . . 104
7.3 Calculated intervalley scattering matrix elements for GeSn in meV, emphasising the dominance of L-L intervalley alloy spin scattering. 104
7.4 Intrinsic spin-relaxation time of GeSn at temperatures T=300K (black), T=200K (red), T=100K (blue) and T=30K (green), as a function of Sn concentration. We include an inset of the spin relaxation time at 300K at low Sn concentration to highlight its decrease with alloy content. 111
7.5 Intrinsic spin-relaxation time of Ge (light blue) and GeSn at Sn concentrations of 5% (purple), 10% (green), 15% (dark blue), 20% (red) and 25% (black), as a function of temperature (in Kelvin). 112
7.6 Spin relaxation time of unstrained (solid) and 1% biaxially tensile strained (dashed) GeSn at 300K (black) and 30K (green), as a function of Sn concentration. 113
7.7 Spin diffusion length of GeSn (in μm) at temperatures T=300K (black), T=200K (red), T=100K (blue) and T=30K (green), as a function of Sn concentration. 115

8.1 Schematic of the L and Γ valleys divided into energy partitions of energy width ΔE in order to be treated using perturbation theory. 123
8.2 Room-temperature absorption coefficient (α) of Ge (black), given in cm^{-1}, compared to the absorption coefficient with only direct transitions considered (red), plotted as a function of photon energy $\hbar\omega$ and wavelength λ. 124

8.3 Room-temperature absorption coefficient (in cm^{-1}) of Ge (black) GeSn at Sn concentrations of 3% (blue), 6% (green), 9% (red) and 12% (pink) against photon energy $\hbar\omega$ and wavelength λ. For 9% and 12% Sn, the absorption curves are truncated at higher photon energies due to the limited energy range of the calculated conduction band states, which was constrained by the chosen k-point sampling. 125
8.4 Comparison of the absorption coefficient of $Ge_0.94Sn_{0.06}$ with and without the inclusion of alloy scattering, plotted as functions of photon energy and wavelength. 126
8.5 Absorption coefficient of Ge (black) and $Ge_{0.88}Sn_{0.12}$ at $300K$ (solid) and $75K$ (dashed) as functions of photon energy and wavelength. 127
8.6 Room-temperature PL spectra of Ge including both phonon assisted and direct transitions (black), compared to the PL spectrum with direct transitions only (red), plotted as a function of photon energy $\hbar\omega$. Intensities are given in arbitrary units (a.u.). 128
8.7 Room-temperature PL spectrum (in arbitrary units) of Ge (black) GeSn at Sn concentrations of 3% (blue), 6% (green), 9% (red) and 12% (pink), as well as experimental data at 9% (red, dotted), plotted against photon energy $\hbar\omega$. 129
8.8 Comparison of the PL spectra of $Ge_{0.94}Sn_{0.06}$ with and without alloy scattering included, plotted as a function of photon energy $\hbar\omega$. Intensities are given in arbitrary units (a.u.). 130
8.9 PL of Ge (black), $Ge_{0.96}Sn_{0.06}$ (blue) and $Ge_{0.88}Sn_{0.12}$ (pink) in arbitrary units at $75K$, plotted against photon energy. 131

List of Tables

2.1 Spin relaxation times (τ_s) for different materials at room temperature ($300K$). 32

4.1 Material constants α (in eV/K^2)and β (in K) at band valleys L and Γ of Ge. 53
4.2 Theoretically (th) calculated bandgaps (in eV), effective masses (in m_e) and lattice constants (in Å) of Ge and α-Sn at room temperature ($300\,\mathrm{K}$) along with experimental (exp) values. The bandgaps are calculated using GW and corrected empirically for temperature. 57

6.1 Calculated intravalley scattering matrix elements (in eV) for all relevant valleys in $Ge_{1-x}Sn_x$. 85
6.2 Calculated intervalley scattering matrix elements (eV) for all relevant valleys in $Ge_{1-x}Sn_x$. 85
6.3 Deformation Potentials for Ge and GeSn. 88
6.4 Phonon Energies for Ge. 88

7.1 Calculated intervalley spin-scattering matrix elements $V_{\alpha\beta}^{\uparrow\downarrow}$ (in meV) which involve the L valley in $Ge_{1-x}Sn_x$, with spin polarisation in the z-direction. The Sn concentration is determined by the VCA applied to the host atoms within the supercell. 105
7.2 Calculated intervalley spin-scattering matrix elements $V_{\alpha\beta}^{\uparrow\downarrow}$ (in meV) for f-type scattering and scattering between the X and $\frac{1}{2}$X valleys in $Ge_{1-x}Sn_x$, with spin-polarisation in the z-direction. The following spin-flips are equivalent: $V_{XZ}^{\uparrow\downarrow} = V_{X-Z}^{\downarrow\uparrow} = V_{YZ}^{\downarrow\uparrow} = V_{Y-Z}^{\uparrow\downarrow}$, and $V_{XZ}^{\downarrow\uparrow} = V_{X-Z}^{\uparrow\downarrow} = V_{YZ}^{\uparrow\downarrow} = V_{Y-Z}^{\downarrow\uparrow}$. 106
7.3 Calculated intravalley spin-conserving alloy scattering matrix elements $V_{\alpha\beta}^{\uparrow\uparrow}$ (in eV) for all relevant valleys in $Ge_{1-x}Sn_x$. 107
7.4 Calculated intervalley spin-conserving alloy scattering matrix elements $V_{\alpha\beta}^{\uparrow\uparrow}$ (in eV) for all relevant valleys in $Ge_{1-x}Sn_x$ (excluding f-type scattering), with spin-polarisation in the z-direction. The subscript “g" represents g-type scattering. 108
7.5 Calculated f-type intervalley spin-conserving alloy scattering matrix elements $V_{\alpha\beta}^{\uparrow\uparrow}$ (in eV) in $Ge_{1-x}Sn_x$, with spin-polarisation in the z-direction. The following parameters are equivalent: $V_{XZ}^{\uparrow\uparrow} = V_{X-Z}^{\downarrow\downarrow} = V_{YZ}^{\downarrow\downarrow} = V_{Y-Z}^{\uparrow\uparrow}$, and $V_{XZ}^{\downarrow\downarrow} = V_{X-Z}^{\uparrow\uparrow} = V_{YZ}^{\uparrow\uparrow} = V_{Y-Z}^{\downarrow\downarrow}$. . 109
7.6 Phonon energies $\hbar\omega_{\mathbf{q}}$ (in meV), displacements $\vec{u}$ and calculated spin-flip deformation potentials $D_{L\Gamma}^{\uparrow\downarrow}$ (in $eV/$Å) for all phonon modes relevant for scattering between the Γ and L bands in $Ge_{1-x}Sn_x$. 110

7.7 Calculated f-type intervalley spin-scattering matrix elements $V_{\alpha\beta}^{\uparrow\downarrow}$ (in meV) in SiGe using a Si supercell with a Ge substitutional impurity (denoted $Si_{63}Ge_1$), and a Ge supercell with a Si substitutional impurity (denoted $Ge_{63}Si_1$), with spin-polarisation in the z-direction. We compare these findings to our GeSn parameters which were calculated using a Ge supercell with a Sn substitutional impurity ($Ge_{63}Sn_1$). 117
7.8 Calculated intervalley spin-scattering matrix elements $V_{\alpha\beta}^{\uparrow\downarrow}$ (in meV) for all relevant valleys (excluding f-type) in SiGe using a Si supercell with a Ge substitutional impurity (denoted $Si_{63}Ge_1$), and a Ge supercell with a Si substitutional impurity (denoted $Ge_{63}Si_1$), with spin-polarisation in the z-direction. Our results are compared to our GeSn parameters calculated using a Ge supercell with a Sn substitutional impurity ($Ge_{63}Sn_1$). 118

I, Kevin Sewell, certify that this thesis is my own work and I have not obtained a degree in this university or elsewhere on the basis of the work submitted in this thesis.

Kevin Sewell

For my family, and for Kate.

List of Acronyms

APA	Alchemical Potential Approximation
BZ	Brillouin Zone
CD	Circular Dichroism
DFT	Density Functional Theory
DP	D'yakonov-Perel
E-ph	Electron-phonon
EY	Elliott-Yafet
FCC	Face-Centred Cubic
GaAs	Gallium-Arsenide
Ge	Germanium
GeSn	Germanium-Tin
GMR	Giant Magnetoresistance
HGH	Hartwigsen-Goedecker-Hutter
HH	Heavy Hole
LDA	Local Density Approximation
LED	Light-Emitting Diode
LH	Light Hole
MTJ	Magnetic Tunnel Junction
PD	Photodetector
QW	Quantum Well
Si	Silicon
Sn	Tin
SO	Split-Off
SOC	Spin-Orbit Coupling
VCA	Virtual Crystal Approximation

Publication List

Journal Publications

1. “First-Principles Calculation of Spin-Relaxation Due to Alloy Scattering and Electron-Phonon Scattering in Strained GeSn", Kevin Sewell, Felipe Murphy-Armando, arXiv preprint arXiv:2505.10350 (2025).
2. “First-principles calculation of alloy scattering and n-type mobility in strained GeSn", Kevin Sewell, Felipe Murphy-Armando, Physical Review Applied, **23**, Issue 1, 014074 (2025).
3. “Efficient In Situ Doping of Strained Germanium Tin Epilayers at Unusually Low Temperature", Maksym Myronov, Pedram Jahandar, Simone Rossi, Kevin Sewell, Felipe Murphy-Armando, Fabio Pezzoli, Advanced Electronic Materials, **10**, Issue 9, 2300811 (2024).
4. “Controlling Electron Spin to Realise a Greener Future", Kevin Sewell, The Boolean Volume 7 (2024).

Conference Talks

1. “Disorder and Strain in Limiting the n-type Mobility of GeSn Alloys: Calculations by First-Principles." Kevin Sewell, Felipe Murphy-Armando, at *GADEST* - Bad Schandau, Germany, September 2024.
2. “First-Principles Calculation of Alloy Scattering for $Ge_{1-x}Sn_x$ and their Contribution to the Electron Mobility", Kevin Sewell, Felipe Murphy-Armando, at *EMRS Spring Meeting* - Strasbourg, France, May 2023.

Conference Posters

1. “First Principles Calculation of Electron Absorption and Recombination in Strained GeSn", Kevin Sewell, Felipe Murphy-Armando, at *GADEST* - Bad Schandau, Germany, September 2024.
2. “Calculation of the Absorption Properties of $Ge_{1-x}Sn_x$", Kevin Sewell, Felipe Murphy-Armando, poster presented at *Photonics Ireland* - Limerick, Ireland, September 2023.
3. “First-Principles Calculation of Alloy Scattering for $Ge_{1-x}Sn_x$ and their Contribution to the Electron Mobility", Kevin Sewell, Felipe Murphy-Armando,

poster presented at *ISTDM-ICSI* - Como, Italy, May 2023.

Acknowledgements

There are so many people that have supported me over the last number of years that I must thank. First, thanks to my supervisor, Dr. Felipe Murphy-Armando, for offering me the opportunity to pursue a PhD with him. I've learned a lot from Philip over the past four years, and our meetings have always had a good atmosphere, which has made my time in Tyndall very enjoyable. He always made himself available to help, and I'm proud of our findings and the papers we published together.

I would like to thank all of the members, past and present, of the Photonics Theory Group at Tyndall National Institute, led by Dr. Stefan Schulz. You have been great friends as well as great colleagues. I was also briefly part of the Materials Theory Group under Prof. Stephen Fahy, and all the members of that group taught me a lot when I began my PhD. My Tyndall colleagues have taught me so much, and it has been a pleasure to work with them and to know them. I wish them all the very best of luck in their future endeavours.

I also would like to give special thanks to Tyndall's EDI team, which I had the privilege of being a part of for two years. Our meetups provided a refreshing break from academia, and through our events and initiatives, I believe that we made Tyndall a more inclusive and welcoming place.

I thank Science Foundation Ireland for providing the funding which supported this research, under the Grant No. 12/IA/1601.

One of the greatest parts of this PhD journey has been making friends along the way - and thankfully, I've made many. Thank you to all members of Tagasaurus Rucks for making tag rugby the most enjoyable of social outlets. My crossword and pints buddies, primarily (but not by any means limited to) Dario, John, Colum and Megan, thank you for brightening up my weekday evenings.

Moving to a new city where I knew next to nobody was daunting, as was moving into an apartment with strangers. Thankfully, I felt at home instantly, and for this I would like to thank Shree, Lorena, Armando and the wonderful late Hellen.

This achievement would have been impossible without the support of my family - my parents Eamonn and Denise and my sister Olivia. You were, and have always been, there for me, whether I was celebrating achieving results or stuck in a research crisis and losing patience. Whether it was taking me on holidays, checking in on the phone on a regular basis, or looking after me in Monaghan, you helped massively. You are the people who made this, and everything I've ever achieved, all possible.

The final word goes to Dr. Kate O'Connor. When I started my PhD, I never could have imagined it would bring me to you. Knowing you as I do now, I'd probably have pursued any PhD - whether in Chinese calligraphy, religious rituals, or even the fluid dynamics of ketchup - if it meant I'd end up with you. You're the bestest.

Abstract

GeSn alloys have attracted significant interest due to their potential applications in next-generation optoelectronic, transport and spintronic devices. The incorporation of Sn into Ge results in a direct bandgap semiconductor, which is crucial for efficient light emission and absorption in photonics, as well as high-mobility transistors. Additionally, GeSn's compatibility with existing silicon technology makes it a promising candidate for monolithic integration with CMOS platforms. GeSn has also emerged as a potential material for spintronic applications due to its strong spin-orbit coupling and tunable electronic structure, which could enable efficient spin manipulation and transport.

However, despite these advantages, the study of GeSn remains limited due to challenges in material synthesis, such as the low solubility of Sn in Ge and the metastable nature of GeSn alloys. These factors complicate the growth of high-quality, defect-free GeSn films, limiting a comprehensive understanding of its structural, electronic, optical, and spintronic properties. Consequently, more research is needed to fully explore its potential for advanced technological applications.

In this thesis, we present a novel theoretical framework for understanding GeSn by investigating three key properties: (i) electronic transport, (ii) spintronic behaviour, and (iii) optoelectronic characteristics.

To fully understand its potential in transport applications, we use first-principles electronic-structure theory to calculate the intra- and intervalley electron-alloy scattering parameters of n-type GeSn. These parameters are used to determine the alloy scattering contributions to the n-type electron mobility of GeSn, which we calculate as functions of Sn concentration and temperature using a first iteration of the Boltzmann transport equation in the relaxation time approximation. For unstrained GeSn, we find that at 300K, a Sn concentration of at least 13.5% is needed to achieve an electron mobility greater than that of Ge. Our results show that the room-temperature mobility of GeSn can be over 25 times higher than the mobility of Ge, while at 15K, under 1% biaxial tensile strain, less than 6% Sn incorporation into Ge quadruples its mobility. Applying biaxial tensile strain to GeSn further increases the mobility and at a lower Sn content than in unstrained GeSn.

We also calculate the electron spin-alloy scattering parameters and the electron spin-phonon scattering parameters in n-type GeSn alloys from first-principles

methods. These parameters are used in calculating the electron-alloy and electron-phonon scattering contributions to the n-type spin relaxation of GeSn, as functions of alloy content, strain, and temperature. Our findings show that the spin-relaxation time of Ge can be substantially increased upon the introduction of sufficient Sn. For unstrained, room-temperature GeSn, we find that a Sn concentration of at least 10% is required to achieve a spin relaxation time greater than Ge, with 17% Sn needed to increase the spin relaxation time from the nanosecond range to the microsecond range. At low temperatures (30K), the addition of 10% Sn can increase the spin relaxation time from 10^{-7}s to 0.1s. Similar to the behaviour of the electron mobility, the application of biaxial tensile strain to GeSn increases the spin relaxation time further and at a lower Sn content compared to unstrained GeSn.

Finally, we investigate the optoelectronic properties of GeSn alloys by calculating the absorption coefficient and photoluminescence as functions of photon energy and temperature for fixed Sn concentrations in the short-wave infrared (SWIR) light range (0.4-1eV). Our approach combines degenerate and non-degenerate perturbation theory to accurately account for both direct and indirect optical transitions, representing the first study to incorporate alloy scattering in the modelling of an alloy's optical properties. We find that both absorption and emission increase with Sn content. In particular, incorporating 12% Sn into Ge enhances the photoluminescence intensity by a factor of 250 compared to pure Ge, while the absorption coefficient at this concentration approaches 10^5 cm^{-1} within the SWIR range. While indirect transitions contribute minimally to absorption, particularly below the direct bandgap, they play a dominant role in light emission in indirect-gap GeSn, where alloy scattering is found to be more significant than electron–phonon interactions.

This work represents a significant step forward in the theoretical understanding of GeSn alloys, offering new insights into their transport, spintronic, and optical responses, and opening pathways for their deployment in advanced electronic and photonic devices.

Part I

Background

Chapter 1

Introduction

1.1 Energy Consumption in Electronics

The rapid advancement of technology over the past few decades has been paralleled by an increasing demand for energy-efficient, high-performance electronic devices. As modern society becomes more dependent on electronics, from consumer gadgets to large-scale data centres, energy consumption has emerged as a critical issue. Currently, the Information and Communication Technology sector is responsible for $\approx 10\%$ of global electricity use, generating 1.4% of greenhouse gas emissions [1, 2]. In Ireland, electricity consumption by data centres has risen from just 5% of the total generated in 2015 to 21% in 2023, according to the Central Statistics Office [3]. Given the ever-increasing number of electronic devices in daily life, these figures are likely to rise even further.

Today, the dominant technology used to build integrated circuits (ICs), including microprocessors, memory chips and other digital logic circuits, is Complementary Metal-Oxide-Semiconductor (CMOS). CMOS uses two types of transistors: NMOS and PMOS (n-type and p-type MOS), which are arranged in pairs to form logic gates. The vast CMOS framework currently offers unparalleled levels of fabrication complexity and high manufacturing volumes and yield. However, CMOS technology is not without its flaws. It relies on charge as the fundamental logic variable, whereby high and low voltage levels represent binary states (0 and 1). Electrons (and thus charge) moving via an electric field is required to switch logic states and transmit information. As electronics have shrunk in size to fit more transistors per area, energy consumption has emerged as a significant bottleneck due to two key factors of power dissipation:

1. **Dynamic power dissipation:** is largely caused by transistors switching between logic states [4]. The NMOS and PMOS transistors remain ON simultaneously for a small period of time, resulting in a direct current path between the power supply and the ground, causing a short-circuit current flow that causes power dissipation in CMOS ICs. Dynamic power is proportional to the square of the supply voltage, the capacitance of the transistors, and the switching frequency. As device dimensions shrink, it becomes harder to reduce supply voltage without compromising performance.
2. **Static power dissipation:** this is caused by the transistor not completely turning off. A small amount of current, known as leakage current, still flows due to insufficient insulation. As the number of transistors on a chip increases, the total leakage current increases, leading to power dissipation.

Both static and dynamic power dissipations have grown exponentially in CMOS processes [4], which has increased device cost and reduced efficiency. Moore's Law [5] states that the number of transistors in an IC doubles about every two years, and with current estimates of a billion transistors per chip, dynamic and static power dissipation will be overwhelming and may destroy the device operation [6]. In addition, the switching of transistors generates heat, which limits the achievable switching rates [7]. Given that transistors are such key components of modern electronic devices, it is essential to maximise their efficiency. All of these factors indicate that classical, charge-based logic is reaching its limits, especially in terms of energy efficiency. As we demand more from our electronics, finding an alternative logic variable is one clear avenue in solving this issue.

1.2 Electron Spin - A New Logic Variable

In contrast to traditional electronics, spintronic (spin-transport-electronic) devices take advantage of either both the charge and the intrinsic angular momentum of electrons (known as “spin") or solely electron spin to store and process information. Spin-based logic operates by changing the spin orientation of electrons (up or down) rather than moving them from one place to another. This additional degree of freedom opens up new possibilities with lower power consumption, since spins can be manipulated with minimal energy using magnetic fields or spin-polarised currents.

Spintronic devices are inherently non-volatile, meaning they retain their state

(0 or 1) without the need for continuous power. This eliminates the static power dissipation seen in charge-based devices, where power is required even when the device is idle just to maintain its state. Such non-volatile devices are particularly appealing for reducing standby power consumption in systems like mobile devices or data centres, where idle power accounts for a large portion of total energy usage [8]. Consequently, spintronics holds promise for applications in a range of applications, including data storage [9, 10], communication technologies [11] and quantum computers [12].

1.2.1 Spintronic Applications and Devices

Here, we examine devices that successfully exploit spin, categorising them into the following groups: (i) GMR-based devices (used for memory), (ii) transistors, (iii) light-emitting devices and (iv) quantum applications.

1.2.1.1 GMR-based Devices

The discovery of Giant Magnetoresistance (GMR) in 1988 [13, 14] revolutionised data storage by enabling electron spin manipulation. GMR (Fig. 1.1) occurs when alternating ferromagnetic and non-magnetic layers exhibit significant changes in electrical resistance depending on the magnetic moments' alignment. This resistance change arises from varying spin-polarised electron scattering rates in parallel versus anti-parallel alignments. Numerous spin-based devices have emerged from exploiting GMR. Spin valves [15] consist of two ferromagnetic layers separated by a non-magnetic metallic spacer, while magnetic tunnel junctions (MTJs) replace the non-magnetic metallic spacer with an insulating layer, yielding even greater conductivity differences [16]. Both MTJs and spin valves are essential components of spintronics devices such as Magnetoresistive Random Access Memory (MRAM), which use spin state changes for information storage [17, 18], consuming less power than conventional DRAM or flash memory. Also, its non-volatility reduces energy use [19]. These technologies have enabled high-density storage in hard drives [6, 16], with MRAM chips now marketed by multiple companies and GMR's sensor market impact estimated at $900 million in 2023 according to Global Market Insights Inc. GMR-based read heads are common in laptops, desktops, and phones [10]. The iPod device developed by Apple Inc. is a prime example of a device that utilises GMR [9, 20].

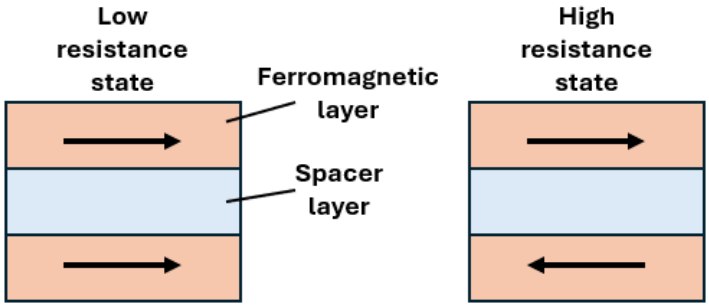

Figure 1.1: A typical GMR structure, where the spacer layer is a non-magnetic material for a spin-valve, or an insulating layer for a MTJ.

1.2.1.2 Spin-based Transistors

A key milestone in spintronics was the 1990 theoretical proposal of the spin field-effect transistor (spin-FET) by Datta and Das [21], where spin orientations represent "1" and "0" states. A spin-FET comprises two ferromagnetic contacts (source and drain) and a semiconductor (with strong spin-orbit coupling) channel between them (e.g., GeSn or GaAs), as seen in Figure 1.2. The ferromagnetic materials polarise the electron spins, while a gate terminal controls spin states, akin to traditional FETs. Spin-FETs require minimal energy to flip spins for switching, and operate faster than conventional FETs due to quicker spin manipulation; thus potentially leading to faster devices.

Standard bipolar junction transistors (BJTs) have a p-n-p or n-p-n structure (as in Fig. 1.2), using both electrons and holes as charge carriers, enabling current amplification when a small input current at the base (middle layer) modulates a larger current between emitter and collector. A spin-BJT (SBJT) is much the same, with the only difference being that the base is ferromagnetic, so the emitter in a SBJT injects spin-polarised electrons into the base. The collector current is influenced by both the spin alignment and charge flow, offering additional control based on electron spin, which could enable lower power consumption and new functionality in electronic devices.

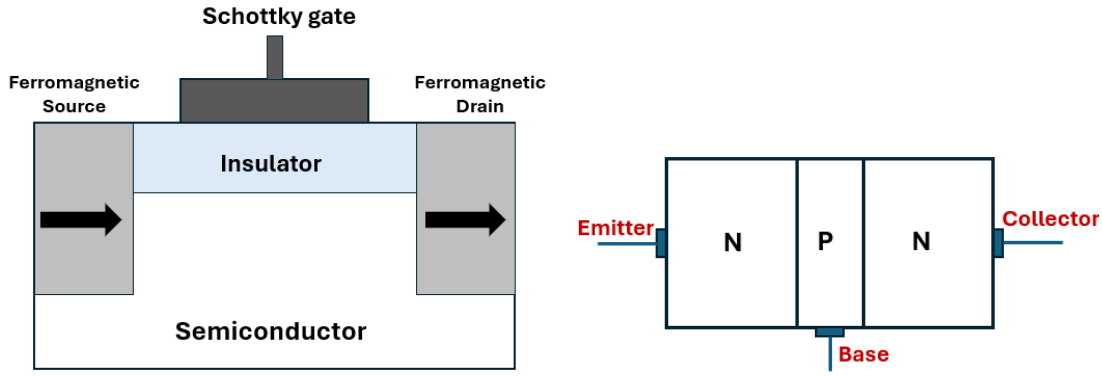

Figure 1.2: Schematic of a spin FET (left), with arrows indicating the magnetisation direction of the source and drain contacts, and an N-P-N Spin Bipolar Junction Transistor (right), with a ferromagnetic base.

1.2.1.3 Opto-spintronics

Spin manipulation can also be advantageous in optoelectronic devices [22]. Standard lasers, comprised of an active (gain) region, a resonant cavity and a pump, are solely dependent on electron charge, and have applications in optical storage, printing, medicine, optical sensing, and display systems [23, 24, 25]. However, spin-polarised lasers (Fig. 1.3), whose main distinction is the spin-polarisation of its electrons in the active region, are expected to outperform standard lasers. Only electrons are considered as spin carriers since the spins of holes decay much faster [26]. Spin-polarised carriers can be achieved either through the use of two magnetic contacts (as per Fig. 1.3) or via optical injection using circularly polarised light. Electrons and holes recombine in the gain region, and depending on the spin orientation of the electrons, the resulting photons emitted will have either right- or left-handed circular polarisation. Transferring spin-polarised electrons to circularly polarised photons in this way results in spin-encoded signal travelling much faster and further [22], offering new avenues of information transfer. Spin-dependent effects such as ultrafast optical switching [27, 28, 29], polarisation control [30, 31, 32] and threshold current reduction [33, 34] have been demonstrated using circularly polarised photo-excitation to generate spin-polarised carriers. The ability to independently control optical polarisation and intensity in spin-polarised lasers make them applicable in reconfigurable optical interconnects, chiroptical spectroscopy, and high-bandwidth telecommunications [35]. Despite significant research progress, opto-spintronic devices have not yet transitioned to commercial products.

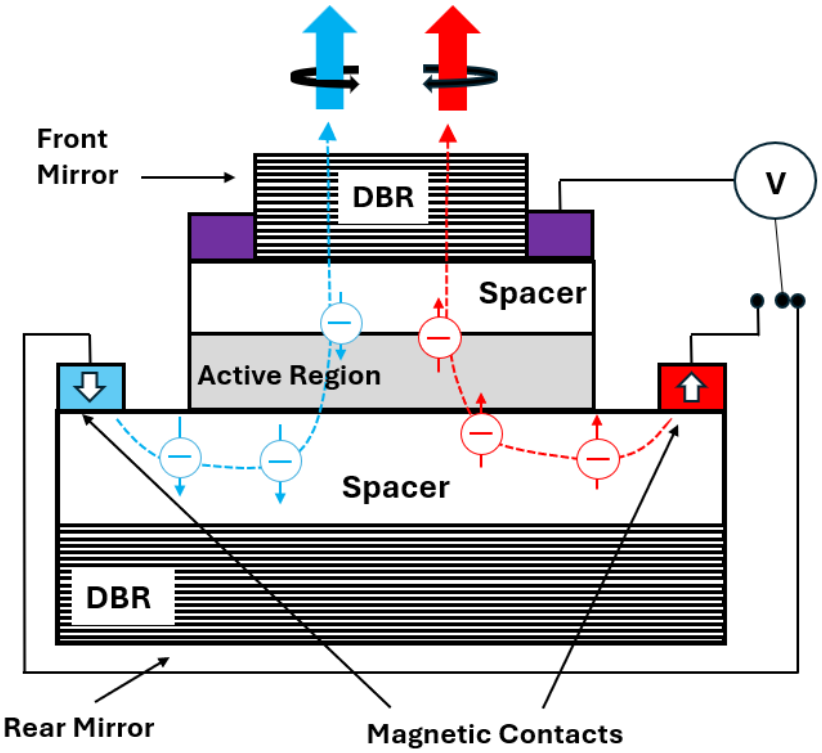

Figure 1.3: Schematic of a spin-laser, where the resonant cavity is formed by two mirrors made of distributed Bragg reflectors (DBRs) and the active region is typically composed of quantum wells/dots. The upper spacer is p-type while the lower spacer is n-type.

1.2.1.4 Quantum Devices

Leveraging quantum mechanical principles such as superposition and entanglement to process information, quantum computing may help solve problems which are beyond the means of classical computers. Unlike classical bits (0s and 1s), quantum bits (qubits) can exist in multiple states simultaneously (superposition) and interact via entanglement, enabling exponentially scalable computations. Spin-based quantum computing, a leading approach for scalable quantum systems, uses semiconductor quantum dots to trap charges and spins, with smaller dots used to create qubits and larger ones for applications in sensors. The spin of a single electron can encode one qubit. Spin qubits have been demonstrated in materials such as GaAs [36, 37], Si [38], Ge [39], and graphene [40]. Intel has developed advanced silicon spin qubit quantum computers [41, 42].

To enable communication between spatially separated qubits, spin buses (or quantum buses), coherent channels for transferring quantum information via

spin interactions, are being explored as a key component for scalable architectures. These buses facilitate long-range entanglement and qubit connectivity, overcoming the limitations of local interactions in densely packed qubit arrays. Fig. 1.4, taken from Ref. [43], provides a detailed schematic of a quantum bus, whereby a quantum dot, which carries a single electron, is formed within a quantum well by multi-layer metallic surface gates, and is shuttled across a 1-D channel. The electron and its spin state are detected by transistor gates at the ends of the quantum bus.

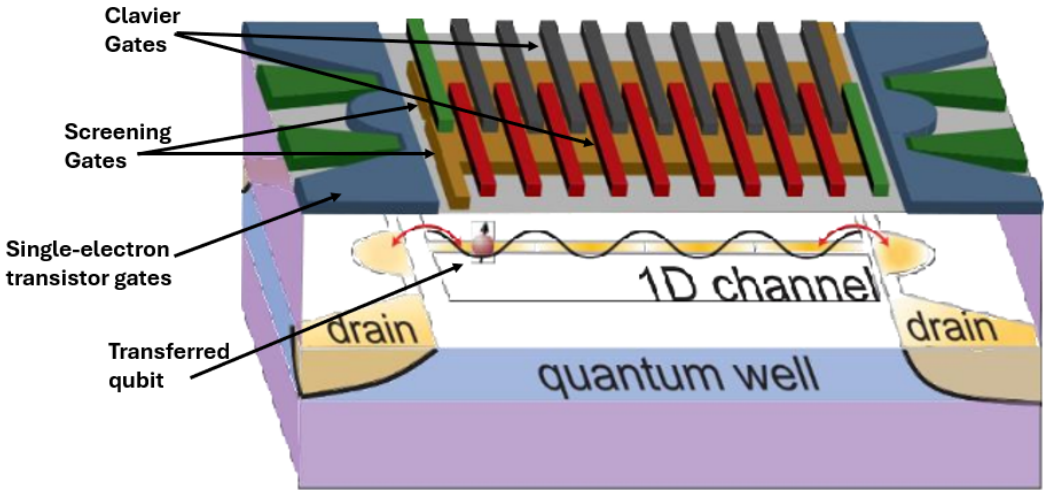

Figure 1.4: Schematic cross section of a quantum bus device.

1.2.2 Challenges - Finding a Candidate Material

Despite its obvious potential, spintronics faces numerous challenges, such as the generation of fully polarised carriers, injection of spin into devices, long-distance spin transfers and the manipulation and detection of the spin orientation of carriers [44]. Solving these issues requires two things: the development of device fabrication and the design of new materials with properties suitable for spintronics. Focusing on the latter, the advancement of spintronics has been significantly driven by the development of materials that can efficiently manipulate electron spin. Materials whose electron spins can be injected, manipulated and detected can broadly be categorised into magnetic materials, topological insulators (TIs) and non-magnetic semiconductors. TIs such as HgTe [45] and $Bi_{1-x}Sb_x$ [46] are insulators in bulk, but metallic on their surface, and are ideal for spin generation and transport. However, to this day, they can only operate at low temperatures [47], and are yet to be used in practical applications.

Magnetic materials can be either spontaneously or non-spontaneously magnetic;

that is, spontaneous magnetism occurs even in the absence of an externally applied magnetic field [48]. Spontaneous magnetism can occur in the form of ferromagnetism (where adjacent electron spins are aligned), anti-ferromagnetism (where adjacent electron spins are anti-aligned) or ferrimagnetism (where adjacent electron spins are anti-aligned, but the magnitudes of these opposing moments are unequal, resulting in a net magnetic moment). All three forms of spontaneous magnetism comes with advantages and disadvantages when it comes to their application in spintronics.

Ferromagnetic materials (such as iron, cobalt, and nickel) serve as spin injectors and detectors in devices such as MTJs and spin valves. However, ferromagnets produce stray magnetic fields which can cause cross-talk between individual components on small length scales, an issue which will only increase as we move towards smaller scale devices. Additionally, ferromagnetics can only supply partially spin-polarised carriers due to their low degree of spin polarisation [44].

Antiferromagnets (like CuMnAs) and ferrimagnets (such as GdFeCo) exhibit a much faster switching speed than ferromagnets [49]. Antiferromagnets possess a range of spin-related phenomena such as spin polarisation [50] and the magnetic spin Hall effect [51, 52]. However, they are complex in their behaviour and are by no means fully understood [44]. In addition, the partially cancelled magnetic moments in ferrimagnets mean that they generally exhibit lower net spin polarisation, which can reduce efficiency in some spintronic applications. Furthermore, (anti-)ferromagnets and ferrimagnets have a Curie temperature and can lose their magnetic properties at higher temperatures.

Regarding materials with non-spontaneous magnetism, paramagnetic materials (due to their unpaired electrons) can align weakly with an external magnetic field, but this alignment disappears when the field is removed. They find limited applications in spintronics since they do not retain magnetisation and thus cannot sustain spin polarisation over time. Interestingly, semiconductors can be made to be ferromagnetic through doping with magnetic ions. Magnetic semiconductors (such as GaMnAs and InMnAs) are of interest due to their easy implementation into devices utilising current semiconductor technology. However, most magnetic semiconductors suffer from low magnetic ordering temperatures, which limits their use in practical applications [44].

The ideal candidate material could be a non-magnetic semiconductor such as silicon (Si), germanium (Ge), or germanium-tin (GeSn), which exhibits sufficient spin properties such as spin-orbit coupling. Non-magnetic semiconducting

materials have emerged as critical to spintronics due to their ability to support both spin and charge transport, allowing for controlled manipulation of spin currents (typically via spin injection), spin transport, and spin detection whilst being seamlessly implemented into modern-day processing and fabrication technologies, bridging spin-based technology and traditional electronics.

To summarise, “spin currents" have the potential to replace conventional charge currents for transfer and storage of information, allowing for faster, low-energy operations [16], in particular through group-IV materials Si, Ge and Sn. In the next section, we will examine these group-IV materials in more detail, ultimately proposing GeSn as a promising semiconductor for future applications, not only in spintronics but also in optoelectronics and transport.

1.3 GeSn - A New Semiconductor

CMOS technology is built on silicon, with over 99% of all semiconductor devices fabricated on Si [53]. Si has been the foundation of the semiconductor industry for over 50 years for a variety of reasons. It is one of the most abundant elements on earth, and it's low bandgap of $1.1eV$ [54, 55] makes it an ideal semiconducting material; effective for switching devices. Si offers excellent thermal resilience, operating reliably at temperatures ranging from -40 to $125\,^oC$ (with relatively low current leakage), allowing its use in diverse environments, from auto-mobile electronics to consumer laptops and smartphones. One of the most important properties of Si is that it forms a stable and high-quality native oxide layer (SiO_2) when exposed to oxygen. SiO_2 acts as an excellent insulator, which allows for precise control over the behaviour of transistors, specifically metal-oxide-semiconductor field-effect transistors (MOSFETs) [53]. In the context of spintronics, Si possesses relatively long-lived electron spins [56, 57]. Spin information in Si can be transported over hundreds of microns [58, 59], which is compatible with on-chip interconnect length scales [60, 61, 62]. Advancements in injecting spin-polarised current into Si [63, 64, 65, 66, 67, 68] indicate the potential for incorporating semiconductor spintronic device concepts into hybrid Si architectures [69].

However, as we continue to push towards further miniaturisation and higher performance, Si is approaching its physical and operational limits [70]. While Si has long dominated digital logic applications, its properties are less suited for analog high-frequency electronics and optoelectronics. One key limitation is

its relatively low electron and hole mobility compared to other group-IV (and most III-V) semiconductors. This causes charge carriers to move more slowly, directly affecting the switching speed of transistors and leading to slower device operation overall. A significant factor contributing to Si's low electron mobility is its indirect bandgap, which limits its effectiveness in many applications. In optoelectronics, Si's indirect bandgap makes it poorly suited for use in light-emitting devices. As a result, Si-based light emitters are not viable options in this field, with III-V materials preferred. Since III–V materials lack both lattice compatibility with silicon and CMOS-process compatibility, research has focused on developing materials that not only provide optimal optoelectronic properties but also integrate seamlessly onto the Si platform. Finding a suitable candidate material would allow electrical and optical processing to coexist on the same chip, improving performance, reducing power consumption, and lowering costs. Silicon can be turned into a photonic material via nanostructuring [71], with recent evidence [72] suggests that some Si nanostructures exceed the performance of equivalent direct-bandgap materials. While nanowire arrays are extremely strong absorbers, with around 95% of solar panels build using Si (according to the US Department of Energy), no light-emitting devices based on Si nanocrystals have reached the market.

Several alternative high-mobility semiconducting materials have been proposed to replace Si, including III-Vs [73], graphene [74], transition metal dichalogenides (TMDs) [75] and most notably, Ge (and its alloys) [76, 77]. Among these alternatives, Ge and its alloys are the most promising candidates to replace Si in CMOS technology, owing to their excellent compatibility with Si processing. Like Si, Ge has a diamond face-centred cubic (FCC) crystal structure - two interpenetrating FCC primitive lattices, as shown in Figure 1.5 (taken from Ref. [78]). Although its abundance is significantly lower than Si, Ge has the benefit of a higher carrier mobility than Si (n-type (x3), p-type (x4)). Despite this advantage, Ge also has an indirect bandgap, making it a poor light emitter. Sufficient biaxial tensile strain can cause an indirect-to-direct bandgap transition in Ge, although the amount of strain required causes the material to approach critical thickness.

Crucially however, introducing sufficient Sn to Ge also induces a direct gap in the material. Sn is a semi-metal (which by definition has a zero direct gap) that can be found in two phases: high-temperature metallic β-Sn and the low temperature semi-metallic α-Sn, with a thermodynamic phase transition of $13.2°C$. When referring to GeSn, α-Sn is the phase of reference since it also has a diamond FCC crystal structure. Therefore, Ge and Sn can be mixed in a solid solution

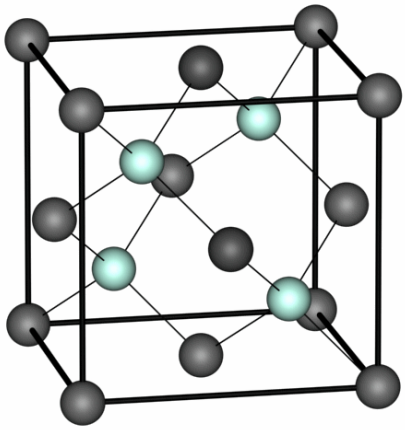

Figure 1.5: Diamond FCC crystallographic structure; the structure for Group IV materials Si, Ge and Sn.

to obtain a semiconductor (for high-Ge content) or semi-metal (for high Sn content), with the same diamond FCC crystal structure of the two elemental materials. In semiconductor physics, the focus is on high-Ge GeSn, and this will be the basis of this work. The lattice parameter of GeSn varies linearly with composition between the lattice constants (a_0) of Ge and Sn, as per Vegard's law [79, 80, 81]. The lattice mismatch between Ge and Sn is quite large (14.7%), and later in this chapter we shall discuss the consequences of this mismatch when using GeSn in processing. In 1982, based on the alloying properties governed by Vegard's Law, Goodman [82] proposed GeSn as a direct-gap semiconductor. A few years later, theoretical studies supported these observations, with Jenkins et al. [83] predicting a direct gap at 20% Sn concentration using the virtual crystal approximation (VCA). In 2007, Moontragoon et al. [84] exploited supercell mixing to predict the indirect to direct transition at 17% Sn, while a year later Yin et al. [85] used density functional theory (DFT) to predict the transition at 6.3% Sn. Today, the indirect-to-direct bandgap transition of GeSn is generally accepted to be in the range of $7 - 9\%$ Sn concentration [86, 87, 88].

There are several reasons why GeSn has become increasingly desirable for applications in the semiconductor industry. Its pseudo-direct and direct bandgap characteristics (discussed in detail in Chapter 4) have driven significant research interest in exploring its transport and optoelectronic properties (especially in the short-wavelength, mid-wavelength and near-infrared range [89]). In addition, GeSn is also a likely candidate for spin-based devices. These factors, along with its compatibility with existing silicon-based semiconductor manufacturing processes is what makes GeSn a hot-topic material. Within this section, we explore much of the recent academic work on GeSn that has led to its proposed

use in a wide range of devices.

1.3.1 Applications of GeSn

1.3.1.1 Transport Applications

GeSn was initially proposed as a high-mobility material due to the absence of polar-optical-phonon scattering; typical in III-V and II-VI compounds [90]. In general, direct gap semiconductors with diamond and zincblende structure have a higher mobility than those with an indirect-gap. Ge has a high room-temperature electron mobility ($3900\ cm^2/(Vs)$ [91, 92]) compared to Si ($1400\ cm^2/(Vs)$ [93]). Upon sufficient introduction of Sn to Ge to induce an indirect-to-direct bandgap transition, a substantial increase in the electron mobility can be expected [7, 94]. Recent experimental findings from Tien et al [95] show an increase in the mobility of tensile strained n-GeSn with increased Sn content and strain, and decreased temperature. Additionally, Ge has a higher room-temperature hole mobility ($1900\ cm^2/(Vs)$) than Si ($450\ cm^2/(Vs)$) [96]. Strained Ge has been proposed as a high hole-mobility material, which have resulted in record-high 2D hole gas mobilities in strained-Ge QW modulation-doped heterostructures [97, 98]. Moreover, Myronov et al [99] have measured a record-high hole mobility of $4.3 \times 10^6\ cm^2/(Vs)$ in strained Ge at $300mK$.

High-mobility materials improve transistor speed and efficiency, prompting significant work on GeSn transistors. In 2011, Gupta et al [100] developed the first p-MOSFET on $Ge_{0.97}Sn_{0.03}$, which showed up to 20% improvement in hole mobility over bulk Ge. Later, Huang et al [101] demonstrated a compressively strained $Ge_{0.9}Sn_{0.1}$ quantum-well p-MOSFET with a hole mobility of $509\ cm^2/(Vs)$. Liu et al [102] achieved an electron mobility of $700\ cm^2/(Vs)$ in tensile-strained $Ge_{0.96}Sn_{0.04}$ n-MOSFETs and a record-low contact resistivity of $1.5 \times 10^{-7}\Omega\ cm^2$. GeSn also shows potential for tunnel field-effect transistors [103, 104].

1.3.1.2 Optoelectronic Applications

Radiative recombination in indirect-gap semiconductors is slower and weaker than in direct-gap materials since it can only occur through the absorption or emission of phonons [105]. Consequently, direct-gap GeSn is a strong candidate for a range of optoelectronic applications.

Photodetectors (PDs) convert optical signals (light) into electrical signals (cur-

rent or voltage), and are key components in cameras, solar cells, fibre-optic communication, and various scientific instruments. GeSn photodetectors extend operation to longer wavelengths compared to pure Ge, due to bandgap engineering. Si-based GeSn PDs have been developed for mid- and short-wave infrared applications [106, 107]. Recent advances include high-broadband GeSn photodiodes for extended-SWIR applications [108] and CMOS-compatible dual-band detectors [109].

The direct bandgap in GeSn enables its use in light-emitting diodes (LEDs) and lasers, traditionally dominated by III-Vs. GeSn has been demonstrated in LEDs initially at 5% [110] and 15% [111] Sn concentration. Also, Huang et al. [112] demonstrated the first electrically injected GeSn vertical-cavity surface emitter on the Si-on-insulator platform. The demonstration of optically pumped lasing in direct bandgap GeSn (at $90K$) in 2015 by Wirths et al [113] initiated the expansion of research in this field. Optically pumped GeSn lasers were demonstrated at temperatures progressively approaching room-temperature [114, 115], with the first electrically pumped laser demonstrated in 2020 at cryogenic temperatures [116]. Since then, significant improvements in the performance of GeSn-based have been achieved [117, 118, 119]. In a recent study, Chen et al [120] have achieved a tensile-strained GeSn microbridge lasers with a tuneable wavelength, whereby the application of strain reduced the laser threshold by almost 70%. Significantly, Buca et al [121] achieved room-temperature lasing in $Ge_{0.86}Sn_{0.14}$ microdisks, showing that the inclusion of biaxial tensile strain enabled laser emission up to $300K$, compared to $265K$ for unstrained microdisks.

GeSn has also been demonstrated in optical interconnects [122, 123], lab-on-chip trace gas detection [124], and monolithic Si photonics for near-infrared and short-wave infrared wavelengths [89, 90, 125, 126, 127]. GeSn waveguides exhibit optical gain at room temperature [128], and has also shown promise for multi-junction solar cells [129].

For a more in-depth review on the potential influence of GeSn in optoelectronics, we recommend reading the review article on “Defects in Ge and GeSn and their impact on optoelectronic properties" by Giunto and Fontcuberta i Morral [130].

1.3.1.3 Integration with Si-technologies

As we’ve discussed, since virtually all processing units are based on Si-CMOS fabrication, integrating photonic components within this established technology

is highly advantageous [131]. However, the inherent limitations of Si as a light emitter highlight the need for alternative materials that can seamlessly integrate with existing CMOS chipsets. From a growth and processing perspective, GeSn seems the most logical choice. With its direct bandgap and ability to be grown directly on Si substrates [132], GeSn presents a unique opportunity to bring both light-emitting and detecting functionalities onto Si chips, enabling a fully integrated CMOS-compatible optoelectronic platform. GeSn has already demonstrated promise in multiple aspects of Si photonics, paving the way for the direct integration of light sources into Si-based circuits.

Integrating group-IV-based light sources on Si substrates has been an active area of research for decades but has yet to achieve significant technological impact. This has largely been due to challenges in material synthesis and the methods used to demonstrate these light sources on Si. However, recent advancements in group-IV-based light source development [114, 115, 133, 134, 135, 136, 137, 138] suggest that these technologies could soon play a transformative role in optoelectronics [139].

1.3.1.4 Spintronic Applications

Spintronic devices usually require materials with long spin relaxation times (explained in Chapter 2) which, in non-magnetic semiconducting materials, depend on the atomic number of the constituent atoms. Ge, with its higher atomic number (32) compared to Si (14), exhibits stronger spin-momentum interactions [140, 141], making it a promising candidate for spin-to-charge conversion [142, 143, 144, 145] and a likely candidate material in spintronics applications [146, 147]. Spin-relaxation times in Ge lie in the nanosecond range, with typical spin-diffusion lengths of micrometers [148, 149, 150].

Cesari et al. [147] demonstrated nanosecond carrier lifetimes in $Ge_{0.95}Sn_{0.05}$ under compressive strain at $300K$, marking the first optical generation of net spin polarisation in GeSn. They hypothesised that α-Sn, which is a heavy Group-IV element with atomic number 50, could further enrich the spin-dependent phenomena observed in Ge. Subsequent studies revealed GeSn's enhanced spin-Hall effect and spin-to-charge conversion efficiency, over ten times that of Ge [149]. This enables spin lasers and quantum phase control via strain and electric fields [102, 151]. More recently, Longo et al [152] investigated spin pumping in strained GeSn, which was shown to be governed by the spin-flip relaxation times induced by alloying effects. This represented the first

step towards the investigation of spin-to-charge conversion properties in GeSn thin films. GeSn also supports spin current injection and manipulation, as shown by Fettu et al. [153], who demonstrated increased spin polarisation with Sn content. They concluded that GeSn can be exploited to achieve quantum coherent manipulation and ultimately lead to quantum sensing. Moreover, Liu et al [102] succeeded in controlling spin orientations via electric fields (top gating) in GeSn/Ge heterostructures. Additional research on phase-coherent transport [154, 155], angular negative magneto-resistance [156] and 2D hole gas conduction [157] indicate the potential of GeSn in spintronics.

The strong spin properties effects of GeSn make it an ideal candidate for spin-based devices such as spin-FETs [158], spin qubits [102, 159] and spin interconnects [61, 160], which can be used in quantum computing, communication and simulation. The use of GeSn in spintronics applications like ultrafast optical switches, which demand short spin lifetimes, can be achieved through careful tuning of the alloy and dopant concentration. Given that the carrier lifetime of GeSn can be engineered by alloy content, strain and temperature, GeSn offers a versatile platform for the integrated implementation of spintronic architectures [149]. Nevertheless, it is clear that despite its promising potential, research on GeSn alloys, particularly in spintronics, remains in its early stages.

1.3.2 Experimental Challenges

Currently, despite over 15 years of extensive research, there are no GeSn-based commercial devices. There are several experimental challenges associated with GeSn which has hindered its rise in electronics. The solubility of Sn in Ge is low due to the large lattice mismatch [161, 162], restricted to 1.1% at $400°C$ [163], and is below 1% at room temperature [164], as we see in Figure 1.6 (taken from Ref. [164]). Sn will segregate out of the Ge crystal without out-of-equilibrium processing, resulting in the formation of β-Sn, which is damaging for opto-electronic devices. Therefore, phase-separation during growth or post-growth thermal processing is problematic. This segregation is kinetically hindered by the low atomic diffusivity at room temperature. However, Sn atoms may acquire sufficient thermal energy to segregate to the material's surface or cluster in the bulk into β-Sn via thermal processing of the material (through doping, annealing or any heat-based CMOS post-growth process) [165, 166]. Sn segregation can also occur if the substrate temperatures are too elevated [167]. It is therefore necessary to prevent Sn segregation by preserving a low thermal budget

throughout growth processes. An excellent review of Sn segregation and thermal instability in GeSn can be found in the paper by Giunto et al. [90].

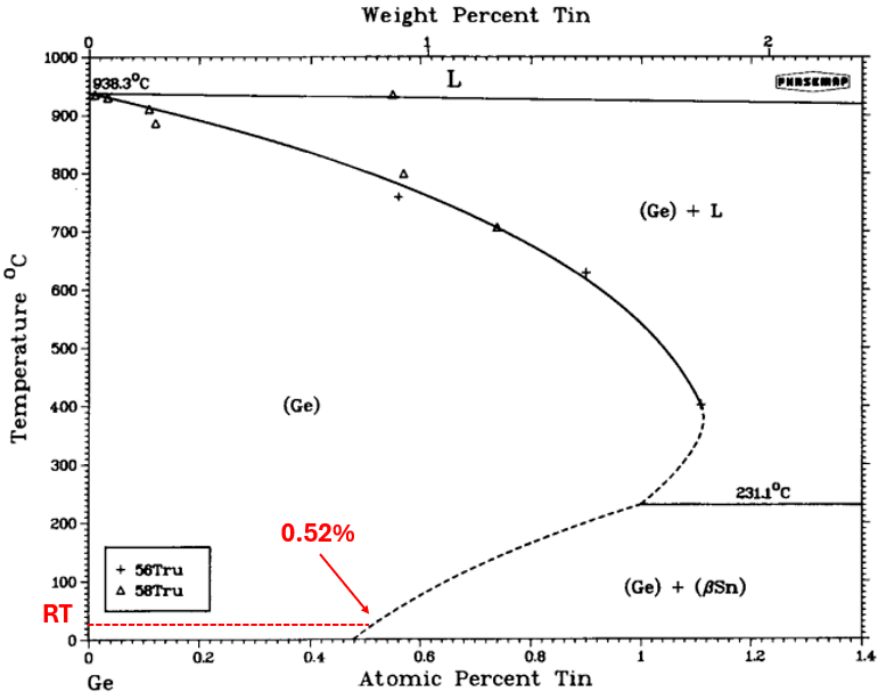

Figure 1.6: Phase Diagram of GeSn under equilibrium conditions.

Issues with the material performance of GeSn also arise from its inability to grow on a suitable substrate without relaxation defects. GeSn is best integrated into devices in a monocrystalline structure in order to avoid the formation of grain boundaries, which would introduce trap states (states within the bandgap where electrons or holes can become trapped). This would increase electron and hole scattering and prove detrimental to carrier transport. To produce monocrystalline GeSn, the alloy must be grown on a substrate with a suitable crystal structure and lattice parameter [90]. The closest material to fit (structurally) this criterion is silicon. However, the lattice mismatch causes strain relaxation via dislocations. This problem can be partially alleviated by growing GeSn on Ge-buffered Si(100) substrates or on Ge substrates [168], leading to a much higher critical thickness for strain relaxation. Epitaxial relaxation defects need to be managed correctly to maximise optoelectronic device performance. Despite these challenges, there has been success in growing GeSn alloys in recent years. In particular, Diao et al [169] have grown GeSn films with Sn content exceeding 25% on InP substrates using a magnetron sputtering growth mechanism. Additionally, Assali et al [170] implemented a multi-layer GeSn heterostructure to facilitate the incorporation

of Sn up to 18% in the top layer. while Schwarz et al [171] utilised molecular beam epitaxy (MBE) to grow GeSn on Ge with Sn concentrations of up to 17%. Results such as these give hope to GeSn being used on an industrial level.

In summary, the growing energy consumption in semiconductor manufacturing and the limitations of CMOS processes, particularly due to silicon's indirect bandgap and low carrier mobility, underscore the need for alternative materials and logic variables. Electron spin offers a promising alternative logic variable for more energy-efficient computing. Additionally, GeSn has emerged as a potential semiconductor material for next-generation technologies due to its higher mobility and potential for integration in spintronics, transport, and optoelectronics. These advances could overcome silicon's limitations and play a crucial role in the development of more efficient and versatile electronic devices. To emphasise its growing intrigue, Figure 1.7 shows the increasing number of publications on GeSn over the last 20 years, according to data found on Ref. [172].

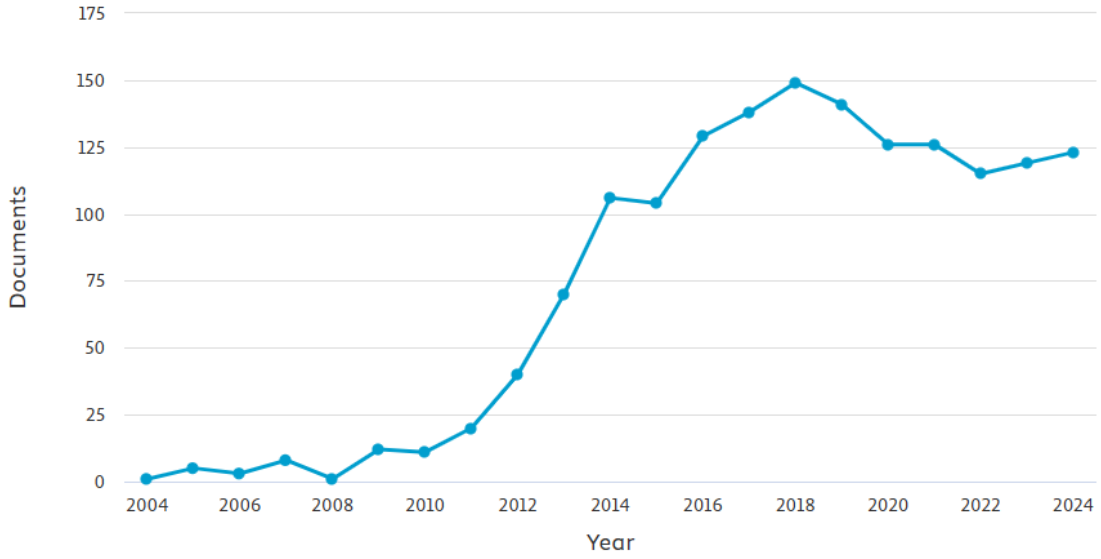

Figure 1.7: GeSn manuscript evolution in the scientific community in the past 20 years (2004-2024).

1.4 Thesis Overview

The remainder of this thesis is outlined as follows:

- Chapter 2 presents a literature review of electron spin, from its theoretical discovery and role in quantum mechanics to modern relaxation mechanisms. We focus primarily on the Elliott-Yafet (EY) mechanism and developments made to it since its proposal in the 1950s.
- In Chapter 3, we review the theoretical methods used in calculating the band structure of GeSn; in particular, Density Functional Theory (DFT), the local density approximation (LDA), plane-waves, pseudopotentials, the GW approximation, **k.p** theory and the Kane model.
- In Chapter 4, we give a detailed description of the band structure properties of GeSn, with a particular emphasis on achieving a direct-gap material, which directly impacts its suitability for transport, spintronic and optoelectronic applications.
- We treat general scattering theory in Chapter 5, using the T-matrix formalism to derive an expression for elastic alloy scattering for a disordered binary alloy. This is done using a supercell approach, whereby a single impurity is substituted into a periodic host lattice. We discuss the frozen phonon method in deriving phonon-parameters crucial to electron-phonon scattering. We also produce an expression for the carrier mobility using the relaxation time approximation and the Boltzmann Transport Equation. Finally, we implement degenerate and non-degenerate perturbation theory to derive an expression for calculating the absorption coefficient and photoluminescence spectrum for indirect and direct transitions.
- In Chapter 6, we calculate the intra- and inter-valley electron-alloy scattering parameters in n-type GeSn alloys. These parameters are used to determine the alloy scattering contributions to the n-type electron mobility of GeSn at $300K$ and $15K$ using a first iteration of the Boltzmann transport equation in the relaxation time approximation. Mobility is calculated as a function of Sn concentration, biaxial tensile strain and temperature. Our findings suggest that GeSn has potential applications as a high mobility 2D electron gas.
- In Chapter 7, we develop the first-principles methods used in Chapter 6 to calculate the spin-alloy scattering parameters of GeSn. We use these

parameters along with electron spin-phonon parameters to calculate the spin relaxation time of GeSn as a function of Sn concentration, temperature and strain. The strong spin-orbit properties tunable bandgap nature of GeSn mean its relaxation time can change by several orders of magnitude, leading to its potential in a range of spintronic applications.

- Chapter 8 presents room-temperature and low-temperature (75K) absorption and emission spectra of GeSn alloys, with a focus on the short-wave infrared light range. The results highlight how small additions in Sn content significantly enhance the material's optoelectronic properties. These findings support the potential of GeSn as a group-IV alternative to III–V semiconductors for CMOS-compatible photonic integration.
- Finally, a summary of conclusions and an outlook of future topics of research are presented in Chapter 9.

This work has led to publications listed in references [99], [173] and [174], including a pre-print submission in Ref. [175].

Chapter 2

Electron Spin: Theoretical Foundations

2.1 The Origin of Electron Spin

Spin can generally be conceptualised as the rotation of a particle about a specific axis. However, elementary particles such as electrons are envisioned as point-particle-like, and cannot rotate in space in the conventional way that solids can. If an electron were to be visualised as a sphere of Lorentz radius r rotating about its own axis, its velocity on the surface would be many times the speed of light in a vacuum. In addition, the simple concept of self-rotation about an axis doesn't explain simple spin features such as its quantised values. Hence, there is no clear-cut explanation as to how spin can emerge at a fundamental level. In the words of Richard Feynman; "It appears to be one of the few places in physics where there is a rule which can be stated very simply, but for which no one has found a simple and easy explanation" [176].

Otto Stern and Walther Gerlach of the University of Hamburg are credited with the discovery of electron spin in the 1920s, albeit by an accidental discovery, as they had not even thought of the concept of spin before. They designed an experiment whereby silver was vapourised in an oven [177], as in Figure 2.1. They sought to measure the magnetic fields produced from electrons orbiting the silver atoms, knowing in advance that moving charges produce magnetic fields. What they hadn't predicted was the silver atoms would form a beam which, when passing through a magnetic field, exhibited two distinct angular momenta, with two discrete accumulation points displayed on the screen rather

a continuous distribution of points. They assumed the two spots observed were due to quantised orbital angular momentum, which they had guessed would be $\pm\hbar$ (where $\hbar$ is the reduced Planck constant). However, in 1927 Ronald Fraser showed that the atoms had no orbital angular momentum, and suggested that the observed magnetic properties were due to electron spin [178], whereby the two possible spin states reflect the electron's alignment relative to an external magnetic field. The conclusion made by Goudsmit and Uhlenbeck [179] was electrons have an intrinsic angular momentum of $\pm\hbar/2$ which is comparable to the angular momentum of a classically spinning object, but they take only specific quantised values. Their theory was largely strengthened by the realisation that the concept of electron spin explained the small energy shifts that produced the fine structure in spectral lines; something which had puzzled scientists for years. We can therefore conclude that while spin is sometimes visualised as the electron rotating around its own axis, a formal definition for spin at a fundamental level in quantum mechanics is as an intrinsic form of angular momentum, independent of classical rotation.

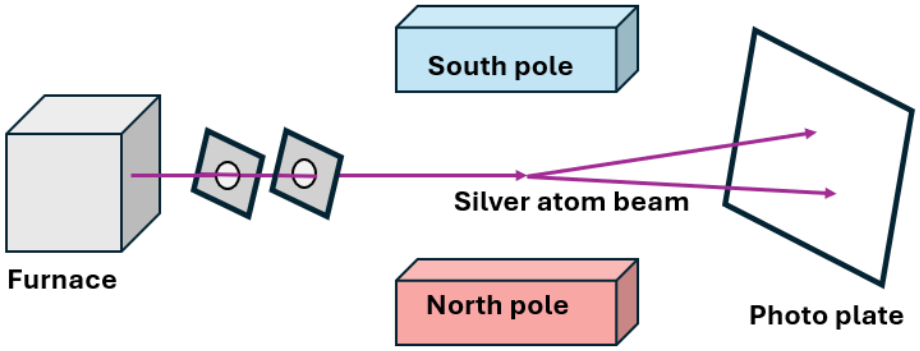

Figure 2.1: Experimental arrangement of the Stern-Gerlach apparatus.

2.2 The Quantum Mechanics of Spin

Initially, the idea seemed controversial, as the notion of a spinning charged particle raised questions about relativistic effects, which were difficult to reconcile with classical physics. Quantum mechanics, as formulated by Schrödinger [180], did not account for relativistic effects. Prior to the discovery of spin, quantum mechanics centred around Bohr's model of the hydrogen atom, which predicted that the electron orbitals were quantised. The principal quantum number n determined the allowed orbital radius, the orbital quantum number l determined

the allowed shapes, while the magnetic quantum number m determined its magnetic behaviour [10]. A fourth quantum number, the spin quantum number s (= $\frac{1}{2}$ for fermions), was introduced to represent the magnitude of this intrinsic angular momentum. The spin magnetic quantum number, m_s, describes its projection along a chosen axis (usually the z-axis). For an electron, m_s can take two values: $+\frac{1}{2}$ (spin-up) or $-\frac{1}{2}$ (spin-down), as demonstrated by the two discrete parts of the beam in the Stern-Gerlach experiment.

Any observable quantity in quantum mechanics is associated with an operator, the eigenvalues for which are the expectation values of the physical quantity. There must consequently be a quantum mechanical operator for spin with eigenvalues $\pm\hbar/2$. Wolfgang Pauli derived what are now known as the Pauli matrices in 1927 [181] to describe the quantum mechanical behaviour of spin-$\frac{1}{2}$ particles. These three 2×2 Hermitian matrices represent the spin angular momentum operators along the x-, y-, and z-axes, allowing the spin angular momentum components to be modelled mathematically and satisfy the correct commutation relations for angular momentum. They also fit into the framework of quantum mechanics, obeying the necessary algebra for operators acting on a two-level quantum system. The dimensionless Pauli matrices are:

$$\sigma_x = \begin{pmatrix} 0 & 1 \\ 1 & 0 \end{pmatrix}, \quad \sigma_y = \begin{pmatrix} 0 & -i \\ i & 0 \end{pmatrix}, \quad \sigma_z = \begin{pmatrix} 1 & 0 \\ 0 & -1 \end{pmatrix}$$

The actual spin angular momentum operators in quantum mechanics for a spin-$\frac{1}{2}$ in the i-direction (where i can be x, y or z) are given by:

$$S_i = \frac{\hbar}{2}\sigma_i$$

The eigenstates of the Pauli matrices represent the quantum states of a particle with spin aligned along a particular axis. For σ_z, which is the most commonly used Pauli matrix, the eigenstates are:

$$\text{Spin-up along } z\text{-axis:} \quad \begin{pmatrix} 1 \\ 0 \end{pmatrix}$$

$$\text{Spin-down along } z\text{-axis: } \begin{pmatrix} 0 \\ 1 \end{pmatrix}$$

corresponding to spin being aligned or anti-aligned with the z-axis, and their eigenvalues are ± 1, which correspond to $\pm\frac{\hbar}{2}$ when considering the physical spin angular momentum. Similarly, the eigenstates of σ_x and σ_y correspond to spin being aligned along the x- and y-axes, respectively, with the same eigenvalue structure. The spin of a particle affects how its wavefunction changes under rotation. When the particle is rotated by an angle θ around the axis of its spin, its quantum state picks up a phase factor of $e^{is\theta}$, where s is the spin of the particle.

In reality, the quantum state ψ of a spin-$\frac{1}{2}$ particle is not necessarily purely spin-up or spin-down, but a two-component "spinor", which is essentially a linear combination of the spin-up and spin-down states along the z-axis:

$$\psi = \begin{pmatrix} \psi_1 \\ \psi_2 \end{pmatrix} = \psi_1 \begin{pmatrix} 1 \\ 0 \end{pmatrix} + \psi_2 \begin{pmatrix} 0 \\ 1 \end{pmatrix} \tag{2.1}$$

where ψ_1 and ψ_2 are complex numbers which satisfy $|\psi_1|^2 + |\psi_2|^2 = 1$, representing the "spin-up" and "spin-down" components of the spinor wavefunction respectively. We can connect this back to our discussion on quantum computing in Chapter 1, whereby quantum computers process qubits which are coherent superpositions of two binary classical bits. In this context, spin polarisation of an electron is the ideal physical implementation of a qubit.

Pauli replaced the original one-component wavefunction in the Schroedinger equation (and thus transformed the Hamiltonian into a 2×2 matrix) with this two-component spinor, giving us what's known as the Pauli equation. However, the Pauli equation is completely non-relativistic. By combining the work of Pauli and Klein and Gordon [182, 183], Paul Dirac produced the Dirac equation [184], which included electron spin as a crucial component of his derivation of relativistic quantum mechanics. Dirac's equation defined electrons (and all fermions) as "spin-$\frac{1}{2}$" particles, which obey the Pauli Exclusion Principle [185], which states that no two fermions can occupy the same quantum state within an atom. This work provided a formal foundation for electron spin.

2.3 Spin-Orbit Coupling

While Pauli matrices and spinors provide a compact and elegant framework for describing the quantum mechanics of spin-$\frac{1}{2}$ particles, they do so in the context of idealised, isolated systems. In real materials, however, electron spin does not evolve in isolation. One of the most significant couplings between spin and the surrounding environment arises through spin-orbit coupling (SOC). SOC (or spin-orbit interaction) is a relativistic interaction of a particle's spin with its motion inside a potential, such as the electric field of the host lattice described by the periodic potential V. An electron orbiting a nucleus feels the electric field because of the nucleus' positive charge. Consequently, a magnetic field with flux density $\vec{B}$ will appear in the rest frame of the electron through a Lorentz transformation [10]. This magnetic field, in turn, interacts with the intrinsic magnetic moment $\vec{\mu}_e$ associated with the particle's spin. The result is a coupling between the particle's spin and its orbital angular momentum. The energy of this interaction is given by:

$$E = -\vec{\mu}_e \cdot \vec{B} \tag{2.2}$$

where:

$$\vec{B} = \frac{\vec{\varepsilon} \times \vec{v}}{2c^2\sqrt{1 - v^2/c^2}} \tag{2.3}$$

where $\vec{\varepsilon}$ is the electric field seen by the electron and $\vec{v}$ is its orbital velocity. It's called the spin-orbit interaction since $\vec{\mu}_e$ arises from the spin and $\vec{B}$ arises from the orbital motion. Given that for a free electron, $\vec{\mu}_e = -\mu_B\vec{\sigma}$, where $\mu_B = e\hbar/2m$ is the Bohr magneton, we can use $\vec{v} = \vec{p}/m$ to rewrite Eq. 2.2 to describe the SOC Hamiltonian:

$$\begin{aligned} H_{SOC} &= \frac{e\hbar}{4m^2c^2\sqrt{1 - v^2/c^2}} (\vec{\varepsilon} \times \vec{p}) \cdot \vec{\sigma} \\ &= -\frac{e\hbar}{4m^2c^2} (\nabla V \times \vec{p}) \cdot \vec{\sigma} \end{aligned} \tag{2.4}$$

where the electric field is related to the electric potential V by $\vec{\varepsilon} = -\vec{\nabla}V$, and we assume $v << c$. SOC leads to the splitting of atomic energy levels that would otherwise be degenerate, a phenomenon known as spin-orbit splitting. The magnitude of SOC depends on the charge of the nucleus and the angular momentum of the electron's orbit. Therefore, heavier elements with larger atomic numbers generally exhibit stronger SOC effects.

Spin-orbit coupling can arise from either the Rashba interaction [186, 187] or the Dresselhaus interaction [188], which vary depending on the nature of the electric field felt by the electrons. The Rashba interaction occurs if there is a strong electric field due to an externally applied electric field or an internal potential gradient caused by band discontinuity in a heterostructure [10]. To examine this effect, let's rewrite Eq. 2.4 by introducing the g-factor, which had been previously assumed to be 2 (for a free electron), whilst also applying the vector identity $\left(\vec{A} \times \vec{B}\right) \cdot \vec{C} = -\vec{A} \cdot \left(\vec{C} \times \vec{B}\right)$:

$$H_R = -\frac{ge\hbar}{8(m^*(\vec{r}))^2 c^2} \varepsilon(\vec{r}) \cdot (\vec{\sigma} \times \vec{p}) \tag{2.5}$$

where H_R is the Rashba Hamiltonian, and we have replaced the electron mass with the effective mass m^* since we are in a crystal. In the presence of a magnetic field, the momentum operator $\vec{p}$ must be replaced by $\vec{p} + e\vec{A}$ for vector potential $\vec{A}$. This gives a general expression for the Hamiltonian describing the Rashba interaction:

$$H_R = \eta(\vec{r}) \cdot (\vec{\sigma} \times (\vec{p} + e\vec{A})) \tag{2.6}$$

where we define:

$$\eta(\vec{r}) = -\frac{ge\hbar}{8(m^*(\vec{r}))^2 c^2} \varepsilon(\vec{r}) \tag{2.7}$$

Eq. 2.7 is simplistic insofar as it neglects band structure effects in a solid [10]. Accounting for such effects, Eq. 2.7 reads:

$$\eta(\vec{r}) = -\frac{e\hbar}{m^*(\vec{r})} \frac{\pi \triangle_s (2E_g + \triangle_s)}{E_g(E_g + \triangle_s)(3E_g + 2\triangle_s)} \varepsilon(\vec{r}) \tag{2.8}$$

where E_g is the bandgap of the semiconductor and $\triangle_s$ is the spin-orbit splitting in the valence band.

The Rashba interaction is vital to spintronics since it can be tuned by and external electric field $\vec{\varepsilon}$. It is the basis of many spintronics devices, such as spin-FETS and spin-based quantum gates [189]. While the Rashba effect is a splitting of otherwise degenerate bands due to SOC and asymmetry of the crystal potential, the Dresselhaus effect examines SOC by means of an electric field which arises from crystallographic inversion asymmetry. Since we are interested in GeSn, which has inversion symmetry due to its crystal structure, we will not discuss the Dresselhaus interaction in detail, and instead recommend Ref. [188] for a

complete derivation of the Dresselhaus Hamiltonian.

2.4 Spin Relaxation

In spintronics, it is essential for a spin-polarised electron population to retain its spin orientation for as long as possible. At the same time, for practical control and manipulation, it should also be possible to change the spin orientation efficiently when needed. Achieving both stability and tunability requires a detailed understanding of the mechanisms through which electron spins lose their initial alignment or coherence over time. In any realistic crystal, electrons are continually scattered by lattice imperfections, phonons, other electrons, and magnetic impurities, which not only hinders the electron's motion but also perturbs its spin state. A key parameter in this context is the *spin relaxation time* (also known as spin-lattice relaxation), which quantifies the rate at which a non-equilibrium spin-polarised population returns to equilibrium.

In general, the relaxation of the z-component of the spin can be modelled by the Bloch equations, which govern the time evolution of the expectation value of the spin operator:

$$\frac{d\langle S_z\rangle}{dt} = -\frac{\langle S_z\rangle - S_{z,eq}}{T_1} \tag{2.9}$$

where T_1 is the longitudinal spin-relaxation time, describing the time for which a spin decays equilibrium, or to put it another way, the time taken for the spins to align back to the magnetic field's direction (along the z-axis). $S_{z,eq}$ is the equilibrium spin value in the presence of the magnetic field. This equation describes the exponential return of the spin to its equilibrium value, governed by interactions with the surrounding lattice. In this work, we do not concern ourselves with the transverse relaxation time T_2, which characterises the decay of spin coherence in the x and y directions, is typically much smaller than T_1 and plays a minor role in the relaxation mechanisms we implement in this work (see Section 2.4.1).

In this section, we provide an overview of key relaxation mechanisms, with particular emphasis on the Elliott–Yafet mechanism.

2.4.1 Spin Relaxation Mechanisms - Elliott-Yafet

There are four major spin relaxation mechanisms of electrons in semiconductor conduction bands: the D'yakonov-Perel (DP) mechanism [190], the Elliott-Yafet (EY) mechanism [191, 192], the Bir-Aronov-Pikus (BAP) mechanism and hyperfine interactions with nuclear spins. The BAP interaction specifically involves electron-hole interactions, and often occurs in p-type semiconductors. Because of the weak electron-hole exchange coupling in group-IV materials, the BAP interaction is not of concern in this work. The hyperfine interaction involves the interaction between an electron's magnetic moment and the magnetic fields generated by nuclear spins. The vast majority of isotopes of group-IV semiconductors have no nuclear spin, therefore we neglect this interaction also. While both the DP and EY mechanisms arise from SOC, the DP process depends on both the Dresselhaus and Rashba interactions. As a result, the DP mechanism is of particular importance for semiconductor materials lacking inversion symmetry, such as zinc-blende structures. We therefore do not concern ourselves with the DP process, a clear explanation of which can be found in [193].

2.4.1.1 The Elliott and Yafet Processes

The EY mechanism is valid for metals and semiconductors (metals in the following) with inversion symmetry and weak SOC. It is split into two parts: the Elliott process and Yafet process. Elliott [191] in 1954 was the first to consider the effect of SOC on general band theory. In EY theory, spin-up and spin-down states maintain degeneracy due to time-reversal invariance, unless disrupted by a magnetic field. This is outlined by Kramer's theorem [194], which basically states that if a physical process is allowed under certain conditions, then the time-reversed process is also allowed, meaning that if the system is time-reversal invariant, then for every energy eigenstate ψ characterised by quantum numbers $\mathbf{k}, \sigma$, there exists another state with the same energy, but with opposite spin, i.e. $\psi_{\mathbf{k},\sigma} = \psi_{-\mathbf{k},-\sigma}$.

The presence of a nearby band results in a mixing of the spin-up and spin-down states within the conduction band by SOC, preserving energy degeneracy. In other words, the spin-up state contains the spin-down state and vice versa (as we saw in Eq. 2.1). Examining Eq. 2.1 in more detail, the degenerate Bloch states corresponding to the lattice momentum $\mathbf{k}$ in the presence of the spin-orbit

coupling can be expressed as:

$$\Psi_{\mathbf{k},n,\uparrow}(\mathbf{r}) = (\alpha_{\mathbf{k},n}(\mathbf{r})\,|\uparrow\rangle + \beta_{\mathbf{k},n}(\mathbf{r})\,|\downarrow\rangle) \cdot e^{i\mathbf{kr}}$$
$$\Psi_{\mathbf{k},n,\downarrow}(\mathbf{r}) = (\alpha^*_{-\mathbf{k},n}(\mathbf{r})\,|\downarrow\rangle - \beta^*_{-\mathbf{k},n}(\mathbf{r})\,|\uparrow\rangle) \cdot e^{i\mathbf{kr}} \tag{2.10}$$

where n signifies the band index, $\uparrow$ and $\downarrow$ signify the effective spins, $|\uparrow\rangle$ and $|\downarrow\rangle$ are the unperturbed spin states with component of angular momentum $\pm 1/2$, while $\alpha_{\mathbf{k},n}$, $\alpha^*_{\text{-}\mathbf{k},n}$, $\beta_{\mathbf{k},n}$ and $\beta^*_{\text{-}\mathbf{k},n}$ contain complex coefficients that determine the probability amplitudes for finding the electron in the spin-up and spin-down states, respectively [195]. Since spin mixing is often small, $|\beta_{\mathbf{k},n}| \ll |\alpha_{\mathbf{k},n}|$ and $|\beta^*_{\mathbf{k},n}| \ll |\alpha^*_{\mathbf{k},n}|$. These coefficients are determined by the L-matrix element of the SOC for the conduction band, which refers to the matrix elements of the orbital angular momentum operator $\vec{L} = \vec{r} \times \vec{p}$, and the corresponding energy separation Δ: $|\beta_{\mathbf{k},n}/\alpha_{\mathbf{k},n}| \approx L/\Delta$ [196]. This is essentially the *Elliott process*; this admixture of the Pauli up and down spin states in the Bloch state.

Overhauser [197] was the first to pinpoint the modulation of the spin–orbit interaction by phonons as the mechanism for spin relaxation due to incoherent electron–phonon (e-ph) scattering processes. His work, combined with that of Elliott, was furthered by Yafet [192], who generalised Elliott's theory for a range of relaxation mechanisms and at lower temperatures. The *Yafet process* arises from a spin-orbit interaction where the SOC of the conduction electrons to the lattice potential can be influenced by lattice vibrations. This results in an interaction where the electron spin becomes coupled to the quantum of the phonon, causing a scattering process in which the electron spin becomes entangled with the vibrational modes of the lattice. Yafet calculated the spin–flip matrix element due to the e-ph interaction (as a function of electronic momentum transfer **q**) which included both the Overhauser and Elliott contributions, revealing that the first few orders in **q** vanish due to a cancellation of Overhauser and Elliott contributions.

This combination of Overhauser and Elliott contributions is called the *EY mechanism*. For materials such as group-IV semiconductors, where inversion symmetry is present, and in low mobility materials, where momentum-relaxation scattering events are frequent, the EY mechanism is the dominant spin-relaxation mechanism, especially at high temperatures ($> 100K$).

2.4.1.2 Relaxation Rates/Times

Equation 2.11 below describes Fermi's Golden Rule [198], which is used calculate the transition rate of a quantum system from one state to another due to a weak perturbation, such as a phonon or impurity, causing the momentum of the electron to change from **k** to **k'**:

$$\Gamma(\mathbf{k'}, \mathbf{k}) = \frac{2\pi}{\hbar} \left| M_{\mathbf{kk'}} \right|^2 \delta(E_f - E_i) \tag{2.11}$$

where $M_{\mathbf{k},\mathbf{k}'} = \langle \psi_{\mathbf{k}'} | H' | \psi_{\mathbf{k}} \rangle$ represents the strength of the interaction between the states $\psi_{\mathbf{k}}$ and $\psi_{\mathbf{k}'}$ caused by a particular scattering mechanism determined by the interaction Hamiltonian H', while the Dirac delta function ensures energy conservation between the initial (i) and final (f) states. Yafet aimed to calculate the spin–flip transition rate for two Kramer's degenerate bands including SOC. Using Eq. 2.10 and Eq. 2.11, the scattering probability of preserving/flipping a spin can be described as:

$$\begin{aligned} P_{\mathbf{k},|\uparrow\rangle \rightarrow \mathbf{k'},|\uparrow\rangle} &= \frac{2\pi}{\hbar} \delta(E_{\mathbf{k}} - E_{\mathbf{k'}}) (V_{\mathbf{kk'}})^2 |\alpha^*_{\mathbf{k'},n} \alpha_{\mathbf{k},n}|^2 \\ P_{\mathbf{k},|\uparrow\rangle \rightarrow \mathbf{k'},|\downarrow\rangle} &= \frac{2\pi}{\hbar} \delta(E_{\mathbf{k}} - E_{\mathbf{k'}}) (V_{\mathbf{kk'}})^2 |\beta^*_{\mathbf{k'},n} \alpha_{\mathbf{k},n}|^2 \end{aligned} \tag{2.12}$$

where for an impurity scattering potential V which varies slowly across the unit cell, the scattering matrix element $M_{\mathbf{kk'}}$ can be approximated as:

$$\begin{aligned} \langle \Psi_{\mathbf{k},\uparrow} | \, V \, | \Psi_{\mathbf{k'},\uparrow} \rangle &\approx V_{\mathbf{kk'}} \, (\alpha^*_{\mathbf{k'},n} \alpha_{\mathbf{k},n}) \\ \langle \Psi_{\mathbf{k},\uparrow} | \, V \, | \Psi_{\mathbf{k'},\downarrow} \rangle &\approx V_{\mathbf{kk'}} \, (\beta^*_{\mathbf{k'},n} \alpha_{\mathbf{k},n}) \end{aligned} \tag{2.13}$$

with $V_{\mathbf{kk'}} = \int e^{i(\mathbf{k}-\mathbf{k'})\cdot\mathbf{r}} \, V(\mathbf{r}) \, d^3r$, which represents the spin-flip and non-spin-flip transition elements.

The relaxation time τ of a scattering event is essentially the inverse of the scattering rate. The general form of the scattering rate due to an e-ph interaction ($(\tau^{e-ph}_{n\mathbf{k}})^{-1}$) can be expressed as:

$$\frac{1}{\tau^{e-ph}_{n\mathbf{k}}} = \frac{2\pi}{\hbar} \sum_{n'\mathbf{q},\nu} |M_{nn'\nu}(\mathbf{k}, \mathbf{q})|^2 \; (N_{\mathbf{q},\nu} + \frac{1}{2} \pm \frac{1}{2}) \; \delta(\epsilon_{n\mathbf{k}} - \epsilon_{n'\mathbf{k}+\mathbf{q}} \pm \hbar\omega_{\mathbf{q},\nu}) \tag{2.14}$$

where $M_{nn'\nu}(\mathbf{k}, \mathbf{q})$ is the e-ph matrix element, q is the phonon wave vector such that $\mathbf{k}' = \mathbf{k} + \mathbf{q}$, ν is the phonon branch, $\omega_{\mathbf{q},\nu}$ is the phonon frequency and $N_{\mathbf{q},\nu}$

is the phonon occupation number. Yafet showed the spin-flip e-ph relaxation times $\tau_{n\mathbf{k}}^{flip}$ could be calculated using a similar expression [192, 199]:

$$\frac{1}{\tau_{n\mathbf{k}}^{flip}} = \frac{4\pi}{\hbar} \sum_{n'\mathbf{q},\nu} \left| M_{nn'\nu}^{flip}(\mathbf{k},\mathbf{q}) \right|^2 \left(N_{\mathbf{q},\nu} + \frac{1}{2} \pm \frac{1}{2} \right) \delta(\epsilon_{n\mathbf{k}} - \epsilon_{n'\mathbf{k}+\mathbf{q}} \pm \hbar\omega_{\mathbf{q},\nu}) \quad (2.15)$$

The temperature-dependent spin-relaxation time $\tau_s(T)$ is easily obtained as an ensemble average (average over $\mathbf{k}$) of the spin-flip relaxation times [192, 199] by integration over the Fermi-surface:

$$\tau_s(T) = \left\langle \frac{1}{\tau_{n,k}^{flip}} \right\rangle_T^{-1} = \left(\frac{\sum_{n\mathbf{k}} \frac{1}{\tau_{n,k}^{flip}} \left(-\frac{\partial f_{n\mathbf{k}}}{\partial E} \right) d\mathbf{k}}{\sum_{n\mathbf{k}} \left(-\frac{\partial f_{n\mathbf{k}}}{\partial E} \right) d\mathbf{k}} \right)^{-1} \quad (2.16)$$

where f represents the electron distribution function. When the EY mechanism is the dominant scattering mechanism, Elliott showed a direct proportionality correlation between τ_{e-ph} and τ_s using first-order time-perturbation treatment:

$$\tau_{e-ph} \approx \alpha \left(\frac{L}{\Delta_s} \right)^2 \tau_s \quad (2.17)$$

where α is a band-dependent constant near unity. Eq. 2.17 is suitable for evaluation from ab initio input. Yafet showed this expression to be temperature-independent, given that E_g and Δ_s have weak temperature dependences [10] (in other words, τ_s and τ_{e-ph} have the same temperature dependence). The direct proportionality between τ_s and τ_{e-ph} is to be expected, since the EY mechanism is caused by momentum relaxation. Therefore, with an increase in temperature, the spin-relaxation rate via the EY mechanism also increases due to enhanced e-ph scattering.

The initial derivations of Elliott and Yafet were based on expressions of wave functions for alkali metals (which included Li, Na and K). They also examined the wavefunctions of Si, predicting that the spin relaxation time is of the order of $10^{-9}s$ at $300K$. Appelbaum et al [65, 200] experimentally determined τ_s for Si in 2007 and their results were in excellent agreement with the theoretical value. Li, Song and Dery [201] calculated the spin relaxation time of Ge to also be in the nanosecond range (see Hamaya et al for a detailed list of previously determined spin-relaxation times of electrons and holes in Ge [148]). In metals, Monod and Beunue [202] provided experimental evidence that confirmed that τ_s and τ_{e-ph} show the same temperature dependence. Often, τ_{e-ph} is of the order

of picoseconds, while usually τ_s is several nanoseconds long. In Table 2.4.1.2, we give a list of spin relaxation times previously determined theoretically or by experiment.

Perhaps surprisingly, both long spin lifetimes and short spin lifetimes can be advantageous, depending on the application. Generally speaking, materials with long spin lifetimes are sought after for applications such as spin-based transistors, quantum computing and spin interconnects. In contrast, other spintronics applications such as ultra-fast optical switches require short spin lifetimes [149, 26].

Table 2.1: Spin relaxation times (τ_s) for different materials at room temperature ($300K$).

Material	**Spin Relaxation Time (τ_s)**	**Reference**
Si	$\approx$ 1 ns	[65, 191, 203]
Ge	$\approx$ 1 ns	[69, 148, 201]
$Ge_{0.95}Sn_{0.05}$	$\approx$ 0.1 ns	[149]
GaAs	50 ps - 2 ns	[204, 205, 206]
GaSb	5-10 ps	[207, 208]
InAs	$\approx$ 20 ps	[207, 209]
InSb	10 - 20 ps	[207, 210, 211]
Bilayer Graphene	100 ps - 2 ns	[212, 213]

2.4.1.3 Developments of the EY Mechanism

Although the EY mechanism has been successful in describing spin relaxation, particularly in light semiconductors and metals with inversion symmetry, it has had several limitations and challenges that have been addressed in the decades since its initial development; most of which have been since the early 2010s. In 2012, Restrepo and Windl [214] produced a new parameter-free first-principles method to obtain spin-relaxation times for phonon and impurity scattering. They demonstrated the possibility of calculating spin-relaxation times without adjustable parameters and without restrictions concerning the nature of the band gap, making it applicable to any type of impurity or defect on spin transport. They applied their method to group-IV materials silicon, diamond, and graphite,

producing results that matched well with experiment. This generalised the EY mechanism, ensuring that it was no longer materials-specific.

The EY mechanism assumes weak spin-orbit coupling in the system (compared to say the DP mechanism). In heavy materials with a strong spin-orbit interaction (such as lead or bismuth), this assumption breaks down. Strong SOC can lead to different spin relaxation mechanisms not captured by the EY mechanism. This brought into question the first-order perturbation treatment used by Elliott. In 2015, Kiss et al [196] generalised the EY mechanism for materials with small SOC compared to energy scales such as band separations and kinetic energy. They implemented a 4-band model which introduced band-specific contributions to the spin relaxation time, meaning that each of the four bands contributed differently to the overall relaxation process. With their model, they recovered the usual EY theory for weak SOC, but more importantly showed using experimental data on gold (provided by Monod and Janossy [215]) that the spin-relaxation rate approached the momentum-relaxation rate in the limit of strong SOC.

The density matrix ρ, shown in Eq. 2.18, provides a framework for analysing a large ensemble of spinors with an initial statistical distribution at time $t = 0$ and tracking their evolution over time by examining the evolution of ρ. The solution of this evolution is governed by the Bloch equations of motion. T_1 dictates how the diagonal elements (population differences) relax to equilibrium, and T_2 describes the decay of off-diagonal elements (coherences), representing dephasing of superpositions between spin-up and spin-down states. We can express ρ as:

$$\rho = |\psi\rangle \langle\psi| = \begin{pmatrix} \alpha \\ \beta \end{pmatrix} \begin{pmatrix} \alpha^* & \beta^* \end{pmatrix} = \begin{pmatrix} |\alpha|^2 & \alpha\beta^* \\ \alpha^*\beta & |\beta|^2 \end{pmatrix} \tag{2.18}$$

where we recall from Eq. 2.10 that $|\alpha|^2+|\beta|^2 = 1$. In Yafet's work, the coherences (off-diagonal elements) were overlooked. Consequently, spin mixing wasn't accounted for, so that pseudo-spin polarisation and actual spin polarisation were treated as equivalent, and thus a $k-$dependent expectation value of $\hat{S}_z$ is not achieved. He therefore could not correctly account for the amount of spin-flips in each scattering transition. This is especially problematic in materials in which the Brillouin zone contains regions of very high spin mixing [216], known as spin hotspots. In 2016, Baral et al [217] developed a torque operator due to the e-ph interaction that determines the spin dynamics; deriving a modified expression for the EY spin relaxation time using a reduced density matrix which

included the off-diagonal elements of ρ. This approach achieved a more accurate description of the dynamics of the spin vector.

The EY mechanism relies on empirical models and symmetry analysis, which are laborious approaches even for simple systems [199]. Even the more modern methods used by Kiss et al depend on empirical models. In addition, methods such as those used by Restrepo and Windl assume direct proportionality between spin-flip and momentum-scattering interactions [199], while other methods [218] depend on the direct proportionality between the relaxation times. In 2019, Park, Zhou and Bernardi [199] presented a first-principles approach for computing the spin-flip matrix elements and the spin-phonon relaxation times without any assumptions on the relationship between the matrix elements or the spin-flip and momentum scattering. They treated the spinor wavefunctions and SOC through fully-relativistic density functional theory, applying their method to Si and diamond; producing results which compared well with experiment. This opened up the possibility to predict spin-phonon relaxation times in a wide range of materials.

In conclusion, it was the discovery and subsequent understanding of electron spin that not only deepened our knowledge of quantum mechanics, thus laying the foundation for the development of spintronics. It wasn't until the late 20^{th} century that it was realised that spin could be used to process digital information encoded with binary bits. As discussed in Chapter 1, spintronics devices harnesses the spin of electrons, using electron spins as information carriers. Since we have proposed GeSn as a potential semiconductor in spintronics devices, we will examining its electronic properties on a fundamental level in a later chapter.

Part II

Theory

Chapter 3

Band Structure Methods

A fundamental understanding of a material's band structure is essential for predicting and tailoring its electronic and optical properties. In this chapter, we introduce the theoretical and computational methods used to model and analyse the electronic structure of semiconductors, with particular emphasis on first-principles approaches, particularly density functional theory and the GW approximation. Key concepts such as plane-wave basis sets, pseudopotentials, and the virtual crystal approximation are addressed, while we also discuss semi-empirical models, including the Kane model and the $\mathbf{k}.\mathbf{p}$ method, which we use for calculating more accurate band structures.

3.1 Density Functional Theory

Density functional theory (DFT) is a highly useful computational approach that enables the quantitative analysis of various material properties in a purely theoretical manner, without the need for experimental data. DFT methods offer the capability to model materials that are challenging to study through experimentation, or as a means to independently validate experimental findings in less explored material systems. The overall aim of DFT is to solve the time-independent Schroedinger equation:

$$H\left|\Psi\right\rangle = E\left|\Psi\right\rangle \tag{3.1}$$

In condensed matter, many properties of materials can be described theoretically

by a Hamiltonian (H) for a system of nuclei and their electrons:

$$H = -\frac{\hbar^2}{2m_e}\sum_i \nabla_i^2 - \sum_I \frac{\hbar^2}{2M_I}\nabla_I^2 - \sum_{i,I}\frac{Z_I e^2}{|\mathbf{r}_i - \mathbf{R}_I|} + \frac{1}{2}\sum_{i\neq j}\frac{e^2}{|\mathbf{r}_i - \mathbf{r}_j|} + \frac{1}{2}\sum_{I\neq J}\frac{Z_I Z_J e^2}{|\mathbf{R}_I - \mathbf{R}_J|} \tag{3.2}$$

For such a Hamiltonian in Eq. 3.1, E represents the eigen-energy of the many-body wave function (Ψ) for the system of electrons and nuclei. In Eq. 3.2, upper-case subscripts denote nuclei with mass M_I and coordinates R_I with charge eZ_I, and lower-case subscripts represents electrons with mass m_e and position r_i. The first and second terms represent the kinetic energies of the electrons and nuclei, respectively. The third, fourth and fifth terms represent the electrons-nuclei interactions, electron-electron interactions and the interaction between nuclei, respectively.

We employ the Born-Oppenheimer approximation, whereby the nuclei masses are assumed to be infinitely heavier than the electrons, thus the electrons respond more rapidly to changes in their surroundings than nuclei. The electrons can therefore be considered to be moving in the field of fixed nuclei. In essence, we are saying that the velocity of the nuclei compared to the electrons is negligible, and therefore the kinetic energy of the nuclei is now zero and the nuclei-nuclei potential energy (which we will now denote as V_{nn}) is a constant. This reduces Eq. 3.2 to Eq. 3.3 below:

$$H = -\frac{\hbar^2}{2m_e}\sum_i \nabla_i^2 - \sum_{i,I}\frac{Z_I e^2}{|\mathbf{r}_i - \mathbf{R}_I|} + \frac{1}{2}\sum_{i\neq j}\frac{e^2}{|\mathbf{r}_i - \mathbf{r}_j|} + V_{nn} \tag{3.3}$$

The system can be thought of as a set of N electrons evolving under the influence of an external potential V_{ext}, such that:

$$V_{ext}(\mathbf{r}_i) = \frac{Z_I e^2}{|\mathbf{r}_i - \mathbf{R}_I|} \tag{3.4}$$

Finally, by defining $U(\mathbf{r}_i, \mathbf{r}_j) = \frac{1}{2}\frac{e^2}{|\mathbf{r}_i - \mathbf{r}_j|}$, we can express the N-electron Hamiltonian as:

$$H = \sum_i^N \left(-\frac{\hbar^2}{2m_e}\nabla_i^2 + V_{ext}(\mathbf{r}_i)\right) - \sum_{i\neq j} U(\mathbf{r}_i, \mathbf{r}_j) \tag{3.5}$$

Finding the eigenvalues and wave functions in such a many-body system is near-impossible for periodic crystals. It is more practical to instead calculate the electronic density, which contains all physically meaningful properties of

the crystal. This is computationally possible thanks to the development of DFT, which allows one to consider a many-body interacting electron gas as a single particle moving in an effective potential V_{eff}. It relies on two theorems, which were proved by Hohenberg and Kohn [219]:

Theorem 1: The external potential V_{ext} acting on the electrons is uniquely determined by the ground-state electron density $n(\mathbf{r})$. Thus, V_{ext} and all other ground state properties can be determined by $n(\mathbf{r})$.

Theorem 2: For any external potential V_{ext}, there exists a universal energy functional $E[n]$ in terms of the density $n(\mathbf{r})$ whose global minimum is the exact ground state energy of the many-body system.

Given these theorems, Kohn and Sham [220] proposed solving the many-body problem by replacing the system with an easier-to-solve auxiliary problem, whereby the ground-state density of the original interacting system is the same as that of non-interacting particles. This leads to the Kohn-Sham equation, which is the non-interacting Schroedinger equation:

$$H_{aux}\psi_i(\mathbf{r}) = \epsilon_i(\mathbf{r})\psi_i(\mathbf{r}) \tag{3.6}$$

where $\psi_i(\mathbf{r})$ are the single particle orbitals. The auxiliary Hamiltonian H_{aux} is given by

$$H_{aux} = \frac{-\hbar^2}{2m_e}\nabla^2 + V_{eff}(\mathbf{r}) \tag{3.7}$$

where V_{eff}, known as the Kohn-Sham potential, is an effective one-particle potential felt only by electrons and yields the same density:

$$n(\mathbf{r}) = \sum_{i=1}^{N} |\psi_i(\mathbf{r})|^2 \tag{3.8}$$

as the interacting system for electrons at position $\mathbf{r}$. If we define the Coulomb interaction energy of the electron density interacting with itself, known as the Hartree potential, V_H, as:

$$V_H\left[n(\mathbf{r})\right] = e^2 \int d^3r' \frac{n(\mathbf{r})}{|\mathbf{r} - \mathbf{r'}|} \tag{3.9}$$

and also account for many-body effects with the exchange-correlation functional energy E_{XC}, which essentially corresponds to the energy difference between the

fully-interacting many-electron system and a non-interacting system of electrons with the same charge density $n(\mathbf{r})$, we can define the effective potential as:

$$V_{eff}(\mathbf{r}) = V_{ext}(\mathbf{r}) + V_H\left[n(\mathbf{r})\right] + V_{XC}[n](\mathbf{r}) \tag{3.10}$$

where $V_{XC}(\mathbf{r}) = \frac{\delta E_{XC}}{\delta n(\mathbf{r})}$ is the potential that defines the exchange and correlation contributions to the single electron equations. A solution to the Kohn-Sham (KS) equations (Eq. 3.6, 3.7, 3.8 and 3.10) is found by performing a self-consistent iterative method:

1. The initial trial electron density ***n(r)*** is defined.
2. Using this electron density, solve the KS equations to find the single-particle wavefunctions $\psi_i(\mathbf{r})$.
3. Calculate the electron density defined by the single-particle wavefunctions ψ_i from step (2), such that $n_{KS}(\mathbf{r}) = 2\sum_i \psi_i^*(\mathbf{r})\psi_i(\mathbf{r})$
4. If $n_{KS}(\mathbf{r}) = n(\mathbf{r})$, this is the ground state electron density which can be used to calculate the total energy. If $n_{KS}(\mathbf{r}) \neq n(\mathbf{r})$, $n(\mathbf{r})$ is updated and the iterative process starts again from step (2).

Ultimately, we are solving Equations 3.6, 3.7, 3.8 and 3.10 iteratively until one achieves self-consistency between the density and the potential V_{eff}, with the condition that the ground-state density of the original interacting system is equal to that of some exactly soluble system of independent-particles. Typically in any DFT calculation, a self-consistent calculation is initially carried out to determine the electron density of the system. This is followed by a non-self-consistent calculation where the band structure and other material properties are determined.

3.1.1 Local Density Approximation

The exchange-correlation energy E_{XC} is unknown, and therefore must be defined. Only the minimum energy value of the exchange-correlation energy functional has physical meaning. At the minimum, the Kohn-Sham energy functional is equal to the ground-state energy of the system of electrons. Several approaches exist for the approximation of E_{XC}, such as the local density approximation (LDA), the generalised gradient approximation (GGA), and the hybrid XC functional. We implement the LDA, whereby the exchange-correlation energy

per particle at any particular point in space is approximated as the exchange-correlation energy per particle of a homogenous electron gas with a constant electron density n at all points in space equivalent to the density at this same point. It is a local approximation, where E_{XC} of the LDA form can be written as:

$$E_{XC}^{LDA}[n(\mathbf{r})] = \int d\mathbf{r}\, n(\mathbf{r})\, \epsilon_{XC}[n(\mathbf{r})] \tag{3.11}$$

where $\epsilon_{XC}[n(\mathbf{r})]$ is the exchange-correlation energy per particle of a homogeneous electron gas of density $n(\mathbf{r})$, and $\epsilon_{XC}[n(\mathbf{r})]$ is multiplied by a weighted probability $n(\mathbf{r})$ that there exists an electron at position $\mathbf{r}$. The exchange-correlation energy is linearly separated into exchange and correlation terms:

$$\epsilon_{XC}[n(\mathbf{r})] = \epsilon_X[n(\mathbf{r})] + \epsilon_C[n(\mathbf{r})] \tag{3.12}$$

The exchange energy arises from the Pauli exclusion principle; accounting for the fact that two electrons with the same spin cannot occupy the same quantum state at the same position simultaneously. It is typically derived exactly for a homogeneous electron gas. If we take a homogenous electron gas of N_e electrons interacting in a volume V which has a positive background charge (keeping the overall charge of the system neutral), the Wigner-Seitz radius r_S is the radius of a sphere whose volume is that of a single electron, such that:

$$\frac{V}{N_e} = \frac{1}{n} = \frac{4\pi r_S^3}{3} \tag{3.13}$$

Isolating r_S in terms of n, the exchange energy per electron can therefore be expressed as:

$$\epsilon_X = \frac{E_X}{N_e} = -\frac{1}{4\pi\epsilon_0}\frac{3e^2}{4\pi}\left(\frac{9\pi}{4}\right)^{\frac{1}{3}}\frac{1}{r_S} \tag{3.14}$$

Applying Eq. 3.14 to Eq. 3.11 give us Eq. 3.15 below, which shows the LDA exchange energy, a more thorough derivation of which can be found in Perdew and Zunger [221].

$$E_X^{LDA}[n(\mathbf{r})] = -\frac{3}{4}\left(\frac{3}{\pi}\right)^{1/3}\int n(\mathbf{r})^{4/3} d\mathbf{r} \tag{3.15}$$

Although the integrand of Eq. 3.15 allows for an analytical solution for the exchange energy contributions ϵ_X, there are no such expressions for ϵ_C, the

correlation contributions. However, it can be parameterised using highly accurate numerical quantum Monte-Carlo simulations of the homogeneous electron gas. The prevailing parameterisation for the correlation functional is the one introduced by Ref. [221] and applied to homogeneous electron gases at different electron densities by Ceperley and Alder [222].

The LDA provides precise results for many materials, particularly structural properties such as lattice constants and bond lengths. Although the LDA is computationally efficient and forms the basis for many DFT calculations, it underestimates band gaps in semiconductors, often predicting materials to be more metallic than they are. The correct way to correct for this underestimation is discussed later in the chapter.

3.1.2 Structural Relaxation

The results in this thesis rely heavily on alloy scattering effects, which arise when substitutional impurities are introduced into the crystal lattice. These impurities cause local distortions by displacing nearby host atoms, which in turn alters the material's band structure and other properties. In such calculations, accounting for structural relaxation is crucial for accurately capturing these effects.

Structural relaxation is an iterative process used to find the equilibrium atomic positions by minimizing the forces acting on atoms and the stress on the unit cell. This involves calculating the total energy, the forces and the stress tensor for a given configuration, then adjusting the atomic positions until the forces and energy converge below specified thresholds. This is possible thanks to the Hellmann-Feyman theorem [223], which states that the force on an atom A can be defined as:

$$F_A = \frac{\partial E}{\partial \mathbf{R}_A} = -\langle\psi| \frac{\partial H}{\partial \mathbf{R}_A} |\psi\rangle \tag{3.16}$$

3.1.3 Plane Waves

Plane waves are a natural basis to represent single-particle wavefunctions ψ_i. In this thesis, we are concerned with the calculation of properties in periodic solids. Bloch's theorem [224] provides a framework for understanding how electrons behave in periodic crystal lattices. It states that the wave function $\psi_{nk}(\vec{r})$ for a bulk material can be expressed as the product of a plane wave term $e^{i\vec{k}.\vec{r}}$ and a

function $u_{nk}(\vec{r})$ with the same periodicity as the lattice:

$$\psi_{nk}(\vec{r}) = \frac{1}{\sqrt{N_{cell}}} e^{i\vec{k}.\vec{r}} u_{nk}(\vec{r}) \tag{3.17}$$

where N_{cell} is the number of primitive cells, n is the n^{th} state corresponding to wavevector $\vec{k}$, and $\vec{r}$ is the position vector. If $\vec{R}$ is a Bravais lattice vector, then:

$$u_{nk}(\vec{r} + \vec{R}) = u_{nk}(\vec{r}) \tag{3.18}$$

This implies that states $\vec{k}$ which lie beyond the first Brillouin zone (BZ) can be translated back into the BZ by adding a suitable reciprocal lattice vector $\vec{G}$. Electron wave functions of the form $\psi_{nk}(\vec{r})$ are called Bloch states. If we plot the energy states E_{nk} in a periodic solid as a function of their corresponding wavevectors $\vec{k}$, this gives the band structure of the solid (which we show in Chapter 4). A proof of Bloch's theorem can be found in Ashcroft and Mermin [225].

The periodic component u_{nk} can be Fourier transformed and expressed in terms of plane waves of the reciprocal lattice vectors $\mathbf{G}$:

$$u_{nk}(\mathbf{r}) = \frac{1}{\sqrt{\Omega_{cell}}} \sum_{\mathbf{G}} c_{nk}\ e^{i\mathbf{G}.r} \tag{3.19}$$

where Ω_{cell} is the primitive cell volume, and $\mathbf{G}$ satisfies $\mathbf{G} \cdot \mathbf{R} = 2\pi \times integer$. Using Bloch's theorem, we can now define a wavefunction of a periodic solid as:

$$\psi_{nk}(\mathbf{r}) = \frac{1}{\sqrt{N_{cell}\Omega_{cell}}} \sum_{\mathbf{G}} c_{nk}\ e^{i(k+\mathbf{G}).r} \tag{3.20}$$

As a result, Eq. 3.6, the Kohn-Sham Equation, can be rewritten as:

$$\sum_{\mathbf{G}'} \left[\frac{\hbar^2}{2m_e} |\mathbf{k} + \mathbf{G}|^2 \delta_{\mathbf{G}\mathbf{G}'} + V_{eff}(\mathbf{G} - \mathbf{G}') \right] c_{nk}(\mathbf{G}) = \epsilon_{nk}\ c_{nk}(\mathbf{G}) \tag{3.21}$$

where the Fourier transform of V_{eff} is:

$$V_{eff}(\mathbf{G}) = \frac{1}{\sqrt{\Omega_{cell}}} \int_{\Omega_{cell}} V_{eff}(\mathbf{r})\ e^{-i\mathbf{G}.r} d\mathbf{r} \tag{3.22}$$

The eigenvalues (eigen-energies) ϵ_{nk} in Eq. 3.21 are discrete, but become

a continuum of bands when the **k**-points lie close to each other. For large systems, **k** is a quasi-continuous variable, but the periodic part of the electronic wavefunctions (u_{nk}) will be almost identical at **k** points very close to each other. This allows the wavefunction to be represented over a small region of reciprocal space by a single **k**-point. The integration over **k**-space required to calculate the density can therefore be reduced to a sum over a **k**-point grid. We can therefore calculate the total energy of the system from electronic states computed on a finite **k**-point grid, provided it is fine enough to capture variations in the electron density. The most common method for generating this finite grid is the Monkhorst and Pack scheme [226].

3.1.4 Pseudopotentials

However, the use of plane waves becomes problematic when dealing with regions near the nuclei. Core electrons are relatively unaffected by an atom's chemical environment, with the majority of physical properties of solids being solely dependent on its valence electrons. Using plane-waves to expand the electron wavefunctions which include both the core and valence electrons is excessively time consuming. Moreover, since valence states are orthogonal to core states, valence electron wavefunctions will have a large number of nodes and would require a large number of plane-waves to describe them. It is therefore practical to replace the strong Coulomb potential of the nucleus with a pseudopotential which accounts for the screening and repulsion of the core electrons, therefore replacing the valence electron wave-functions with pseudo-wave-functions. Unlike valence electron wave-functions, the pseudo-wave-functions vary smoothly in the core region. Pseudopotentials essentially reduce the computational cost of solving the Schrödinger equation by approximating electron behaviour in a way that reduces the need to consider the behaviour of the nucleus and inner electrons.

Since the crystal potential is periodic, so too is the pseudopotential, and it can be expanded into a Fourier series over the reciprocal lattice. Electronic-structure software employing pseudopotentials (such as ABINIT, VASP or Quantum ESPRESSO) will usually incorporate relativistic effects on core electrons in an approximate manner by using scalar-relativistic pseudopotentials. This is a computationally efficient and quite reliable approach. The most popular pseudopotentials are norm-conserving. We use Hartwigsen-Goedecker-Hutter (HGH) type pseudopotentials [227], which are LDA pseudopotentials and are

norm-conserving.

3.1.5 ABINIT

ABINIT [228] is an open-source software package used to perform first-principles electronic structure calculations on materials. These first-principles calculations are based on DFT, using pseudopotentials and plane-wave basis sets to represent the electronic structures of materials. For band structure calculations on ABNIIT, a self-consistent field (SCF) calculation is performed whereby the density is outputted, followed by a second calculation which uses this density in a non-SCF band structure calculation. ABINIT is capable of predicting the electronic structures, crystal structures, optical properties, and vibrational properties of materials, and can also take advantage of parallel computing. Its user-friendly interface and extensive documentation makes it one of the most used packages in DFT. In this thesis, we will use ABINIT within the DFT framework to solve the KS equations iteratively for a system of atoms from first principles.

ABINIT also includes a post-processor code called "Cut 3-Dimensional" (Cut3d), which analyses any file produced by ABINIT that contains 3D real space data, such as potential files, density files and wavefunction files. In the case of wave-function files, analysis of only one wave function at a time may be performed, where the user must specify the k-point, band number and (where necessary) the spinor-component. This was necessary for several calculations in this work, including determining the momentum matrix elements, which are used in the calculation of optical properties, and wavefunction overlaps, which are essential in computing scattering matrix elements.

3.1.5.1 Convergence Testing in ABINIT

In DFT calculations using plane-wave basis sets, as implemented in ABINIT, the accuracy of the computed results is closely tied to the choice of the plane-wave energy cut-off parameter, denoted as E_{cut}. The plane-wave energy cut-off defines the maximum kinetic energy of the plane waves included in the basis set used to expand the electronic wavefunctions. Since DFT calculations involve solving the Kohn-Sham equations self-consistently, it is crucial to ensure that the truncation of the basis set does not compromise the reliability of the results. The plane-wave basis set employed in ABINIT is truncated by restricting the kinetic energy of the included plane waves to a value below E_{cut}. In other words, if we recall Eq.

3.21, the kinetic energy term has upper bound:

$$\frac{\hbar^2}{2m_e}|\mathbf{k}+\mathbf{G}|^2 < E_{cut} \tag{3.23}$$

for all k in the Brillouin Zone. A higher cut-off energy allows the inclusion of more plane waves, resulting in a more accurate description of the electronic wavefunctions and, consequently, more precise total energies, forces, and stress tensors. However, an excessively high cut-off can lead to unnecessary computational cost without significant improvement in accuracy, since plane-waves with higher energies contribute less to the wavefunction. Therefore, it is essential to perform convergence tests to determine the minimum E_{cut} that yields converged results within an acceptable tolerance for the system under investigation. Typically, the total energy or lattice parameter is calculated at incrementally increased values of E_{cut} until the differences between successive calculations are within a chosen tolerance.

Performing plane-wave pseudopotential calculations also requires defining the k-point grid to sample the Brillouin zone effectively. The *ngkpt* variable in ABINIT is used to define a Monkhorst-Pack k-point grid, which defines the number of k-points along each axis in the reciprocal space grid. For instance, a value of 4x4x4 creates a grid with four k-points along each of the three lattice directions (giving a total of $4^3 = 64$ points). It is once again essential to establish clear convergence criteria in a similar manner to E_{cut}. The accurate sampling of k-points plays a crucial role in ensuring the accuracy and efficiency of these computations.

3.2 GW Method

Whilst DFT gives an accurate total energy for the many-body system, and for many systems treated in this work the bands produced are a very good approximation for calculating different material properties, the energy eigenvalues of the KS Hamiltonian are not the correct excitation energies of the system. The eigenvalues produced are those that correspond to a one-electron potential that has the same total density as the many-body system. More precisely, the exchange-correlation functionals describing the interactions between electrons often fail to capture the electron-electron interactions accurately, which leads to a bandgap underestimation. Therefore, properties such as the band gap are

not well produced and require another method of calculation to obtain true accuracy.

One such method is GW, which operates by finding the response of a system that is perturbed by transitioning an electron to higher energy states. These energy transitions correspond to the observable energies. The name GW stems from the Green's function G, which describes the propagation of an electron in a solid, and the screened Coulomb interaction W which represents the interaction between electrons, taking into account the screening effect due to other electrons.

Using ABINIT, we implement the single-shot GW method (G_0W_0), which begins with a zeroth-order approximation (a DFT calculation) of the wavefunctions and energies. This is followed by a calculation of the screening (KS susceptibility χ^0 and then inverse dielectric matrix ϵ^{-1}), such that:

$$W(\mathbf{r}, \mathbf{r}'; \omega) = \int d\mathbf{r}''\, \epsilon^{-1}(\mathbf{r}, \mathbf{r}''; \omega)\, v(\mathbf{r}'' - \mathbf{r}') \tag{3.24}$$

where v is the bare Coulomb interaction. The KS band structure and W are then used to evaluate the matrix elements of the self-energy $\Sigma = iGW$, finally obtaining the quasi-particle corrections. In this process, we check for convergence of the screening with respect to both the number of bands and plane-waves, as well as convergence of the self-energy with respect to the number of bands.

GW is very computationally expensive, and is best used to find bandgaps for a small number of k-points rather than to produce an entire band structure. While the GW method captures the different many-body effects at the Γ and L points in GeSn, a simple scissors shift applies a uniform correction to all states and cannot correct the relative difference between these gaps, which DFT miscalculates. An excellent review of the mathematics behind GW can be found in Ref. [229].

3.3 Virtual Crystal Approximation

The virtual crystal approximation (VCA) is a simple and yet effective theoretical framework used for studying alloys. Its purpose is due to the fact that electronic structures become more complex when impurities are introduced into the crystal lattice, as in any alloy. The VCA is an interpolation of the behaviours of the constituent atoms, and can be used in determining many properties of an alloy, including the bulk modulus or lattice constant.

In electronic structure calculations, we implement the alchemical potential

approximation (APA), which is essentially the VCA applied to potentials. The APA works by treating each atom in the system as an "alloy" by averaging the potentials V of the individual constituents. In the case of a GeSn alloy of Sn concentration x:

$$V_{GeSn} = (1 - x)V_{Ge} + xV_{Sn}$$

where V_{Ge} and V_{Sn} are the potentials of Ge and Sn respectively. This approximation essentially smooths out the abrupt changes in the potential energy landscape created by the atomic disorder, making it simpler to solve the quantum mechanical equations that describe the electronic structure. By solving the Schrödinger equation with the effective potential and composition, one can calculate the electronic band structure of the virtual crystal. Pseudopotentials are often used in the APA.

However, as we will see in later chapters, the APA does not work when calculating elastic scattering parameters, since it doesn't capture certain effects such as local atomic fluctuations or short-range order. Methods beyond the APA are required to find the elastic scattering contributions.

3.4 Kane Model

Given the underestimation of the band energies using the LDA and the high computational cost of the GW method, an alternative approach is needed to accurately model the band structure dispersion near the bandgap for multiple $\mathbf{k}$-points.

A suitable theoretical framework for such an issue is the Kane model [230] which, in bulk (3D) semiconductors, provides a compact yet effective way to capture the energy-momentum relationship near the Brillouin zone centre (the Γ point). The Kane model centres around constructing a Kane Hamiltonian which couples the material's conduction and valence bands through momentum matrix elements. A four-band Kane model is commonly used (eight-band when SOC is considered), which considers one conduction band state and three valence band states (light-hole, heavy-hole, and split-off bands). In this case, the model is constructed as a 4×4 matrix Hamiltonian (below) describing the coupling between these states, taking into account the $3D$ crystal momentum:

$$\mathbf{H}(k_x, k_y, k_z) = \begin{bmatrix} E_c & bk_x & bk_y & bk_z \\ bk_x & E_v & 0 & 0 \\ bk_y & 0 & E_v & 0 \\ bk_z & 0 & 0 & E_v \end{bmatrix}$$

In this Hamiltonian, the conduction band energy $E_c = a(k_x^2+k_y^2+k_z^2)+E_g$, where E_g is the direct gap, and the valence band energy $E_v = -a(k_x^2+k_y^2+k_z^2)$, where the parameter $a \approx \frac{\hbar^2}{2m^*}$. The parameter $b = \frac{\hbar^2}{2m^*}|p|$ represents the coupling between the conduction and valence bands, typically involving the momentum matrix elements **p**. The calculated DFT eigen-energies are fitted to the eigenvalues of this matrix, whereby we solve for a and b.

Unlike the scissors shift, which applies a rigid bandgap correction, the Kane model accounts for band coupling between the conduction and valence bands and resulting non-parabolicity, providing a more physically accurate description of the electronic structure in narrow-gap semiconductors. This is essential for describing the effective mass and mobility of electrons in 3D systems.

3.5 k.p Theory

k.p theory is based on time-independent perturbation theory, employed to study how the electronic structure and energy levels of a material change in response to external perturbations (such as an external electric field or strain) with various levels of refinement. For example, the number of basis states (bands) can be varied (e.g. single-band, 8-band) [231].

k.p theory operates by expanding the electronic wave functions and Hamiltonian (i.e. calculating the eigenvalues and eigenvectors) around a reference **k**-point ($\mathbf{k_0}$), usually a high-symmetry point in the BZ such as the Γ-point. The resulting Hamiltonian is a sum of the free-electron term H_0 and the **k**-dependent term H_k, such that:

$$\begin{aligned} H_0 &= \frac{\mathbf{p}^2}{2m} + V \\ H_k &= \frac{\hbar}{m}(\mathbf{k}.\mathbf{p}) + \frac{\hbar^2\mathbf{k}^2}{2m} \end{aligned} \tag{3.25}$$

where **k** is a simple vector that characterises the periodicity of the wavefunction,

and the momentum operator $\mathbf{p} \neq \hbar\mathbf{k}$. Thus, the band structure over the entire BZ can be extrapolated from the BZ centre energy gaps and optical matrix elements [105]. Following Schulz and O'Reilly [232], applying this Hamiltonian to a Bloch wavefunction, second-order perturbation theory can be used to evaluate the variation of the energy levels $E_n(\mathbf{k})$ at band n with wavevector $\mathbf{k}$ close to the reference point $\mathbf{k_0}$, shown in Eq. 3.26 below:

$$E_n(\mathbf{k}) = E_n(\mathbf{k_0}) + \frac{\hbar}{m}\mathbf{k}.\mathbf{p}_{nn} + \frac{\hbar^2\mathbf{k}^2}{2m} + \frac{\hbar^2}{m^2}\sum_{n\neq n'}\frac{|\mathbf{k}.\mathbf{p}_{nn'}|^2}{E_n(\mathbf{k_0}) - E_{n'}(\mathbf{k_0})} \tag{3.26}$$

where $\mathbf{p}_{nn'}$ denotes the momentum matrix element between the nth and $n'th$ states at $\mathbf{k_0}$.

The **k.p** method is particularly useful in estimating the effective masses of bands by perturbatively calculating the energy dispersion about the known BZ point. We exploit the fact that all of the important information in GeSn can be extracted from the Γ point. Using this, we can use a **k.p** model to correct the DFT band structure for GW using the momentum matrix elements at Γ. A detailed description of how **k.p** theory can be found in Ref. [233].

Chapter 4

Band Structure of GeSn

The electronic structure methods discussed in the previous chapter provide the theoretical foundation for analysing and predicting the band structures of semiconducting materials. In this chapter, we apply these electronic structure techniques to calculate the band structure in GeSn alloys. Special attention is given to how Sn incorporation and strain modify the conduction bands, leading to the transition from an indirect to a direct band gap. The insights gained from these models enable the understanding of key properties such as effective masses and the density of states; parameters that are essential for evaluating the potential of GeSn in electronic, spintronic and optoelectronic applications.

4.1 Band structures of Ge and Sn

Changes in the band structure of GeSn with composition can be understood by examining the electronic band structures of its constituent elements, Ge and Sn. Germanium is an indirect-gap semiconductor, with a conduction band minimum of $0.66\ eV$ at the L point and a higher-energy direct gap of $0.80\ eV$ at the Γ point [91, 234, 235, 236] at room temperature. The relatively small energy difference of just $140\ meV$ between the L and Γ valleys gives Ge a pseudo-direct band gap character. In contrast, α-Sn exhibits a negative direct band gap (or anti-gap) of $-0.41\ eV$ at the Γ point [237], resulting in a semimetallic nature.

Figures 4.1 and 4.2 show the band structures of bulk Ge and Sn respectively, calculated using DFT and corrected with GW and a 100-band $\mathbf{k}.\mathbf{p}$ model. These figures show the bands for states near the highest filled valence bands and lowest unoccupied conduction bands, with the zero of the energy taken at the valence

band maximum. The critical symmetry points of the conduction band, known as valleys, at Γ, L and Δ represent $\vec{k} = \frac{2\pi}{a_0}[0,0,0]$, $\frac{2\pi}{a_0}[\frac{1}{2},\frac{1}{2},\frac{1}{2}]$ and $\frac{2\pi}{a_0}[0.83,0,0]$ respectively. The L band has 4 equivalent valleys, located in the $[111]$, $[\bar{1}11]$, $[1\bar{1}1]$ and $[11\bar{1}]$ directions, while the Δ band has 6 equivalent valleys in the $[100]$, $[\bar{1}00]$, $[010]$, $[0\bar{1}0]$, $[001]$ and $[00\bar{1}]$ directions.

The valence band for GeSn (at any concentration) reaches its maximum at $\vec{k} = 0$ (the Γ point). In Ge, the constant energy surfaces around this point are made up of three warped spheres: the heavy-hole (HH), light hole (LH) and split-off (SO) bands. Only in the presence of spin-orbit coupling do we see the breakage in degeneracy of the LH and HH bands, with the SO band being slightly lower again.

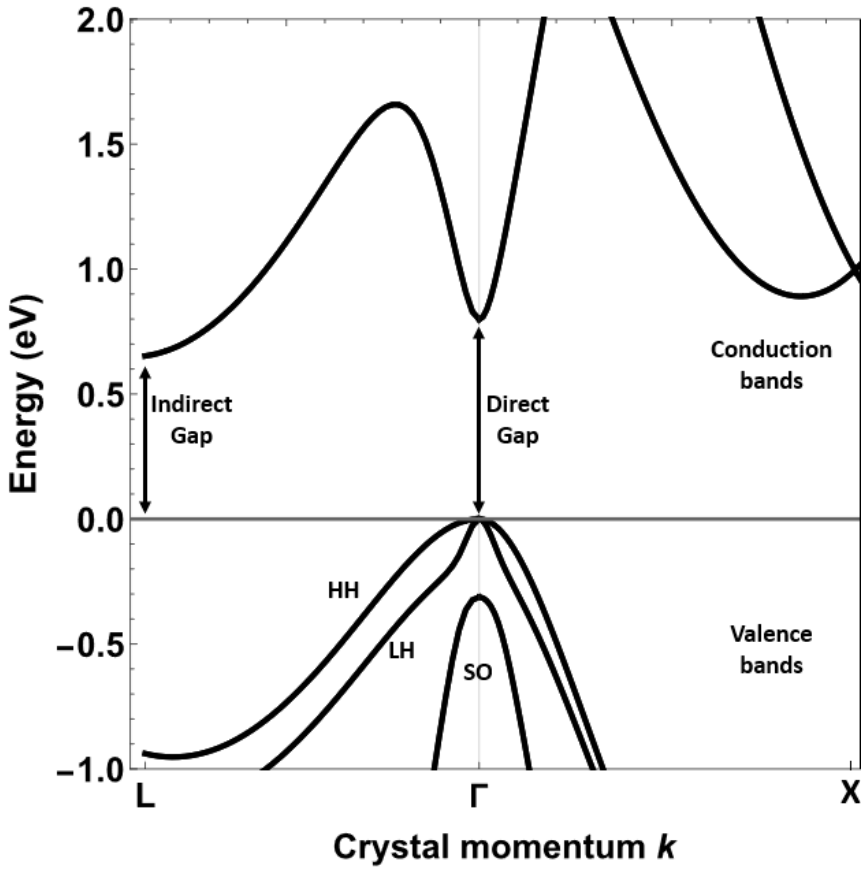

Figure 4.1: Electronic band structure of Ge in eV.

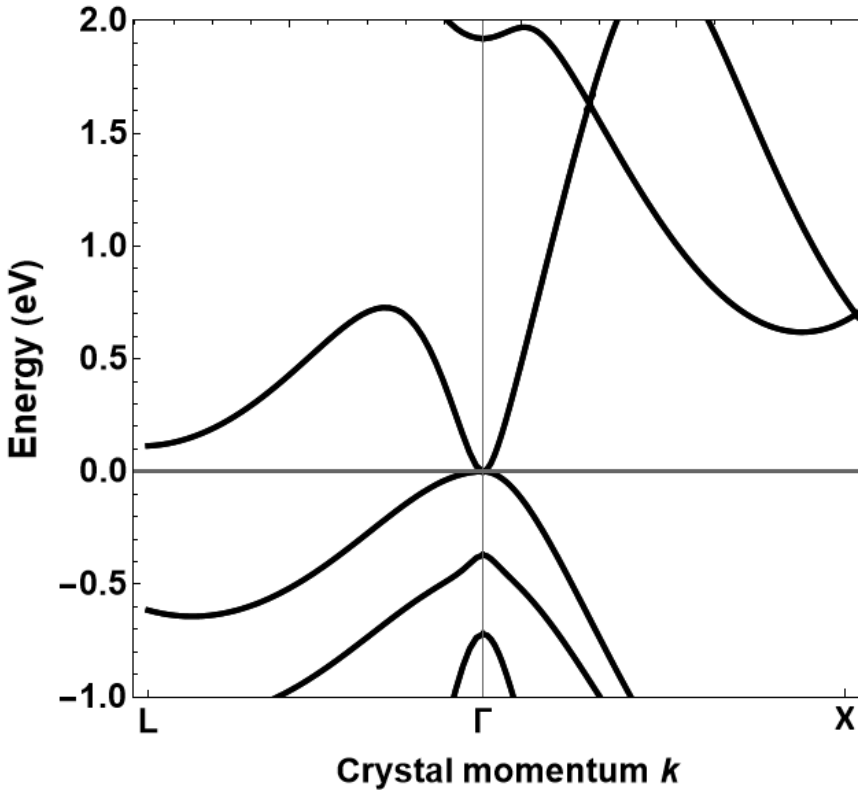

Figure 4.2: Electronic band structure for Sn in eV.

The bandgaps at critical points α of the BZ can be calculated using an interpolation of the two elements along with the respective bowing parameter b_α, which describes the deviation from linearity in the interpolation:

$$E_\alpha^{GeSn} = (1-x)E_\alpha^{Ge} + xE_\alpha^{Sn} + b_\alpha^{GeSn}x(1-x) \tag{4.1}$$

4.2 Achieving a Direct Gap in GeSn

In Chapter 1, we discussed the advantages of direct-gap semiconductors for electronic transport and optoelectronic applications. We also noted that recent research efforts to engineer a direct band gap in GeSn have primarily focused on two strategies: incorporating a sufficient amount of Sn [7, 238] and applying biaxial tensile strain to the bulk alloy.

4.2.1 Direct Gap through Addition of Sn

Alloying Ge with Sn causes the conduction band to shift downward relative to the valence band, with the energy at the Γ valley decreasing more rapidly than at

the L valley. Figures 4.3 and 4.4 shows our calculated changes in the direct and indirect band gaps of GeSn at room-temperature and 0K respectively, as functions of Sn concentration. The results indicate that GeSn becomes a direct band gap semiconductor at a Sn content of approximately 8.4% or higher. We calculated the bandgaps using DFT and firstly corrected using the GW approximation, which is also done at $0K$. The gaps were then corrected empirically for temperature using Varshni's empirical expression [239], shown in Equation 4.2, where the material-specific constants α and β, which quantify the rate at which the energy band gap decreases with temperature. These constants are also taken from Ref. [239], and are displayed in Table 4.1.

$$E_g(T) = E_g(0) - \frac{\alpha T^2}{T + \beta} \tag{4.2}$$

Table 4.1: Material constants α (in eV/K^2)and β (in K) at band valleys L and Γ of Ge.

	L	**Γ**
α	4.8×10^{-4}	5.82×10^{-4}
β	235	296

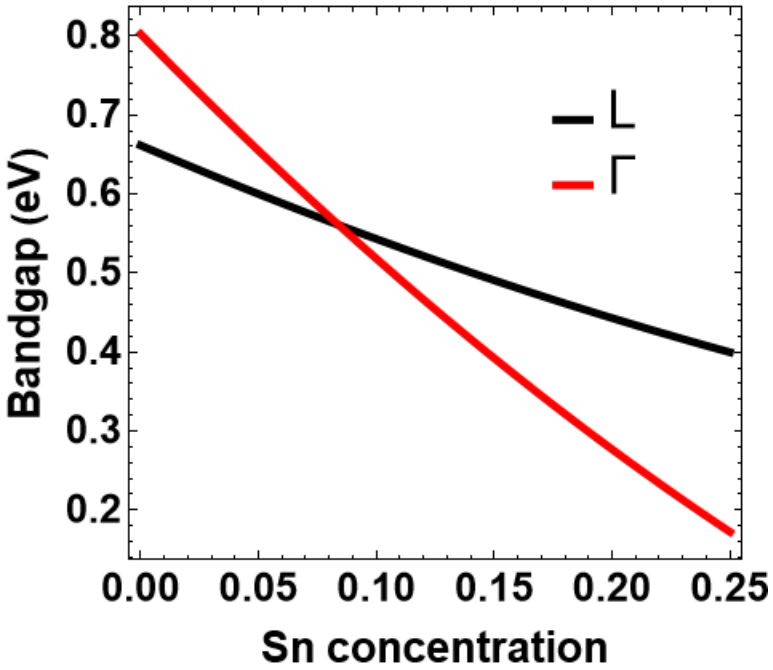

Figure 4.3: Calculated energy (eV) of Γ (red) and L (black) valleys in GeSn against Sn concentration at $300K$.

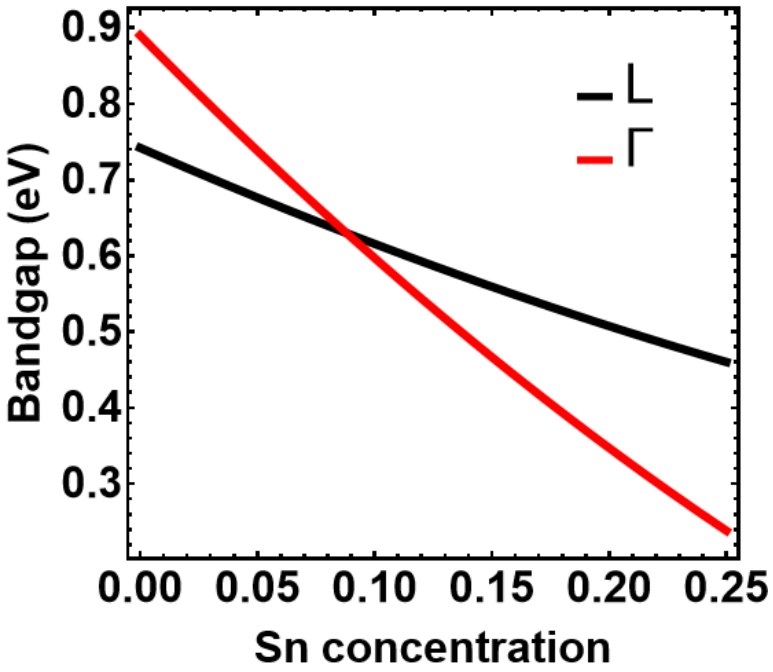

Figure 4.4: Calculated energy (eV) of Γ (red) and L (black) valleys in GeSn against Sn concentration at $0K$.

4.2.2 Direct Gap through Strain

When strain is applied to a semiconductor, it alters the interatomic spacings and symmetry of the lattice, thereby modifying the band structure. Mathematically, strain is described by the strain tensor ϵ_{ij}, a second-rank symmetric tensor that quantifies the relative displacement between atoms in different crystallographic directions. For small deformations, the strain tensor components are defined as:

$$\epsilon_{ij} = \frac{1}{2}\left(\frac{\partial(\delta R_i)}{\partial R_j} + \frac{\partial(\delta R_j)}{\partial R_i}\right) \tag{4.3}$$

where δR_i is the displacement vector field and R_i are the spatial coordinates. The parameters which describe the changes in the electronic structure with respect to atomic displacements are the deformation potentials. Within the framework of deformation potential theory, which was developed by Bardeen and Shockley [240] and generalised by Herring and Vogt [241], the energy shift of a band extremum α is expanded in terms of the components of the strain tensor:

$$\Delta E^{(\alpha)} = \sum_{ij} D_{ij}^{(\alpha)} \epsilon_{ij} \tag{4.4}$$

where the tensor quantity D_{ij} is the deformation potential. The deformation potential tensor obeys the same symmetry as the strain tensor, giving $D_{ij}^{(\alpha)} = D_{ji}^{(\alpha)}$, limiting the number of independent components of the deformation tensor is six. In a cubic lattice, the edges of the conduction band are located on symmetry lines. Therefore, the deformation potential operator of a particular band can be expressed via two or three deformation potential constants. We list these values for GeSn in Chapter 6.

Similar to the addition of Sn to Ge, biaxial tensile strain reduces the energy at the Γ valley faster than at the L valley. In this case, we have $\epsilon_{xx}^{i} = \epsilon_{yy}^{i} = \frac{a_i - a_0}{a_0} > 0$ at $i\%$ strain, where a_i and a_0 are the lattice constants of the strained and unstrained material, respectively. In DFT calculations, these values are fixed, while ϵ_{zz}^{i} is determined by atomic relaxation, yielding the Poisson ratio of the material or the Young's modulus.

In Figure 4.5 we show the variation of the L and Γ valley conduction band energies in Ge with biaxial tensile strain. We find a direct-gap occurs at around 1.5% strain, which is in excellent agreement with literature [235, 236, 242]. Menendez et al [243] have predicted that tensile-strained Ge exceeding 2% is achievable before breakage, which has been achieved in Refs [244, 245].

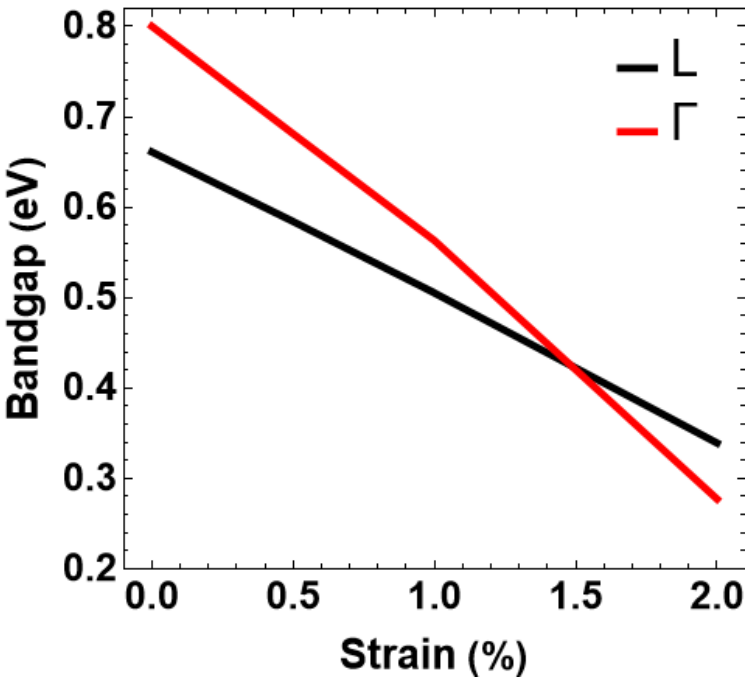

Figure 4.5: Calculated energy (eV) of Γ (red) and L (black) valleys in Ge against strain percentage at $300K$.

4.3 Effective Masses

An important consequence of the band structure is the curvature of the energy bands near their extrema, which directly influences the behaviour of charge carriers in a semiconductor. This curvature is quantitatively described by the concept of effective mass, which is the mass that an electron (or any particle) appears to have when responding to forces or interacting with other identical particles. In a three-dimensional system, the effective mass tensor m^*_{ij} is calculated using the second derivative of the calculated energy bands with respect to k-space, as per Eq. 4.5:

$$\frac{1}{m^*_{ij}} = \frac{1}{\hbar^2}\frac{\partial^2 E(\vec{k})}{\partial k_i \partial k_j} \tag{4.5}$$

where i and j are the components of the wavevector $\vec{k}$ in different directions. Effective masses at band minimum α can be differentiated by their direction of motion: the longitudinal mass m^α_l for transport along the longitudinal axis direction $\vec{k}_\alpha$, and the transverse mass m^α_t for transport along the transverse axes perpendicular to $\vec{k}_\alpha$. This description is particularly relevant for conduction band minima that form anisotropic energy surfaces. Since all relevant effective masses in this thesis are calculated in the longitudinal and transverse directions, we can utilise a simplified expression given in Eq. 4.6.

$$\frac{1}{m^*_i} = \frac{1}{\hbar^2}\frac{\partial^2 E(\vec{k})}{\partial k_i^2} \tag{4.6}$$

The surfaces of constant energy in GeSn at the L and Δ valleys represent eight half-ellipsoids and six full ellipsoids of revolution, respectively. The axes of revolution are parallel to the direction of the valley $\vec{k}_\alpha$, as we show in Fig. 4.6. The parabolicity of the L valley allows its carriers to be considered as free electrons with effective masses m^L_l and m^L_t. Expressions for the effective masses of GeSn at the L valley are given in Equations 4.7 and 4.8 as functions of Sn concentration x. The masses were calculated at different concentrations of Sn (in increments of 3% Sn) and fitted to a quadratic model.

$$m^L_l = (1.636 - 0.117x + 0.313x^2)m_e \tag{4.7}$$

$$m^L_t = (0.074 - 0.036x - 0.029x^2)m_e \tag{4.8}$$

In contrast, the conduction band at the Γ point in Ge exhibits strong non-

parabolicity, especially beyond the immediate vicinity of the band edge. Although the dispersion near the conduction band minimum at Γ is approximately parabolic, this holds only within a narrow energy range. As the energy increases, the band rapidly deviates from a simple quadratic form, transitioning toward a more linear-like dispersion due to strong coupling with higher conduction bands. This results in electrons in Ge possessing a low effective mass and higher group velocity, which as we will show in Chapter 6, leads to a high electron mobility. The addition of Sn leads to even larger deviations from a simple parabolic shape. Consequently, in GeSn, the band dispersion is such that the effective masses tends to 0, with an increased group velocity and electron mobility.

The effective masses of Ge at the Γ and L valleys can be found in Table 4.2 (in units of electron mass m_e), along with the bandgaps of Ge and Sn at L and Γ, and their lattice constants. Our calculated values for Ge are compared with experiments.

Table 4.2: Theoretically (th) calculated bandgaps (in eV), effective masses (in m_e) and lattice constants (in Å) of Ge and α-Sn at room temperature ($300\,\text{K}$) along with experimental (exp) values. The bandgaps are calculated using GW and corrected empirically for temperature.

Parameter	**Ge$_{\text{th}}$**	**Ge$_{\text{exp}}$**	**α-Sn**
$\mathbf{E_L}$	0.66	0.67$\pm$0.015 [246, 247, 248]	0.09
$\mathbf{E_\Gamma}$	0.8	0.805$\pm$0.01 [246, 249, 250]	-0.41
$\mathbf{m_l^L}$	1.636	1.64 [251]	1.83
$\mathbf{m_t^L}$	0.074	0.08 [251]	0.008
$\mathbf{m^\Gamma}$	0.04	0.049 $\pm$ 0.07 [242]	-
$\mathbf{a_0}$	5.58	5.65 [252, 238]	6.41

4.4 Scattering in GeSn

The transport of electrons and holes in a semiconductor is not determined solely by the band structure and effective masses; it is also significantly influenced by the frequency and nature of scattering events that disrupt carrier motion. Electrons in the conduction band undergo frequent collisions with phonons,

impurities, and other charge carriers. These scattering processes randomise the carriers' momentum and, in some cases, their energy, thereby limiting their ability to contribute to electrical conduction.

These scattering processes are closely tied to the band structure of the host material, particularly the positions and degeneracies of the conduction band minima. In indirect-gap GeSn, electron scattering is primarily governed by intravalley and intervalley transitions between the equivalent L valleys. In Figure 4.6, we label intervalley scattering between the L valleys as LL. With increased Sn concentration, scattering between the L and Γ valleys, as well as intravalley scattering at Γ, become dominant. Scattering between the Δ valleys can be of critical importance in GeSn with the application of an electric field or compressive strain via a Si substrate, whereby Δ bands can become the band minima. Scattering between the Δ valleys is characterised by g-type scattering, which is intra-axis scattering ($[100] \rightarrow [\bar{1}00]$) and f-type scattering, where an electron scattering from one Cartesian axis to another ($[100] \rightarrow [010]$), as shown in Figure 4.6. We often denote the six X points as $\pm X$, $\pm Y$ and $\pm Z$.

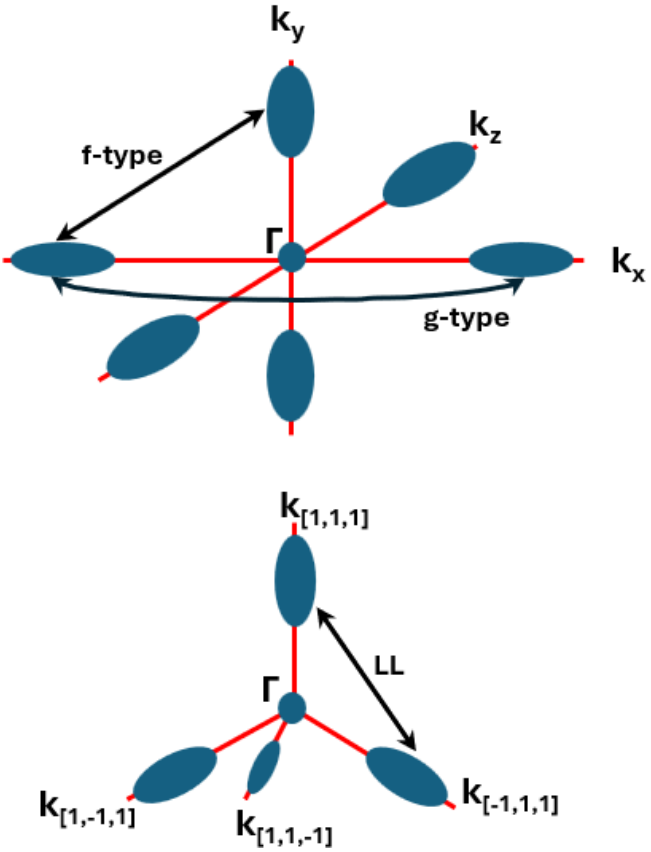

Figure 4.6: Schematics of the intervalley g-type and f-type scattering between the six equivalent Δ points, and the intervalley LL scattering between the four equivalent L points.

In the next chapter, we will discuss in depth the dominant scattering processes in GeSn, which include derivations of expressions for the various scattering rates. We will also examine photon absorption processes, where electrons become excited and move from the valence band to the conduction band, and photon emission processes, where electrons move down energy bands, emitting a photon.

Chapter 5

Scattering Theory

This chapter focuses on the theoretical framework and derivations necessary to understand key scattering mechanisms that influence electron transport, spin dynamics, absorption and emission in GeSn alloys.

In Section 5.1, we begin by using Fermi's Golden Rule to present the expressions for alloy and electron–phonon scattering rates, following established formulations from the literature, which govern transport and spin-relaxation in GeSn. We derive expressions for the alloy scattering matrix elements, which govern alloy scattering processes, and describe the frozen phonon method, which is used to determine the deformation potential associated with a particular phonon - a key parameter in determining the intervalley scattering rate by phonons. We summarise the standard derivation of the electron mobility from the Boltzmann Transport Equation in the relaxation-time approximation in Section 5.2. Finally, in Section 5.3, we use quasi-degenerate perturbation theory to derive an expression used to calculate the absorption coefficient and photoluminescence of GeSn over a wide spectral range. Our derivations in Section 5.3 present a simplified adaptation of previous work [253].

5.1 Electron Scattering

From Ashcroft and Mermin [254], in bulk cubic materials, the formal definition of the relaxation time $\tau^{(\alpha)}(\mathbf{k})$ at band valley α (and thus the total momentum scattering rate $R(\mathbf{k}_\alpha)$) is given by:

$$\frac{1}{\tau^{(\alpha)}(\mathbf{k})} = R(\mathbf{k}_\alpha) = \sum_\beta \int \frac{d^3\mathbf{k}'_\beta}{(2\pi)^3}\, \Gamma(\mathbf{k}'_\beta, \mathbf{k}_\alpha) \tag{5.1}$$

where $\Gamma(\mathbf{k'}_\beta, \mathbf{k}_\alpha)$ is the total scattering kernel from the state $\mathbf{k}$ in valley α to the state $\mathbf{k'}$ in valley β. This transition rate, as we've seen in Chapter 2, is described using Fermi's Golden Rule (FGR), where the change in state is caused by a perturbation H':

$$\Gamma(\mathbf{k'}_\beta, \mathbf{k}_\alpha) = \frac{2\pi}{\hbar} \left|\left\langle \psi_{\mathbf{k'}_\beta} \middle| H' \middle| \psi_{\mathbf{k}_\alpha} \right\rangle\right|^2 \delta\left(E(\mathbf{k}_\alpha) - E(\mathbf{k'}_\beta)\right) \tag{5.2}$$

By applying the formal definition of the density of states (DOS) per unit volume:

$$\rho_\beta(E) = \int \frac{1}{(2\pi)^3} \delta\left(E(\mathbf{k}_\alpha) - E(\mathbf{k'}_\beta)\right) d^3\mathbf{k} \tag{5.3}$$

Eq. 5.1 can be re-expressed as:

$$R(E(\mathbf{k}_\alpha)) = \frac{2\pi}{\hbar} \sum_\beta \left|\left\langle \psi_{\mathbf{k'}_\beta} \middle| H' \middle| \psi_{\mathbf{k}_\alpha} \right\rangle\right|^2 \rho_\beta(E) \tag{5.4}$$

where we define the scattering matrix element from initial state $|i\rangle$ to final state $|f\rangle$ as $M_{fi} = |\langle f| H' |i\rangle| = \left\langle \psi_{\mathbf{k'}_\beta} \middle| H' \middle| \psi_{\mathbf{k}_\alpha} \right\rangle$. The DOS per unit volume for parabolic bands can be described by the analytic expression:

$$\rho(E) = \frac{\sqrt{2}\, m^{3/2} \sqrt{E - E_c}}{\pi^2 \hbar^3} \Theta(E - E_c) \tag{5.5}$$

where E_c is the conduction band edge, m is the effective mass at the conduction band and $\Theta(x)$ is the Heaviside function, where $\Theta(x) = 1$ if $x > 1$, 0 otherwise, which stresses the fact that there are no conduction band states below E_c. Eq. 5.5 can be easily derived from Eq. 5.3.

As electrons predominantly scatter due to phonons and alloy impurities in GeSn, we have two key goals in the remainder of this section: (i) to derive an expression for the alloy scattering matrix elements using the T-matrix formalism in order to determine the alloy scattering rate and (ii) to outline all necessary expressions for calculating the phonon scattering rates relevant to GeSn, which includes a description of how to calculate the deformation potentials using the frozen phonon method.

5.1.1 Derivation of the Alloy Scattering Matrix

To fully understand electron scattering in GeSn, it is critical to be able to determine the alloy scattering parameters that give the strengths of the scattering between the various conduction band valleys. In this section, we follow the work

of Murphy-Armando and Fahy [255] to derive expressions for the alloy scattering parameters. We begin by examining the T-matrix Formalism; a framework used in quantum mechanics to describe and calculate the probability amplitudes of transitions between quantum states due to a perturbation.

5.1.1.1 T-matrix Formalism

Let's consider a Hamiltonian $H = H_0 + V$ with eigenstates $|\phi\rangle$, where H_0 is a perturbation-free Hamiltonian with eigenstates $|\psi\rangle$, and V is a perturbation. We can therefore rearrange the Schrödinger equation $H|\phi\rangle = E|\phi\rangle$ to obtain the expression:

$$\begin{aligned} H_0|\phi\rangle + V|\phi\rangle &= E|\phi\rangle \\ |\phi\rangle &= (E - H_0)^{-1} V|\phi\rangle \end{aligned} \tag{5.6}$$

If we consider the Hellmann–Feynman theorem [223, 256, 257, 258], which requires the energy eigenvalues of the Hamiltonian to change continuously with continuous changes in the Hamiltonian, we would therefore require $|\phi\rangle \to |\psi\rangle$ as $V \to 0$. In other words, as the distance from the scattering centre $\mathbf{r} \to \infty$, $|\phi(\mathbf{r}) - \psi(\mathbf{r})|^2 \to 0$, meaning the effect of the perturbing potential V vanishes at a sufficiently large distance from the scattering centre [255]. This gives us what's known as the Lippmann-Schwinger equation:

$$|\phi\rangle = |\psi\rangle + (E - H_0)^{-1} V|\phi\rangle \tag{5.7}$$

where the second term describes the scattering effects caused by V. Assuming a strong correspondence between the eigenstates $|\phi\rangle$ and $|\psi\rangle$, we can rewrite Eq. 5.7 explicitly in terms of the wavefunction $|\psi\rangle$ by defining a linear operator T such that:

$$T|\psi\rangle = V|\phi\rangle \tag{5.8}$$

where T is known as the Transition Matrix. By left-multiplying Eq. 5.7 by V, we can apply Eq. 5.8 to Eq. 5.7:

$$T|\psi\rangle = V|\psi\rangle + V(E - H_0)^{-1} T|\psi\rangle \tag{5.9}$$

5.1.1.2 Alloy Scattering Matrix Elements

From Fermi's Golden Rule, the scattering between these two wavefunctions will be proportional to the T-matrix element squared: $T = \langle f| H' |i\rangle = \langle \psi| T |\phi\rangle$. If we now consider two ideal crystal states $|\psi_{\mathbf{k}}\rangle$ and $|\psi_{\mathbf{k}'}\rangle$ of equal energy, we can equivalently express T as a function of the initial and final wavefunctions at wavevectors $\mathbf{k}'$ and $\mathbf{k}$:

$$T(\mathbf{k}, \mathbf{k}') = \langle \psi_{\mathbf{k}}| T |\psi_{\mathbf{k}'}\rangle = \langle \psi_{\mathbf{k}}| \Delta V |\phi_{\mathbf{k}'}\rangle$$

where we apply the T-matrix formalism to produce Eq. 5.10, with ΔV denoting the perturbing potential due to an impurity in the alloy, and $|\phi_{\mathbf{k}'}\rangle$ is the exact eigenstate of the Hamiltonian with an impurity present.

The scattering amplitude for each site i is therefore given by:

$$T_i(\mathbf{k}, \mathbf{k}') = \langle \psi_{\mathbf{k}}| V_i |\phi_{\mathbf{k}'}\rangle \tag{5.10}$$

where V_i is the change in potential due to an impurity at site i.

In any alloy composed of atoms A and B which are randomly distributed, the crystal potential V is not periodic. In general, the crystal potential of an alloy can be represented as a sum of an average potential $\bar{V}$, which is periodic, and a fluctuating potential δV. To obtain a first-principles expression for the total scattering amplitude due to an alloy impurity, we follow the work of Murphy-Armando [255] by expressing $T_i(\mathbf{k}, \mathbf{k}') = \bar{T}_i(\mathbf{k}, \mathbf{k}') + \delta T_i(\mathbf{k}, \mathbf{k}')$, where $\bar{T}_i(\mathbf{k}, \mathbf{k}')$ is the average of over the entire system and $\delta T_i(\mathbf{k}, \mathbf{k}')$ is the variation from the average. Given that we can express the total scattering amplitude as:

$$T(\mathbf{k}, \mathbf{k}') = \sum_{i=1}^{N} T_i(\mathbf{k}, \mathbf{k}') \tag{5.11}$$

where N is the total number of sites, the average of the square of the scattering amplitude over the entire ensemble of configurations of the random alloy is

therefore given by:

$$\begin{aligned}\left\langle |T(\mathbf{k},\mathbf{k}')|^2 \right\rangle &= \sum_{i=1}^{N}\sum_{j=1}^{N}\left\langle \left(\bar{T}_i^*(\mathbf{k},\mathbf{k}') + \delta T_i^*(\mathbf{k},\mathbf{k}')\right)\left(\bar{T}_j(\mathbf{k},\mathbf{k}') + \delta T_j(\mathbf{k},\mathbf{k}')\right)\right\rangle \\ &= \sum_{i=1}^{N}\sum_{j=1}^{N}\langle \delta T_i^*(\mathbf{k},\mathbf{k}')\delta T_j(\mathbf{k},\mathbf{k}')\rangle \\ &= \sum_{i=1}^{N}\left\langle |\delta T_i(\mathbf{k},\mathbf{k}')|^2 \right\rangle \\ &= N\left\langle |\delta T_i(\mathbf{k},\mathbf{k}')|^2 \right\rangle \end{aligned} \tag{5.12}$$

where we assume that the average crystal does not scatter, implying that the mean scattering matrix satisfies $\bar{T}_j(\mathbf{k},\mathbf{k}') = 0$. This assumption aligns with the Coherent Potential Approximation (CPA) [259, 260]. Additionally, we utilise the property that $\langle \delta T_i^*(\mathbf{k},\mathbf{k}')\delta T_j(\mathbf{k},\mathbf{k}')\rangle$ represents the covariance between T_i and T_j. If we assume that Ge and Sn are weak scatterers in the alloy, allowing us to treat each site as scattering carriers independently, this covariance is zero unless $i = j$. The final step in Eq. 5.12 is plausible based on the knowledge that $\left\langle |\delta T_i(\mathbf{k},\mathbf{k}')|^2 \right\rangle$ is the variance of $T_i(\mathbf{k},\mathbf{k}')$, which is the same for all sites.

In GeSn, these sites are occupied by either Ge (with probability $1-x$) or Sn (with probability x). In that sense, we can let $T_i = T_A = \langle \psi_{\mathbf{k}} | V_A | \phi_{\mathbf{k}'} \rangle$, where $A =$ Ge or Sn. We can therefore express T in terms of the scattering produced by the substitution of an atom of one type for another:

$$\begin{aligned}\left\langle |T(\mathbf{k},\mathbf{k}')|^2 \right\rangle &= N\left\langle |\delta T_i(\mathbf{k},\mathbf{k}')|^2 \right\rangle \\ &= Nx(1-x)\left|T_{Ge} - T_{Sn}\right|^2 \\ &= Nx(1-x)\left|\langle \psi_{\mathbf{k}}| V_{Ge} |\phi_{\mathbf{k}'}\rangle - \langle \psi_{\mathbf{k}}| V_{Sn} |\phi_{\mathbf{k}'}\rangle\right|^2 \end{aligned} \tag{5.13}$$

Finally, since the matrix elements do not depend strongly on the wave-vector $\mathbf{k}$, we remove the k-dependence from the last equation; instead expressing the wavefunctions in terms of specific BZ valleys α and β:

$$\begin{aligned}\left\langle |T(\mathbf{k},\mathbf{k}')|^2 \right\rangle &= Nx(1-x)\left|T_{Ge}^{\alpha\beta} - T_{Sn}^{\alpha\beta}\right|^2 \\ &= Nx(1-x)\left|\langle \psi_{\alpha}| V_{Ge} |\phi_{\beta}\rangle - \langle \psi_{\alpha}| V_{Sn} |\phi_{\beta}\rangle\right|^2 \end{aligned} \tag{5.14}$$

5.1.1.3 Alloy Scattering Rate

To determine the elastic scattering rate at valley α due to alloy disorder, consider that site i in a GeSn alloy occupies a volume of $\frac{a_0^3}{8}$ for lattice constant a_0, i.e. half the volume of a FCC primitive cell. As a result, the volume of the system $V = N\frac{a_0^3}{8}$. Combining Eq. 5.4 with Eq. 5.14 in Section 5.1.1, and removing the k-dependence, we find:

$$R(E(\mathbf{k}_\alpha)) = \frac{2\pi}{\hbar} x(1-x)\frac{a_0^3}{8}\sum_\beta \left|\langle V_{\alpha\beta}\rangle\right|^2 \rho_\beta(E) \tag{5.15}$$

where we define:

$$\begin{aligned}\langle V_{\alpha\beta}\rangle &= \left\langle V_{\alpha\beta}^{Sn}\right\rangle - \left\langle V_{\alpha\beta}^{Ge}\right\rangle \\ &= N(\langle\psi_\alpha|\,\Delta V^{Sn}\,|\phi_\beta\rangle - \langle\psi_\alpha|\,\Delta V^{Ge}\,|\phi_\beta\rangle)\end{aligned} \tag{5.16}$$

5.1.2 Electron-Phonon Scattering

5.1.2.1 Frozen Phonon Method

In this section, the frozen phonon method of calculating the deformation potentials (often denoted $D_{\mathbf{q}}$ for phonon wavevector $\mathbf{q}$) is described. This is a necessary step in determining the e-ph matrix elements M_{fi}, and thus the corresponding scattering rate via FGR. Results obtained using this method are used in Chapter 7 to determine the electron spin-phonon scattering rate between the Γ and L valleys in GeSn.

The frozen phonon method is a widely used computational technique whereby atomic displacements corresponding to specific phonon modes are "frozen" into the crystal lattice, and the resulting distorted structure is analysed using first-principles methods, such as DFT.

The displacement ($\delta\mathbf{R}_i = \mathbf{R}_i - \mathbf{R}_i^0$) of atom i from $\mathbf{R}_i^0$ to $\mathbf{R}_i$ due to a phonon of momentum $\mathbf{q}$ is given by Eq. 5.17:

$$\mathbf{R}_i = \mathbf{R}_i^0 + A\ \mathbf{u}\ e^{i\mathbf{q}\cdot\mathbf{R}_i^0} \tag{5.17}$$

where $\mathbf{u}$ is the phonon eigenvector, which describes the atomic displacement pattern for a given phonon mode. This is typically calculated using density functional perturbation theory (DFPT), which can also be used to compute deformation potentials. In this work, however, we use the frozen phonon

method for the latter, as it is computationally more efficient. The parameter A is the displacement amplitude, typically set to some small number whereby matrix elements should converge with decreasing A. This convergence must be checked systematically.

For a given wavevector $\mathbf{q}$, we choose the smallest supercell in which $\mathbf{q}$ is compatible with periodic boundary conditions. Using this supercell, $D_{\mathbf{q}}$ is defined as:

$$D_{\mathbf{q}}(\mathbf{k}) = \frac{\delta E_n(\mathbf{k})}{\delta R_{\mathbf{q}}} \tag{5.18}$$

where $\delta E_n(\mathbf{k})$ is the band energy of electronic state n at wavevector $\mathbf{k}$. We will now show how these deformation potentials can be used in determining the e-ph scattering rates.

5.1.2.2 Electron-Phonon Scattering Rate

For momentum scattering due to phonons, the matrix element M_{fi} depends primarily on deformation potentials, the phonon frequency $\omega_{\mathbf{q}}$ and the phonon occupation number $N_{\mathbf{q}}$, which is given by the Bose-Einstein distribution:

$$N_{\mathbf{q}} = \frac{1}{e^{\hbar\omega_{\mathbf{q}}/k_B T} - 1} \tag{5.19}$$

For phonon absorption, the probability scales as $N_{\mathbf{q}}$, while for emission, it scales as $N_{\mathbf{q}} + 1$. We calculate the e-ph scattering in GeSn by following Fischetti and Laux [91] and Jacoboni and Reggiani [261] using the deformation potential method. We must consider intra-valley acoustic phonon scattering, intra-valley optical phonon scattering, and inter-valley electron-phonon scattering. The relaxation rates for the latter two processes can be described more straightforwardly compared to acoustic phonon scattering, as bulk cubic materials retain symmetry under reflections around the Cartesian planes [91].

Optical (op) phonons are short wavelength (higher-energy) waves where atoms in the unit cell move out of phase. When an electron scatters as a result of optical phonons, the square of the matrix element M_{fi} can be expressed as:

$$|M_{fi}|^2 = \frac{D_{\mathbf{q}}^2 \hbar}{2\rho V \omega_{\mathbf{q}}} \begin{bmatrix} N_{\mathbf{q}} \\ N_{\mathbf{q}} + 1 \end{bmatrix} \tag{5.20}$$

where ρ is the material density and V is the primitive cell volume. This results

in the following expression for the e-ph scattering rate for optical phonons:

$$R_{op} = \frac{(D_{op})^2 m^{3/2}}{\sqrt{2}\pi\rho\hbar^3\omega_{op}} \begin{bmatrix} N_{op} \\ N_{op}+1 \end{bmatrix} \sqrt{E - E_c \pm \hbar\omega_{op})} \times \left[1 + \frac{5}{2}\gamma(E - E_c \pm \hbar\omega_{op})\right] \tag{5.21}$$

where D_{op}, ω_{op} and N_{op} represent the deformation potential, the frequency and the distribution of optical phonons, respectively. The final term accounts for any non-parabolicity in the bands [261], where γ is the valley-dependent non-parabolicity factor (formula shown in Chapter 6), and the rooted term ensures the conservation of energy is obeyed.

Acoustic (ac) phonons behave like sound waves where atoms in the unit cell move in phase. They are long-wavelength (low frequency) vibrations, such that $\hbar\omega_{\mathbf{q}} << k_B T$. For small x, we can use a first order Taylor series to expand e^x, resulting in $e^x \approx 1 + x$. Applying this to the Bose-Einstein distribution gives $N_{\mathbf{q}} = \frac{k_B T}{\hbar\omega_{\mathbf{q}}}$. For acoustic phonons, we also replace $D^2_{\mathbf{q}}$ is Eq. 5.20 with $\Xi^2\mathbf{q}^2$ [261], where Ξ is $\mathbf{q}$-independent. As we discussed in Chapter 4, the deformation potential operator for a given band can be expressed in terms of two or three deformation potential constants, depending on the crystal symmetry. These are often denoted by Ξ_u, the uniaxial deformation potential constant, and Ξ_d, the dilatation deformation potential constant, which we list for Ge in Chapter 6, along with all relevant deformations in Ge. Equation 5.22 describes the squared matrix element for acoustic phonons, which is expressed as a sum over each phonon mode η:

$$|M_{fi}|^2 = \sum_{\eta} \frac{\Xi^2_{ac} k_B T}{\rho V \nu^2_{\eta}} \tag{5.22}$$

where ν_η is the average sound velocity such that $\omega_{\mathbf{q}} = \nu_\eta |\mathbf{q}|$, and $k_B T$ is the thermal energy. Eq. 5.23 shows the relaxation rate due to intra-valley acoustic phonon emission and absorption (R_{ac}):

$$R_{ac} = \sum_{\eta} \frac{\sqrt{2}\,\Xi^2_{ac} m^{3/2} k_B T}{\pi\rho\hbar^4\nu^2_{\eta}} \sqrt{E - E_c}\left[1 + \frac{5}{2}\gamma(E - E_c)\right] \tag{5.23}$$

For intervalley e-ph scattering processes, electrons are scattered either by optical or acoustic phonons. The phonon wave vector $\mathbf{q}$ for such a transition is very close to Δk, the distance between the initial and final valleys [261]. Therefore, $\hbar\omega_{\mathbf{q}}$ is roughly constant for a given branch of phonons, since the phonon wave vector

lies near the BZ edge, where the phonon dispersion is relatively flat. This is also true of intravalley optical phonon e-ph scattering. Consequently, intervalley scattering is formally treated in the same way as intravalley scattering by optical phonons, but with two distinct differences. Firstly, the energy term E becomes $E - \Delta E_{fi}$ in Eq. 5.21, where ΔE_{fi} is the difference in energies of the initial and final bands. Secondly, since the electrons can scatter into multiple degenerate valleys, we include the term Z_f in the numerator, which represents the number of possible final conduction band valleys in the scattering process.

5.2 Mobility from the Boltzmann Transport Equation

5.2.1 The Boltzmann Transport Equation

In order to describe the movement of carriers in a solid, we begin by defining the carrier distribution function $f_k(\mathbf{r}, t)$ as the probability that a state in a region near $\mathbf{r}$ with momentum $\mathbf{k}$ at time t is occupied. If we assume that the carriers remain in thermal equilibrium in the absence of an external field, f_k equates to the Fermi-Dirac (FD) distribution function:

$$f_k^0 = \frac{1}{e^{\frac{E_\mathbf{k} - \mu_F}{k_B T}} + 1} \tag{5.24}$$

where μ_F is the chemical potential, which at $T = 0$ is equal to the Fermi energy E_F. The superscript 0 denotes the distribution f is at equilibrium.

The total differential of a distribution function $f_k(\mathbf{r}, t)$ is given as:

$$\begin{aligned} df &= \frac{\partial f}{\partial t} dt + \nabla_\mathbf{r} f \cdot d\mathbf{r} + \nabla_\mathbf{p} f \cdot d\mathbf{p} \\ &= \frac{\partial f}{\partial t} dt + \mathbf{v} \cdot \nabla_\mathbf{r} f \; dt + \frac{1}{\hbar} \mathbf{F} \cdot \nabla_\mathbf{k} f \; dt \end{aligned} \tag{5.25}$$

recalling that $\mathbf{p} = \hbar\mathbf{k}$, and the rate of change of the momentum $\mathbf{k}$ is given by the external force $\mathbf{F}$ acting on the particle. Taking the derivative with respect to time gives us the Liouville equation, which governs the evolution of $f_k(\mathbf{r}, t)$:

$$\frac{df}{dt} = \frac{\partial f}{\partial t} + \mathbf{v} \cdot \nabla_\mathbf{r} f + \frac{1}{\hbar} \mathbf{F} \cdot \nabla_\mathbf{k} f \tag{5.26}$$

where on the right hand side of Eq. 5.26, the first term gives the change in f

with time at a fixed point, the second term captures how f changes as particles move through space with velocity $\mathbf{v}$ and the third term describes the change due to external forces acting on the particles. In the absence of any scattering events, the left-hand side is 0. However, if we include scattering, we obtain the Boltzmann Transport Equation (BTE):

$$\left(\frac{\partial f_{\mathbf{k}}}{\partial t}\right)_{scatt} = \frac{\partial f_{\mathbf{k}}}{\partial t} + \mathbf{v_g} \cdot \nabla_{\mathbf{r}} f_{\mathbf{k}} + \frac{1}{\hbar}\mathbf{F} \cdot \nabla_{\mathbf{k}} f_{\mathbf{k}} \tag{5.27}$$

where v_g is the group velocity, which defines the trajectory of the particles in a crystal, and the external force $\mathbf{F} = -e(\mathcal{E} + \mathbf{v}_g \times \mathbf{B})$ is the force felt by the electrons due to an external electromagnetic field. Eq. 5.27 essentially explains how distributions evolve over time. Mathematically, the group velocity can be expressed as in Eq. 5.28 below:

$$v_g \equiv \frac{\partial \omega}{\partial k} = \frac{1}{\hbar}\frac{\partial E}{\partial k} \tag{5.28}$$

where ω is the angular frequency of the wave. For a steady-state system ($f_{\mathbf{k}}$ does not explicitly depend on time), then the first term on the right-hand side of Eq. 5.27 becomes 0. We can make two other assumptions of consequence: one is we assume consistent atomic distributions in our alloy, given that local variation in composition (such as clusters) are often minimised through advanced fabrication techniques. We also assume that the applied electric field is uniform and there are no thermal gradients, meaning the driving forces affecting the carriers are the same throughout the material. As a result, $f_{\mathbf{k}}$ remains spatially uniform, leading to the second term on the right-hand side of Eq. 5.27 vanishing. This leaves us with a simplified expression of the BTE:

$$\left(\frac{\partial f_{\mathbf{k}}}{\partial t}\right)_{scatt} = \frac{1}{\hbar}\mathbf{F} \cdot \nabla_{\mathbf{k}} f_{\mathbf{k}} \tag{5.29}$$

5.2.2 The Relaxation Time Approximation

The Relaxation Time Approximation (RTA) is a simplification used in the BTE to model how a system relaxes back to equilibrium after a weak out-of-equilibrium perturbation. In this approximation, the collision term $\left(\frac{\partial f_{\mathbf{k}}}{\partial t}\right)_{scatt}$ is assumed to cause the distribution function f_k to relax towards the equilibrium distribution f_k^0 with a characteristic time constant τ (the relaxation time), which is representing

the average time between scattering events, such that:

$$\left(\frac{\partial f_{\mathbf{k}}}{\partial t}\right)_{scatt} \approx -\frac{f_{\mathbf{k}} - f^0_{\mathbf{k}}}{\tau_{\mathbf{k}}} = \frac{1}{\hbar}\mathbf{F}\cdot\nabla_{\mathbf{k}} f_{\mathbf{k}} \tag{5.30}$$

Thus, the distribution of carriers becomes:

$$\begin{aligned} f_k &= f^0_k - \frac{1}{\hbar}\tau_k \nabla_k f_k \cdot \mathbf{F} \\ &\approx f^0_k - \frac{1}{\hbar}\tau_k \nabla_k f^0_k \cdot \mathbf{F} \end{aligned} \tag{5.31}$$

where we have considered a weak applied field, whereby $f \approx f^0$.

5.2.3 Mobility from the BTE and the RTA

The current density (charge per unit time that flows through a unit area of a chosen cross section) can be expressed generally as:

$$\mathbf{j} = -2e\int_{BZ} \frac{d^3\mathbf{k}}{(2\pi)^3}\, f_{\mathbf{k}}\, v_g(\mathbf{k}) \tag{5.32}$$

where the 2 in the numerator accounts for the two possible spin states. By substituting Eq. 5.31 into Eq. 5.32, we have:

$$\mathbf{j} = -\frac{2e}{(2\pi)^3}\int_{BZ} d^3\mathbf{k}\left(f^0_k - \frac{1}{\hbar}\tau_k\nabla_k f^0_k\cdot\mathbf{F}\right) v_g(\mathbf{k}) \tag{5.33}$$

$$\approx -\frac{2e^2}{(2\pi)^3}\int_{BZ} d^3\mathbf{k}\,\frac{1}{\hbar}\tau_k\nabla_k f^0_k\cdot\mathcal{E}\; v_g(\mathbf{k}) \tag{5.34}$$

where the external force is given by $F = -e\mathcal{E}$. The equilibrium term vanishes in Eq. 5.33 because the Fermi–Dirac distribution is even in $\mathbf{k}$ while the group velocity is odd, so their product integrates to zero over the Brillouin zone. We now remove the $\mathbf{k}$ subscript, and instead introduce the superscript α to denote the band valley. For an isotropic material, considering the electric field $\mathcal{E}$ along the λ axis, the carrier mobility at a given band α is given by:

$$\mu^{(\alpha)}_\lambda = \frac{j^{(\alpha)}_\lambda}{n^{(\alpha)} e\mathcal{E}} \tag{5.35}$$

where $n^{(\alpha)}$ is the carrier concentration at valley α, which is calculated using Eq. 5.36, where N_c denotes the valley degeneracy:

$$n^\alpha = N_c\int_0^\infty \rho^\alpha(E) f(E) dE \tag{5.36}$$

We can therefore express the mobility at band α as:

$$\mu_{\lambda}^{(\alpha)} = -\frac{e}{\hbar\, n^{(\alpha)}} \int_{BZ} \frac{d^3\mathbf{k}}{4\pi^3} \frac{\partial f}{\partial \mathbf{k}}\, v_g^{(\alpha)} \tau_{\lambda}^{(\alpha)} \tag{5.37}$$

Finally, we perform a change of variables, such that $\frac{\partial}{\partial \mathbf{k}} = \frac{\partial E}{\partial \mathbf{k}} \frac{\partial}{\partial E}$. Recalling the definition of the group velocity in Eq. 5.28, we have our final expression for the carrier mobility at band α:

$$\mu_{\lambda}^{(\alpha)} = \frac{e}{n^{(\alpha)}} \int_{BZ} \frac{d^3\mathbf{k}}{4\pi^3} \frac{\left(v_g^{(\alpha)}\right)^2}{R_{\lambda}^{(\alpha)}} \left(\frac{-\partial f}{\partial E}\right) \tag{5.38}$$

where R is the total scattering rate such that $\frac{1}{\tau} = R$.

5.2.4 Carrier Mobility for Parabolic Bands

While Eq. 5.38 is applicable for the carrier mobility at any conduction band valley, it is computationally simpler to express the mobility as an integral over energy as opposed to k-space, in particular for parabolic bands. We can perform a change of variables using the energy-momentum relationship for a free electron ($E = \frac{\hbar^2 k^2}{2m}$). We find:

1. $v_g^2 = \frac{2E}{m}$
2. $\int d^3k = 4\pi^3 \int E\, \rho(E)\, dE$

However, at a given band valley α, the transverse and longitudinal effective masses differ in materials with anisotropic band structures, where the electron's energy depends differently on the direction of its momentum. We also introduce the non-parabolicity factor γ into the DOS to account for deviations from a purely parabolic energy-momentum relationship [91]. Therefore, Eq. 5.5 becomes:

$$\rho^{\alpha}(E) = \frac{\sqrt{2}\sqrt{m_l^{\alpha}} m_t^{\alpha} \sqrt{(E - E_c^{\alpha})(1 + \gamma^{\alpha}(E - E_c^{\alpha}))}(1 + 2\gamma^{\alpha}(E - E_c^{\alpha}))}{\pi^2 \hbar^3} \Theta(E - E_c^{\alpha}) \tag{5.39}$$

We also introduce a non-parabolicity term into the mobility, leading to our updated expression for the carrier mobility (as per Fischetti and Laux [91]):

$$\mu_{\lambda}^{(\alpha)} = \frac{2e}{3n^{(\alpha)} m_{\lambda}^{(\alpha)}} \int_0^{\infty} dE\, \frac{E\rho^{(\alpha)}(E)\left(\frac{-\partial f}{\partial E}\right)}{R_{\lambda}^{(\alpha)}(E)} (1 + \gamma^{(\alpha)} E/2) \tag{5.40}$$

where the 3 in the denominator can be attributed to the equipartition theorem, describing how energy is distributed among the degrees of freedom of a system in thermal equilibrium. The total mobility is obtained by summing over the bands:

$$\mu = \sum_{\alpha} r^{(\alpha)} \mu^{(\alpha)} \tag{5.41}$$

where $r^{(\alpha)} = \frac{n^{(\alpha)}}{n}$ is the carrier concentration ratio, and $n = \sum_{\alpha} n^{(\alpha)}$ is the total carrier concentration.

In Chapter 6, where we present our results on the electron mobility of GeSn, we employ both Eq. 5.38 and Eq. 5.40, as GeSn exhibits parabolic band dispersion at the L valley and non-parabolic behaviour at the Γ point.

5.3 Optical Properties: Absorption and Emission Mechanisms

The absorption coefficient α of a medium can be expressed using Eq. 5.42 below:

$$\alpha = \frac{\omega \epsilon_i}{cn} \tag{5.42}$$

where ω represents the frequency of the photon, ϵ_i is the imaginary part of the dielectric function ($\tilde{\epsilon} = \epsilon_r + \epsilon_i i$) and n is the real part of the refractive index, such that ($\tilde{n} = n + i\kappa$), where κ is known as the extinction coefficient. Given that the real and imaginary parts of the dielectric function can be written as $\epsilon_r = n^2 - \kappa^2$ and $\epsilon_i = 2n\kappa$ respectively, we can describe n as:

$$n = \sqrt{\frac{\epsilon_r + \sqrt{\epsilon_r^2 + \epsilon_i^2}}{2}} \tag{5.43}$$

We can also express the material's photoluminescence (PL) in terms of its refractive index and dielectric function. We use the van Roosbroek-Shockley relation [262], given in Eq. 5.44, which computes the total rate of radiative recombination per unit volume [263]:

$$PL = \frac{2n}{\pi c^3} \frac{\omega^3 \epsilon_i}{e^{(\hbar\omega - \Delta\mu)/k_B T} - 1} \tag{5.44}$$

where $\hbar\omega$ is the photon energy and $\Delta\mu = \mu_c - \mu_v$ is the difference in the quasi-Fermi levels for electrons (μ_c) and holes (μ_v), which is 0 in thermal equilibrium.

We calculate μ_c and μ_v by assuming a steady-state condition in which the electron (e) and hole (h) populations are fixed and equal ($n_e = n_h$).

Following Section 6.2 of Yu and Cardona [105], for an electric field E, ϵ_i can be described by:

$$\epsilon_i = \frac{2R\hbar}{\epsilon_0 |E|^2} \tag{5.45}$$

where R is the transition rate (given by Fermi's Golden Rule) of an electron transitioning from initial state $|i\rangle$, with energy E_i at wavevector $\vec{k}_i$ to final state $|f\rangle$, with energy E_f at wavevector $\vec{k}_f$. To determine ϵ_r, we use the Kramer's-Kronig relations (KKRs) [264, 265], shown in Eq. 5.46, assuming the incident field is weak enough for polarisation to depend linearly on the electric field. Expressing these parameters as functions of the photon frequency ω, $\epsilon(\omega) = \epsilon_r(\omega) + i\epsilon_i(\omega)$ represents the medium's linear response, which inherently satisfies the KKRs.

$$\epsilon_r(\omega) = 1 + \frac{2}{\pi}\mathcal{P}\int_0^\infty \frac{\omega' \epsilon_i(\omega') d\omega'}{\omega'^2 - \omega^2} \tag{5.46}$$

Optical absorption and emission processes in semiconductors are governed by the energy of the photon absorbed/emitted and the material's electronic band structure. Electrons can get excited into the conduction band (c), or recombine into the valence band (v), either directly ($\vec{k}_v = \vec{k}_c$), as in many III–V semiconductors, or indirectly ($\vec{k}_v \neq \vec{k}_c$), as is primarily the case at low photon energies for indirect-gap semiconductors.

We have seen that the band structure of GeSn enables a continuous transition from indirect to direct bandgap behaviour through compositional tuning. As a result, both direct and indirect transitions contribute significantly to their absorption and emission properties, with their contributions depending on the Sn content and temperature. Understanding and quantifying these processes is essential for optimising optoelectronic devices based on GeSn.

In the remainder of this section, we derive expressions for ϵ_i for (i) direct transitions between the valence and conduction bands, and (ii) indirect transitions from $|k\rangle$ to $|k'\rangle$ in a particular band using non-degenerate perturbation theory, as well as (iii) transitions into quasi-degenerate conduction band states using degenerate perturbation theory. This approach largely follows the unified formalism introduced by Tiwari et al. [253], where a single expression is derived to govern all optical transitions. This approach enables a detailed and accurate description of the optical response across the full range of GeSn compositions. The derived expressions can then be applied to calculate the absorption coeffi-

cient and PL over a range of frequencies ω using equations 5.42, 5.43 and 5.46, results for which are given in Chapter 8.

5.3.1 Direct Transitions

The scattering rate for the direct transition of electrons can be derived using first-order perturbation theory. Consider the Hamiltonian $H = H_0 + H_\gamma$, where $H_0 = \frac{p^2}{2m_e} + V(\vec{r})$ is the unperturbed one-electron Hamiltonian, where $\vec{p}$ is the momentum operator, m_e is the free electron mass and V represents the periodic potential of the crystal lattice, while $H_\gamma = \frac{e}{m_e c}\vec{A} \cdot \vec{p}$ represents the electron-radiation interaction. The vector potential $\vec{A}$, given by Eq. 5.47, describes an electromagnetic field:

$$\vec{A}(\vec{r}, t) = \frac{-E}{2k} e^{i(\vec{k}\cdot\vec{r}-\omega t)} + c.c \tag{5.47}$$

for wavevector $\vec{k}$ at position $\vec{r}$. The complex conjugate term ($c.c$) corresponds to stimulated emission. We therefore apply the first term for absorption and the complex conjugate for emission. The mathematical reasoning for this can be found in Ref. [105]. Without it, $\vec{A}$ describes absorption, and its field strength must be weak enough to apply perturbation theory to calculate R. Using a Coulomb gauge ($\nabla \cdot \vec{A} = 0$) for simplicity and defining $\vec{A} = A\vec{e}$, where $\vec{e}$ is a unit vector parallel to $\vec{A}$, we obtain the matrix element:

$$\begin{aligned} |\langle c| H_\gamma |v\rangle|^2 &= \left(\frac{e}{m_e c}\right)^2 |A|^2 \, |\langle c| \vec{e}\cdot\vec{p}|v\rangle|^2 \\ &= \left(\frac{e}{m_e c}\right)^2 \left(\frac{E(\omega)}{2k}\right)^2 |P_{cv}(\vec{k})|^2 \end{aligned} \tag{5.48}$$

where $P_{cv} = \langle c| \vec{e}\cdot\vec{p}|v\rangle$ is the momentum matrix element (also called the electric-dipole matrix element), which quantifies how likely an electron is to transition between states at a given point in k-space due to interaction with light (which has an electric field $\vec{E}$). Accurate computation of P_{cv} requires proper evaluation of wavefunction derivatives in real space. However, as discussed in Chapter 3, DFT employs the pseudopotential method, which smooths pseudo-wavefunctions in the core region, whereas true wavefunctions exhibit strong oscillations near atomic cores. This discrepancy results in inaccuracies in momentum matrix elements. To correct for this, standard adjustments have been implemented in

ABINIT post-processing, as outlined below:

$$P_{cv} = \langle c| \vec{e} \cdot \vec{p} |v\rangle + \frac{im_e}{\hbar} \langle c| [U, \vec{r}] |v\rangle \tag{5.49}$$

where U is the non-local part of the pseudopotential and $\vec{r}$ is the positional vector.

Using $k = \omega/c$, we combine equations 5.4, 5.45 and 5.48 to obtain the following relation for direct transitions:

$$\epsilon_i(\omega) = \frac{\pi e^2}{\epsilon_0 m_e V} \frac{1}{N} \frac{1}{\omega^2} \sum_{\vec{k}} |P_{cv}(\vec{k})|^2 \, \delta(E_c(\vec{k}) - E_v(\vec{k}) - \hbar\omega) \tag{5.50}$$

where the summation runs over a uniform BZ grid with N points, and V is the primitive cell volume. In GeSn, by confining the photon energy within a $0-1eV$ range, this only encompasses transitions from around the top of the three uppermost valence bands around the Γ valley to points around the conduction band at Γ.

5.3.2 Indirect Transitions

Indirect absorption occurs when an electron transitions not only between energy bands via photon absorption/emission, but also between wavevectors within a band. This intra-band scattering can occur either through phonon absorption/emission or by alloy scattering. The resulting Hamiltonian takes the form $H = H_0 + H_\gamma + H_{ep} + H_{al}$, where H_{ep} is the electron-phonon (e-ph) interaction, the matrix element for which is shown in Eq. 5.20, and H_{al} is the alloy scattering Hamiltonian, derived in Section 5.1.1. Second order perturbation theory is applied to obtain the transition rate for indirect absorption [105]. The correction to the final eigenstate $|f\rangle$ is given generally by:

$$|f'\rangle = |f\rangle + \sum_{m \neq f} \frac{\langle m| H_{ep} |f\rangle}{E_f - E_m} |m\rangle \tag{5.51}$$

where $|m\rangle$ is some intermediate state. The scattering rate for indirect transitions is thus given by Eq. 5.52:

$$R_{ind} = \frac{2\pi}{\hbar} \sum_{\vec{k}_f, \vec{k}_i} \left| \sum_m \frac{\langle f| H_{ep} |m\rangle \langle m| H_\gamma |i\rangle}{E_m - E_f \pm E_p} \right|^2 \delta(E_f - E_i - \hbar\omega \pm E_p) \tag{5.52}$$

In Eq. 5.52, $E_p = \hbar\omega_q$ is the phonon energy, whereby the $\pm$ represents phonon absorption/emission, respectively, and $\vec{k_f} = \vec{k_i} + \vec{q}$ for phonon wavevector $\vec{q}$. The matrix element is a sum over all possible intermediate states $|m\rangle$. In GeSn, within a 0-1eV range, phonon or alloy-assisted transitions only will occur between points around the Γ valley and the four L valleys. Applying Eq. 5.20 and Eq. 5.52 to Eq. 5.45 gives:

$$\epsilon_i(\omega) = \frac{\pi e^2}{\epsilon_0 m_e V}\frac{1}{N}\frac{1}{\omega^2}\left(\begin{bmatrix} N_q \\ N_q + 1 \end{bmatrix} D_{\Gamma L}^2\left(\frac{\hbar}{2\rho V\omega_q}\right) + (x(1-x)V_{L\Gamma})^2\right) \times \sum_{\vec{k}_f,\vec{k}_i}\left|\frac{P_{cv}}{E_m - E_f \pm E_p}\right|^2 \delta(E_f(\vec{k}_f) - E_i(\vec{k}_i) - \hbar\omega \pm E_p) \tag{5.53}$$

where x is the alloy content and $V_{L\Gamma}$ is the alloy scattering potential between the L and Γ valleys.

5.3.3 Transitions into Quasi-Degenerate Bands

From the denominator of Eq. 5.52, it is evident that the equation breaks down when $E_m = E_f \pm E_p$, whereby the energy of the intermediate state approaches degeneracy with the energy of the final state plus/minus phonon energy, causing the transition amplitude to diverge. Consequently, Eqs. 5.50 and 5.53 alone are insufficient, as they fail to accurately account for such transitions.

To address this, we follow the approach of Tiwari et al. [253] by implementing degenerate perturbation theory to accurately describe optical transitions into quasi-degenerate conduction band states. In our GeSn calculations, shown in Chapter 7, we focus on the short-wave infrared light range, in which only optical transitions between the top of the valence band (at Γ) and the conduction band minima around the Γ valley and the four L valleys are considered. Consequently, in this framework, the diagonal elements of the effective Hamiltonian correspond to the energies around the Γ and L valleys, with phonon energies added or subtracted to represent phonon absorption or emission, respectively. Assuming negligible intravalley scattering and intervalley scattering between the 4 L bands, the only off-diagonal elements are the interactions due to phonons and alloy disorder between the Γ and L energies (we assume a constant electron-phonon interaction term between the states rather than a $\mathbf{q}$-dependent term to reduce computational cost. Below (Fig. 5.1) is a schematic of the Hamiltonian matrix

for such as system, whereby we utilise the following notation:

- E_{Γ_1}, E_{Γ_2}, etc are the energies of the states around the Γ valley, while E_{L_1}, E_{L_2}, etc are the energies of the states around the L valley.
- M_{fi}^{ab} and M_{fi}^{em} denote the intervalley electron-phonon interaction terms for absorption and emission, respectively, as described in Eq. 5.20.
- $V_{\Gamma L}$ represents the intervalley alloy scattering parameter between the Γ and L valleys, and expression for which is given in Eq. 5.14. This parameter is calculated in Chapter 6.

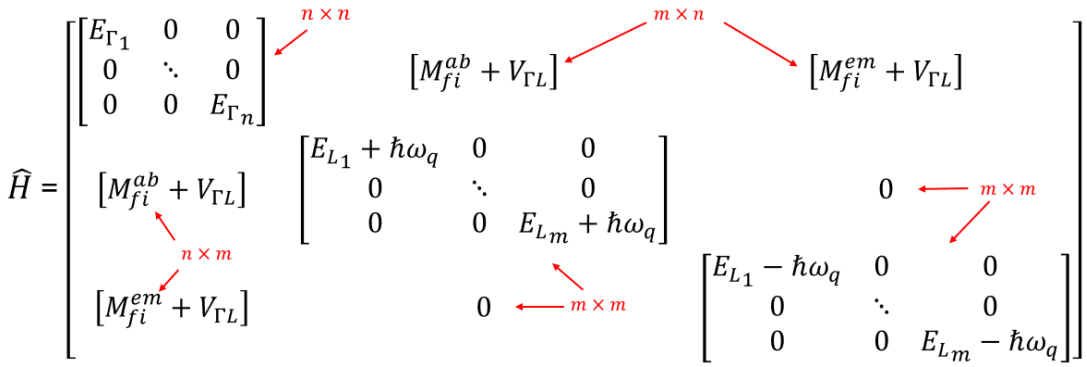

Figure 5.1: Schematic of the Hamiltonian matrix describing electron–phonon and alloy interactions between conduction band states near the band edge, specifically the Γ and the L valleys.

In this system, each mixed (eigen-)state $|\psi_i\rangle$ is a weighted linear combination of the unperturbed conduction band states, with the weights given by the components of the corresponding eigenvector $v^{(i)}$, which effectively acts as the diagonaliser of the perturbation, while the energy of each state is given by the corresponding eigenvalue of the matrix. If N is the number of mixed states, we can express each new state $|\psi_i\rangle$ as:

$$|\psi_i\rangle = \sum_{j}^{n} v_j^{(i)} |\Gamma_j\rangle + \sum_{j=n+1}^{m} v_j^{(i)} |L_j + \hbar\omega_q\rangle + \sum_{j=m+1}^{N} v_j^{(i)} |L_j - \hbar\omega_q\rangle \tag{5.54}$$

where n and m are the number of unperturbed Γ and L states, respectively, where $N = n + 2m$. The states $|\Gamma_j\rangle$ and $|L_j \pm \hbar\omega_q\rangle$ represent the wavefunctions of the states around the Γ and L valleys, respectively. Given that an electron will only transition between the valence and conduction band into states around the Γ valley, only the components of the eigenvectors corresponding to the

unperturbed Γ states contribute to the momentum matrix elements. The resulting expression for the imaginary part of the dielectric function for transitions into quasi-degenerate bands is given in Eq. 5.55

$$\epsilon_i(\omega) = \frac{\pi e^2}{\epsilon_0 m_e V} \frac{1}{N} \frac{1}{\omega^2} \sum_{\vec{k}}^{N} \sum_{\vec{k_\Gamma}}^{n} |v_{\vec{k_\Gamma}}^{(\vec{k})}|^2 \, |P_{cv}(\vec{k})|^2 \, \delta(E_c(\vec{k}) - E_v(\vec{k}) - \hbar\omega) \tag{5.55}$$

where $\vec{k_\Gamma}$ runs over the n unperturbed Γ states.

This approach largely follows the work of Tiwari et al. [253], with a few key distinctions. Our expression of ϵ_i is a simplified form of their Eq. 48, as the photon energies of interest limit the indirect transitions to conduction-band–to–conduction-band processes, excluding contributions from the top of the valence band at L. Their work also considers $\mathbf{q}$-dependent electron-phonon interaction terms, while we assume a constant valued term. Additionally, we include and alloy scattering interaction between the Γ and L valleys, since we are operating with an alloy. This is the first study to include alloy disorder in optical transitions.

Part III

Results

Chapter 6

Transport Properties of GeSn

Carrier mobility, expressions for which are derived in Chapter 5, measures how quickly charge carriers (electrons or holes) move through a material when subjected to an electric field. High-mobility semiconductors are desirable for several reasons in the context of electronic devices and integrated circuits. In particular, the speed at which a transistor can switch between on and off states is determined in part by the mobility of charge carriers. However, a material's mobility is limited by carrier scattering, and this scattering (in particular electron-phonon scattering) produces heat, which limits the achievable switching rates of transistors [7]. High-mobility semiconductors ultimately enable faster switching speeds in transistors, leading to more responsive and efficient devices.

As discussed in Chapter 4, the addition of Sn to Ge induces an indirect-to-direct bandgap transition between $6-11\%$ Sn concentration. Since the Γ valley usually has the lightest effective mass m^* in diamond semiconductors, GeSn has already been proposed as a high-mobility semiconductor. We can therefore expect that when the material achieves a direct gap, the steepness of the Γ band will cause the electron mobility of GeSn to increase. We also know that the application of biaxial tensile strain can cause an indirect-to-direct bandgap transition at a lower Sn concentration, which is desirable given the solubility issues associated with the mixing of Ge with Sn (discussed in Chapter 1).

However, by introducing Sn to Ge, we are now working with an alloy (we assume an ordered, random alloy), and as a result, alloy scattering will occur in the material. This additional scattering should therefore cause the carrier mobility to decrease, thereby potentially offsetting the advantages achieved by alloying Ge with Sn [91]. To accurately calculate the electron mobility of

GeSn, we must therefore calculate the alloy-scattering parameters of GeSn from first-principles methods using methods described in Chapter 5. This includes all intravalley and intervalley scattering processes between the L and Γ valleys, since the band minima in Ge and Sn are at L and Γ, respectively. In a previous calculation of the electron mobility of GeSn, Sau and Cohen [7] calculated a single alloy scattering parameter using a first-principles method developed by Murphy-Armando and Fahy [255], predicting an electron mobility of order 10^6 for $Ge_{0.92}Sn_{0.08}$. However, given that both intra- and intervalley alloy scattering to and from the L valley were not included in their calculation, this is likely to be an overestimation, even in direct-gap GeSn [266], since the L-mobility is much more dominant than the Γ-mobility at 8% Sn due to its 33-times larger density of states.

In this work, we concentrate specifically on electron mobility in the $[100]$ direction, which has higher symmetry and serves as a standard reference direction, allowing for better comparability with results for other semiconductor materials such as Si [267, 268] or Ge [91, 269]. Since most semiconductor devices operate under ambient conditions, our primary interest is in the room-temperature electron mobility. However, low-temperature electron mobility is also of significant interest for understanding fundamental physical processes and in specialised applications such as quantum computation, which is done near $0K$. In fact, GeSn is already a candidate material in quantum computation [99, 270]. We wish to add to recent experimental findings cited in Chapter 1 by calculating the electron mobility of (strained) GeSn at low temperatures.

The remainder of this chapter is divided into two primary sections. In Section 6.1, we discuss the theoretical framework behind the calculation of the alloy scattering parameters of GeSn, which was introduced in Chapter 5. We also display the results of these first-principles calculations, and summarise the significance of our findings. In Section 6.2, we first detail the theoretical model of the our temperature-dependent calculation of the electron mobility of GeSn, based on our derivations in Chapter 5. We must note at this point that in our derivation of the mobility, we implemented the energy-dependent, anisotropic relaxation time, which is suitable for anisotropic energy valleys such as those of GeSn, as well as the effects of the non-parabolicity and multiplicity of the valleys, unlike the constant relaxation time approximation. We subsequently outline in detail our findings on the room-temperature electron mobility of GeSn. We then look at the effect of biaxial tensile strain on the electron mobility. We also examine the mobility at low temperature ($15K$), before looking at a

temperature-dependent calculation of the mobility at fixed Sn concentrations. We finish the chapter by summarising our main conclusions from this work. The parameters we calculate for this body of work, while first-principles, are easily transferable to models used to simulate devices, time-dependent models and other applications.

6.1 Alloy Scattering Parameters of GeSn

In real alloy systems, the local atomic environments play a crucial role in determining electronic and scattering properties. The VCA typically neglects these local environment effects and does not account for structural variations or local distortions that can impact the electronic structure and, consequently, scattering properties. To calculate the alloy scattering parameters in any alloy, one must understand how host atoms in a crystal respond to substitutional impurities, or how an electron's direction or velocity may change depending on which atoms it scatters between. Such transitions are not captured by the VCA, since each atom is treated as an alloy and are in effect equal to each other. In order to investigate the scattering properties of an alloy, one must analyse a supercell. Elastic momentum alloy scattering occurs due to the breaking of the translational symmetry by disorder. This effect can be determined by introducing one small change in composition in a periodic crystal [255].

6.1.1 Theoretical Framework

We calculate the alloy scattering parameters $\langle V_{\alpha\beta} \rangle$ using Eq. 5.16 in Chapter 5. The perturbing potential ΔV^A is calculated by inserting an atom of type A as a substitutional defect in a supercell of $N-1$ host atoms, and the host atoms are relaxed around the impurity using DFT. ΔV^A tends to 0 at a large distance from the impurity site. The intervalley scattering parameters can be obtained directly from the conduction band splittings. However, a problem that occurs in finding the correct intravalley scattering matrix elements from a finite supercell is that the zero of the potential is arbitrary. The intravalley terms depend on the overall shift in the band edge energy of the supercell with N host atoms and the supercell with $N-1$ host atoms and an impurity. To examine the potentials of the two supercells, we average the local DFT potential over points in the supercell far away from the impurity and compare with the same average in the pure supercell. The difference in these averages shows the necessary reference

shift in the potentials. This potential difference converges to a constant, which then gets subtracted from the conduction band eigenvalues. In a supercell larger than 16 atoms, the distance from the impurity can be sufficiently large so that the average difference in potentials is well defined [255]. The supercell used to calculate the scattering rate must be large enough to allow for realistic structural relaxation of the host around the substitutional Ge or Sn atom. Also, the Bloch state wave vectors considered are limited by periodic boundary conditions being applied on the supercell single-particle wave functions. Supercells of sizes 64 and 128 atoms were used to find the scattering matrices between degenerate Bloch states. In the case where Sn is placed as a substitutional impurity into a Ge supercell, the reference shift was calculated to be $-270meV$ for a 64-atom cell and $-130meV$ for a 128-atom cell.

Another issue arises in finding the scattering matrix elements, which is that the presence of the impurity breaks the translational symmetry of the host and therefore mixing bands which are (nearly) degenerate in the host supercell. Due to this breakage in symmetry, the boundary condition $\phi(\vec{r}) = \psi(\vec{r})$ cannot be met. We therefore must define a state $|\phi_\beta\rangle$, which is a linear combination of the M nearly degenerate energy eigenstates $|\phi_i\rangle$ with energies E_i, $i = 1, ..., M$ which has maximum overlap with the Bloch state $|\psi\rangle$ with energy $E_0 \approx E_i$. Then, we have:

$$|\phi_\beta\rangle = \sum_{i=1}^{M} |\phi_i\rangle \langle\phi_i| \psi_\beta\rangle$$

and therefore the scattering matrix elements are:

$$\langle\psi_\alpha| \Delta V |\phi_\beta\rangle = \langle\psi_\alpha| \sum_{i=1}^{M} dE_i |\phi_i\rangle \langle\phi_i| \psi_\beta\rangle$$

where $dE_i = E_i - E_0$. Using a 64-atom supercell, we have $M = 17$ to include the Γ state, the four L states, the six $\frac{1}{2}X$ states and the six X states.

The alloy scattering parameters have not been previously calculated theoretically for GeSn, and generally they are difficult to determine from experimentally measured quantities [255]. First-principles methods developed in Ref. [255] are employed to determine the intravalley and intervalley electronic scattering parameters due to alloy scattering in n-type $Ge_{1-x}Sn_x$ alloys. We consider 17 conduction band states, with only the intravalley and intervalley scattering parameters between L and Γ affecting our mobility calculation. Therefore, we seek four scattering matrix parameters: the intravalley elements (V_L and V_Γ), the

intervalley term between the L valleys (V_{LL}) and the intervalley term between L and Γ ($V_{\Gamma L}$ or $V_{L\Gamma}$). However, we do report on the intravalley and g-type and f-type intervalley scattering in the X and $\frac{1}{2}X$ Brillouin zone points, since they become important to determine the scattering of the Δ conduction band valleys in measurements where an electric field causes electrons to accelerate to higher energies, or when Ge(Sn) is grown on Si [271]. The alloy scattering parameters weakly depend on Sn concentration and can be considered as roughly independent of the host lattice at low Sn concentration [255]. The first-principles calculations are performed using Hartwigsen-Goedecker-Hutter (HGH) [272] plane-wave pseudopotentials in all of our Density Functional Theory calculations with ABINIT code [273, 274]. We converge our results using an energy cut-off of 950eV and 8x8x8 Monkhorst-pack k-meshes for the first Brillouin zone integration. We apply the local density approximation for the exchange-correlation for stable and fast convergence.

6.1.2 Results

In Figure 6.1 below, we show the alloy scattering parameters that contribute to the electron mobility of GeSn, where we denote the intravalley terms at L and Γ as V_L and V_Γ, respectively, while the intervalley elements between the L valleys and the Γ and L valleys are V_{LL} and $V_{L\Gamma}$, respectively. In Tables 6.1 and 6.2, we show a more complete set of the intravalley and intervalley alloy scattering parameters of GeSn respectively. It is important to consider atomic relaxation near the impurity in the supercell, which affects the matrix elements by up to $1eV$ in magnitude, as we show in Fig. 6.1. In general, the inclusion of atomic relaxation results in increased scattering, which is likely due to disorder of the atomic coordinates, enlarging the scattering area around the impurity atom. The same trend is observed in SiGe [255].

We find that the calculated alloy scattering parameters for GeSn are 3-4 times larger than those for SiGe [255], resulting in GeSn having alloy scattering 9-16 times stronger than SiGe. Overall, the inter- and intravalley matrix elements are similar in magnitude. We also note that our intravalley alloy scattering parameter at the Γ valley is significantly larger than the $0.788\ eV$ value calculated by Sau and Cohen [7]. This may be a consequence of atomic relaxation, where Sau and Cohen only consider atomic relaxation around the impurity up to second nearest neighbours, rather than relaxing all atoms in the supercell.

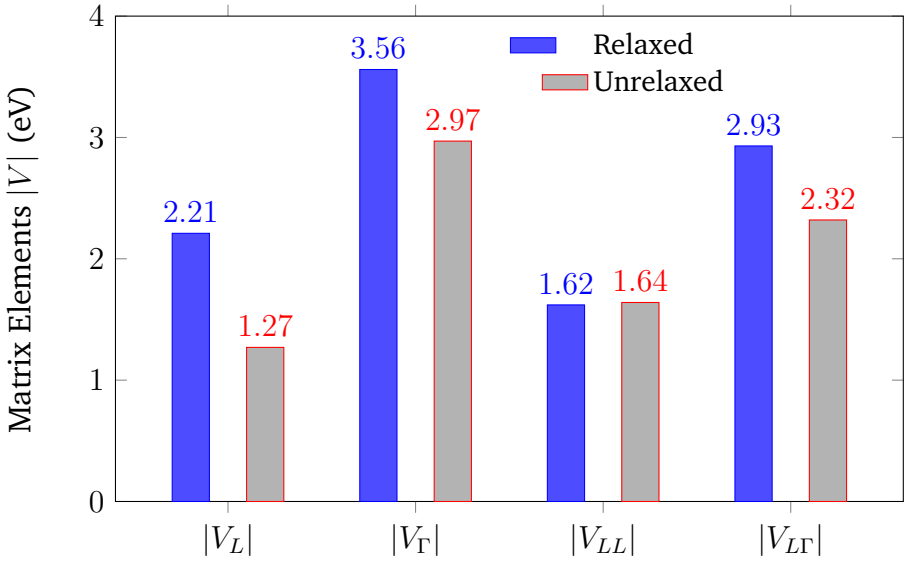

Figure 6.1: Calculated intravalley and intervalley scattering matrix elements for $Ge_{1-x}Sn_x$ with relaxed and unrelaxed atomic positions around the perturbing atom. All parameters are calculated using a 64-atom supercell, with Ge as the host atom and a single Sn impurity.

Table 6.1: Calculated intravalley scattering matrix elements (in eV) for all relevant valleys in $Ge_{1-x}Sn_x$.

Symbol	V_L	V_Γ	$V_{\frac{1}{2}X}$	V_X
Value	-2.21	-3.56	-0.86	-0.76

Table 6.2: Calculated intervalley scattering matrix elements (eV) for all relevant valleys in $Ge_{1-x}Sn_x$.

Symbol	V_{LL}	$V_{L\Gamma}$	V_{LX}	$V_{\frac{1}{2}X_f}$	$V_{\frac{1}{2}X_g}$	V_{X_f}	V_{X_g}	$V_{\Gamma\frac{1}{2}X}$	$V_{\Gamma X}$
Value	-1.62	-2.93	0.83	-0.28	0.34	0.23	-0.47	-1.34	-1.73

6.2 Electron Mobility

Given that the band minima of Ge and Sn occur at the L and Γ valleys respectively, electrons in GeSn alloys primarily occupy these two valleys. Therefore, all necessary parameters required to determine the total mobility of GeSn are calculated at these two valleys. From Fischetti and Laux [91], the total electron

mobility μ in the [100] direction is given as a weighted sum of the mobilities at L and Γ, which we denote μ^L and μ^Γ respectively:

$$\mu = \frac{4}{3} r^L (\mu_l^L + 2\mu_t^L) + r^\Gamma \mu^\Gamma \tag{6.1}$$

where the parameters r^L and r^Γ are the carrier concentration ratios of the L and Γ bands respectively, while the l and t denote the longitudinal and transverse directions, respectively. The 4 on the L-part comes from the 4-fold degeneracy of the L-valley, since all 4 L valleys contribute to transport in the $[100]$-direction. The prefactor $1/3$ arises from the anisotropic nature of the L valley mobility tensor and the geometric projection of each valley's mobility onto the $[100]$ direction. Each L valley has a mobility tensor consisting of a longitudinal component (μ_l^L) along the valley axis ($[111]$) and two orthogonal transverse components ($\mu_{t,\parallel}^L$ and $\mu_{t,\perp}^L$). To determine the contribution of a single L valley to transport along $[100]$, the tensor must be projected onto the $[100]$ axis. The longitudinal direction forms an angle θ with $[100]$, such that $cos^2\theta = 1/3$, leading to a projected contribution of $\mu_l^L/3$. The transverse directions, typically taken as $[1\bar{1}0]$ and $[11\bar{2}]$, are orthogonal to $[111]$ and contribute according to the squares of their directional cosines with $[100]$, which are $cos^2\theta = 1/2$ and $cos^2\theta = 1/6$, respectively. Assuming the transverse mobilities are equal ($\mu_{t,\parallel}^L = \mu_{t,\perp}^L$), the total projected mobility from a single L valley is: $\mu_{[100]}^L = 1/3(\mu_l^L + 2\mu_t^L)$.

This Section is organised as follows: We firstly outline the theoretical framework used, reminding the reader of the detailed expressions for the electron mobility of a semiconductor and how we calculated all relevant parameters in its determination. We focus in particular on the calculation of the DOS at the non-parabolic Γ-valley. We subsequently present our results for the the electron mobility of GeSn, particularly focusing on the effect of alloy scattering, bandgap nature, strain and temperature on the mobility.

6.2.1 Theoretical Framework

Vital to our methodology was the difference in the shape of the L and Γ bands. Recall that the L-bands are more-or-less parabolic, and any non-parabolicity can be accounted for by introducing a non-parabolicity factor (γ^L) to many of our mathematical expressions. Recalling formula 5.37 from Chapter 5, we can

describe the intrinsic electron mobility at the L-valley in the direction λ (μ_λ^L) as:

$$\mu_\lambda^L = \frac{2e}{3n^L m_\lambda^L} \int_0^\infty dE \, \frac{E\rho^L(E)\left(-\frac{\partial f}{\partial E}\right)}{R_\lambda^L(E)}(1+\gamma^L E/2) \tag{6.2}$$

where m represents the effective masses (given in Table 4.2 in Chapter 4), and the isotropic non-parabolicity parameters ($\gamma_{Ge}^L = 0.43\ eV^{-1}$ and $\gamma_{Sn}^L = 0.52\ eV^{-1}$), shown in Eq. 6.3, are in good agreement with previous calculations [275].

$$\gamma^L = \frac{1}{E_{L_{3v}} - E_{L_{1c}}} \tag{6.3}$$

The DOS per unit volume at the L valley (ρ^L) is expressed analytically (Eq. 5.39 in Chapter 5). In contrast, the Γ-band becomes increasingly non-parabolic with increasing Sn concentration, such that the effective mass at Γ $m_\Gamma \to 0$. As a result, the analytic expression for the DOS breaks down, meaning Eq. 6.2 is not applicable to the Γ-mobility. We instead express the intrinsic electron mobility at the Γ-valley using Equation 5.38 from Chapter 5:

$$\mu_\lambda^\Gamma = \frac{e}{n^\Gamma} \int_0^\infty \frac{d^3k}{4\pi^3} \, \frac{\left(v_g^\Gamma(k)\right)^2}{R_\lambda^\Gamma\left(E(k)\right)} \left(\frac{-\partial f}{\partial E}\right) \tag{6.4}$$

In Equations 6.2 and 6.4, f describes the in-equilibrium distribution of electrons in the conduction band, given by Fermi-Dirac (FD) distribution (see Eq. 5.24). However, as we approach room temperature, the energy E of the conduction band state is much higher than the Fermi energy ($E - E_F >> kT$). As a result, FD distribution simplifies to Boltzmann distribution.

The momentum scattering rates R^α in Equations 6.2 and 6.4 are sums of the alloy-scattering and electron-phonon scattering at valley α. We calculate phonon scattering following Fischetti and Laux [91] using the deformation potential method (shown in Eqs. 5.21 and 5.23 in Chapter 5). Since we confine our calculations to Sn compositions below 25%, we used the phonon energies and deformation potentials for Ge, which have been previously calculated by Murphy-Armando and can be found in Refs. [276, 277]. For the Γ valley, intravalley scattering with optical phonons vanishes around the mainly s-type wavefunctions [91]. The intravalley Γ deformation potential is a linear interpolation Ge [277] and Sn [238] values. The phonon parameters used are given in Tables 6.3 and 6.4, with the phonon energies taken from Ref. [277].

Table 6.3: Deformation Potentials for Ge and GeSn.

Scattering Type	Valleys	Symbol	Value	Unit	Reference
intravalley	L	$(D_L)_{op}$	363	$10^8 eV/m$	[277]
		Ξ_u	16.975	eV	[276]
		Ξ_d	-6.265	eV	[276]
	Γ	$(D_\Gamma)_{ac}$	$-5.3 - 0.7x$	eV	[94]
intervalley	LL	(D_{LL})	78.8	$10^8 eV/m$	[277]
	$L\Gamma$	$(D_{L\Gamma})$	286	$10^8 eV/m$	[277]

Table 6.4: Phonon Energies for Ge.

Scattering Type	Valleys	Symbol	Value	Unit
intravalley	L	$\hbar\omega_{op}$	37	meV
intervalley	LL	$\hbar\omega_{LL}$	29	meV
	$L\Gamma$	$\hbar\omega_{L\Gamma}$	30	meV

Both the total scattering rate (via Fermi's Golden Rule) and the carrier concentration (Eq. 5.36) at the Γ valley depend on the DOS at Γ (ρ^Γ). Rather than implementing the analytic expression, we instead express the DOS as a sum of delta-functions centred at the discrete energy levels E_k:

$$\rho^{(\alpha)}(E) \equiv \sum_k \delta\left(E - E_k\right) = \int \delta\left(E - E_k\right) d^3\vec{k} \tag{6.5}$$

We can rewrite this expression by utilising a change of variables $d^3\vec{k} = d\vec{S}dh$, where $h = E - E_k$ and $d\vec{S}$ is the surface in k-space at constant h, i.e. perpendicular to dh [278]. We can then exploit the scaling properties of a delta function applied to a function, whereby $\delta\left(f(x)\right)$ can be written as a sum of δs at the zeros of f:

$$\delta(f(x)) = \sum_i \frac{\delta(x - x_i)}{|f'(x_i)|} \tag{6.6}$$

Applying this to the DOS gives:

$$\rho^{(\alpha)}(E) = \int d\vec{S}\, dh \frac{\delta(h)}{|\nabla_{\vec{k}} h|} \tag{6.7}$$

Finally, integrating over h, we obtain our analytical expression (Eq. 6.8) for the

DOS using the sifting property of the delta function $\int_{-\infty}^{\infty} f(x)\delta(x-x_0)\,dx = f(x_0)$:

$$\Rightarrow \rho^{(\alpha)}(E) = \frac{d\vec{S}}{|\nabla_{\vec{k}} h|}\Big|_{\vec{k}|h=0}$$
$$\Rightarrow \rho^{\Gamma}(E) = \frac{d\vec{S}}{|\nabla_{\vec{k}}(E - E_{\vec{k}})|}\Big|_{\vec{k}|E=E_{\vec{k}}} \tag{6.8}$$

In order to accurately determine E_k, the conduction band energies around the Γ-point, we first use DFT to find the band dispersion around the Γ-point. We then fit the DFT eigen-energies to a $3D$-Kane model [230], as described in Section 3.4 of Chapter 3. The DFT eigen-energies are fitted to the eigenvalues of the 4×4 Hamiltonian matrix, whereby we solve for parameters a and b. We finally correct the DFT-calculated direct-gap E_g for GW and temperature. Using these energies around the Γ-point, we calculated the group velocity of the electrons, defined by $v_g^{(\alpha)}(k) \equiv \frac{1}{\hbar}\frac{\partial E}{\partial k}$. Since we are interested in calculating the electron mobility in the $[100]$-direction, we calculate the group velocity of the electrons in the x-direction.

In all our calculations on unstrained GeSn, we consider Sn concentrations of up to 25%, keeping with the realistic amount of Sn that can be incorporated into Ge. While as much as 2% strain has been successfully applied to Ge, we apply 0.5% and 1% biaxial tensile strain to GeSn, where we consider Sn concentrations up to 20%. We expect that alloy scattering will reduce the electron mobility of Ge upon the introduction of Sn. However, once the alloy transitions to a direct-gap material, we anticipate that the mobility will increase to many times that of intrinsic Ge, especially with the application of strain.

6.2.2 Results

6.2.2.1 Room Temperature Mobility of unstrained GeSn

We first examine the behaviour of the room-temperature intrinsic n-type electron mobility of unstrained GeSn, where we assume a random alloy. Figure 6.2 shows the behaviour of the mobility of unstrained GeSn as a function of Sn concentration. We calculated the mobility of Ge to be $4300\ cm^2/(Vs)$, which is comparable to the 3900 observed by Fischetti and Laux [91] and experimentally [92]. As Sn is introduced, the mobility decreases due to alloy scattering, becoming as low as $510\ cm^2/(Vs)$ at 8.75% Sn (just beyond the indirect-to-direct gap transition). Thereafter, the mobility increases rapidly as the electrons begin to populate the

Γ valley, where the mobility is much higher than at the L valley. To achieve an electron mobility above that of Ge by alloying with Sn, a Sn concentration of at least 13.5% must be added. Figure 6.2 shows that at 17.5% Sn, GeSn has a mobility 5 times greater than that of Ge, while $Ge_{0.75}Sn_{0.25}$ has a mobility over 25 times greater than that of Ge.

Figure 6.2 also shows in the subplot the carrier concentration ratios of the Γ and L valleys (r_Γ and r_L respectively) for intrinsic unstrained GeSn, which displays the gradual rise in the electron population at Γ due to the high temperature (Boltzmann distribution).

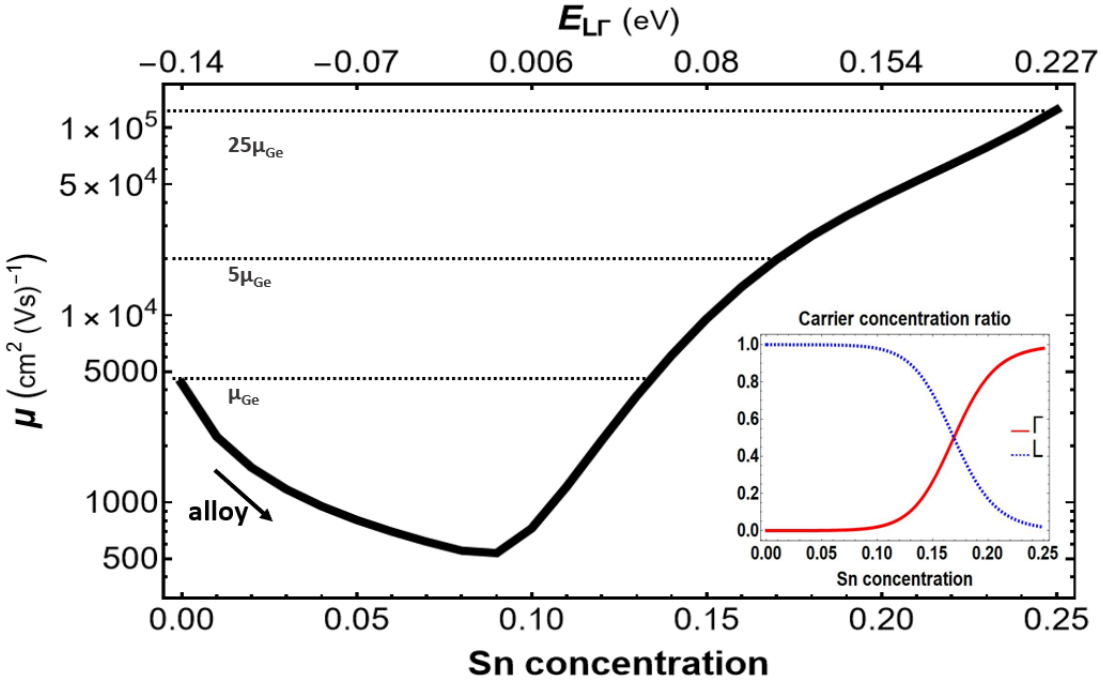

Figure 6.2: Room-temperature intrinsic n-type electron mobility of unstrained GeSn as a function of Sn concentration and difference in bandgaps $E_{L\Gamma} = E_L - E_\Gamma$ (in eV). The second scale is better representative of the behaviour of the electron mobility, since the mobility only begins to rise after $E_{L\Gamma}$ becomes positive, and Sn concentration may not correspond to $E_{L\Gamma}$ directly due to clustering.

Perhaps surprisingly, the mobility continues to rise when the carriers have almost entirely populated the Γ-valley, with no eventual decay as a result of alloy scattering. This can be attributed to two key reasons: one is an increase in the group velocities of the electrons with Sn concentration, and two is the lowering of the DOS at Γ with Sn concentration. In Figures 6.3 and 6.4, we show the thermal averages of the group velocity and Γ-DOS as functions of Sn

concentration, whereby we integrate each quantity over all states weighted by the distribution function.

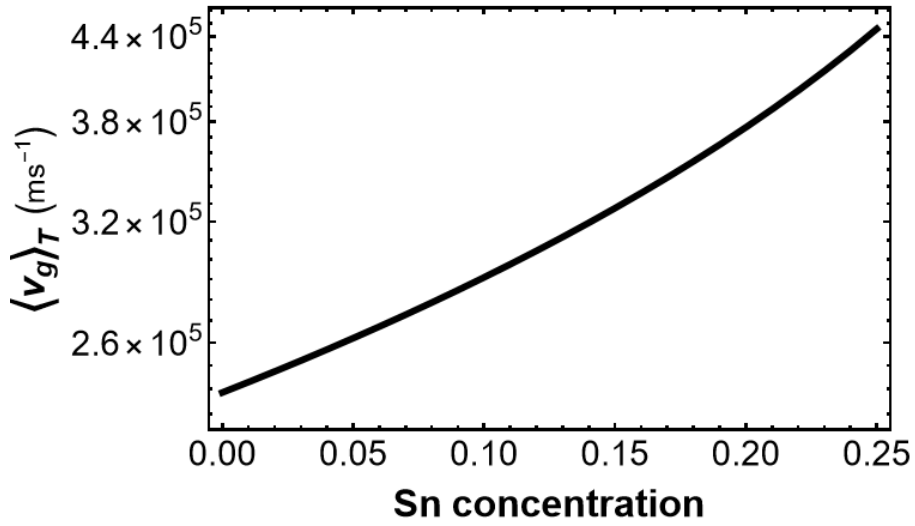

Figure 6.3: Thermal average of the group velocity at Γ of GeSn in m/s as a function of Sn concentration.

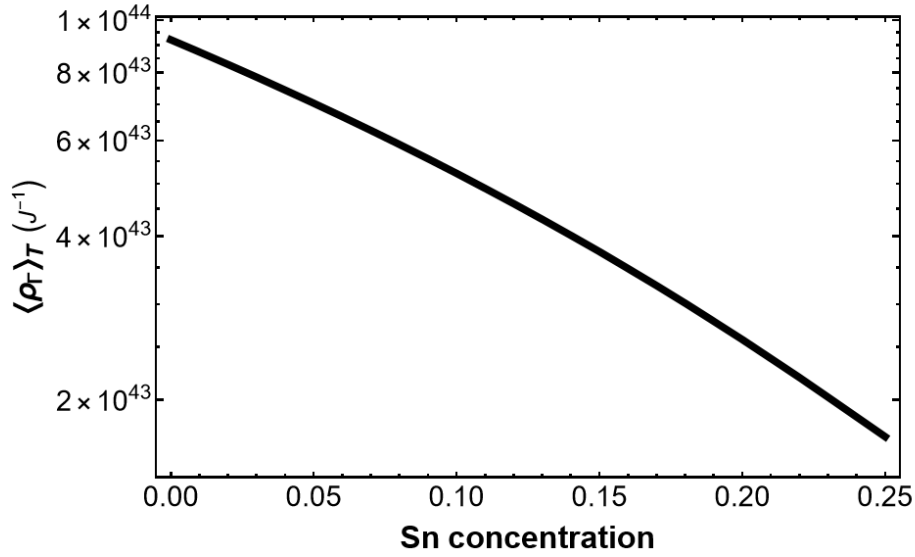

Figure 6.4: Thermal average of DOS of the Γ valley as a function of Sn concentration.

Despite this continuous increase in mobility beyond 8.75% Sn, it is nevertheless limited by alloy scattering. The full effect of alloy scattering in presented in Figure 6.5. The black line corresponds to the mobility of GeSn at room temperature, as was shown in Figure 6.2. The red and blue lines are the

hypothetical mobilities disregarding intervalley alloy scattering and all alloy scattering, respectively. Clearly, intervalley alloy scattering affects the mobility at Sn concentrations $0 - 11\%$. The fact that the outcomes are several orders of magnitude different highlights that intravalley alloy scattering in particular needs to be considered with precision.

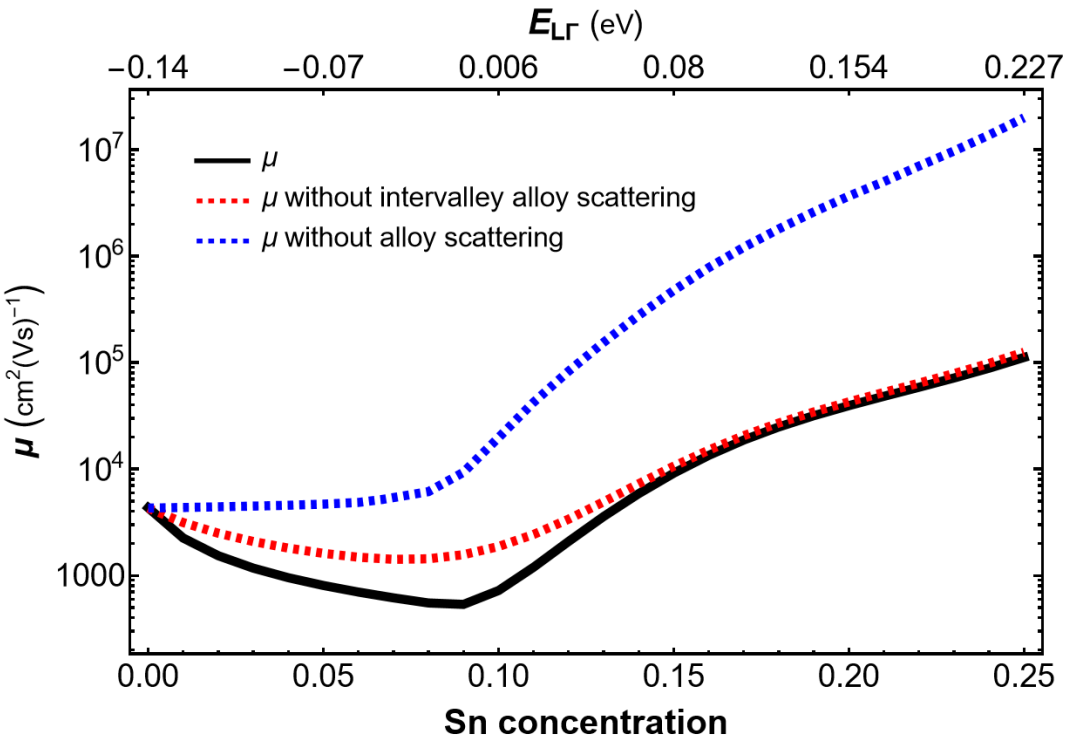

Figure 6.5: Room temperature mobility with alloy scattering (black), without intervalley alloy scattering (red) and without alloy scattering (blue) contributions, as a function of Sn concentration.

6.2.2.2 Room Temperature Mobility of biaxially tensile strained GeSn

The application of biaxial tensile strain induces an indirect-to-direct bandgap transition at lower Sn concentrations (as we showed in Figure 4.5 in Chapter 4), Consequently, electrons populate the Γ valley at lower Sn concentrations where there is less alloy scattering, resulting in a higher electron mobility. In order to achieve mobility higher than that of unstrained Ge, a Sn concentration of at least 11.8% with 0.5% strain is required, or 9% Sn with 1% strain. In Figure 6.6, we see that under 1% strain, a Sn concentration of just 13% is required to achieve a mobility 5 times higher than Ge. This makes biaxially strained GeSn experimentally more attractive than unstrained GeSn, given the segregation issues in GeSn would likely lead to a significant loss in mobility.

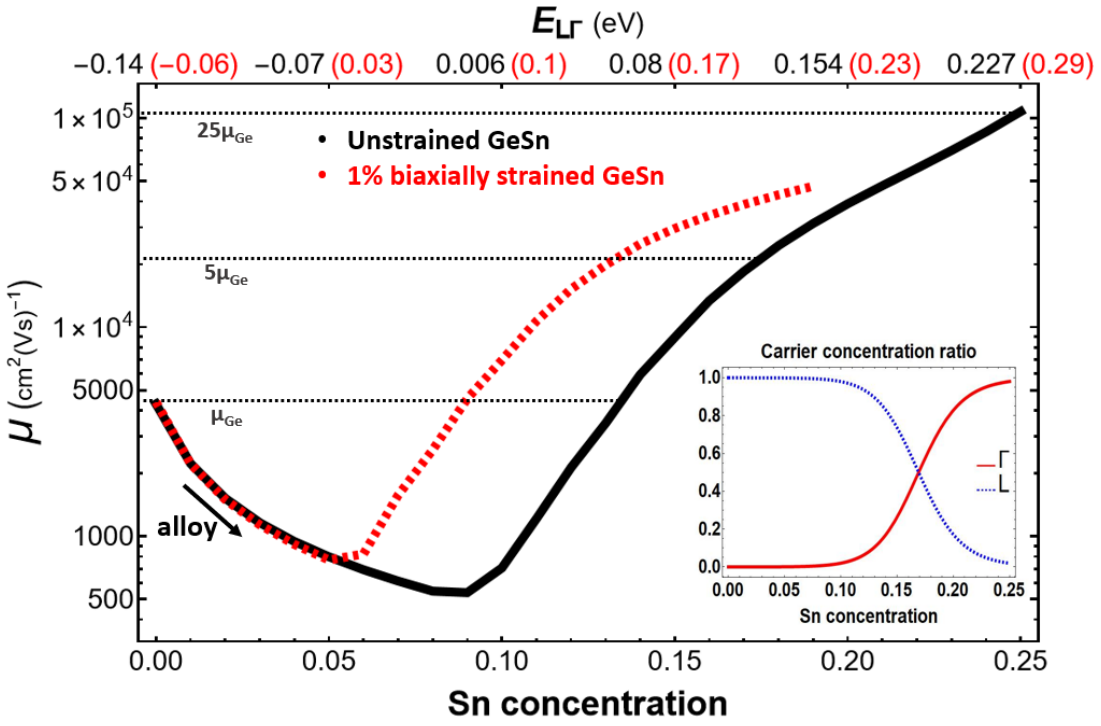

Figure 6.6: Room-temperature intrinsic n-type electron mobility of unstrained GeSn (black) and 1% biaxially tensile strained GeSn (red), as a function of Sn concentration and difference in bandgaps $E_{L\Gamma} = E_L - E_\Gamma$ (in eV).

6.2.2.3 Low Temperature Mobility (15K) of (strained) GeSn

We now examine the electron mobility of GeSn at $15K$. At such a low temperature, the electron distribution $f_0(E)$ from Equations 5.40 and 6.4 describes the Fermi-Dirac (FD) distribution, which behaves like a step-function. We can therefore expect changes in the electron distribution across the L and Γ valleys (and by extension the mobility) to be less gradual compared to higher temperatures.

In Figure 6.7, we show the electron mobility of unstrained and 1% biaxially strained GeSn, as well as the carrier concentration ratios of unstrained GeSn at $15K$. The electron mobility for unstrained Ge is $2.52 \times 10^4\ cm^2/(Vs)$, almost ten times the room-temperature value, since electron-phonon scattering is orders of magnitude lower than at room temperature. Beyond the indirect-to-direct bandgap transition (8.8% Sn in unstrained GeSn), electrons quickly populate the Γ valley (as we see in the subplot of the carrier concentration ratios), causing the mobility to rise rapidly. A Sn concentration of 9.1% is needed to achieve a mobility higher than the Ge value, where the L valley is $4.6\ meV$ above the Γ valley and the carrier concentration ratio of electrons in Γ is 0.022. The mobility

has an order of magnitude of 10^6 beyond 25% Sn for unstrained GeSn.

With the addition of tensile strain, a direct gap occurs at a lower Sn concentration, causing the mobility to increase at a lower Sn concentration, with less alloy scattering as a result. At 0.5% and 1% strain, GeSn transitions to a direct gap material at 7.75% and 5.57% Sn respectively. As more Sn is introduced beyond these concentrations, the mobility is almost immediately higher than for strained Ge. Under 1% strain, as we see in Figure 6.7, the mobility of GeSn is 10^5 at 5.95% Sn, where $E_{L\Gamma} \simeq 0$ and the carrier concentration ratio of electrons in Γ is 0.58. At high Sn concentrations, the effect of strain in increasing the mobility of GeSn in minimal.

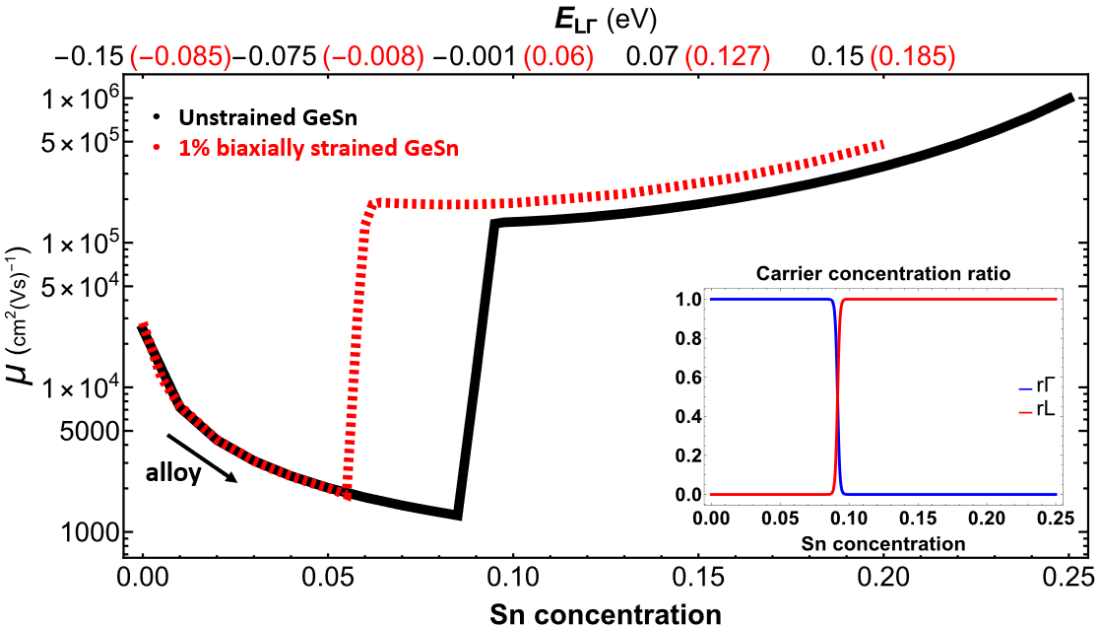

Figure 6.7: Low-temperature (15K) intrinsic n-type electron mobility and carrier concentration ratios at L and Γ as a function of Sn concentration and difference in bandgaps.

6.2.2.4 The Effect of Temperature on the Mobility of (strained) GeSn

Reducing temperature increases the electron mobility of GeSn for two reasons. Firstly, electron-phonon scattering decreases with decreasing temperatures. Secondly, the Fermi-distribution becomes increasingly step-function-like at lower temperatures, causing the carriers to populate the Γ valley at the indirect-to-direct bandgap transition at lower $E_{L\Gamma}$ energy difference than at higher temperatures. This results in a higher electron mobility at lower Sn concentrations. From an experimental perspective it is easier to observe transport via the direct

Γ valley by varying the temperature, since this is easier to control than the Sn concentration. Therefore in Figure 6.8, we highlight the effect of temperature on the mobility of unstrained Ge, $Ge_{0.9}Sn_{0.1}$ and $Ge_{0.85}Sn_{0.15}$, as well as $Ge_{0.93}Sn_{0.07}$ under 1% biaxial strain. We can see from Figure 6.8 that across the temperature range of $15 - 300K$, $Ge_{0.85}Sn_{0.15}$ provides the optimal mobility. However, as temperature decreases, the mobility of $Ge_{0.9}Sn_{0.1}$ becomes increasingly comparable to $Ge_{0.85}Sn_{0.15}$ and may be preferred experimentally to show the transition of $L \rightarrow \Gamma$ transport. In addition, below $50K$, the mobility of $Ge_{0.93}Sn_{0.07}$ at 1% biaxial strain is almost the same as unstrained $Ge_{0.9}Sn_{0.1}$, which may be even more desirable experimentally due to the lower Sn concentration.

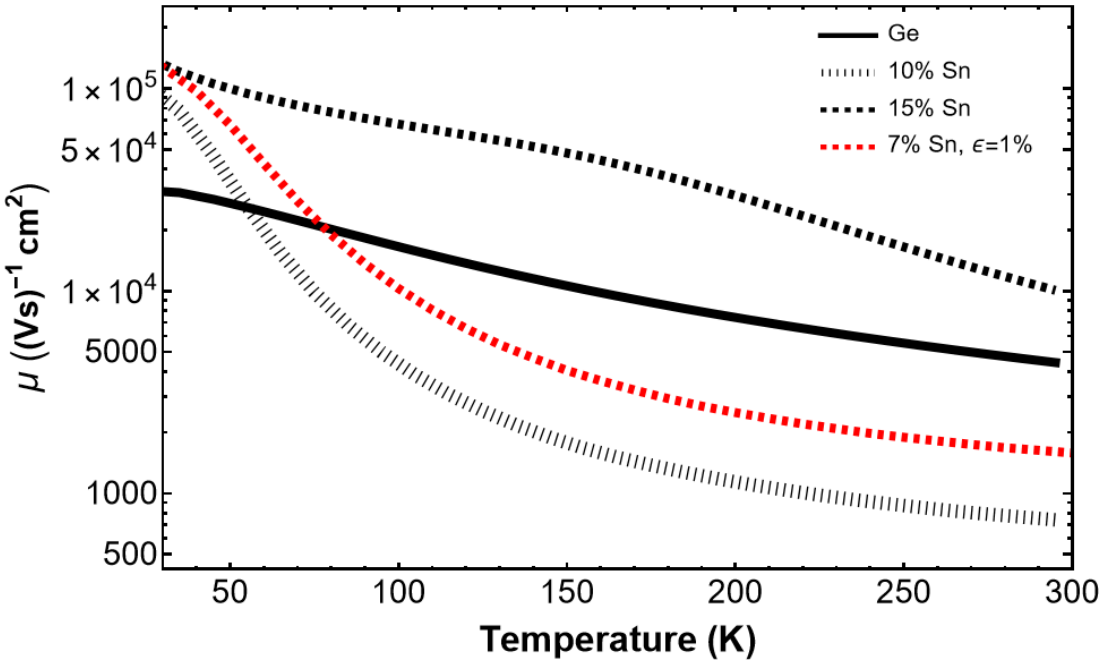

Figure 6.8: Intrinsic n-type electron mobility of Ge and $Ge_{0.9}Sn_{0.1}$ as a function of temperature (K).

6.3 Conclusions

The overall aim of this chapter was to calculate the intrinsic n-type electron mobility of GeSn as a function of alloy content, temperature and biaxial tensile strain. We began by presenting a full ab initio calculation of the n-type intra- and intervalley scattering parameters of GeSn, where atomic relaxation was critical in determining accurate parameters. Our values were larger than those for SiGe, with both our intra- and intervalley scattering parameters having a substantial

impact on limiting the electron mobility of GeSn.

Our alloy scattering parameters were used to determine the mobility of GeSn using a first iteration of the Boltzmann transport equation. We find that alloy scattering causes an initial decrease in the mobility to 10% of that of Ge at Sn concentrations of up to 9%. However, the indirect-to-direct bandgap transition initiates a steep increase in the mobility. At room temperature, the electron mobility of unstrained GeSn can rise to above 25 times higher than Germanium's mobility at sufficient Sn concentrations. The inclusion of a biaxial tensile strain reduces the Sn content required to achieve a high mobility. At cryogenic temperatures, the considerable increase in mobility occurs at the Sn concentration of the indirect-to-direct transition, requiring much less Sn than at room temperature. We propose that measuring the mobility against temperature in an alloy of 10% Sn content will clearly show the dramatic effects of the indirect-to-direct transition.

Our approach allows for the transfer of parameters to multi-scale models, enabling more comprehensive and accurate modelling of carrier transport phenomena in semiconductor heterostructures. This model can be used in the future as part of a larger model that includes both n-type and p-type carriers. Given the promise of 2D hole gas mobilities in strained Ge, we propose the use of strained GeSn for n-type 2D electron gases. The broader impact of these findings could lead to significant advancements in electronic device performance. By enabling faster carrier transport and reducing energy dissipation, strained GeSn-based devices have the potential to support the development of next-generation low-power, high-speed transistors. This has direct implications for improving processor speeds, extending battery life in mobile electronics, and enhancing energy efficiency in data centres and high-performance computing applications.

Comparing our calculated mobilities to recent experimental measurements, Tien et al. [279] reported an electron mobility of $Ge_{0.88}Sn_{0.12}$ to be 1500 cm^2/Vs at room temperature, which compares reasonably well with our calculated value of 2085 cm^2/Vs. At 15 K, their measured mobility was 6200 cm^2/Vs, significantly lower than our predicted value of 8.07×10^4 cm^2/Vs. The lower experimental mobility can be attributed to two main factors: (i) the mobility in GeSn alloys is highly sensitive to Sn content in the range of $8.5 - 12\%$, especially at lower temperatures, where even small variations in composition can lead to significant changes in mobility, and (ii) the presence of additional defects in experimental samples, such as point defects, dislocations, and other imperfections, can further

reduce the mobility compared to idealised theoretical predictions.

As we will see in the next chapter, where we explore the potential of GeSn in spintronics, the alloy scattering parameters can be used as a foundation to determine the spin-dependent alloy scattering parameters, which will help us to understand the extent to which electrons change their spin polarisation as they scatter off alloy impurities.

Chapter 7

Spin Relaxation in GeSn

The ultimate goal of this chapter is to calculate the intrinsic spin relaxation time and the spin-diffusion length of GeSn as a function of temperature and Sn concentration. Adding Sn to Ge introduces a novel degree of freedom to tailor its spin properties. As a consequence of the large SOC of Sn, we expect there to be “spin-flips" as a result of alloy scattering in GeSn; that is, a certain proportion of electrons will change their spin-orientation as they scatter due to alloy impurities. In this chapter, we calculate the spin-dependent alloy scattering parameters from first-principles. In addition, we calculate all necessary phonon parameters which define spin-dependent scattering to and from the Γ valley, which plays an important role at higher Sn concentrations. This is the first theoretical calculation of the spin relaxation time of GeSn, and our findings could be vital in the development of future design of spintronic devices, such as those mentioned in Chapter 1.

This chapter is divided into three sections. In Section 7.1, we present the theoretical framework for determining the spin relaxation time for GeSn, with an emphasis on our first-principles methods used to calculate the spin-dependence of the alloy and electron-phonon scattering parameters. We show our results in Section 7.2 and our conclusions in Section 7.3.

7.1 Theoretical Framework

To calculate the spin relaxation time τ^α at the valley minimum α, we use the fact that $\tau^\alpha = \frac{1}{\langle R^\alpha \rangle}$ [192, 280], where $\langle R^\alpha \rangle$ is the thermal average of the scattering

rate $R^{\alpha}(E)$, such that:

$$\langle R^{\alpha} \rangle = \frac{\int R^{\alpha}(E) \, \frac{\partial f}{\partial E} \, \rho(E) \, dE}{\int \frac{\partial f}{\partial E} \, \rho(E) \, dE} \tag{7.1}$$

Each $R^{\alpha}(E)$ is a sum of the electron spin-phonon scattering rate and spin-alloy scattering rate. Given the nature of the band structure of GeSn, the total spin relaxation time τ is a weighted sum of the relaxation times at the L and Γ valleys:

$$\tau = r_L \tau_L + r_{\Gamma} \tau_{\Gamma} \tag{7.2}$$

where both τ_L and τ_{Γ} include intravalley and intervalley spin relaxation as a result of e-ph and alloy scattering, and the carrier concentration ratio r_L is for the four L valleys. In this section, we discuss our methods of calculating the spin-scattering parameters due to alloy scattering and e-ph scattering.

7.1.1 Spin-Alloy Scattering

Calculating the alloy scattering parameters in GeSn in Chapter 6 was a stepping stone in determining the spin-alloy scattering parameters in GeSn, i.e the potentials $V_{\alpha\beta}^{\sigma'\sigma}$ that measure the likelihood of an electron scattering from BZ valley α with spin orientation σ to valley β with spin orientation σ'.

Our methodology largely follows that found in Section 6.1. However, the presence of SOC results in a more complicated process for determining the spin-dependence of the alloy scattering parameters. The scattering rate for spin-flips caused by alloy impurities is given by Eq. 5.16 in Chapter 5, with the matrix element now dependent on a change in spin orientation. We will denote this parameter as $V_{\alpha\beta}^{\uparrow\downarrow}$. Consequently, we modify Eq. 5.16 to instead read:

$$\left\langle V_{\alpha\beta}^{\uparrow\downarrow} \right\rangle = N(\left\langle \psi_{\alpha}^{\uparrow} \right| \Delta V_{Sn} \left| \phi_{\beta}^{\downarrow} \right\rangle - \left\langle \psi_{\alpha}^{\uparrow} \right| \Delta V_{Ge} \left| \phi_{\beta}^{\downarrow} \right\rangle) \tag{7.3}$$

whereby the wavefunction $|\psi\rangle = (\psi_{\Uparrow}, \psi_{\Downarrow})^T$ can be decomposed into effective up and down spin-states $\psi_{\Uparrow}$ and $\psi_{\Downarrow}$, which diagonalise the spin operator $S^{\alpha} = \frac{\hbar}{2}\sigma^{\alpha}$ in the Kramers degenerate subspace [199], where σ^{α} denotes the Pauli matrices corresponding to the Cartesian components $\alpha = x, y, z$:

$$\begin{aligned} \langle \psi_{\Uparrow} | \, S_{\alpha} \, | \psi_{\Uparrow} \rangle &= - \langle \psi_{\Downarrow} | \, S_{\alpha} \, | \psi_{\Downarrow} \rangle \\ \langle \psi_{\Uparrow} | \, S_{\alpha} \, | \psi_{\Downarrow} \rangle &= 0 \end{aligned} \tag{7.4}$$

The effective spin states are calculated from the spin matrix $S(k)$, which represents the spin operator in the wave function basis. The matrix elements of the spin operator in the Bloch state basis are given by

$$\sigma_{m,s;n,s'}(k) = \langle \psi_{m,k,s} | \, \sigma^{\alpha} \, | \psi_{n,k,s'} \rangle \tag{7.5}$$

Here, $|\psi_{n,k,s}\rangle$ denotes the Bloch state at wavevector k, band index n, and spin s. We take the spin quantisation axis to be aligned with the z-axis. We separately diagonalise each degenerate subspace in S at each k-point, obtaining the unitary matrices D_k that make each of the subspaces in $D_k S(k) D_k^{\dagger}$ diagonal, with eigenvalues equal to the effective spin [199]. The spin-flip alloy matrix elements $V_{\alpha\beta}^{\uparrow\downarrow}$ are then computed using Eq. 7.3 for all pairs of states with opposite effective spin. A 64-atom supercell (one Sn substitutional impurity in a VCA host) is used to find the scattering matrices between degenerate Bloch states.

We calculate all intravalley and intervalley alloy-spin scattering parameters between 20 high-symmetry points in the Brillouin Zone: the Γ point, the four L points, the six X points (denoted X, $-X$, Y, $-Y$, Z, $-Z$) and the six $\frac{1}{2}X$ points. We expect that both intravalley scattering and g-type (intra-axis, i.e. $X \rightarrow -X$) intervalley spin-flip alloy scattering will be forbidden as a consequence of rotational symmetry about each Cartesian axis. Consider a rotation of π radians about any Cartesian axis (we arbitrarily choose the z-axis), which is denoted as $C_2(z)$ in group theory. On average in an alloy, $C_2(z)$ is an element of the alloy substitutional defect symmetry group T_d [281]. Therefore, it commutes with the alloy scattering Hamiltonian perturbation. If we examine the transformation of spin-up $\psi_{z,\uparrow}$ and spin-down state $\psi_{z,\downarrow}$ at the Z valley in the BZ zone under $C_2(z)$, we find:

$$\begin{aligned} C_2(z) \, |\psi_{z,\uparrow}\rangle &= -i \, |\psi_{z,\uparrow}\rangle \\ C_2(z) \, |\psi_{z,\downarrow}\rangle &= i \, |\psi_{z,\downarrow}\rangle \end{aligned} \tag{7.6}$$

Since the up and down states transform differently under $C_2(z)$, the matrix element of the Hamiltonian H between them is zero. Thus:

$$\langle \psi_{z,\uparrow} | \, H \, | \psi_{z,\downarrow} \rangle = 0 \tag{7.7}$$

Eq. 7.7 confirms that no intravalley spin-flip alloy scattering processes are

allowed in GeSn. Since we can apply Eqs. 7.6 to the $-Z$ valley, this yields:

$$\langle \psi_{z,\uparrow} | \, H \, | \psi_{-z,\downarrow} \rangle = 0 \tag{7.8}$$

which confirms that g-type alloy scattering where spin-orientation changes is forbidden also.

Our Hamiltonian is also time reversal symmetric ($H = THT^{-1}$ for the time symmetry operator T), which for any two wavefunctions $|\psi\rangle$ and $|\phi\rangle$ means that $\langle \psi | \, H \, | \phi \rangle = \langle T\phi | \, H \, | T\psi \rangle^*$. This ensures that:

$$\langle \psi_{z,\uparrow} | \, H \, | \psi_{z,\uparrow} \rangle = \langle \psi_{-z,\downarrow} | \, H \, | \psi_{-z,\downarrow} \rangle^* \tag{7.9}$$

However, since the substitutional defect in our supercell removes the inversion symmetry of the diamond structure, we cannot necessarily guarantee that $\langle \psi_{z,\uparrow} | \, H \, | \psi_{z,\uparrow} \rangle = \langle \psi_{z,\downarrow} | \, H \, | \psi_{z,\downarrow} \rangle$. Eqs. 7.6, 7.7, 7.8 and 7.9 apply to valleys along the x and y axes also.

7.1.2 Electron Spin-Phonon Scattering

To accurately model spin transport in GeSn, it is essential to evaluate the full spectrum of electron–phonon scattering mechanisms that contribute to spin relaxation. In this section, we calculate all relevant scattering parameters in the L and Γ valleys of the Brillouin zone. Intravalley and intervalley scattering within the L valley have been previously reported in the literature, particularly for Ge, and serve as a reference point for GeSn. However, additional mechanisms become important in GeSn due to its evolving band structure, specifically the intervalley scattering between the L and Γ valleys and intravalley scattering at the Γ point. Each of these processes is treated individually.

We follow the work of Tang et al [69] to calculate the spin relaxation time due to intra- and intervalley electron spin-phonon scattering between the L-valleys. We implement the phonon parameters for Ge, since we are confining our calculations to low Sn compositions, and in doing so, we assume that the phonon parameters depend weakly on Sn concentration. The phonon frequencies and deformation potentials used are obtained directly from Ref. [69].

To calculate the spin relaxation time for intravalley scattering at the Γ valley, we follow the work of Tamborenea et al [282], who calculated the spin relaxation time in GaAs due to electron-electron (e-e) EY scattering at the Γ valley. They

describe the spin-flip transition rate using Fermi's Golden Rule, expressing the matrix element as a product of the spin-independent matrix element and the overlap integral, such that the scattering rate $R_{\psi_{\mathbf{k}\uparrow,\mathbf{k}'\downarrow}}$ is given by:

$$R_{\psi\mathbf{k}\uparrow,\mathbf{k}'\downarrow} = \frac{2\pi}{\hbar} \left|\langle\psi_{\mathbf{k}'\downarrow}| V |\psi_{\mathbf{k}\uparrow}\rangle\right|^2 \delta\left(E_{\mathbf{k}'} - E_{\mathbf{k}}\right) \tag{7.10}$$

$$\approx \frac{2\pi}{\hbar} V(\mathbf{k}-\mathbf{k}')^2 \left|\langle\psi_{\mathbf{k}'\downarrow}|\psi_{\mathbf{k}\uparrow}\rangle\right|^2 \delta\left(E_{\mathbf{k}'} - E_{\mathbf{k}}\right) \tag{7.11}$$

We can factorise the matrix element, as shown in Eq. 7.11, by assuming that the potential V is slowly varying on the scale of a unit cell [283]. We replace their e-e matrix element with the equivalent e-ph matrix element for GeSn, found in Table 6.3 in Chapter 6. The scalar product is given by:

$$\langle\psi_{\mathbf{k}'\downarrow}|\psi_{\mathbf{k}\uparrow}\rangle = C(k_z k'_+ - k'_z k_+) \tag{7.12}$$

where $k_+ = k_x + ik_y$. We calculate the proportionality constant C by calculating the wavefunction overlaps of a dense set of k-points near the Γ valley using DFT, and comparing to the right hand side of Eq. 7.12 for the same set of k-points. Simple integration over $\mathbf{k}$ and $\mathbf{k}'$ obtains an expression of the spin relaxation time due to intravalley scattering at the Γ point.

We use the frozen phonon supercell approach (described in Section 5.1.2.1) to calculate the deformation potential ($D_{\mathbf{q}}$) for intervalley scattering between the L and Γ bands. We use long 4-atom supercells (see Fig. 7.1 below) to obtain the energy splittings and wavefunctions due to a phonon wave-vector $\mathbf{q}$ in the $[111]$-direction, since this is the smallest cell in which phonons with the momentum transfer needed to simulate $L-\Gamma$ transitions can be modelled. The phonon frequencies ($\hbar\omega_{\mathbf{q}}$) and phonon eigenvectors $\mathbf{u}$ were calculated using DFPT with ABINIT for all six phonon modes: three acoustic (one longitudinal and two transverse) and three optical (one longitudinal and two transverse). We set the scattering amplitude $A = 0.0025$ and $A = 0.005$, where we ensure our findings show convergence. We use a k-point grid of 6x6x6 and an energy cut-off of $950eV$.

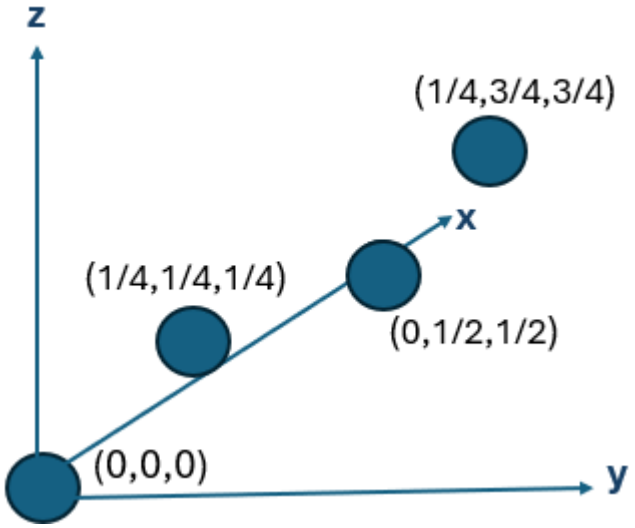

Figure 7.1: Schematic of the long 4-atom supercell used to calculate the intervalley electron spin-phonon scattering parameters of GeSn between the L and Γ valleys, showing the Cartesian coordinates of each atom.

7.2 Results

7.2.1 Spin-Alloy Scattering Parameters

Our calculations confirm that intravalley and intra-axis (g-type) spin-flips are negligible, which includes interactions from Γ to the six X and $\frac{1}{2}X$ valleys. This indicates that intravalley and g-type scattering preserves the spin orientation of the electrons. Consequently, the intravalley and g-type scattering parameters that describe electron dynamics calculated in Chapter 6 are not affected by the inclusion of SOC.

We first analyse the spin-flip scattering parameters relevant to the spin relaxation time of GeSn, that is, the scattering parameters between the Γ and L valleys, calculated using Eq. 7.3. Figure 7.2 shows $V_{LL}^{\uparrow\downarrow}$ calculated using a supercell with a VCA host at 0% Sn content (effectively representing a pure Ge supercell with a single substitutional Sn impurity). Scattering between L valleys separated along the z direction (denoted with blue arrows) is stronger at 5.82 meV than scattering between L valleys in the x or y directions (shown with red arrows), which is 4.33 meV. From this point, $L-L$ intervalley spin-alloy scattering parameters will be denoted as V_{LL}^{x} and V_{LL}^{z}, where the superscripts indicate that the initial and final valleys are separated along the x (or equivalently y) direction and the z direction, respectively. Although it may not be immediately apparent that L_1 and L_2 in the figure are separated along the z-axis, L_1 corresponds to the L-point at $(\frac{1}{2}, \frac{-1}{2}, \frac{3}{2})$, which lies along the z-axis relative to L_2. There is a similar

correspondence between L_3 and L_4.

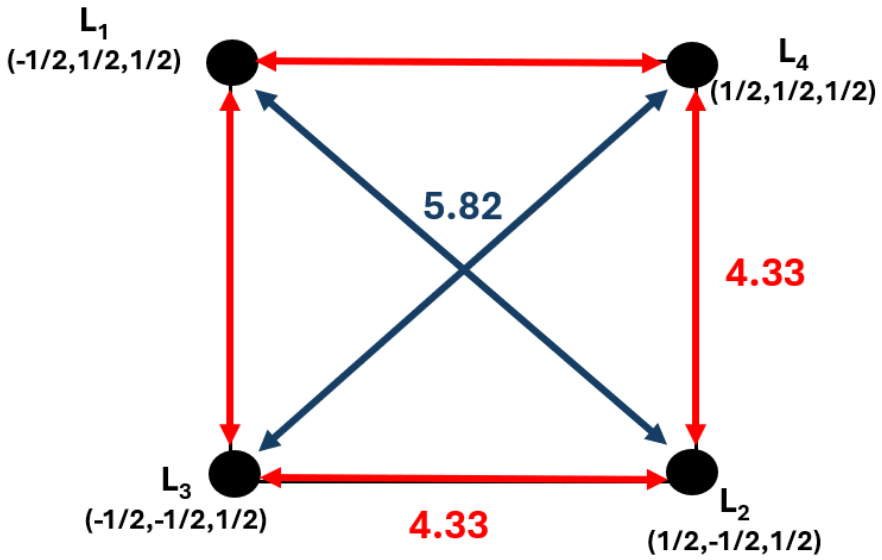

Figure 7.2: Intervalley spin-alloy scattering parameters between the L valleys of GeSn (in meV) with spin-polarisation in the z-direction.

In Fig. 7.3 we compare the $L-L$ spin-flip scattering parameters to spin-flips between L and Γ, which is over one full order of magnitude weaker, revealing that spin-flips due to alloy scattering are more prominent in high-Ge GeSn compared to direct-gap GeSn.

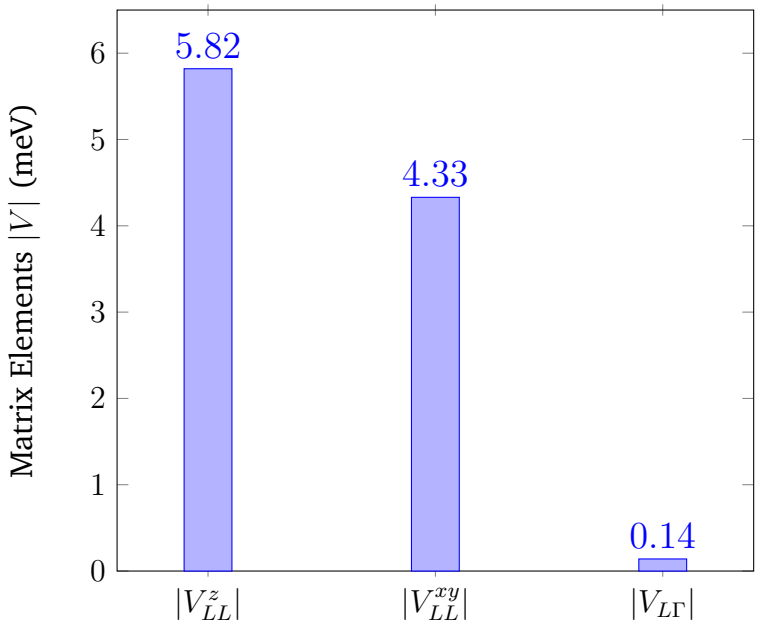

Figure 7.3: Calculated intervalley scattering matrix elements for GeSn in meV, emphasising the dominance of L-L intervalley alloy spin scattering.

To capture the Sn-dependence of the spin-alloy scattering parameters, we calculate the spin-alloy scattering matrix using supercells with host atoms of varying VCA compositions (6%, 12% and 18%), with Tables 7.1 and 7.2 showing our findings for complete set of intervalley spin-flip scattering matrix elements (in meV) for $Ge_{1-x}Sn_x$. We include interactions involving the six X and $\frac{1}{2}X$ points, as they would be prominent in spin-scattering calculations for SiGeSn. The tables are divided such that Table 7.1 contains all interactions involving the L valley, while Table 7.2 includes f-type scattering (inter-axis scattering between the various X and $\frac{1}{2}$X points, where the direction of alignment of the spins had a profound bearing on the scattering parameters).

In general, $V_{\alpha\beta}^{\uparrow\downarrow}$ largely exhibits a weak quadratic dependence on the Sn concentration of the VCA of the host atom in the supercell. Our findings show that the intervalley spin-alloy scattering parameters can vary by almost three orders of magnitude, depending on the initial and final BZ valleys involved in the process. For f-type scattering between the X and Y valleys, the scattering magnitude is of the order of meV, and $V_{XY}^{\uparrow\downarrow} = V_{XY}^{\downarrow\uparrow}$. However, for f-type scattering involving transitions to or from the Z or $\frac{1}{2}Z$ valleys, not only does the magnitude increase significantly, ranging from $10 - 100$ meV, but the up-to-down and down-to-up spin-flips differ slightly from one another. Additionally, these values swap when scattering occurs into the $-Z$ valley as opposed to the $+Z$ valley.

Table 7.1: Calculated intervalley spin-scattering matrix elements $V_{\alpha\beta}^{\uparrow\downarrow}$ (in meV) which involve the L valley in $Ge_{1-x}Sn_x$, with spin polarisation in the z-direction. The Sn concentration is determined by the VCA applied to the host atoms within the supercell.

Symbol	**Value (meV)**
$V_{\Gamma L}$	$0.14 + 0.799x + 0.625x^2$
V_{LL}^{z}	$5.818 + 15.625x - 7.639x^2$
V_{LL}^{xy}	$4.334 + 12.15x - 4.17x^2$
V_{XL}	$11.585 + 21.417x - 6.944x^2$
V_{ZL}	$16.295 + 31.583x - 20.833x^2$
$V_{\frac{1}{2}XL}$	$22.6 + 25x - 27.778x^2$
$V_{\frac{1}{2}ZL}$	$31.89 + 32.333x - 27.778x^2$

Our results for f-type intervalley spin-alloy scattering in GeSn respect time-reversal symmetry and obey Kramers theorem, as expected, ensuring that each state $\psi_{\vec{k},\sigma}$ has a degenerate partner $\psi_{-\vec{k},-\sigma}$, and spin-dependent alloy transitions are symmetric under time-reversal symmetry. However, inversion symmetry is broken due to the explicit alloy disorder in the supercell model. The presence of substitutional Sn atoms locally disrupts the centro-symmetry of the lattice, leading to asymmetries in the spin-dependent scattering rates that are not constrained by inversion/parity. This explains the difference in scattering in the $+Z$ direction as opposed to the $-Z$ direction. However, our substitutional impurity was arbitrarily placed at one end of a [111] bond. In the random alloy, there would be equal numbers at either end of the [111] bond. A true random alloy model would result in a single spin-flip parameter for each f-type transition (i.e. $V_{XZ}^{\uparrow\downarrow} = V_{XZ}^{\downarrow\uparrow}$, etc). We therefore recommend taking the average of our calculated values for use in future calculations.

Table 7.2: Calculated intervalley spin-scattering matrix elements $V_{\alpha\beta}^{\uparrow\downarrow}$ (in meV) for f-type scattering and scattering between the X and $\frac{1}{2}$X valleys in $Ge_{1-x}Sn_x$, with spin-polarisation in the z-direction. The following spin-flips are equivalent: $V_{XZ}^{\uparrow\downarrow} = V_{X-Z}^{\downarrow\uparrow} = V_{YZ}^{\downarrow\uparrow} = V_{Y-Z}^{\uparrow\downarrow}$, and $V_{XZ}^{\downarrow\uparrow} = V_{X-Z}^{\uparrow\downarrow} = V_{YZ}^{\uparrow\downarrow} = V_{Y-Z}^{\downarrow\uparrow}$.

	Symbol	**Value (meV)**
X-Y	V_{XY}	$10.403 - 9.708x + 9.028x^2$
	$V_{\frac{1}{2}X\frac{1}{2}Y}$	$3.048 - 7.117x + 15.278x^2$
	$V_{\frac{1}{2}XY}$	$12 + 21x - 27.778x^2$
X-Z	$V_{XZ}^{\uparrow\downarrow}$	$27.595 + 40.75x - 34.722x^2$
	$V_{XZ}^{\downarrow\uparrow}$	$42.38 + 25.5x - 13.889x^2$
	$V_{\frac{1}{2}X\frac{1}{2}Z}^{\uparrow\downarrow}$	$87.895 + 24.083x - 6.944x^2$
	$V_{\frac{1}{2}X\frac{1}{2}Z}^{\downarrow\uparrow}$	$92.215 + 12.75x + 20.8333x^2$
	$V_{\frac{1}{2}XZ}^{\uparrow\downarrow}$	$51.625 + 42.08x - 34.72x^2$
	$V_{\frac{1}{2}XZ}^{\downarrow\uparrow}$	$66.61 + 24.33x - 27.78x^2$
	$V_{X\frac{1}{2}Z}^{\uparrow\downarrow}$	$68.525 + 64.59x - 76.39x^2$
	$V_{X\frac{1}{2}Z}^{\downarrow\uparrow}$	$49.71 + 1.83x + 13.89x^2$

For completion, we include the non-flip intravalley and intervalley scattering parameters ($V_{\alpha\beta}^{\uparrow\uparrow}$ or $V_{\alpha\beta}^{\downarrow\downarrow}$) in Tables 7.3, 7.4 and 7.5 respectively, where the values at $x = 0$ closely correspond to our scattering parameters in Tables 6.1 and 6.2 from Chapter 6. Table 7.3 displays the intravalley spin-conserving scattering parameters, while the intervalley terms are divided into two tables: f-type (Table 7.5) and non-f-type (Table 7.4). In our f-type scattering parameters, we observe the same breakage in symmetry as the corresponding spin-flips, where Z and $-Z$ are non-degenerate, and $V_{\alpha\beta}^{\uparrow\uparrow} \neq V_{\alpha\beta}^{\downarrow\downarrow}$ for f-type scattering involving the Z-valley.

Table 7.3: Calculated intravalley spin-conserving alloy scattering matrix elements $V_{\alpha\beta}^{\uparrow\uparrow}$ (in eV) for all relevant valleys in $Ge_{1-x}Sn_x$.

Symbol	**Value (eV)**
V_Γ	$-3.48 - 2.277x + 4.984x^2$
V_L	$-2.157 + 0.433x - 0.463x^2$
V_X	$-0.75 + 0.814x - 3.92x^2$
$V_{\frac{1}{2}X}$	$-0.83 + 0.817x - 2.863x^2$

Table 7.4: Calculated intervalley spin-conserving alloy scattering matrix elements $V_{\alpha\beta}^{\uparrow\uparrow}$ (in eV) for all relevant valleys in $Ge_{1-x}Sn_x$ (excluding f-type scattering), with spin-polarisation in the z-direction. The subscript "g" represents g-type scattering.

Symbol	**Value (eV)**
$V_{\Gamma L}$	$2.927 + 0.072x - 1.15x^2$
$V_{\Gamma X}$	$1.73 - 0.361x + 0.031x^2$
$V_{\Gamma \frac{1}{2} X}$	$1.348 + 0.219x - 0.377x^2$
V_{LL}	$1.629 - 0.433x$
V_{LX}	$0.838 - 0.214x + 0.069x^2$
V_{LZ}	$0.827 - 0.223x$
V_{X_g}	$0.471 - 0.141x + 0.07x^2$
$V_{\frac{1}{2} X_g}$	$0.328 - 0.44x + 0.278x^2$
$V_{\frac{1}{2} XX}$	$1.94 - 1.154x + 1.2x^2$
$V_{\frac{1}{2} X-X}$	$0.043 + 0.1128x - 2.33x^2 + 8.951x^3$

Table 7.5: Calculated f-type intervalley spin-conserving alloy scattering matrix elements $V^{\uparrow\uparrow}_{\alpha\beta}$ (in eV) in $Ge_{1-x}Sn_x$, with spin-polarisation in the z-direction. The following parameters are equivalent: $V^{\uparrow\uparrow}_{XZ} = V^{\downarrow\downarrow}_{X-Z} = V^{\downarrow\downarrow}_{YZ} = V^{\uparrow\uparrow}_{Y-Z}$, and $V^{\downarrow\downarrow}_{XZ} = V^{\uparrow\uparrow}_{X-Z} = V^{\uparrow\uparrow}_{YZ} = V^{\downarrow\downarrow}_{Y-Z}$.

Symbol	Value (eV)
V_{XY}	$0.2347 - 0.113x$
$V_{\frac{1}{2}X\frac{1}{2}Y}$	$0.296 - 0.224x + 0.347x^2$
$V_{\frac{1}{2}XY}$	$0.13 + 0.04x - 0.278x^2$
$V^{\uparrow\uparrow}_{XZ}$	$0.2247 - 0.113x$
$V^{\downarrow\downarrow}_{XZ}$	$0.2397 - 0.13x$
$V^{\uparrow\uparrow}_{\frac{1}{2}X\frac{1}{2}Z}$	$0.285 - 0.258x + 0.417x^2$
$V^{\downarrow\downarrow}_{\frac{1}{2}X\frac{1}{2}Z}$	$0.28 - 0.234x + 0.347x^2$
$V^{\uparrow\uparrow}_{\frac{1}{2}XZ}$	$0.124 + 0.175x - 2.22x^2 + 6.94x^3$
$V^{\downarrow\downarrow}_{\frac{1}{2}XZ}$	$0.105 + 0.129x - 2.33x^2 + 7.56x^3$
$V^{\uparrow\uparrow}_{X\frac{1}{2}Z}$	$0.107 + 0.158x - 2.22x^2 + 6.94x^3$
$V^{\downarrow\downarrow}_{X\frac{1}{2}Z}$	$0.122 + 0.142x - 2.22x^2 + 6.94x^3$

7.2.2 Electron Spin-Phonon Scattering Parameters

For our frozen phonon calculation, our non-flip intervalley scattering parameters were found to be in excellent agreement with Ref. [278]. Our phonon energies (in meV), their corresponding eigenvectors and calculated deformation potentials (in $eV/\text{Å}$) for each of the six LO phonon modes are shown in Table 7.6. These will be used to calculate the scattering rate and spin relaxation time due to intervalley scattering between the L and Γ valleys.

Table 7.6: Phonon energies $\hbar\omega_{\mathbf{q}}$ (in meV), displacements $\vec{u}$ and calculated spin-flip deformation potentials $D^{\uparrow\downarrow}_{L\Gamma}$ (in $eV/\text{Å}$) for all phonon modes relevant for scattering between the Γ and L bands in $Ge_{1-x}Sn_x$.

Mode	$\hbar\omega_{\mathbf{q}}$ **(meV)**	$\tilde{\mathbf{u}}$	$\mathbf{D^{\uparrow\downarrow}_{L\Gamma}}$ $(\mathbf{eV/\text{Å}})$
1	5.83	$\begin{bmatrix} 0.58 \\ 0.26-0.006i \\ 0.26+0.006i \end{bmatrix}$	0.0102
2	5.83	$\begin{bmatrix} -0.005i \\ 0.5 \\ -0.5-0.005i \end{bmatrix}$	0.0204
3	21.56	$\begin{bmatrix} 0.41 \\ -0.41 \\ -0.41 \end{bmatrix}$	9.805×10^{-5}
4	23.23	$\begin{bmatrix} 0.41 \\ -0.41 \\ -0.41 \end{bmatrix}$	9.804×10^{-5}
5	27.69	$\begin{bmatrix} 0.01+0.11i \\ -0.48+0.11i \\ 0.49 \end{bmatrix}$	0.02163
6	27.69	$\begin{bmatrix} -0.57 \\ -0.28+0.09i \\ -0.28-0.09i \end{bmatrix}$	0.02145

7.2.3 Spin Relaxation of unstrained GeSn

Figure 7.4 shows the calculated intrinsic spin relaxation time τ (in seconds) at different fixed temperatures (T=30,100,200,300K) as a function of Sn concentration. Our results confirm that at room temperature (black), the spin relaxation of Ge lies in the nanosecond range. At any fixed temperature, the relaxation time initially decreases upon the introduction of Sn to Ge due to alloy scattering, especially at lower temperatures, where alloy scattering is more dominant than e-ph scattering. The effect of spin-alloy scattering is very small compared to electron spin-phonon scattering at room temperature.

However, beyond the indirect-to-direct bandgap transition, τ increases by several orders of magnitude, primarily as a result of low levels of alloy scattering from the Γ valley. Clearly, the behaviour of the spin-relaxation time of GeSn as a function of Sn concentration is similar to its electron mobility seen in Chapter 6. At room temperature, alloying Ge with Sn results in an increase in the spin relaxation time from below the nanosecond range at 10% Sn to the microsecond range above 17% Sn. At lower temperatures, this increase at the indirect-to-

direct bandgap transition (8.4% Sn concentration) is much more rapid as a result of reduced electron spin-phonon scattering. This results in a relaxation time which approaches 0.1 seconds at 25% Sn concentration at 30K.

In terms of applications, our figure tells us that for applications requiring a long spin lifetime, direct-gap GeSn is desirable, while Ge is more applicable for short spin lifetime applications, irrespective of temperature.

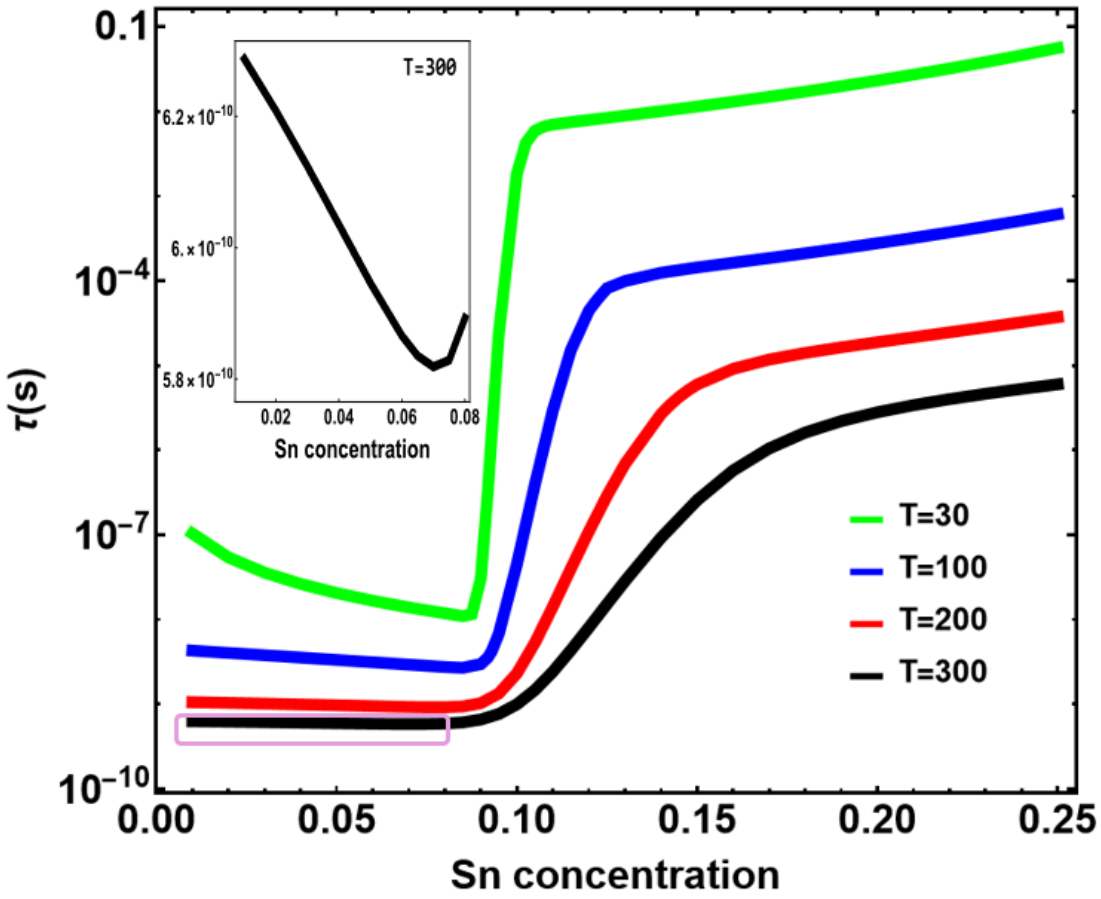

Figure 7.4: Intrinsic spin-relaxation time of GeSn at temperatures T=300K (black), T=200K (red), T=100K (blue) and T=30K (green), as a function of Sn concentration. We include an inset of the spin relaxation time at 300K at low Sn concentration to highlight its decrease with alloy content.

Experimentally, since it is easier to vary temperature as opposed to Sn concentration, we plot the spin relaxation time against temperature at Sn concentrations of 0%, 5%, 10%, 15%, 20% and 25%, shown in Figure 7.5. In general, it is clear that across a $15-300$K temperature range, spin relaxation decreases as temperature increases, which is a consequence of increased electron spin-phonon scattering.

It is also clear from this graph that to achieve a high spin relaxation time in GeSn, it must have a direct bandgap. Our Ge plot (light blue) is in good agreement with calculations by Tang et al [69], where $\tau \approx 0.5$ ns at room temperature, and approaches the microsecond range as $T \to 0$.

Above 100K, at least 15% Sn is required to increase the spin relaxation time by several orders of magnitude. At low temperatures however, the spin relaxation time can be increased by up to six orders of magnitude with the introduction of 10% Sn. Due to the change in the behaviour of the distribution function with temperature, the spin relaxation time for $Ge_{0.9}Sn_{0.1}$ changes by almost five orders of magnitude with temperature. Beyond 15% Sn concentration, there is little advantage in adding further Sn to increase the relaxation time, especially at lower temperatures.

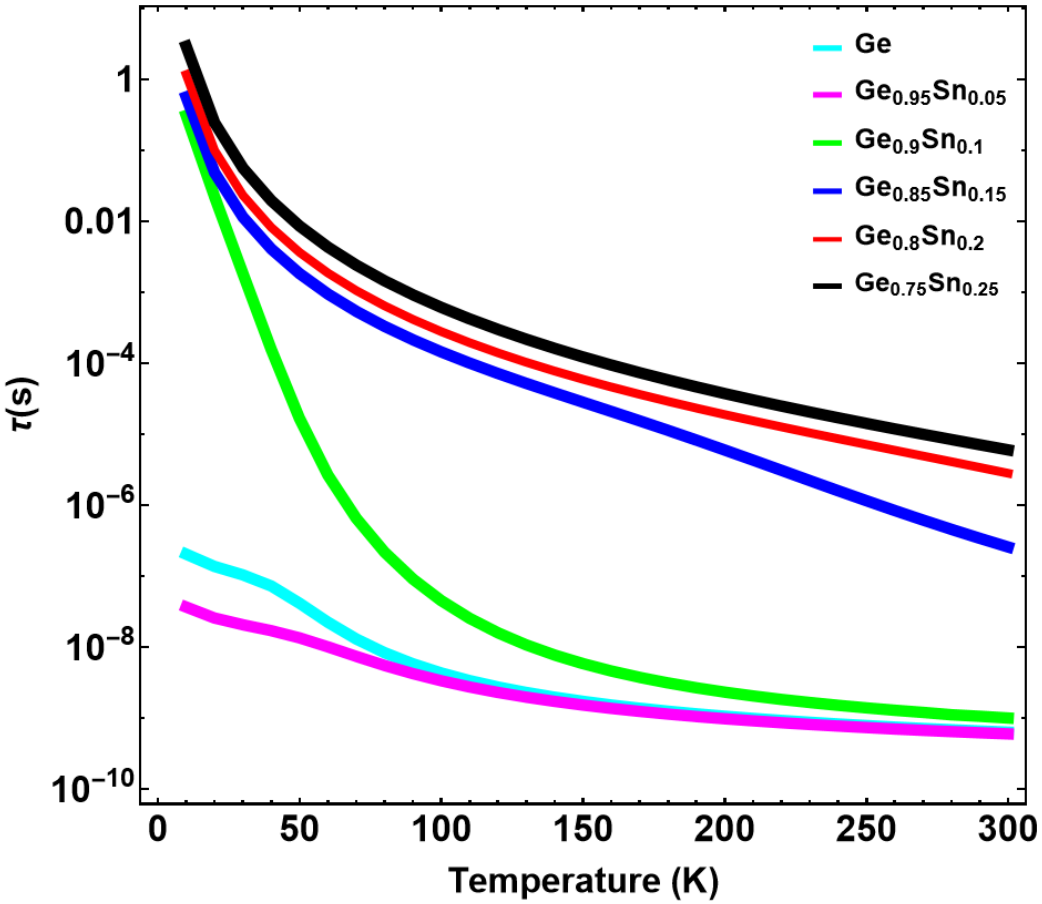

Figure 7.5: Intrinsic spin-relaxation time of Ge (light blue) and GeSn at Sn concentrations of 5% (purple), 10% (green), 15% (dark blue), 20% (red) and 25% (black), as a function of temperature (in Kelvin).

7.2.4 The Effect of Strain

The behaviour of the spin relaxation time of GeSn under biaxial tensile strain is analogous to that of unstrained GeSn. The difference is that strain induces an indirect-to-direct bandgap transition at lower Sn concentrations, resulting in electrons populating the Γ valley at lower Sn concentrations; the consequence of which is a higher spin relaxation time at any given temperature. Figure 7.6 below shows the spin relaxation time of 1% biaxially tensile strained GeSn (at $T = 300K$ and $30K$) as a function of Sn concentration. Our graph shows that at room temperature, beyond 5% Sn concentration, 1% biaxial tensile strain can increase the spin relaxation time by almost two full orders of magnitude. At $30K$, adding 6.7% Sn to 1% strained GeSn is equivalent to introducing $10 - 15\%$ Sn to unstrained GeSn to increase the spin relaxation time. At 30K, 1% strain increases τ by almost six orders of magnitude between $6 - 9\%$ Sn.

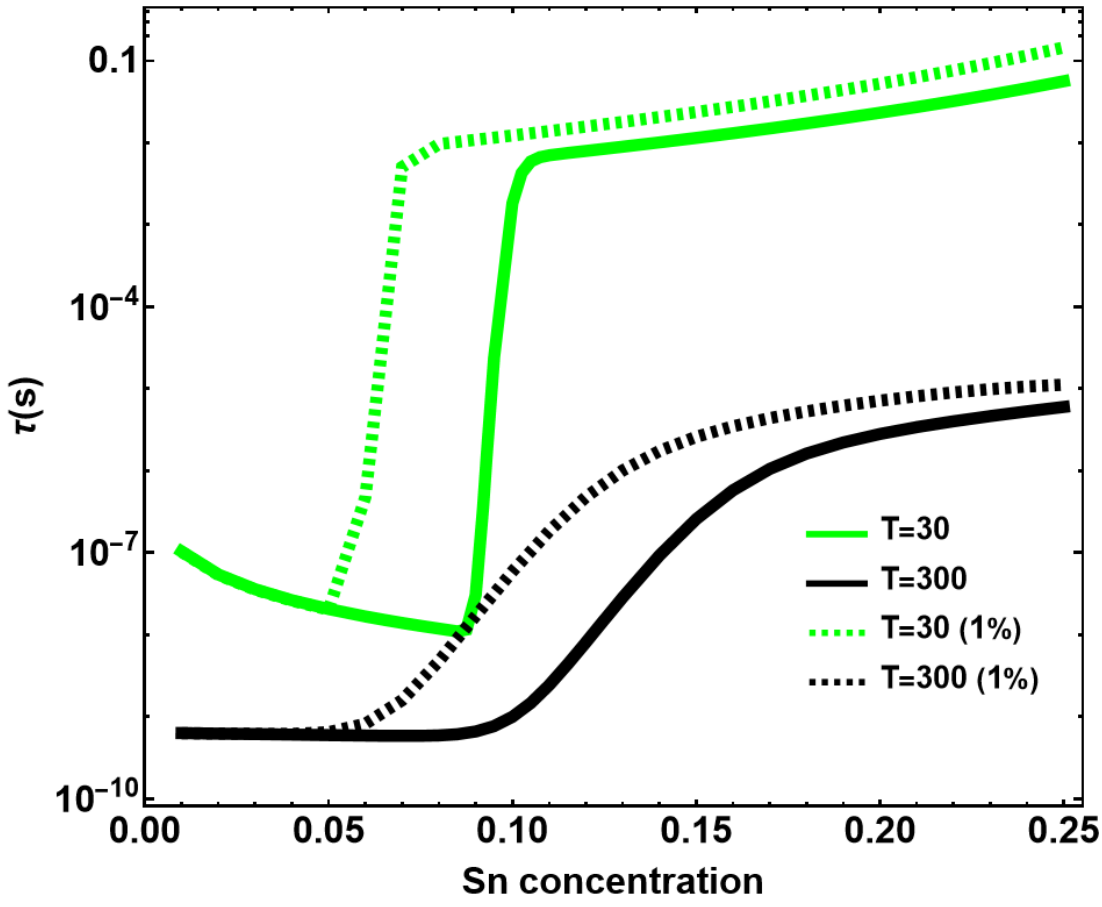

Figure 7.6: Spin relaxation time of unstrained (solid) and 1% biaxially tensile strained (dashed) GeSn at 300K (black) and 30K (green), as a function of Sn concentration.

7.2.5 Spin Diffusion Length

The spin diffusion length (L_s) is the average distance a spin-polarised electron travels before its relaxes, and is a key parameter in spintronics. It can be expressed as the product of the drift velocity v_d and the spin relaxation time τ. Since the drift velocity is proportional to the electron mobility ($v_d = \mu E$), where E is the electric field), the spin diffusion length is given by:

$$L_s = \mu \tau E \tag{7.13}$$

If we assume a voltage of 1V and a piece of material of length $1\mu m$, we have $E = 1\ Vm^{-1}$, and Eq. 7.13 reduces to $L_s = \mu\tau$. We combine our findings in Section 7.2.3 with those in Chapter 6 to calculate the spin diffusion length as a function of Sn concentration. We calculate the spin diffusion length at 300K, 200K, 100K, and 30K, with our results given in Figure 7.7, where L_d is given in micrometers. In general, the behaviour of the spin diffusion length mirrors that of the spin relaxation time and the mobility of GeSn, in that it decreases with Sn concentration until the indirect-to-direct bandgap transition, before increasing by several orders of magnitude. We calculate the room-temperature spin-diffusion length of Ge to be 275μm. At least 11% Sn concentration is required to increase the spin diffusion length at room temperature, with a Sn concentration of 25% increasing L_d to 100m. As temperature decreases, we achieve a higher spin-diffusion length, with $Ge_{0.75}Sn_{0.25}$ possessing a spin-diffusion length of the order of 1000km at 30K. In reality, over such large distances, other factors such as impurities, doping and crystal defects would take effect, likely reducing the spin diffusion length by several orders of magnitude.

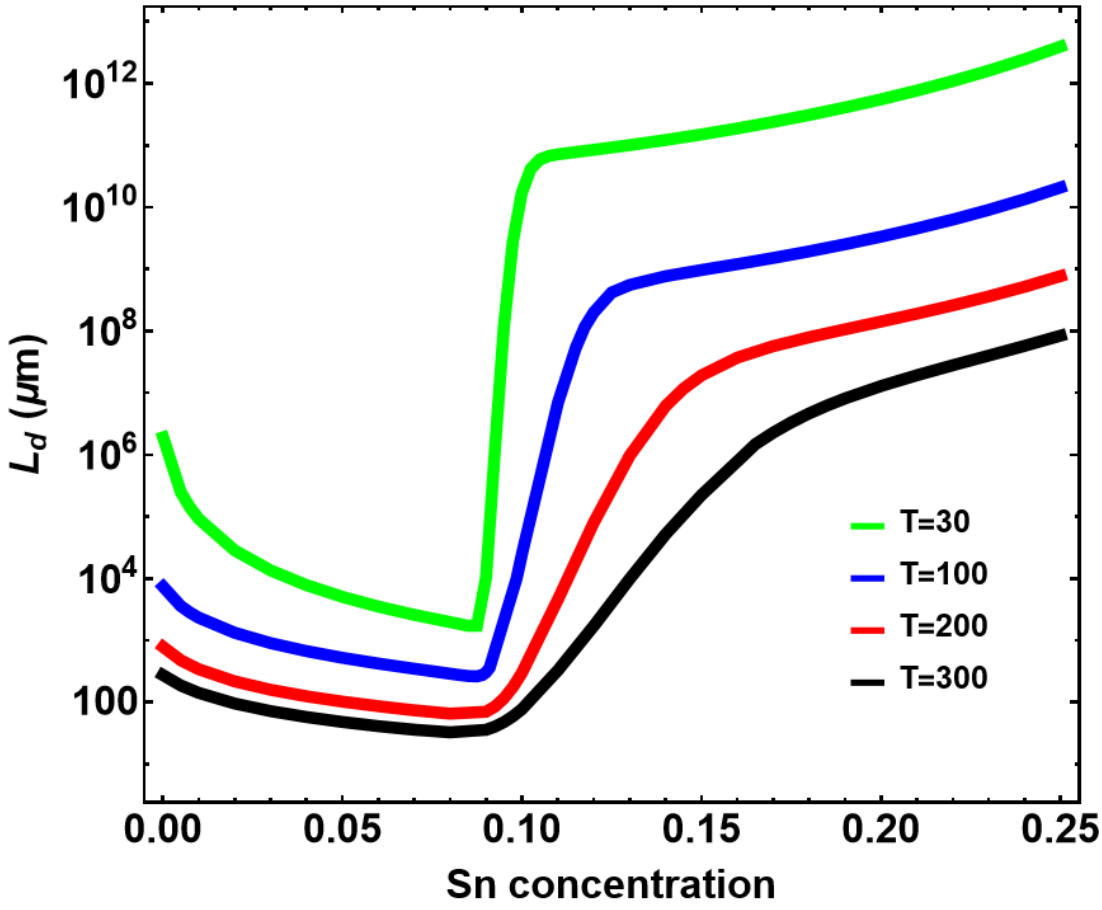

Figure 7.7: Spin diffusion length of GeSn (in μm) at temperatures T=300K (black), T=200K (red), T=100K (blue) and T=30K (green), as a function of Sn concentration.

7.2.6 Spin-Alloy Scattering in SiGe

In order to gain a more complete understanding of spin-alloy scattering in group-IV alloys, we also calculated the spin-alloy scattering parameters of SiGe. We calculated the parameters using two supercell systems: a Ge supercell with a Si impurity, and a Si supercell with a Ge impurity. In our calculations, we considered 17 conduction band states: the Γ valley, the four L valleys, the six X valleys and the six $\frac{1}{2}X$ valleys. However, for a Si supercell with a Ge impurity, we exclude the Γ valley as it plays a negligible role in scattering effects due to the band structure of Si.

Our findings for the spin-flips are divided into two tables: f-type scattering (Table 7.7) and all other relevant scattering parameters (Table 7.8), which includes scattering from Γ to L, scattering from one of the L valleys to another

L valley, one of the X valleys or one of the $\frac{1}{2}X$ valleys. We list two values per each scattering parameter since our two supercells produced two different values. In future work, these two parameters should be used as part of a concentration-dependent expression that could be obtained by calculating the spin-alloy scattering parameters at different VCA concentrations. There are no intravalley or intra-axis spin-flips in SiGe, consistent with GeSn. The scattering parameters calculated using a Ge supercell are all larger than the parameters calculated using a Si supercell, all within the same order of magnitude.

We compare both sets of parameters in Tables 7.7 and 7.8 with their corresponding GeSn parameters, which were calculated using a Ge supercell with a Sn impurity. The scattering parameters in a Ge supercell with a Sn impurity are generally higher than those with a Si impurity, due to the stronger SOC associated with Sn. For f-type scattering, we observe the same pattern as in GeSn, whereby the degeneracy between the Z and $-Z$ valleys is broken, and the up-to-down and down-to-up flips differ from one another.

Table 7.7: Calculated f-type intervalley spin-scattering matrix elements $V_{\alpha\beta}^{\uparrow\downarrow}$ (in meV) in SiGe using a Si supercell with a Ge substitutional impurity (denoted $Si_{63}Ge_1$), and a Ge supercell with a Si substitutional impurity (denoted $Ge_{63}Si_1$), with spin-polarisation in the z-direction. We compare these findings to our GeSn parameters which were calculated using a Ge supercell with a Sn substitutional impurity ($Ge_{63}Sn_1$).

Symbol	**Value (meV)**		
	$\mathbf{Si_{63}Ge_1}$	$\mathbf{Ge_{63}Si_1}$	$\mathbf{Ge_{63}Sn_1}$
V_{XY}	4.11	5.17	10.4
$V_{\frac{1}{2}X\frac{1}{2}Y}$	2.07	4.07	3.05
$V_{\frac{1}{2}XY}$	3.18	6.61	12
$V_{XZ}^{\uparrow\downarrow}$	5.85	22.1	27.6
$V_{XZ}^{\downarrow\uparrow}$	11.7	29.4	42.38
$V_{\frac{1}{2}X\frac{1}{2}Z}^{\uparrow\downarrow}$	27.7	47.1	87.9
$V_{\frac{1}{2}X\frac{1}{2}Z}^{\downarrow\uparrow}$	30.6	41.3	92.21
$V_{\frac{1}{2}XZ}^{\uparrow\downarrow}$	14.2	30.4	51.63
$V_{\frac{1}{2}XZ}^{\downarrow\uparrow}$	19.8	37.7	66.61
$V_{\frac{1}{2}ZX}^{\uparrow\downarrow}$	18.6	28.6	49.71
$V_{\frac{1}{2}ZX}^{\downarrow\uparrow}$	15.4	39.5	68.53

Table 7.8: Calculated intervalley spin-scattering matrix elements $V_{\alpha\beta}^{\uparrow\downarrow}$ (in meV) for all relevant valleys (excluding f-type) in SiGe using a Si supercell with a Ge substitutional impurity (denoted $Si_{63}Ge_1$), and a Ge supercell with a Si substitutional impurity (denoted $Ge_{63}Si_1$), with spin-polarisation in the z-direction. Our results are compared to our GeSn parameters calculated using a Ge supercell with a Sn substitutional impurity ($Ge_{63}Sn_1$).

Symbol	**Value (meV)**		
	$\mathbf{Si_{63}Ge_1}$	$\mathbf{Ge_{63}Si_1}$	$\mathbf{Ge_{63}Sn_1}$
$V_{\Gamma L}$	-	0.039	0.14
V_{LL}^{z}	2.13	6.1	5.82
V_{LL}^{xy}	1.5	4.2	4.33
V_{XL}	3.26	9.3	11.59
V_{ZL}	4.61	13.1	16.3
$V_{\frac{1}{2}XL}$	5.67	14.1	22.6
$V_{\frac{1}{2}ZL}$	8.01	19.9	31.89

7.3 Conclusions

In this chapter, we used first-principles methods to calculate the spin-dependent alloy and e-ph scattering parameters of GeSn in order to determine the spin-relaxation time and diffusion length of GeSn as a function of Sn concentration, temperature and biaxial tensile strain. Our results show that changes in spin orientation only occur by means of intervalley alloy scattering, and not by intravalley alloy scattering. We find that intervalley alloy-spin scattering is an order of magnitude stronger when electrons scatter to/from the direction of spin-alignment. We also implemented the frozen-phonon method to calculate the electron spin-phonon scattering parameters between the L and Γ valleys. By using these parameters along with electron spin-phonon parameters from literature, we were able to accurately calculate the spin relaxation time of GeSn.

Our calculations show that at low Sn concentrations, spin-alloy scattering reduces the spin-relaxation time, especially at lower temperatures. However, beyond the indirect-to-direct bandgap transition, the spin relaxation time increases by

several orders of magnitude. At room temperature, the spin relaxation time of GeSn are up to 1000 times that of Ge at Sn concentrations above 25%. At cryogenic temperatures, less Sn is required for such an increase in the spin-lifetime compared to room-temperature GeSn, with 11% Sn enough to achieve a spin-lifetime 10^5 times higher than Ge at $30K$. Including biaxial tensile strain further reduces the Sn content required to achieve such a rise. For applications which require a long spin relaxation time, we propose an alloy of 15% Sn above 50K, or 10% below 50K. Compared to other direct-gap materials such as III-Vs (see Chapter 2), GeSn possesses a much longer spin relaxation time.

Our calculations also reveal a high spin-diffusion length in GeSn beyond the indirect-to-direct bandgap transition. These findings highlight the potential GeSn has as a promising material for spintronic applications, especially those which require a long spin-lifetime such as spin buses, spin interconnects and quantum computing. Our model facilitates parameter transfer for multi-scale models, enabling accurate spin-relaxation and spin-diffusion length calculations for materials under arbitrary material compositions, temperatures, and strain conditions.

Chapter 8

Optical Properties of GeSn

In Chapter 1, we discussed some of the past experimental research demonstrating the potential of GeSn to replace III-V materials in optoelectronics in the future, primarily due to its direct bandgap (at sufficient Sn concentration and/or strain) and compatability with current CMOS processes. In this chapter, we present our findings on two key properties that define the optoelectronic behaviour of GeSn: the absorption coefficient and photoluminescence spectrum.

Electron absorption is a fundamental process in semiconductors and optoelectronic devices, where electrons gain energy by absorbing photons. This mechanism is crucial for applications such as solar cells, photodetectors and absorption modulators, as it governs the efficiency of light-matter interactions. The absorption coefficient, an expression for which is given in Eq. 5.42 in Chapter 5, quantifies how far photons of a given wavelength can penetrate the material before being absorbed. A high absorption coefficient is desirable in photovoltaic materials to maximise light harvesting, while a low value is beneficial in transparent conductive films such as waveguides [284]. Understanding electron absorption and its coefficient is essential for designing efficient electronic and photonic devices. The absorption coefficient of Ge has been previously calculated [253, 285] and measured [286, 287]. Hsieh et al [288] have calculated the absorption coefficient of GeSn for direct transitions at Sn concentrations of up to 10% in a photon energy range of $0.66 - 1$eV, showing a general increase in the absorption coefficient with Sn concentration, owing to the decreasing bandgap. There are several well established methods of calculating the absorption coefficient over a wide spectral range, such as DFT [253] and tight-binding [289]. However, the spectral region near the bandgap energy is of particular importance

for optoelectronic applications, as it critically influences the efficiency of photon absorption processes that govern device performance.

Photoluminescence (PL), shown in Eq. 5.44 in Chapter 5, is the emission of a photon when an electron that has been excited into the conduction band recombines with a hole in the valence band. Like absorption, photoluminescence is stronger in direct bandgap materials. Efficient PL emission is critical for LEDs and laser diodes, where radiative recombination directly impacts performance. The PL of Ge is well established [290, 291], whereby a peak occurs at the direct gap of Ge. Measurements [87, 292, 293] of the PL of GeSn is also largely defined by a singular peak at the direct gap. However, theoretical calculations of the absorption and emission of GeSn which include indirect transitions have not been previously determined over a wider spectral range. As we discussed in Chapter 5, Tiwari et al [253] provided us with the first unified theory of optical absorption and emission which includes direct and indirect processes in Ge (as well as Si and GaAs), finding that at photon energies below the direct gap, indirect absorption is dominant in Ge. However, no such calculations currently exist for GeSn, where indirect transitions are also prevalent due to alloy scattering processes.

Building on the theoretical framework established in Section 5.3 of Chapter 5, we apply degenerate and non-degenerate perturbation theory to calculate absorption and emission spectra across a range of Sn compositions (up to 12% Sn). By incorporating both direct and indirect transitions, as well as transitions into energy-degenerate bands, our findings provide a comprehensive picture of the optical properties of GeSn. We focus on a photon energy range of $0.4 - 1$ eV ($800 - 3000$nm), which encompasses short-wave infrared (SWIR) light ($1400 - 3000$nm). This is the first work to introduce the effect of alloy disorder on the optoelectronic properties of an alloy in this range of wavelengths. Light with these wavelengths are essential in a range of biomedical applications [139] (particularly laser-based devices), such as optical coherence tomography - a non-invasive cross-sectional imaging method using an optical interferometer [294]. Additionally, SWIR imaging is used in a variety of applications including solar cell inspection surveillance, anti-counterfeiting and process quality control.

The remainder of this chapter is laid out as follows: in Section 8.1, we summarise the theoretical framework used in extension with the formulae derived in Chapter 5. Our results are discussed in Section 8.2. Finally, Section 8.3 presents our conclusions.

8.1 Theoretical Framework

Following Section 5.3 in Chapter 5, we calculate the absorption coefficient and photoluminescence of GeSn at fixed Sn concentrations up to 12%. To accurately capture the these properties in the SWIR region, we consider a dense k-point system centred at the Γ point . We need only consider transitions from the three uppermost valence bands (HH, LH, SO) to the lowest conduction band. All necessary band energies and momenta are computed at these k-points using DFT, with the energies corrected using a scissors shift. All DFT calculations are performed using ABINIT under the same criteria as Chapter 6. We use a Gaussian function to approximate the δ-function in Fermi's Golden Rule.

To consider indirect transitions, we use Eq. 8.1 to calculate the energies $E_L(k)$ of k-points around the L valley, since Ge shows an ellipsoidal energy dispersion in this region:

$$E_L(k) = \frac{\hbar^2}{2}\left(\frac{k_x^2}{m_{L,l}} + \frac{k_y^2}{m_{L,t}} + \frac{k_z^2}{m_{L,t}}\right) + E_L \tag{8.1}$$

Each state is treated using degenerate and non-degenerate perturbation theory, following Sections 5.3.2 and 5.3.3 in Chapter 5. To calculate the eigenstates of the mixed states, we incorporate the unperturbed band energies into the diagonal elements of our Hamiltonian matrix, while the alloy and phonon interactions are included in the off-diagonal elements, as shown in Fig. 5.1 in Chapter 5. However, applying degenerate perturbation theory to such dense k-point systems is very computationally expensive. Instead, we follow Tiwari et al [253] in partitioning the photon energy range into a series of intervals of energy width ΔE, as shown in Fig. 8.1 below. The choice of ΔE is important as it must be checked for convergence in the limit $\Delta E \to \infty$. Within each interval, each state is treated using degenerate perturbation theory, while alloy and phonon-assisted transitions from states outside each interval are treated using non-degenerate perturbation theory.

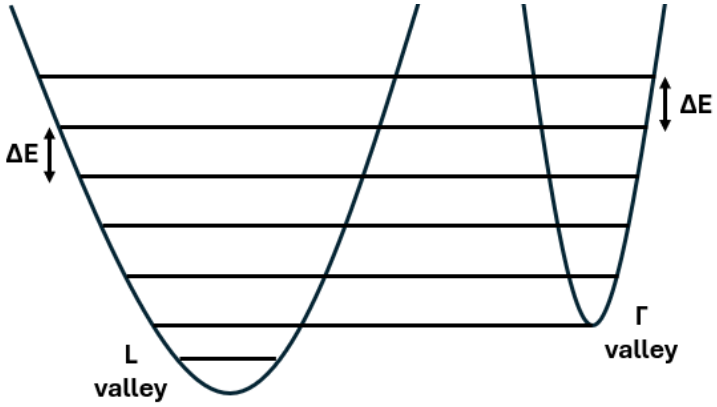

Figure 8.1: Schematic of the L and Γ valleys divided into energy partitions of energy width ΔE in order to be treated using perturbation theory.

8.2 Results

8.2.1 Absorption Coefficient of GeSn

We first examine the absorption coefficient of Ge in the SWIR range, previously calculated in Ref. [253], providing a basis for validating our model against established results. Figure 8.2 presents the room temperature absorption coefficient of Ge, highlighting the role of indirect transitions by contrasting the complete calculation with one that includes only direct transitions. Including indirect transitions slightly enhances the absorption coefficient above the direct gap, but more importantly, introduces pronounced indirect-gap absorption arising from electron–phonon scattering. In the direct-transition absorption calculation, a sharp drop is expected at the onset of the direct bandgap. However, the application of Gaussian broadening, used to produce a smooth and continuous spectrum, artificially softens this edge, resulting in a more gradual decline in the absorption coefficient. We find an absorption coefficient of 4.5×10^4 cm^{-1} at 1eV (1250nm). Overall, our findings are in good agreement with Ref. [253].

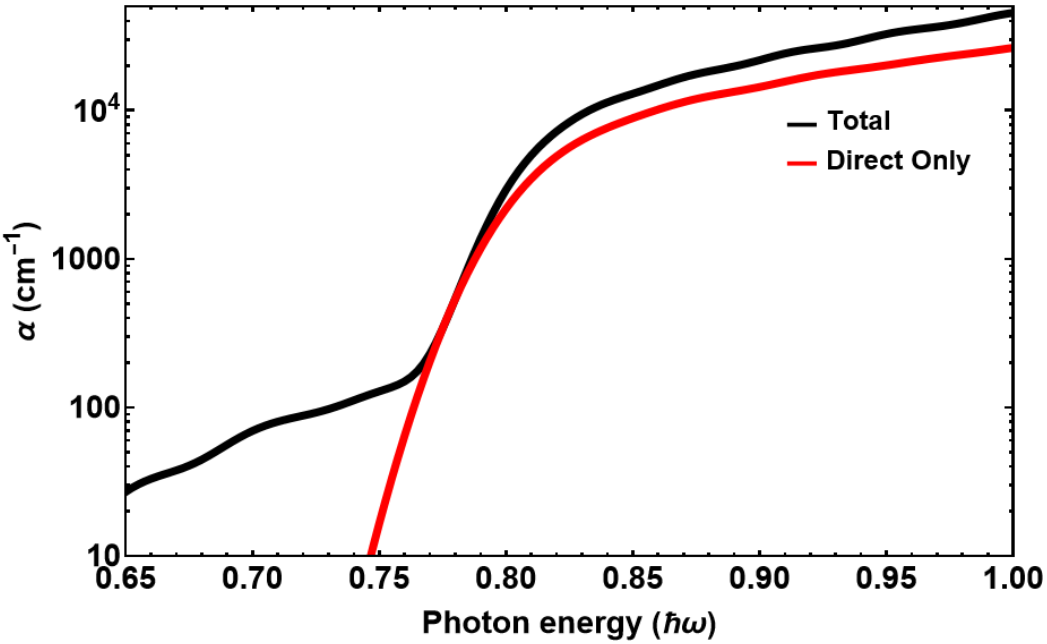

Figure 8.2: Room-temperature absorption coefficient (α) of Ge (black), given in cm^{-1}, compared to the absorption coefficient with only direct transitions considered (red), plotted as a function of photon energy $\hbar\omega$ and wavelength λ.

The room-temperature absorption coefficients of Ge and GeSn alloys with Sn concentrations of 3%, 6%, 9%, and 12% are shown in Fig. 8.3. As expected, increasing Sn content leads to a higher absorption coefficient and extends the absorption edge to longer wavelengths, consistent with the reduction in bandgap energy and in agreement with Refs. [285, 286, 287]. In indirect-gap GeSn (3% and 6% Sn), both electron-phonon scattering and alloy scattering enable notable absorption below the direct gap, making the absorption coefficient non-zero even in that regime, especially at increased Sn concentration. Additionally, in these indirect-gap compositions, the absorption coefficient rises more sharply with photon energy once the photon energy exceeds the direct-gap threshold. In contrast, for direct-gap GeSn (9% and 12% Sn), the absorption behaviour closely resembles that of Ge above the band edge, but with the onset occurring at lower photon energies. In direct-gap GeSn, alloy scattering plays a minimal role, and the absorption coefficient increases rapidly just above the bandgap. Notably, in the SWIR range (0.4–1eV), direct-gap GeSn ($9-12\%$) achieves absorption coefficients approaching 10^5 cm^{-1}, making it highly suitable for photonic and optoelectronic applications in this spectral range.

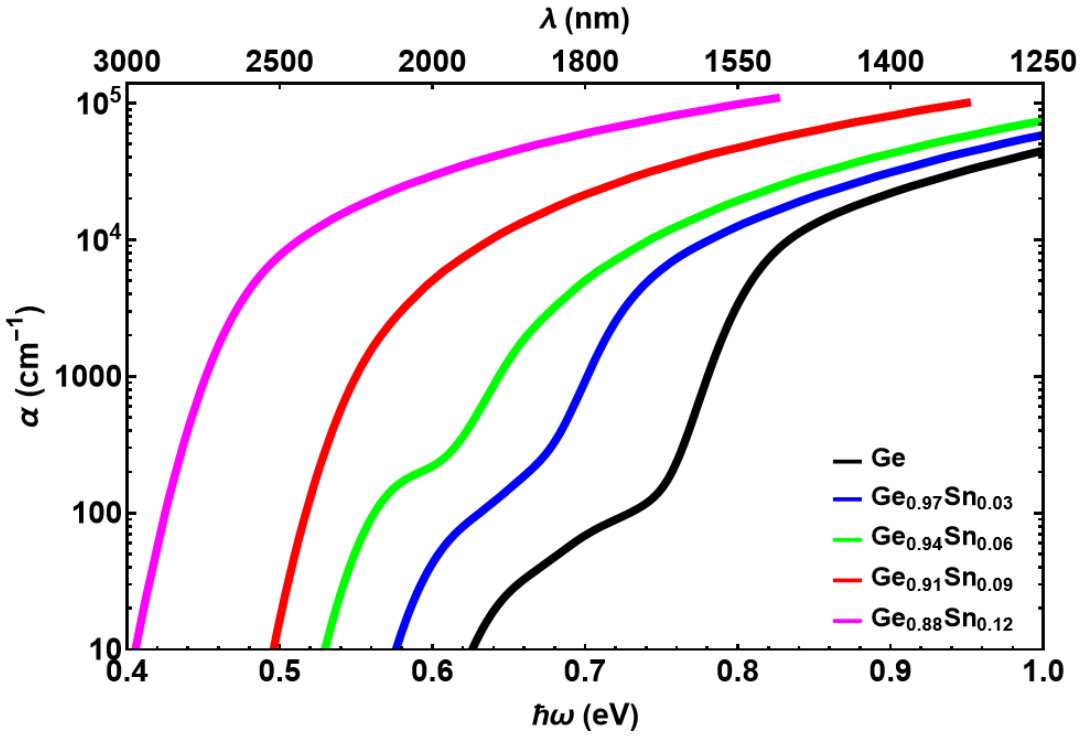

Figure 8.3: Room-temperature absorption coefficient (in cm^{-1}) of Ge (black) GeSn at Sn concentrations of 3% (blue), 6% (green), 9% (red) and 12% (pink) against photon energy $\hbar\omega$ and wavelength λ. For 9% and 12% Sn, the absorption curves are truncated at higher photon energies due to the limited energy range of the calculated conduction band states, which was constrained by the chosen k-point sampling.

We highlight the importance of alloy disorder in Fig. 8.4, where we compare the absorption coefficient of $Ge_{0.94}Sn_{0.06}$ with the corresponding absorption coefficient where alloy scattering is ignored. Below the direct gap, omitting alloy scattering can result in an absorption coefficient a full order of magnitude below its true value. However, beyond the direct gap, our plots converge, with absorption dominated by direct transitions into the conduction band.

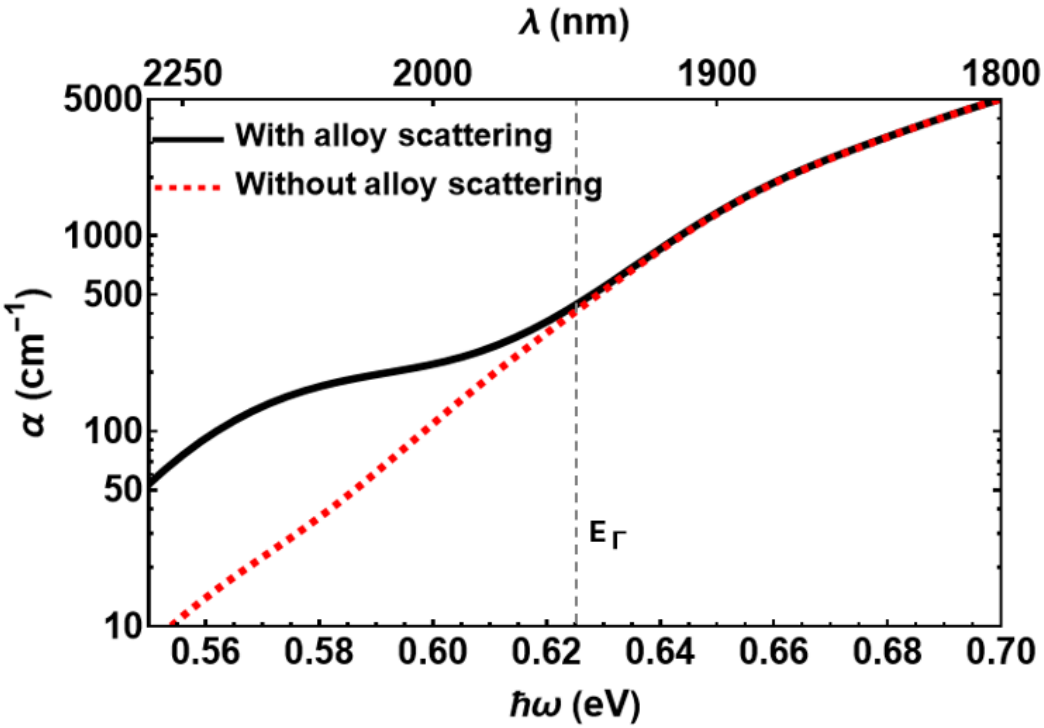

Figure 8.4: Comparison of the absorption coefficient of $Ge_{0.94}Sn_{0.06}$ with and without the inclusion of alloy scattering, plotted as functions of photon energy and wavelength.

Finally, we examine the effect of temperature on the absorption coefficient by comparing room-temperature and low-temperature calculations. In Fig. 8.5, we compare the absorption coefficients of Ge and $Ge_{0.88}Sn_{0.12}$ at 300K and 75K. As expected, the absorption coefficient decreases at a given photon energy with decreasing temperature, owing to the increase in the bandgap at lower temperatures, shifting the absorption edge to higher photon energies.

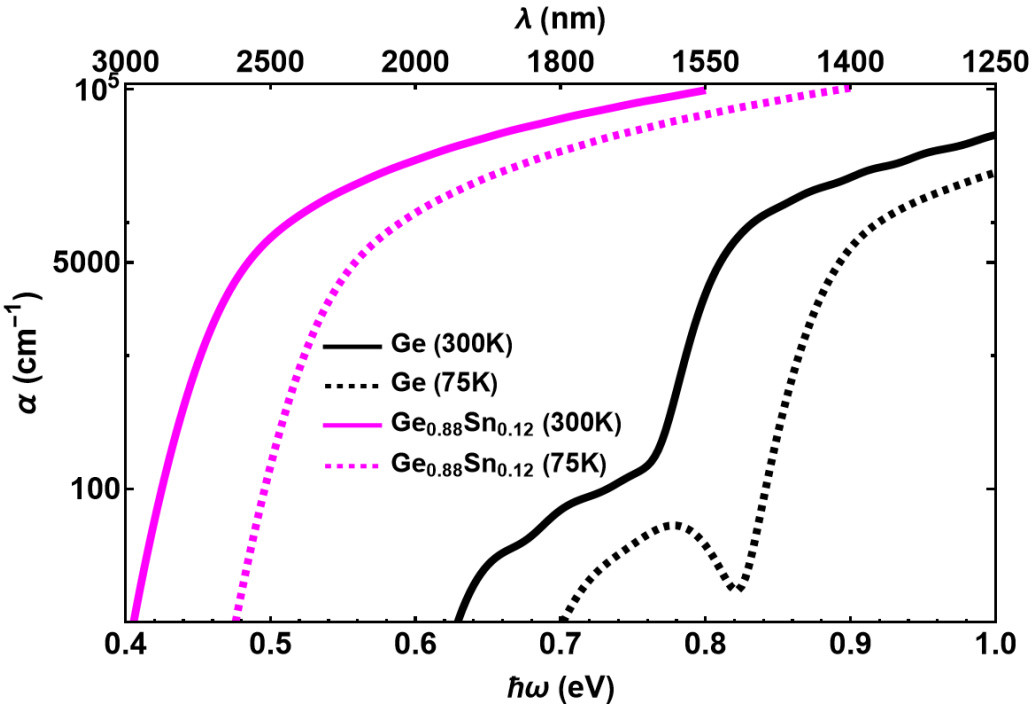

Figure 8.5: Absorption coefficient of Ge (black) and $Ge_{0.88}Sn_{0.12}$ at $300K$ (solid) and $75K$ (dashed) as functions of photon energy and wavelength.

8.2.2 Photoluminescence of GeSn

We begin by analysing the room-temperature emission spectrum of Ge, shown in Fig. 8.6, where we compare results that include phonon-assisted transitions with those that account only for direct transitions. We can see that the most significant contribution to the PL is from phonon-assisted light emission, whereby electrons scattering from L to Γ via optical phonons before recombining in the valence band at Γ by photon assistance. This underscores the importance of using non-degenerate perturbation theory to capture these processes. Additionally, applying degenerate perturbation theory for quasi-degenerate states results in a noticeable enhancement near the direct bandgap. Our findings are in good agreement with Ref. [253]. Clearly, indirect transitions play a much more pivotal role in light emission compared to absorption in Ge.

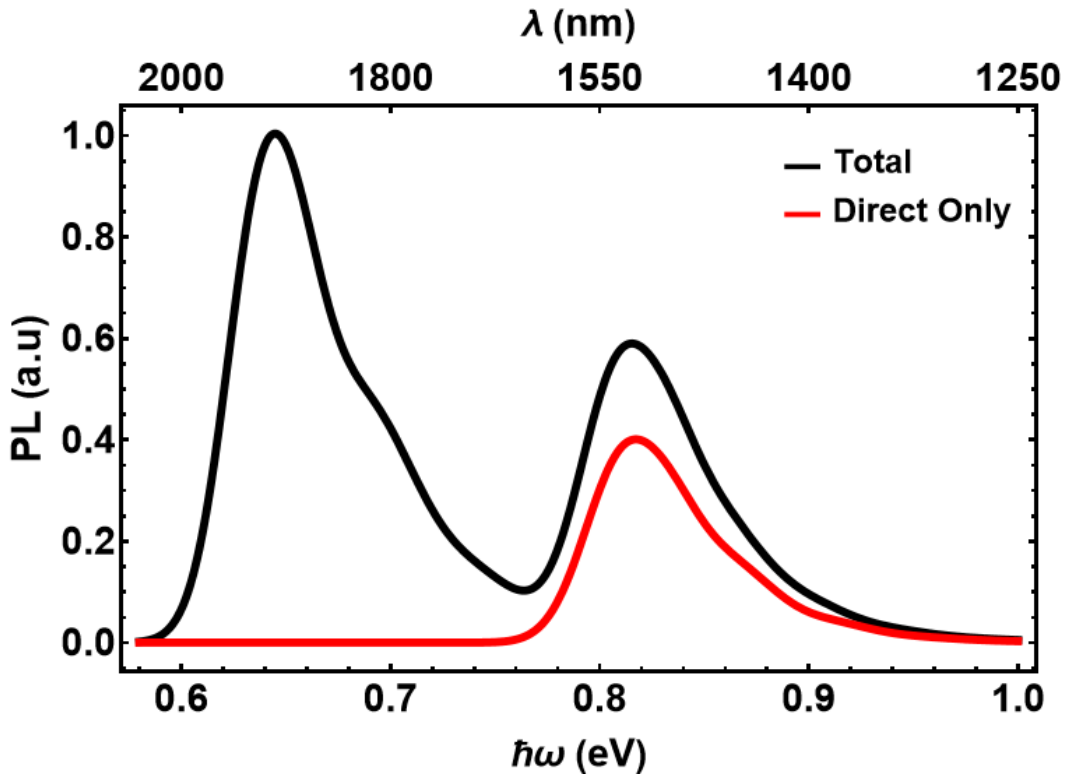

Figure 8.6: Room-temperature PL spectra of Ge including both phonon assisted and direct transitions (black), compared to the PL spectrum with direct transitions only (red), plotted as a function of photon energy $\hbar\omega$. Intensities are given in arbitrary units (a.u.).

Figure 8.7 shows the room-temperature PL spectra of Ge and GeSn alloys with Sn concentrations of 3%, 6%, 9% and 12%, plotted as functions of photon energy. Overall, we observe an increase in the PL intensity with Sn content. Like in pure Ge, in indirect-gap GeSn, two distinct peaks are observed: a smaller one at the direct bandgap and a more prominent one at the indirect bandgap. When the material transitions into a direct-gap material, a single stronger peak emerges at the direct gap, which is broadened by phonon-assisted transitions. Notably, the PL intensity of $Ge_{0.88}Sn_{0.12}$ is up to 250 times higher than that of Ge, underscoring the significant enhancement in radiative efficiency achieved by Sn incorporation. We compare our findings to experimental data at 9% Sn, measured by Ref. [87] (also at room-temperature).

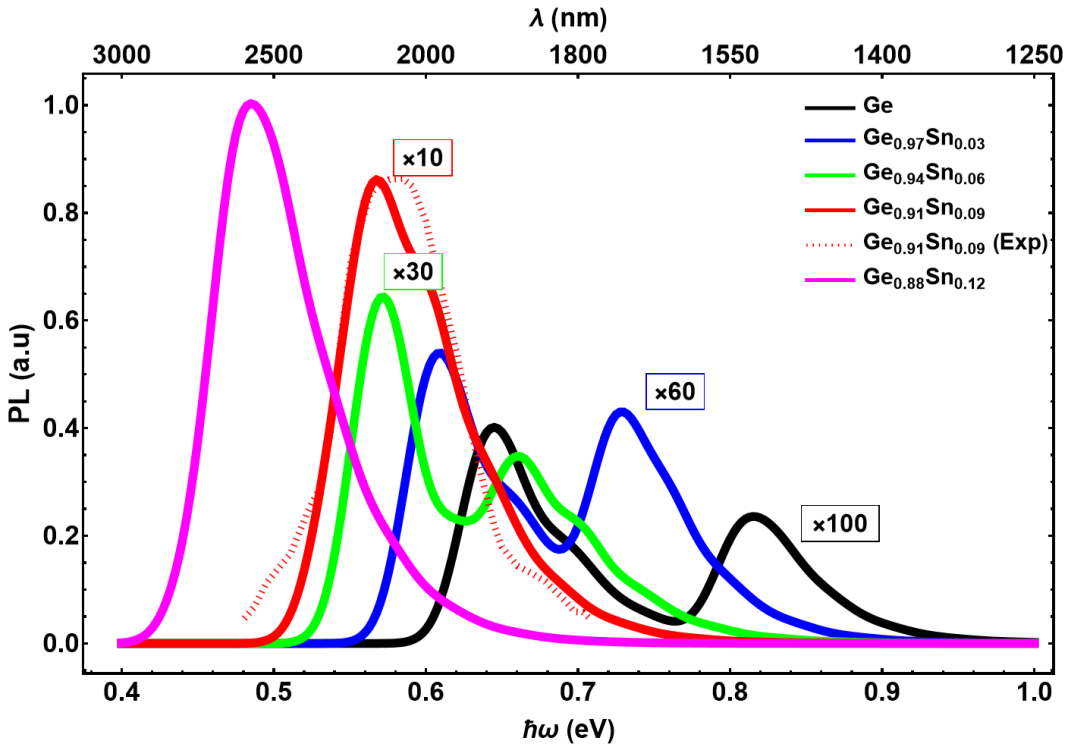

Figure 8.7: Room-temperature PL spectrum (in arbitrary units) of Ge (black) GeSn at Sn concentrations of 3% (blue), 6% (green), 9% (red) and 12% (pink), as well as experimental data at 9% (red, dotted), plotted against photon energy $\hbar\omega$.

To highlight the effect of alloy scattering on the emission spectrum of GeSn, we compare the calculated PL of GeSn at 6% Sn concentration with the corresponding PL where alloy scattering is neglected. This comparison is shown in Fig. 8.8, where a clear difference appears at the indirect-gap peak, which is significantly enhanced when alloy scattering is included. This contrast is a consequence of alloy scattering being 2.5 times stronger than e-ph scattering in $Ge_{0.94}Sn_{0.06}$ at room temperature, and is even more prevalent at lower temperatures.

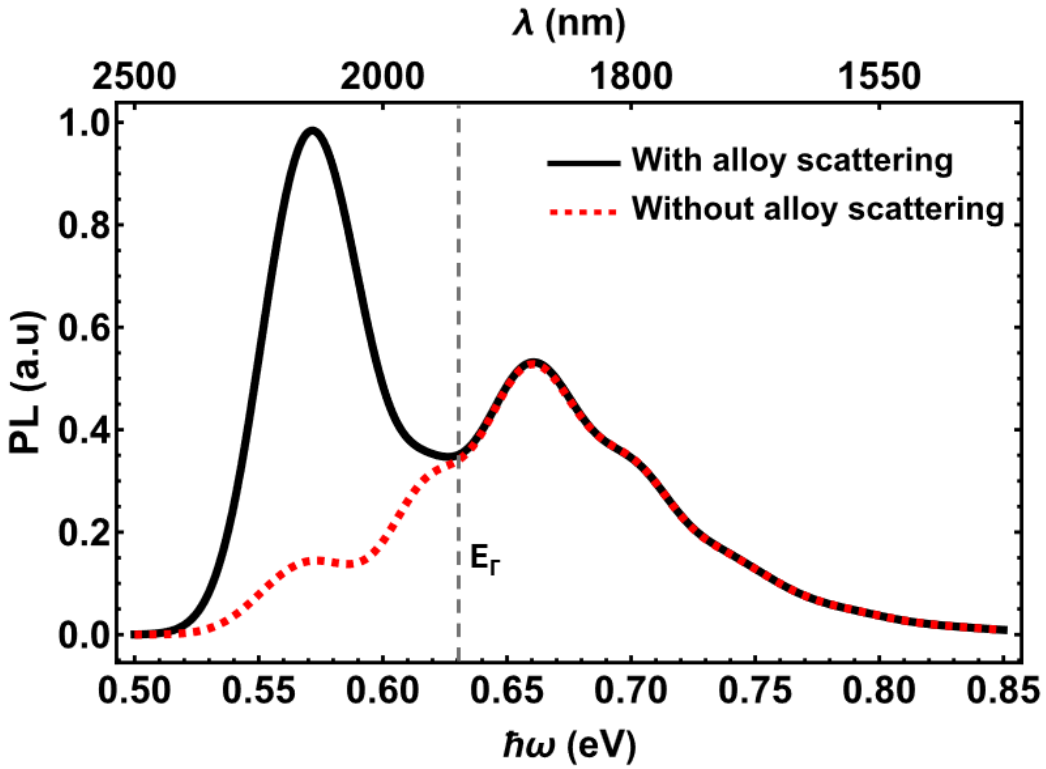

Figure 8.8: Comparison of the PL spectra of $Ge_{0.94}Sn_{0.06}$ with and without alloy scattering included, plotted as a function of photon energy $\hbar\omega$. Intensities are given in arbitrary units (a.u.).

We also calculate the PL of Ge, $Ge_{0.94}Sn_{0.06}$, and $Ge_{0.88}Sn_{0.12}$ at low temperature (75K), where phonon absorption is minimal. At such low temperatures, the photon distribution function $\omega^3/[exp\{(\hbar\omega - \Delta\mu)/k_BT\} - 1]$ in Eq. 5.44 becomes sharply peaked near the band edge, significantly suppressing higher-energy transitions. As a result, PL features associated with the direct bandgap in both Ge and indirect-gap GeSn are strongly diminished. The emission in GeSn becomes dominated by a single peak corresponding to its absolute bandgap. Notably, at 75K, the PL of $Ge_{0.88}Sn_{0.12}$ is up to 20 times stronger than that of pure Ge. These results are in excellent agreement with the calculations on Ge provided by Tiwari et al [253] and experimental observations reported in Ref. [87].

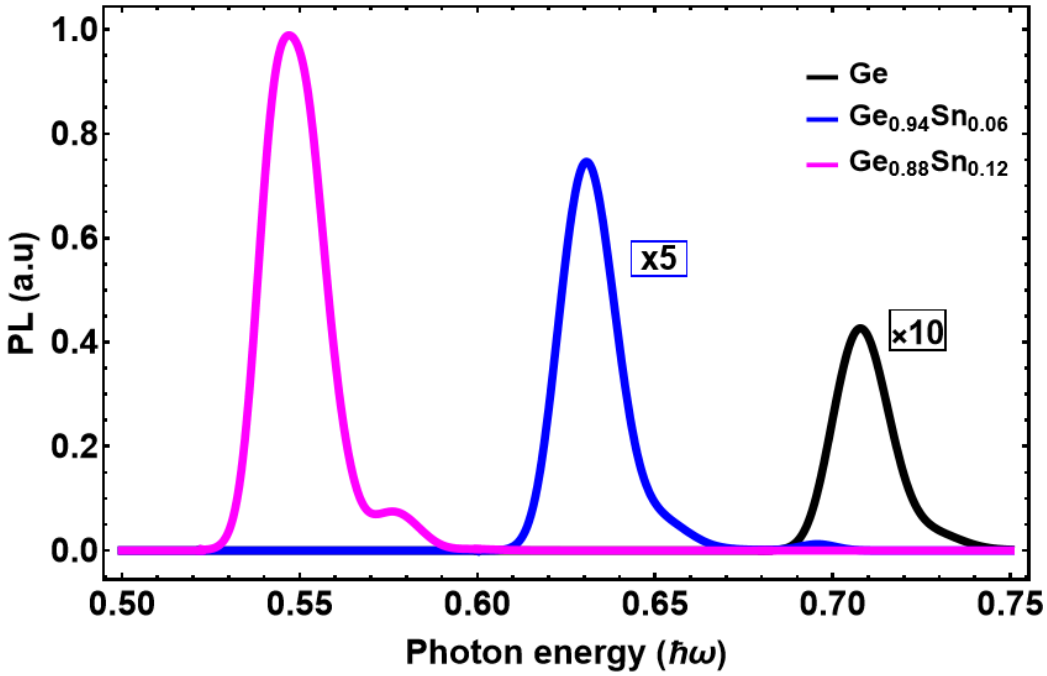

Figure 8.9: PL of Ge (black), $Ge_{0.96}Sn_{0.06}$ (blue) and $Ge_{0.88}Sn_{0.12}$ (pink) in arbitrary units at $75K$, plotted against photon energy.

8.3 Conclusions

In conclusion, we calculate the absorption coefficient and photoluminescence of GeSn as a function of photon energy $\hbar\omega$ (and light wavelength λ), employing both degenerate and non-degenerate perturbation theory to include all direct and indirect transitions. This study presents the first quantitative treatment of the optoelectronic properties of an alloy that explicitly incorporates indirect transitions enabled by alloy scattering. Our calculations focus on the short-wavelength infrared spectral range, considering only direct transitions between the conduction band minimum and the three uppermost valence bands around the Γ point. All relevant band energies and momentum matrix elements were obtained using DFT, with the band energies corrected by GW and for temperature.

Our results demonstrate a significant increase in absorption with increasing Sn concentration in GeSn. The room-temperature absorption coefficient increases by up to an order of magnitude relative to pure Ge, reaching values exceeding 10^5 cm^{-1} in the SWIR light range for direct-gap GeSn alloys. Reducing temperature reduces the absorption coefficient. In this light range, we find that optical absorption is primarily governed by direct transitions around the Γ point, with

alloy scattering contributing only modestly, particularly in Ge and indirect-gap GeSn where electrons can be absorbed into the four L bands.

Adding Sn to Ge also results in an increase in the emission spectra in the SWIR light range. In contrast to absorption however, alloy scattering plays a much more significant role in light emission. In both pure Ge and indirect-gap GeSn, the PL spectrum exhibits a peak at the direct band edge and a stronger peak at the indirect gap. In GeSn, the intensity of the indirect peak is largely driven by alloy-assisted recombination, which dominates over phonon-mediated processes. For direct-gap GeSn, the PL spectrum shows a single, pronounced peak at the band edge. At room temperature, the PL intensity of $Ge_{0.88}Sn_{0.12}$ exceeds that of Ge by a factor of 250 in the SWIR range. At lower temperatures, the PL peaks become narrower, with higher energy transitions suppressed by the Bose-Einstein function. At 75K, the peak of the PL of $Ge_{0.88}Sn_{0.12}$ is over 20 times the Ge value. Our findings are in excellent agreement with experiment.

We predict that applying biaxial tensile strain could further enhance both the absorption and emission in GeSn by modifying the band structure in favour of direct transitions.

Additionally, we expect electron–hole (e-h) excitonic interactions to boost optical response by slightly lowering transition energies. However, they should have only a minor influence on the optical response, as such effects are relatively weak ($\approx meV$) in bulk materials and become significant mainly under strong confinement.

Given our findings, coupled with its ability to be grown directly on Si substrates, makes GeSn a possible candidate to replace III-V materials in optoelectronic applications, paving the way for the integration of photonic components into established CMOS technology.

Part IV

Summary, Conclusions and Outlook

Chapter 9

Summary, Conclusions and Outlook

9.1 Summary and Conclusions

This thesis has delivered a detailed theoretical analysis of the transport, spintronic, and optical properties of GeSn alloys, advancing our understanding of this emerging group-IV semiconductor.

To understand the electronic transport properties of GeSn, we carried out a full *ab initio* calculation of n-type intra- and intervalley alloy scattering parameters for GeSn alloys, using supercell methods to numerically represent the alloy scattering problem. These parameters, which were previously unknown and difficult to determine from experiments, were up to 3-4 times larger than another group-IV alloy in SiGe. In particular, intravalley scattering in the L and Γ valleys, as well as intervalley scattering between the L valleys and Γ and L are prominent. This evidence alone suggests alloy scattering should significantly impact on the transport properties of GeSn.

We used our calculated scattering parameters with phonon parameters from the literature in the Boltzmann Transport Equation to find the n-type mobility of GeSn as a function of Sn concentration, temperature and biaxial tensile strain. Our results shows that previous calculations of the mobility have been overestimations, as the effects of alloy scattering were not fully considered, and the mobility is significantly limited by alloy scattering. Nonetheless, sufficient addition of Sn to Ge beyond a threshold composition causes the mobility to increase by up to 25 times the room-temperature value. Applying biaxial tensile strain reduces the Sn content necessary to invoke an increase of this magnitude. Our findings could prompt further work on GeSn transistors.

In the second part of this thesis, we calculated the key spin-dependent alloy scattering and electron-phonon scattering parameters of GeSn. Our findings indicate that electrons undergo spin polarisation changes due to alloy impurities only due to intervalley scattering. Specifically, for $L - L$ scattering, the spin-flip scattering strength is on the order of meV, while for $\Gamma - L$ transitions, it is an order of magnitude lower.

Using these parameters, we computed the spin relaxation time of GeSn. We found that when sufficient Sn (and strain) is introduced to Ge to induce an indirect-to-direct bandgap transition, the spin relaxation time can increase by several orders of magnitude. At higher temperatures, electron-spin-phonon scattering dominates, and alloy spin-scattering has a minimal effect on the spin relaxation time. In particular, above 50K, the incorporation of 15% Sn (without strain) is enough to significantly improve spin relaxation, while only 10% Sn is necessary below 50K. These results highlight the potential of GeSn as a candidate material for spin-based transistors, quantum computing, and spin interconnects.

Finally, in the third part of this project, we calculated the absorption and photoluminescence spectra of GeSn at room temperature and low temperature (75K) in the SWIR light range. Our methods involved the implementation of degenerate and non-degenerate perturbation theory, making this not only the second work to use degenerate perturbation theory in the determination of the optoelectronic properties of a semiconducting material, but also the first ever calculation to introduce the effect of alloy disorder on the indirect and direct transitions.

We have demonstrated that GeSn alloys exhibit significantly enhanced optoelectronic properties compared to pure Ge. At room temperature, the absorption coefficient of $Ge_{0.88}Sn_{0.12}$ approaches 10^5 cm^{-1}, more than twice that of pure Ge. Furthermore, PL intensity in the SWIR region increases dramatically, with $Ge_{0.88}Sn_{0.12}$ exhibiting PL nearly 250 times stronger than Ge. Perturbation theory proved essential for accurately modelling both the absorption and emission spectra, especially in indirect-gap GeSn. While alloy scattering was found to have a limited impact on the absorption coefficient, it played a central role in shaping the PL response. In indirect-gap GeSn, the PL spectrum is dominated by a peak corresponding to the material's indirect bandgap, driven primarily by alloy scattering and further influenced by electron-phonon interactions.

These findings highlight the potential of GeSn as a tunable group-IV material for SWIR optoelectronic applications, and underscore the importance of including both alloy disorder and phonon-assisted processes in theoretical modelling to

fully describe its optical behaviour.

The results in this thesis not only highlight GeSn's suitability for integration into next-generation electronic, spintronic, and photonic devices, but also provide a robust theoretical foundation to guide future experimental validation and device engineering in this rapidly developing field. Our approach in all of our calculations is applicable for a range of semiconductors, particularly group-IV alloys.

9.2 Outlook

Overall, the findings presented in this thesis provide a more comprehensive understanding of the properties of GeSn. However, our work can still be extended in many directions.

Future research should be able to prove that straining GeSn in the [111]-direction should lead to both a higher electron mobility and a higher spin-relaxation time compared to unstrained GeSn, as this would remove scattering between the L valleys. This could be advantageous for indirect-gap GeSn, where intervalley scattering between the L valleys is dominant.

Our spin-alloy scattering parameters for SiGe could be used to calculate the spin-relaxation time of SiGe using the same approach as in Chapter 7. This could be crucial for developing spintronic devices that are highly compatible with existing silicon technology, offering better integration than GeSn. Additionally, unlike GeSn, SiGe poses fewer fabrication challenges.

Another promising direction for future work lies in bridging the spin-dependent carrier dynamics studied in Chapter 7 with the optical absorption and emission processes explored in Chapter 8. Specifically, the use of circularly polarised light offers a route to generate spin-polarised carrier populations in GeSn. Using this approach, one could investigate how spin-polarised electrons evolve and recombine in GeSn. Recent experimental research by Rossi et al [295] has already demonstrated spin-to-charge conversion in GeSn by directly injecting optical spin-polarised currents into the alloy. Further studies would enable a deeper understanding of spin-dependent optical transitions, including the potential for circularly polarised photoluminescence, spin-selective absorption, or even spin-lasing in engineered GeSn structures.

Part V

Bibliography

References

[1] E. Gelenbe, "Electricity consumption by ict: Facts, trends, and measurements," *Ubiquity*, vol. 2023, no. August, pp. 1–15, 2023.

[2] J. Malmodin, N. Lövehagen, P. Bergmark, and D. Lundén, "Ict sector electricity consumption and greenhouse gas emissions–2020 outcome," *Telecommunications Policy*, vol. 48, no. 3, p. 102701, 2024.

[3] Central Statistics Office, "Data centres metered electricity consumption 2023: Key findings," 2024. Accessed: 2025-01-26.

[4] N. Romli, K. Minhad, M. Reaz, and M. S. Amin, "An overview of power dissipation and control techniques in cmos technology," *J. Eng. Sci. Technol*, vol. 10, no. 3, pp. 364–382, 2015.

[5] G. Moore, "Moore's law," *Electronics Magazine*, vol. 38, no. 8, p. 114, 1965.

[6] P. Ghising, C. Biswas, and Y. H. Lee, "Graphene spin valves for spin logic devices," *Advanced Materials*, vol. 35, no. 23, p. 2209137, 2023.

[7] J. D. Sau and M. L. Cohen, "Possibility of increased mobility in ge-sn alloy system," *Physical Review B*, vol. 75, no. 4, p. 045208, 2007.

[8] A. K. Biswas, J. Atulasimha, and S. Bandyopadhyay, "An error-resilient non-volatile magneto-elastic universal logic gate with ultralow energy-delay product," *Scientific reports*, vol. 4, no. 1, p. 7553, 2014.

[9] S. M. Yakout, "Spintronics: future technology for new data storage and communication devices," *Journal of superconductivity and novel magnetism*, vol. 33, no. 9, pp. 2557–2580, 2020.

[10] S. Bandyopadhyay and M. Cahay, *Introduction to spintronics*. CRC press, 2008.

[11] S. Sanvito, "Molecular spintronics," *Chemical Society Reviews*, vol. 40, no. 6, pp. 3336–3355, 2011.

[12] G. Burkard, T. D. Ladd, A. Pan, J. M. Nichol, and J. R. Petta, "Semiconductor spin qubits," *Reviews of Modern Physics*, vol. 95, no. 2, p. 025003, 2023.

[13] M. N. Baibich, J. M. Broto, A. Fert, F. N. Van Dau, F. Petroff, P. Etienne, G. Creuzet, A. Friederich, and J. Chazelas, "Giant magnetoresistance of (001) fe/(001) cr magnetic superlattices," *Physical review letters*, vol. 61, no. 21, p. 2472, 1988.

[14] G. Binasch, P. Grünberg, F. Saurenbach, and W. Zinn, "Enhanced magnetoresistance in layered magnetic structures with antiferromagnetic interlayer exchange," *Physical review B*, vol. 39, no. 7, p. 4828, 1989.

[15] B. Dieny, V. S. Speriosu, S. S. Parkin, B. A. Gurney, D. R. Wilhoit, and D. Mauri, "Giant magnetoresistive in soft ferromagnetic multilayers," *Physical Review B*, vol. 43, no. 1, p. 1297, 1991.

[16] C. Chappert, A. Fert, and F. N. Van Dau, "The emergence of spin electronics in data storage," *Nature materials*, vol. 6, no. 11, pp. 813–823, 2007.

[17] J. S. Moodera, L. R. Kinder, T. M. Wong, and R. Meservey, "Large magnetoresistance at room temperature in ferromagnetic thin film tunnel junctions," *Physical review letters*, vol. 74, no. 16, p. 3273, 1995.

[18] T. Miyazaki and N. Tezuka, "Giant magnetic tunneling effect in fe/al2o3/fe junction," *Journal of magnetism and magnetic materials*, vol. 139, no. 3, pp. L231–L234, 1995.

[19] J. P. Singh, R. Bhardwaj, A. Sharma, B. Kaur, S. O. Won, S. Gautam, and K. H. Chae, "Fabrication of magnetic tunnel junctions," in *Advanced Applications in Manufacturing Enginering*, pp. 53–77, Elsevier, 2019.

[20] W. P. McCray, "How spintronics went from the lab to the ipod," *Nature Nanotechnology*, vol. 4, no. 1, pp. 2–4, 2009.

[21] S. Datta and B. Das, "Electronic analog of the electro-optic modulator," *Applied Physics Letters*, vol. 56, no. 7, pp. 665–667, 1990.

[22] I. Žutić, G. Xu, M. Lindemann, P. E. F. Junior, J. Lee, V. Labinac, K. Stojšić, G. M. Sipahi, M. R. Hofmann, and N. C. Gerhardt, "Spin-lasers: spin-

tronics beyond magnetoresistance," *Solid State Communications*, vol. 316, p. 113949, 2020.

[23] S. L. Chuang, N. Peyghambarian, and S. Koch, "Physics of optoelectronic devices," *Physics Today*, vol. 49, p. 62, 1996.

[24] L. A. Coldren, S. W. Corzine, and M. L. Mashanovitch, *Diode lasers and photonic integrated circuits*. John Wiley & Sons, 2012.

[25] A. Yariv, "Optical electronics in modern communications," *Oxford University Press*, 1997.

[26] I. Žutić, J. Fabian, and S. D. Sarma, "Spintronics: Fundamentals and applications," *Reviews of modern physics*, vol. 76, no. 2, p. 323, 2004.

[27] H. Wang, Z. Hu, J. Deng, X. Zhang, J. Chen, K. Li, and G. Li, "All-optical ultrafast polarization switching with nonlinear plasmonic metasurfaces," *Science Advances*, vol. 10, no. 8, p. 3882, 2024.

[28] H. Höpfner, M. Lindemann, N. C. Gerhardt, and M. R. Hofmann, "Controlled switching of ultrafast circular polarization oscillations in spin-polarized vertical-cavity surface-emitting lasers," *Applied Physics Letters*, vol. 104, no. 2, p. 022409, 2014.

[29] S. Hallstein, J. Berger, M. Hilpert, H. Schneider, W. Rühle, F. Jahnke, S. Koch, H. Gibbs, G. Khitrova, and M. Oestreich, "Manifestation of coherent spin precession in stimulated semiconductor emission dynamics," *Physical Review B*, vol. 56, no. 12, p. R7076, 1997.

[30] T. Nan, C. X. Quintela, J. Irwin, G. Gurung, D.-F. Shao, J. Gibbons, N. Campbell, K. Song, S.-Y. Choi, L. Guo, *et al.*, "Controlling spin current polarization through non-collinear antiferromagnetism," *Nature communications*, vol. 11, no. 1, p. 4671, 2020.

[31] D. Younis, D. F. Gordon, and B. Hafizi, "Spin-polarization control of photoelectrons using poincaré fields," *Physical Review Letters*, vol. 133, no. 4, p. 043201, 2024.

[32] H. Ando, T. Sogawa, and H. Gotoh, "Photon-spin controlled lasing oscillation in surface-emitting lasers," *Applied Physics Letters*, vol. 73, no. 5, pp. 566–568, 1998.

[33] J. Lee, S. Bearden, E. Wasner, and I. Žutić, "Spin-lasers: From threshold reduction to large-signal analysis," *Applied Physics Letters*, vol. 105, no. 4, p. 042411, 2014.

[34] J. Rudolph, D. Hägele, H. Gibbs, G. Khitrova, and M. Oestreich, "Laser threshold reduction in a spintronic device," *Applied physics letters*, vol. 82, no. 25, pp. 4516–4518, 2003.

[35] M. Holub, J. Shin, D. Saha, and P. Bhattacharya, "Electrical spin injection and threshold reduction in a semiconductor laser," *Physical Review Letters*, vol. 98, no. 14, p. 146603, 2007.

[36] S. Q. Dots, "Coherent manipulation of coupled electron spins in," *condensed-matter physics*, vol. 5, p. 6, 2005.

[37] H. Bluhm, S. Foletti, I. Neder, M. Rudner, D. Mahalu, V. Umansky, and A. Yacoby, "Dephasing time of gaas electron-spin qubits coupled to a nuclear bath exceeding 200 μs," *Nature Physics*, vol. 7, no. 2, pp. 109–113, 2011.

[38] S. Wang, C. Querner, T. Dadosh, C. H. Crouch, D. S. Novikov, and M. Drndic, "Collective fluorescence enhancement in nanoparticle clusters," *Nature communications*, vol. 2, no. 1, p. 364, 2011.

[39] H. Watzinger, J. Kukučka, L. Vukušić, F. Gao, T. Wang, F. Schäffler, J.-J. Zhang, and G. Katsaros, "A germanium hole spin qubit," *Nature communications*, vol. 9, no. 1, p. 3902, 2018.

[40] B. Trauzettel, D. V. Bulaev, D. Loss, and G. Burkard, "Spin qubits in graphene quantum dots," *Nature Physics*, vol. 3, no. 3, pp. 192–196, 2007.

[41] M. Boerkamp, "Intel releases 12-qubit silicon quantum chip," *Physics World*, vol. 36, no. 8, p. 11ii, 2023.

[42] S. K. Moore, "What intel is planning for the future of quantum computing: Hot qubits, cold control chips, and rapid testing," *IEEE Spectrum*, vol. 57, no. 8, 2020.

[43] V. Langrock, J. A. Krzywda, N. Focke, I. Seidler, L. R. Schreiber, and Ł. Cywiński, "Blueprint of a scalable spin qubit shuttle device for coherent mid-range qubit transfer in disordered si/sige/sio 2," *PRX Quantum*, vol. 4, no. 2, p. 020305, 2023.

[44] X. Li and J. Yang, "First-principles design of spintronics materials," *National Science Review*, vol. 3, no. 3, pp. 365–381, 2016.

[45] M. König, S. Wiedmann, C. Brüne, A. Roth, H. Buhmann, and L. Molenkamp, "Xiao-liang. qi, and shou-cheng zhang. quantum spin hall insulator state in hgte quan-tum wells," *Science*, vol. 318, no. 5851, pp. 766–770, 2007.

[46] D. Hsieh, D. Qian, L. Wray, Y. Xia, Y. S. Hor, R. J. Cava, and M. Z. Hasan, "A topological dirac insulator in a quantum spin hall phase," *Nature*, vol. 452, no. 7190, pp. 970–974, 2008.

[47] S. Islam, S. Bhattacharyya, H. Nhalil, M. Banerjee, A. Richardella, A. Kandala, D. Sen, N. Samarth, S. Elizabeth, and A. Ghosh, "Low-temperature saturation of phase coherence length in topological insulators," *Physical Review B*, vol. 99, no. 24, p. 245407, 2019.

[48] S. H. Simon, *The Oxford solid state basics*. OUP Oxford, 2013.

[49] M. Fiebig, N. P. Duong, T. Satoh, B. B. Van Aken, K. Miyano, Y. Tomioka, and Y. Tokura, "Ultrafast magnetization dynamics of antiferromagnetic compounds," *Journal of Physics D: Applied Physics*, vol. 41, no. 16, p. 164005, 2008.

[50] L. Šmejkal, R. González-Hernández, T. Jungwirth, and J. Sinova, "Crystal time-reversal symmetry breaking and spontaneous hall effect in collinear antiferromagnets," *Science advances*, vol. 6, no. 23, p. 8809, 2020.

[51] Y. Zhang, J. Železnỳ, Y. Sun, J. Van Den Brink, and B. Yan, "Spin hall effect emerging from a noncollinear magnetic lattice without spin–orbit coupling," *New Journal of Physics*, vol. 20, no. 7, p. 073028, 2018.

[52] J. Železnỳ, Y. Zhang, C. Felser, and B. Yan, "Spin-polarized current in noncollinear antiferromagnets," *Physical review letters*, vol. 119, no. 18, p. 187204, 2017.

[53] S. Nekrashevich and V. Gritsenko, "Electronic structure of silicon dioxide (a review)," *Physics of the Solid State*, vol. 56, pp. 207–222, 2014.

[54] A. R. Zanatta, "Revisiting the optical bandgap of semiconductors and the proposal of a unified methodology to its determination," *Scientific reports*, vol. 9, no. 1, p. 11225, 2019.

[55] J. I. Pankove and D. A. Kiewit, "Optical processes in semiconductors," *Journal of The Electrochemical Society*, vol. 119, no. 5, p. 156Ca, 1972.

[56] J. J. Morton, D. R. McCamey, M. A. Eriksson, and S. A. Lyon, "Embracing the quantum limit in silicon computing," *Nature*, vol. 479, no. 7373, pp. 345–353, 2011.

[57] P. Li and H. Dery, "Spin-orbit symmetries of conduction electrons in silicon," *Physical Review Letters*, vol. 107, no. 10, p. 107203, 2011.

[58] B. Huang, H.-J. Jang, and I. Appelbaum, "Geometric dephasing-limited hanle effect in long-distance lateral silicon spin transport devices," *Applied Physics Letters*, vol. 93, no. 16, p. 162508, 2008.

[59] L. Qing, J. Li, I. Appelbaum, and H. Dery, "Spin relaxation via exchange with donor impurity-bound electrons," *Physical Review B*, vol. 91, no. 24, p. 241405, 2015.

[60] O. Chalaev, Y. Song, and H. Dery, "Suppressing the spin relaxation of electrons in silicon," *Physical Review B*, vol. 95, no. 3, p. 035204, 2017.

[61] H. Dery, Y. Song, P. Li, and I. Zutić, "Silicon spin communication," *Applied Physics Letters*, vol. 99, no. 8, p. 082502, 2011.

[62] I. Žutić and H. Dery, "Taming spin currents," *Nature materials*, vol. 10, no. 9, pp. 647–648, 2011.

[63] A. Spiesser, H. Saito, Y. Fujita, S. Yamada, K. Hamaya, S. Yuasa, and R. Jansen, "Giant spin accumulation in silicon nonlocal spin-transport devices," *Physical Review Applied*, vol. 8, no. 6, p. 064023, 2017.

[64] A. Dankert, R. S. Dulal, and S. P. Dash, "Efficient spin injection into silicon and the role of the schottky barrier," *Scientific reports*, vol. 3, no. 1, p. 3196, 2013.

[65] I. Appelbaum, B. Huang, and D. J. Monsma, "Electronic measurement and control of spin transport in silicon," *Nature*, vol. 447, no. 7142, pp. 295–298, 2007.

[66] B. T. Jonker, G. Kioseoglou, A. T. Hanbicki, C. H. Li, and P. E. Thompson, "Electrical spin-injection into silicon from a ferromagnetic metal/tunnel barrier contact," *Nature Physics*, vol. 3, no. 8, pp. 542–546, 2007.

[67] L. Grenet, M. Jamet, P. Noé, V. Calvo, J.-M. Hartmann, L. Nistor, B. Rodmacq, S. Auffret, P. Warin, and Y. Samson, "Spin injection in silicon at zero magnetic field," *Applied Physics Letters*, vol. 94, no. 3, p. 032502, 2009.

[68] S. P. Dash, S. Sharma, R. S. Patel, M. P. de Jong, and R. Jansen, "Electrical creation of spin polarization in silicon at room temperature," *Nature*, vol. 462, no. 7272, pp. 491–494, 2009.

[69] J.-M. Tang, B. T. Collins, M. E. Flatté, *et al.*, "Electron spin-phonon interaction symmetries and tunable spin relaxation in silicon and germanium," *Physical Review B*, vol. 85, no. 4, p. 045202, 2012.

[70] T. J. Flack, B. N. Pushpakaran, and S. B. Bayne, "Gan technology for power electronic applications: a review," *Journal of Electronic Materials*, vol. 45, pp. 2673–2682, 2016.

[71] P. Bettotti, M. Cazzanelli, L. Dal Negro, B. Danese, Z. Gaburro, C. Oton, G. V. Prakash, and L. Pavesi, "Siliconnanostructures for photonics," *Journal of Physics: Condensed Matter*, vol. 14, no. 35, p. 8253, 2002.

[72] F. Priolo, T. Gregorkiewicz, M. Galli, and T. F. Krauss, "Silicon nanostructures for photonics and photovoltaics," *Nature nanotechnology*, vol. 9, no. 1, pp. 19–32, 2014.

[73] J. A. Del Alamo, "Nanometre-scale electronics with iii–v compound semiconductors," *Nature*, vol. 479, no. 7373, pp. 317–323, 2011.

[74] F. Schwierz, "Graphene transistors," *Nature nanotechnology*, vol. 5, no. 7, pp. 487–496, 2010.

[75] G. Fiori, F. Bonaccorso, G. Iannaccone, T. Palacios, D. Neumaier, A. Seabaugh, S. K. Banerjee, and L. Colombo, "Electronics based on two-dimensional materials," *Nature nanotechnology*, vol. 9, no. 10, pp. 768–779, 2014.

[76] R. Pillarisetty, "Academic and industry research progress in germanium nanodevices," *Nature*, vol. 479, no. 7373, pp. 324–328, 2011.

[77] C. Schulte-Braucks, R. Pandey, R. N. Sajjad, M. Barth, R. K. Ghosh, B. Grisafe, P. Sharma, N. von den Driesch, A. Vohra, G. B. Rayner, *et al.*, "Fabrication, characterization, and analysis of ge/gesn heterojunction

p-type tunnel transistors," *IEEE Transactions on Electron Devices*, vol. 64, no. 10, pp. 4354–4362, 2017.

[78] H. C. Weerasinghe, "Electrical characterization of metal-to-insulator transition in iron silicide thin films on silicon substrates," 2006.

[79] M. Polak, P. Scharoch, and R. Kudrawiec, "The electronic band structure of ge1- xsnx in the full composition range: indirect, direct, and inverted gaps regimes, band offsets, and the burstein–moss effect," *Journal of Physics D: Applied Physics*, vol. 50, no. 19, p. 195103, 2017.

[80] C. Xu, C. L. Senaratne, R. J. Culbertson, J. Kouvetakis, and J. Menéndez, "Deviations from vegard's law in semiconductor thin films measured with x-ray diffraction and rutherford backscattering: The ge1-ysny and ge1-xsix cases," *Journal of Applied Physics*, vol. 122, no. 12, p. 125702, 2017.

[81] S. Magalhães, M. Dias, B. Nunes, F. Oliveira, M. Cerqueira, and E. Alves, "Confronting vegard's rule in ge1- x sn x epilayers: from fundamentals to the effect of defects," *Journal of Physics D: Applied Physics*, vol. 55, no. 29, p. 295301, 2022.

[82] C. Goodman, "Direct-gap group iv semiconductors based on tin," *IEE Proceedings I (Solid-State and Electron Devices)*, vol. 129, no. 5, pp. 189–192, 1982.

[83] D. W. Jenkins and J. D. Dow, "Electronic properties of metastable ge x sn 1- x alloys," *Physical Review B*, vol. 36, no. 15, p. 7994, 1987.

[84] P. Moontragoon, Z. Ikonić, and P. Harrison, "Band structure calculations of si–ge–sn alloys: achieving direct band gap materials," *Semiconductor science and technology*, vol. 22, no. 7, p. 742, 2007.

[85] W.-J. Yin, X.-G. Gong, and S.-H. Wei, "Origin of the unusually large band-gap bowing and the breakdown of the band-edge distribution rule in the sn x ge 1- x alloys," *Physical Review B—Condensed Matter and Materials Physics*, vol. 78, no. 16, p. 161203, 2008.

[86] L. Jiang, J. Gallagher, C. L. Senaratne, T. Aoki, J. Mathews, J. Kouvetakis, and J. Menendez, "Compositional dependence of the direct and indirect band gaps in ge1- ysny alloys from room temperature photoluminescence: implications for the indirect to direct gap crossover in intrinsic and n-type materials," *Semiconductor Science and Technology*, vol. 29, no. 11, p. 115028, 2014.

[87] S. A. Ghetmiri, W. Du, J. Margetis, A. Mosleh, L. Cousar, B. R. Conley, L. Domulevicz, A. Nazzal, G. Sun, R. A. Soref, *et al.*, "Direct-bandgap gesn grown on silicon with 2230 nm photoluminescence," *Applied Physics Letters*, vol. 105, no. 15, p. 151109, 2014.

[88] J. Gallagher, C. L. Senaratne, J. Kouvetakis, and J. Menendez, "Compositional dependence of the bowing parameter for the direct and indirect band gaps in ge1- ysny alloys," *Applied Physics Letters*, vol. 105, no. 14, p. 142102, 2014.

[89] O. Moutanabbir, S. Assali, X. Gong, E. O'Reilly, C. Broderick, B. Marzban, J. Witzens, W. Du, S.-Q. Yu, A. Chelnokov, *et al.*, "Monolithic infrared silicon photonics: The rise of (si) gesn semiconductors," *Applied Physics Letters*, vol. 118, no. 11, p. 110502, 2021.

[90] A. Giunto *et al.*, "The gesn alloy and its optoelectronic properties: A critical review of the current understanding," *arXiv preprint arXiv:2309.10584*, 2023.

[91] M. V. Fischetti and S. E. Laux, "Band structure, deformation potentials, and carrier mobility in strained si, ge, and sige alloys," *Journal of Applied Physics*, vol. 80, no. 4, pp. 2234–2252, 1996.

[92] M. Prince, "Drift mobilities in semiconductors. i. germanium," *Physical Review*, vol. 92, no. 3, p. 681, 1953.

[93] G. Ludwig and R. Watters, "Drift and conductivity mobility in silicon," *Physical Review*, vol. 101, no. 6, p. 1699, 1956.

[94] B. Mukhopadhyay, G. Sen, R. Basu, S. Mukhopadhyay, and P. K. Basu, "Prediction of large enhancement of electron mobility in direct gap ge1-xsnx alloy," *physica status solidi (b)*, vol. 254, no. 11, p. 1700244, 2017.

[95] K.-Y. Tien, C.-Y. Liu, P.-Y. Chiu, Y. Chuang, H.-S. Kao, and J.-Y. Li, "Electron mobility enhancement in n-gesn epitaxial layers by tensile strain," in *International Conference on Solid State Devices and Materials*, 2021.

[96] S. M. Sze, Y. Li, and K. K. Ng, *Physics of semiconductor devices*. John wiley & sons, 2021.

[97] G. Scappucci, C. Kloeffel, F. A. Zwanenburg, D. Loss, M. Myronov, J.-J. Zhang, S. De Franceschi, G. Katsaros, and M. Veldhorst, "The germanium

quantum information route," *Nature Reviews Materials*, vol. 6, no. 10, pp. 926–943, 2021.

[98] M. Y. Melnikov, A. Shashkin, V. Dolgopolov, S.-H. Huang, C. Liu, and S. Kravchenko, "Ultra-high mobility two-dimensional electron gas in a sige/si/sige quantum well," *Applied Physics Letters*, vol. 106, no. 9, p. 092102, 2015.

[99] M. Myronov, J. Kycia, P. Waldron, W. Jiang, P. Barrios, A. Bogan, P. Coleridge, and S. Studenikin, "Holes outperform electrons in group iv semiconductor materials," *Small Science*, vol. 3, no. 4, p. 2200094, 2023.

[100] S. Gupta, R. Chen, B. Magyari-Kope, H. Lin, B. Yang, A. Nainani, Y. Nishi, J. S. Harris, and K. C. Saraswat, "Gesn technology: Extending the ge electronics roadmap," in *2011 International Electron Devices Meeting*, pp. 16–6, IEEE, 2011.

[101] Y.-S. Huang, Y.-J. Tsou, C.-H. Huang, C.-H. Huang, H.-S. Lan, C. W. Liu, Y.-C. Huang, H. Chung, C.-P. Chang, S. S. Chu, *et al.*, "High-mobility cvd-grown ge/strained ge 0.9 sn 0.1/ge quantum-well pmosfets on si by optimizing ge cap thickness," *IEEE Transactions on Electron Devices*, vol. 64, no. 6, pp. 2498–2504, 2017.

[102] C.-Y. Liu, Y. Chuang, C.-T. Tai, H.-S. Kao, K.-Y. Tien, and J.-Y. Li, "High-performance gesn electronic devices and spin-orbit coupling in gesn/ge heterostructures," in *2021 IEEE Photonics Society Summer Topicals Meeting Series (SUM)*, pp. 1–2, IEEE, 2021.

[103] C. Hu, "Green transistor as a solution to the ic power crisis," in *2008 9th International Conference on Solid-State and Integrated-Circuit Technology*, pp. 16–20, IEEE, 2008.

[104] S. Sant and A. Schenk, "Pseudopotential calculations of strained-gesn/sigesn hetero-structures," *Applied Physics Letters*, vol. 105, no. 16, p. 162101, 2014.

[105] Y. Peter and M. Cardona, *Fundamentals of semiconductors: physics and materials properties*. Springer Science & Business Media, 2010.

[106] H. Tran, T. Pham, J. Margetis, Y. Zhou, W. Dou, P. C. Grant, J. M. Grant, S. Al-Kabi, G. Sun, R. A. Soref, *et al.*, "Si-based gesn photodetectors toward mid-infrared imaging applications," *ACS Photonics*, vol. 6, no. 11, pp. 2807–2815, 2019.

[107] D. Zhang, X. Hu, D. Liu, X. Lin, W. Wang, Z. Ding, Z. Wang, B. Cheng, and C. Xue, "Gesn on si avalanche photodiodes for short wave infrared detection," in *Optical Sensing and Imaging Technologies and Applications*, vol. 10846, pp. 327–334, SPIE, 2018.

[108] M. R. Atalla, S. Assali, S. Koelling, A. Attiaoui, and O. Moutanabbir, "High-bandwidth extended-swir gesn photodetectors on silicon achieving ultrafast broadband spectroscopic response," *ACS Photonics*, vol. 9, no. 4, pp. 1425–1433, 2022.

[109] E. Talamas Simola, V. Kiyek, A. Ballabio, V. Schlykow, J. Frigerio, C. Zucchetti, A. De Iacovo, L. Colace, Y. Yamamoto, G. Capellini, *et al.*, "Cmos-compatible bias-tunable dual-band detector based on gesn/ge/si coupled photodiodes," *ACS photonics*, vol. 8, no. 7, pp. 2166–2173, 2021.

[110] C. Chang, T.-W. Chang, H. Li, H. H. Cheng, R. Soref, G. Sun, and J. R. Hendrickson, "Room-temperature 2-μm gesn pin homojunction light-emitting diode for inplane coupling to group-iv waveguides," *Applied Physics Letters*, vol. 111, no. 14, p. 141105, 2017.

[111] C. Cardoux, L. Casiez, N. Pauc, V. Calvo, N. Coudurier, P. Rodriguez, J. Richy, P. Barritault, O. Lartigue, C. Constancias, *et al.*, "Room temperature spectral characterization of direct band gap ge0. 85sn0. 15 leds and photodiodes," in *Silicon Photonics XVII*, vol. 12006, pp. 54–63, SPIE, 2022.

[112] B.-J. Huang, C.-Y. Chang, Y.-D. Hsieh, R. A. Soref, G. Sun, H.-H. Cheng, and G.-E. Chang, "Electrically injected gesn vertical-cavity surface emitters on silicon-on-insulator platforms," *ACS Photonics*, vol. 6, no. 8, pp. 1931–1938, 2019.

[113] S. Wirths, R. Geiger, N. Von Den Driesch, G. Mussler, T. Stoica, S. Mantl, Z. Ikonic, M. Luysberg, S. Chiussi, J.-M. Hartmann, *et al.*, "Lasing in direct-bandgap gesn alloy grown on si," *Nature photonics*, vol. 9, no. 2, pp. 88–92, 2015.

[114] Y. Zhou, W. Dou, W. Du, S. Ojo, H. Tran, S. A. Ghetmiri, J. Liu, G. Sun, R. Soref, J. Margetis, *et al.*, "Optically pumped gesn lasers operating at 270 k with broad waveguide structures on si," *Acs Photonics*, vol. 6, no. 6, pp. 1434–1441, 2019.

[115] A. Elbaz, D. Buca, N. von den Driesch, K. Pantzas, G. Patriarche, N. Zerounian, E. Herth, X. Checoury, S. Sauvage, I. Sagnes, *et al.*, "Ultra-low-threshold continuous-wave and pulsed lasing in tensile-strained gesn alloys," *Nature Photonics*, vol. 14, no. 6, pp. 375–382, 2020.

[116] Y. Zhou, Y. Miao, S. Ojo, H. Tran, G. Abernathy, J. M. Grant, S. Amoah, G. Salamo, W. Du, J. Liu, *et al.*, "Electrically injected gesn lasers on si operating up to 100 k," *Optica*, vol. 7, no. 8, pp. 924–928, 2020.

[117] Y. Kim, S. Assali, D. Burt, Y. Jung, H.-J. Joo, M. Chen, Z. Ikonic, O. Moutanabbir, and D. Nam, "Improved gesn microdisk lasers directly sitting on si," in *Silicon Photonics XVII*, vol. 12006, pp. 151–157, SPIE, 2022.

[118] S. Ojo, Y. Zhou, S. Acharya, N. Saunders, S. Amoah, Y.-T. Jheng, H. Tran, W. Du, G.-E. Chang, B. Li, *et al.*, "Silicon-based electrically injected gesn lasers," in *Physics and Simulation of Optoelectronic Devices XXX*, vol. 11995, pp. 78–83, SPIE, 2022.

[119] B. Marzban, L. Seidel, T. Liu, K. Wu, V. Kiyek, M. H. Zoellner, Z. Ikonic, J. Schulze, D. Grutzmacher, G. Capellini, *et al.*, "Strain engineered electrically pumped sigesn microring lasers on si," *ACS Photonics*, vol. 10, no. 1, pp. 217–224, 2022.

[120] M. Chen, H.-J. Joo, Y. Kim, E. H. Toh, E. Quek, Z. Ikonic, W. Du, S.-Q. Yu, and D. Nam, "Tensile-strained gesn microbridge lasers with lithographically controllable emission wavelengths," *ACS Photonics*, vol. 11, pp. 4502–4506, 2024.

[121] D. Buca, A. Bjelajac, D. Spirito, O. Concepción, M. Gromovyi, E. Sakat, X. Lafosse, L. Ferlazzo, N. von den Driesch, Z. Ikonic, *et al.*, "Room temperature lasing in gesn microdisks enabled by strain engineering," *Advanced Optical Materials*, vol. 10, no. 22, p. 2201024, 2022.

[122] D. A. Miller, "Device requirements for optical interconnects to silicon chips," *Proceedings of the IEEE*, vol. 97, no. 7, pp. 1166–1185, 2009.

[123] J. Liu, H. Deng, W. Zhang, and J. Yao, "On-chip sensor for simultaneous temperature and refractive index measurements based on a dual-passband microwave photonic filter," *Journal of Lightwave Technology*, vol. 36, no. 18, pp. 4099–4105, 2018.

[124] V. M. Lavchiev and B. Jakoby, "Photonics in the mid-infrared: challenges in single-chip integration and absorption sensing," *IEEE Journal of Selected Topics in Quantum Electronics*, vol. 23, no. 2, pp. 452–463, 2016.

[125] B. Dutt, H. Lin, D. S. Sukhdeo, B. M. Vulovic, S. Gupta, D. Nam, K. C. Saraswat, and J. S. Harris Jr, "Theoretical analysis of gesn alloys as a gain medium for a si-compatible laser," *IEEE Journal of Selected Topics in Quantum Electronics*, vol. 19, no. 5, pp. 1502706–1502706, 2013.

[126] J. Liu, X. Sun, D. Pan, X. Wang, L. C. Kimerling, T. L. Koch, and J. Michel, "Tensile-strained, n-type ge as a gain medium for monolithic laser integration on si," *Optics express*, vol. 15, no. 18, pp. 11272–11277, 2007.

[127] S. Wirths, Z. Ikonic, A. Tiedemann, B. Holländer, T. Stoica, G. Mussler, U. Breuer, J. Hartmann, A. Benedetti, S. Chiussi, *et al.*, "Tensely strained gesn alloys as optical gain media," *Applied physics letters*, vol. 103, no. 19, p. 192110, 2013.

[128] Z. Li, Y. Zhao, J. Gallagher, D. Lombardo, A. Sarangan, I. Agha, J. Kouvetakis, J. Menéndez, and J. Mathews, "Room temperature emission spectroscopy of gesn waveguides under optical pumping," *AIP Advances*, vol. 12, no. 7, p. 075016, 2022.

[129] B. R. Conley, H. Naseem, G. Sun, P. Sharps, and S.-Q. Yu, "High efficiency mj solar cells and tpv using sigesn materials," in *2012 38th IEEE Photovoltaic Specialists Conference*, pp. 001189–001192, IEEE, 2012.

[130] A. Giunto and A. Fontcuberta i Morral, "Defects in ge and gesn and their impact on optoelectronic properties," *Applied Physics Reviews*, vol. 11, no. 4, p. 041333, 2024.

[131] T. Hu, B. Dong, X. Luo, T.-Y. Liow, J. Song, C. Lee, and G.-Q. Lo, "Silicon photonic platforms for mid-infrared applications," *Photonics Research*, vol. 5, no. 5, pp. 417–430, 2017.

[132] G. He and H. A. Atwater, "Interband transitions in sn x ge 1- x alloys," *Physical review letters*, vol. 79, no. 10, p. 1937, 1997.

[133] W. W. Chow, "Model for direct-transition gain in a ge-on-si laser," *Applied Physics Letters*, vol. 100, no. 19, p. 191113, 2012.

[134] D. Stange, S. Wirths, R. Geiger, C. Schulte-Braucks, B. Marzban, N. Von Den Driesch, G. Mussler, T. Zabel, T. Stoica, J.-M. Hartmann, *et al.*,

"Optically pumped gesn microdisk lasers on si," *ACS photonics*, vol. 3, no. 7, pp. 1279–1285, 2016.

[135] S. Al-Kabi, S. A. Ghetmiri, J. Margetis, T. Pham, Y. Zhou, W. Dou, B. Collier, R. Quinde, W. Du, A. Mosleh, *et al.*, "An optically pumped 2.5 μm gesn laser on si operating at 110 k," *Applied Physics Letters*, vol. 109, no. 17, p. 171105, 2016.

[136] V. Singh, P. T. Lin, N. Patel, H. Lin, L. Li, Y. Zou, F. Deng, C. Ni, J. Hu, J. Giammarco, *et al.*, "Mid-infrared materials and devices on a si platform for optical sensing," *Science and technology of advanced materials*, vol. 15, no. 1, p. 014603, 2014.

[137] N. Von Den Driesch, D. Stange, S. Wirths, G. Mussler, B. Hollander, Z. Ikonic, J. Hartmann, T. Stoica, S. Mantl, D. Grutzmacher, *et al.*, "Direct bandgap group iv epitaxy on si for laser applications," *Chemistry of Materials*, vol. 27, no. 13, pp. 4693–4702, 2015.

[138] E. M. Fadaly, A. Dijkstra, J. R. Suckert, D. Ziss, M. A. Van Tilburg, C. Mao, Y. Ren, V. T. van Lange, K. Korzun, S. Kölling, *et al.*, "Direct-bandgap emission from hexagonal ge and sige alloys," *Nature*, vol. 580, no. 7802, pp. 205–209, 2020.

[139] M. K. Hudait, F. Murphy-Armando, D. Saladukha, M. B. Clavel, P. S. Goley, D. Maurya, S. Bhattacharya, and T. J. Ochalski, "Design, theoretical, and experimental investigation of tensile-strained germanium quantum-well laser structure," *ACS Applied Electronic Materials*, vol. 3, no. 10, pp. 4535–4547, 2021.

[140] A. Giorgioni, S. Paleari, S. Cecchi, E. Vitiello, E. Grilli, G. Isella, W. Jantsch, M. Fanciulli, and F. Pezzoli, "Strong confinement-induced engineering of the g factor and lifetime of conduction electron spins in ge quantum wells," *Nature communications*, vol. 7, no. 1, p. 13886, 2016.

[141] A. Giorgioni, E. Vitiello, E. Grilli, M. Guzzi, and F. Pezzoli, "Valley-dependent spin polarization and long-lived electron spins in germanium," *Applied Physics Letters*, vol. 105, no. 15, p. 152404, 2014.

[142] S. Dushenko, M. Koike, Y. Ando, M. Myronov, and M. Shiraishi, "Spin transport in n-type germanium epilayers at room temperature.," in *JSAP Annual Meetings Extended Abstracts The 75th JSAP Autumn Meeting 2014*, pp. 1904–1904, The Japan Society of Applied Physics, 2014.

[143] S. Dushenko, M. Koike, Y. Ando, T. Shinjo, M. Myronov, and M. Shiraishi, "Experimental demonstration of room-temperature spin transport in n-type germanium epilayers," *Physical review letters*, vol. 114, no. 19, p. 196602, 2015.

[144] S. Oyarzún, A. Nandy, F. Rortais, J.-C. Rojas-Sánchez, M.-T. Dau, P. Noël, P. Laczkowski, S. Pouget, H. Okuno, L. Vila, *et al.*, "Evidence for spin-to-charge conversion by rashba coupling in metallic states at the fe/ge (111) interface," *Nature communications*, vol. 7, no. 1, p. 13857, 2016.

[145] F. Bottegoni, C. Zucchetti, S. Dal Conte, J. Frigerio, E. Carpene, C. Vergnaud, M. Jamet, G. Isella, F. Ciccacci, G. Cerullo, *et al.*, "Spin-hall voltage over a large length scale in bulk germanium," *Physical Review Letters*, vol. 118, no. 16, p. 167402, 2017.

[146] A. Hoffmann and S. D. Bader, "Opportunities at the frontiers of spintronics," *Physical Review Applied*, vol. 4, no. 4, p. 047001, 2015.

[147] S. De Cesari, A. Balocchi, E. Vitiello, P. Jahandar, E. Grilli, T. Amand, X. Marie, M. Myronov, and F. Pezzoli, "Spin-coherent dynamics and carrier lifetime in strained ge 1- x sn x semiconductors on silicon," *Physical Review B*, vol. 99, no. 3, p. 035202, 2019.

[148] K. Hamaya, Y. Fujita, M. Yamada, M. Kawano, S. Yamada, and K. Sawano, "Spin transport and relaxation in germanium," *Journal of Physics D: Applied Physics*, vol. 51, no. 39, p. 393001, 2018.

[149] A. Marchionni, C. Zucchetti, F. Ciccacci, M. Finazzi, H. Funk, D. Schwarz, M. Oehme, J. Schulze, and F. Bottegoni, "Inverse spin-hall effect in gesn," *Applied Physics Letters*, vol. 118, no. 21, p. 212402, 2021.

[150] C. Zucchetti, M. Bollani, G. Isella, M. Zani, M. Finazzi, and F. Bottegoni, "Doping dependence of the electron spin diffusion length in germanium," *APL Materials*, vol. 7, no. 10, p. 101122, 2019.

[151] B. Ferrari, F. Marcantonio, F. Murphy-Armando, M. Virgilio, and F. Pezzoli, "Quantum spin hall phase in gesn heterostructures on silicon," *Physical Review Research*, vol. 5, no. 2, p. L022035, 2023.

[152] E. Longo, O. Concepción, R. Mantovan, M. Fanciulli, M. Myronov, E. Bonera, J. Pedrini, D. Buca, and F. Pezzoli, "Spin pumping in epitaxial ge1-xsnx alloys," *Advanced Quantum Technologies*, p. 2400508, 2024.

[153] G. Fettu, J. E. Sipe, and O. Moutanabbir, "Mid-infrared optical spin injection and coherent control," *Physical Review B*, vol. 107, no. 16, p. 165202, 2023.

[154] D. Weißhaupt, H. S. Funk, M. Kern, M. M. Dettling, D. Schwarz, M. Oehme, C. Sürgers, J. Van Slageren, I. A. Fischer, and J. Schulze, "Weak localization and weak antilocalization in doped ge1-y sn y layers with up to 8% sn," *Journal of Physics: Condensed Matter*, vol. 33, no. 8, p. 085703, 2020.

[155] P. Kaul, O. Concepción, D. H. Wielens, P. Zellekens, C. Li, Z. Ikonic, K. Ishibashi, Q.-T. Zhao, A. Brinkman, D. Grützmacher, *et al.*, "Phase-coherent transport in gesn alloys on si," *Advanced Electronic Materials*, vol. 11, p. 2400565, 2024.

[156] K. Shu, N. Wang, N. Huo, F. Wan, J. Li, and C. Xue, "Negative magnetoresistance in the gesn strip," *ACS Applied Materials & Interfaces*, vol. 13, no. 25, pp. 29960–29964, 2021.

[157] C.-T. Tai, P.-Y. Chiu, C.-Y. Liu, H.-S. Kao, C. T. Harris, T.-M. Lu, C.-T. Hsieh, S.-W. Chang, and J.-Y. Li, "Strain effects on rashba spin-orbit coupling of 2d hole gases in gesn/ge heterostructures," *Advanced Materials*, vol. 33, no. 26, p. 2007862, 2021.

[158] P. Chuang, S.-C. Ho, L. W. Smith, F. Sfigakis, M. Pepper, C.-H. Chen, J.-C. Fan, J. Griffiths, I. Farrer, H. E. Beere, *et al.*, "All-electric all-semiconductor spin field-effect transistors," *Nature nanotechnology*, vol. 10, no. 1, pp. 35–39, 2015.

[159] N. Hendrickx, D. Franke, A. Sammak, G. Scappucci, and M. Veldhorst, "Fast two-qubit logic with holes in germanium," *Nature*, vol. 577, no. 7791, pp. 487–491, 2020.

[160] I. Žutić, A. Matos-Abiague, B. Scharf, H. Dery, and K. Belashchenko, "Proximitized materials," *Materials Today*, vol. 22, pp. 85–107, 2019.

[161] A. Ayan, D. Turkay, B. Unlu, P. Naghinazhadahmadi, S. N. B. Oliaei, C. Boztug, and S. Yerci, "strain engineering of germanium nanobeams by electrostatic actuation," *Scientific Reports*, vol. 9, no. 1, p. 4963, 2019.

[162] C. D. Thurmond, "Equilibrium thermochemistry of solid and liquid alloys of germanium and of silicon. i. the solubility of ge and si in elements of groups iii, iv and v," *The Journal of Physical Chemistry*, vol. 57, no. 8, pp. 827–830, 1953.

[163] K. Momma and F. Izumi, "Vesta 3 for three-dimensional visualization of crystal, volumetric and morphology data," *Journal of applied crystallography*, vol. 44, no. 6, pp. 1272–1276, 2011.

[164] R. Olesinski, N. Kanani, and G. Abbaschian, "Bulletin of alloy phase diagrams," 1985.

[165] H. Li, Y. Cui, K. Wu, W. Tseng, H. Cheng, and H. Chen, "Strain relaxation and sn segregation in gesn epilayers under thermal treatment," *Applied Physics Letters*, vol. 102, no. 25, p. 251907, 2013.

[166] N. von den Driesch, S. Wirths, R. Troitsch, G. Mussler, U. Breuer, O. Moutanabbir, D. Grützmacher, and D. Buca, "Thermally activated diffusion and lattice relaxation in (si) gesn materials," *Physical review materials*, vol. 4, no. 3, p. 033604, 2020.

[167] S. Wu, L. Zhang, B. Son, Q. Chen, H. Zhou, and C. S. Tan, "Insights into the origins of guided microtrenches and microholes/rings from sn segregation in germanium–tin epilayers," *The Journal of Physical Chemistry C*, vol. 124, no. 37, pp. 20035–20045, 2020.

[168] R. People and J. Bean, "Calculation of critical layer thickness versus lattice mismatch for ge x si1- x/si strained-layer heterostructures," *Applied Physics Letters*, vol. 47, no. 3, pp. 322–324, 1985.

[169] Y. Diao, J. Yang, Z. Wang, W. Meng, G. Liu, Z. Huang, J. Zhou, and S. Ke, "Magnetron sputtering growth and growth mechanism of gesn films with sn content exceeding 25% on inp substrates," *Applied Surface Science*, vol. 699, p. 163122, 2025.

[170] S. Assali, J. Nicolas, and O. Moutanabbir, "Enhanced sn incorporation in gesn epitaxial semiconductors via strain relaxation," *Journal of Applied Physics*, vol. 125, no. 2, p. 025304, 2019.

[171] D. Schwarz, H. S. Funk, M. Oehme, and J. Schulze, "Alloy stability of ge 1- x sn x with sn concentrations up to 17% utilizing low-temperature molecular beam epitaxy," *Journal of Electronic Materials*, vol. 49, pp. 5154–5160, 2020.

[172] J. F. Burnham, "Scopus database: a review," *Biomedical digital libraries*, vol. 3, pp. 1–8, 2006.

[173] K. Sewell and F. Murphy-Armando, "First-principles calculation of alloy scattering and n-type mobility in strained ge-sn," *Physical Review Applied*, vol. 23, no. 1, p. 014074, 2025.

[174] K. Sewell, "Controlling electron spin to realise a greener future," *The Boolean: Snapshots of Doctoral Research at University College Cork*, pp. 37–42, 2024.

[175] K. Sewell and F. Murphy-Armando, "First-principles calculation of spin-relaxation due to alloy and electron-phonon scattering in strained gesn," *arXiv preprint arXiv:2505.10350*, 2025.

[176] R. P. Feynman, R. B. Leighton, M. Sands, and E. M. Hafner, "The feynman lectures on physics; vol. i," *American Journal of Physics*, vol. 33, no. 9, pp. 750–752, 1965.

[177] O. Stern and W. Gerlach, "Das magnetische moment des silberatoms [the magnetic moment of the silver atom]," *Z. Phys*, vol. 9, p. 349, 1922.

[178] R. G. Fraser, "The effective cross section of the oriented hydrogen atom," *Proceedings of the Royal Society of London. Series A, Containing Papers of a Mathematical and Physical Character*, vol. 114, no. 767, pp. 212–221, 1927.

[179] G. E. Uhlenbeck and S. Goudsmit, "Ersetzung der hypothese vom unmechanischen zwang durch eine forderung bezüglich des inneren verhaltens jedes einzelnen elektrons," *Die Naturwissenschaften*, vol. 13, no. 47, pp. 953–954, 1925.

[180] E. Schrödinger, "Schrödinger 1926c," *Annalen der Physik*, vol. 79, p. 734, 1926.

[181] W. Pauli Jr, "On the quantum mechanics of magnetic electrons," *Nature*, vol. 119, p. 282, 1927.

[182] O. Klein, "Quantentheorie und fünfdimensionale relativitätstheorie," *Zeitschrift für Physik*, vol. 37, no. 12, pp. 895–906, 1926.

[183] W. Gordon, "Der comptoneffekt nach der schrödingerschen theorie," *Zeitschrift für Physik*, vol. 40, no. 1, pp. 117–133, 1926.

[184] P. A. M. Dirac, "The quantum theory of the electron," *Proceedings of the Royal Society of London. Series A, Containing Papers of a Mathematical and Physical Character*, vol. 117, no. 778, pp. 610–624, 1928.

[185] W. Pauli, "Pauli exclusion principle," *Naturwiss*, vol. 12, p. 741, 1924.

[186] E. I. Rashba, "Spin-orbit coupling in condensed matter physics," *Sov. Phys. Solid State*, vol. 2, p. 1109, 1960.

[187] Y. A. Bychkov and E. I. Rashba, "Oscillatory effects and the magnetic susceptibility of carriers in inversion layers," *Journal of physics C: Solid state physics*, vol. 17, no. 33, p. 6039, 1984.

[188] G. Dresselhaus, "Spin-orbit coupling effects in zinc blende structures," *Physical Review*, vol. 100, no. 2, p. 580, 1955.

[189] S. Bandyopadhyay, "Self-assembled nanoelectronic quantum computer based on the rashba effect in quantum dots," *Physical Review B*, vol. 61, no. 20, p. 13813, 2000.

[190] M. I. Dyakonov and V. Perel, "Current-induced spin orientation of electrons in semiconductors," *Physics Letters A*, vol. 35, no. 6, pp. 459–460, 1971.

[191] R. Elliott, "Theory of the effect of spin-orbit coupling on magnetic resonance in some semiconductors," *Physical Review*, vol. 96, no. 2, p. 266, 1954.

[192] Y. Yafet, "g factors and spin-lattice relaxation of conduction electrons," in *Solid State Physics*, vol. 14, pp. 1–98, New York: Elsevier, 1963.

[193] S. Patibandla, G. Atkinson, S. Bandyopadhyay, and G. Tepper, "Competing d'yakonov–perel'and elliott–yafet spin relaxation in germanium," *Physica E: Low-dimensional Systems and Nanostructures*, vol. 42, no. 5, pp. 1721–1726, 2010.

[194] H. A. Kramers, "Théorie générale de la rotation paramagnétique dans les cristaux," *Proc. Acad. Amst*, vol. 33, no. 6, 1930.

[195] J. Fabian, A. Matos-Abiague, C. Ertler, P. Stano, and I. Zutic, "Semiconductor spintronics," *arXiv preprint arXiv:0711.1461*, 2007.

[196] A. Kiss, L. Szolnoki, and F. Simon, "The elliott-yafet theory of spin relaxation generalized for large spin-orbit coupling," *Scientific Reports*, vol. 6, no. 1, p. 22706, 2016.

[197] A. W. Overhauser, "Paramagnetic relaxation in metals," *Physical Review*, vol. 89, no. 4, p. 689, 1953.

[198] E. Fermi, *Nuclear physics: a course given by Enrico Fermi at the University of Chicago*. University of Chicago Press, 1950.

[199] J. Park, J.-J. Zhou, and M. Bernardi, "Spin-phonon relaxation times in centrosymmetric materials from first principles," *Physical Review B*, vol. 101, no. 4, p. 045202, 2020.

[200] B. Huang, D. J. Monsma, and I. Appelbaum, "Coherent spin transport through a 350 micron thick silicon wafer," *Physical Review Letters*, vol. 99, no. 17, p. 177209, 2007.

[201] P. Li, Y. Song, and H. Dery, "Intrinsic spin lifetime of conduction electrons in germanium," *Physical Review B—Condensed Matter and Materials Physics*, vol. 86, no. 8, p. 085202, 2012.

[202] P. Monod and F. Beuneu, "Conduction-electron spin flip by phonons in metals: Analysis of experimental data," *Physical Review B*, vol. 19, no. 2, p. 911, 1979.

[203] J. Cheng, M. Wu, and J. Fabian, "Theory of the spin relaxation of conduction electrons in silicon," *Physical Review Letters*, vol. 104, no. 1, p. 016601, 2010.

[204] R. Seymour and R. Alfano, "Time-resolved measurement of the electron-spin relaxation kinetics in gaas," *Applied Physics Letters*, vol. 37, no. 2, pp. 231–233, 1980.

[205] Y. Ohno, R. Terauchi, T. Adachi, F. Matsukura, and H. Ohno, "Spin relaxation in gaas (110) quantum wells," *Physical Review Letters*, vol. 83, no. 20, p. 4196, 1999.

[206] S. Oertel, J. Huebner, and M. Oestreich, "High temperature electron spin relaxation in bulk gaas," *Applied Physics Letters*, vol. 93, no. 13, p. 132112, 2008.

[207] P. H. Song and K. Kim, "Spin relaxation of conduction electrons in bulk iii-v semiconductors," *Physical Review B*, vol. 66, no. 3, p. 035207, 2002.

[208] C. Hautmann, F. Jaworeck, K. Kashani-Shirazi, M. Amann, and M. Betz, "Temperature and doping dependence of electron spin relaxation in gasb," *Semiconductor science and technology*, vol. 24, no. 2, p. 025018, 2009.

[209] T. F. Boggess, J. Olesberg, C. Yu, M. E. Flatte, and W. H. Lau, "Room-temperature electron spin relaxation in bulk inas," *Applied physics letters*, vol. 77, no. 9, pp. 1333–1335, 2000.

[210] S. Bandyopadhyay, M. I. Hossain, H. Ahmad, J. Atulasimha, and S. Bandyopadhyay, "Coherent spin transport and suppression of spin relaxation in insb nanowires with single subband occupancy at room temperature," *Small*, vol. 10, no. 21, pp. 4379–4385, 2014.

[211] P. Murzyn, C. Pidgeon, P. Phillips, M. Merrick, K. Litvinenko, J. Allam, B. Murdin, T. Ashley, J. Jefferson, A. Miller, *et al.*, "Suppression of d'yakonov–perel spin relaxation in inas and insb by n-type doping at 300 k," *Applied physics letters*, vol. 83, no. 25, pp. 5220–5222, 2003.

[212] T.-Y. Yang, J. Balakrishnan, F. Volmer, A. Avsar, M. Jaiswal, J. Samm, S. Ali, A. Pachoud, M. Zeng, M. Popinciuc, *et al.*, "Observation of long spin-relaxation times in bilayer graphene at room temperature," *Physical review letters*, vol. 107, no. 4, p. 047206, 2011.

[213] H. Idzuchi, A. Fert, and Y. Otani, "Revisiting the measurement of the spin relaxation time in graphene-based devices," *Physical Review B*, vol. 91, no. 24, p. 241407, 2015.

[214] O. D. Restrepo and W. Windl, "Full first-principles theory of spin relaxation in group-iv materials," *Physical Review Letters*, vol. 109, no. 16, p. 166604, 2012.

[215] P. Monod and A. Janossy, "Conduction electron spin resonance in gold," *Journal of Low Temperature Physics*, vol. 26, pp. 311–316, 1977.

[216] D. Steiauf, C. Illg, and M. Fähnle, "Extension of yafet's theory of spin relaxation to ferromagnets," *Journal of magnetism and magnetic materials*, vol. 322, no. 6, pp. L5–L7, 2010.

[217] A. Baral, S. Vollmar, S. Kaltenborn, and H. C. Schneider, "Re-examination of the elliott–yafet spin-relaxation mechanism," *New Journal of Physics*, vol. 18, no. 2, p. 023012, 2016.

[218] M. Kurpas, M. Gmitra, and J. Fabian, "Spin-orbit coupling and spin relaxation in phosphorene: Intrinsic versus extrinsic effects," *Physical Review B*, vol. 94, no. 15, p. 155423, 2016.

[219] P. Hohenberg and W. Kohn, "Inhomogeneous electron gas," *Physical review*, vol. 136, no. 3B, p. B864, 1964.

[220] W. Kohn and L. J. Sham, "Self-consistent equations including exchange and correlation effects," *Physical review*, vol. 140, no. 4A, p. A1133, 1965.

[221] J. P. Perdew and A. Zunger, "Self-interaction correction to density-functional approximations for many-electron systems," *Physical Review B*, vol. 23, no. 10, p. 5048, 1981.

[222] D. M. Ceperley and B. J. Alder, "Ground state of the electron gas by a stochastic method," *Physical review letters*, vol. 45, no. 7, p. 566, 1980.

[223] R. P. Feynman, "Forces in molecules," *Physical review*, vol. 56, no. 4, p. 340, 1939.

[224] F. Bloch, "Über die quantenmechanik der elektronen in kristallgittern," *Zeitschrift für physik*, vol. 52, no. 7-8, pp. 555–600, 1929.

[225] N. W. Ashcroft and N. D. Mermin, *Solid state physics*. Cengage Learning, 2022.

[226] H. J. Monkhorst and J. D. Pack, "Special points for brillouin-zone integrations," *Physical review B*, vol. 13, no. 12, p. 5188, 1976.

[227] C. Hartwigsen, S. Gœdecker, and J. Hutter, "Relativistic separable dual-space gaussian pseudopotentials from h to rn," *Physical Review B*, vol. 58, no. 7, p. 3641, 1998.

[228] X. Gonze, B. Amadon, P.-M. Anglade, J.-M. Beuken, F. Bottin, P. Boulanger, F. Bruneval, D. Caliste, R. Caracas, M. Côté, *et al.*, "Abinit: First-principles approach to material and nanosystem properties," *Computer Physics Communications*, vol. 180, no. 12, pp. 2582–2615, 2009.

[229] W. G. Aulbur, M. Städele, and A. Görling, "Exact-exchange-based quasiparticle calculations," *Physical Review B*, vol. 62, no. 11, p. 7121, 2000.

[230] E. O. Kane, "Band structure of indium antimonide," *Journal of Physics and Chemistry of Solids*, vol. 1, no. 4, pp. 249–261, 1957.

[231] D. Chaudhuri, M. O'Donovan, T. Streckenbach, O. Marquardt, P. Farrell, S. K. Patra, T. Koprucki, and S. Schulz, "Multiscale simulations of the electronic structure of iii-nitride quantum wells with varied indium content:

Connecting atomistic and continuum-based models," *Journal of Applied Physics*, vol. 129, no. 7, p. 073104, 2021.

[232] S. Schulz and E. P. O'Reilly, "Electronic band structure," in *Handbook of Optoelectronic Device Modeling and Simulation*, pp. 3–34, CRC Press, 2017.

[233] Y. Kodama and H. Yeh, "The kp theory and mach reflection," *Journal of fluid mechanics*, vol. 800, pp. 766–786, 2016.

[234] D. Rideau, M. Feraille, L. Ciampolini, M. Minondo, C. Tavernier, H. Jaouen, and A. Ghetti, "Strained si, ge, and si 1- x ge x alloys modeled with a first-principles-optimized full-zone k p method," *Physical Review B*, vol. 74, no. 19, p. 195208, 2006.

[235] M. El Kurdi, G. Fishman, S. Sauvage, and P. Boucaud, "Band structure and optical gain of tensile-strained germanium based on a 30 band k p formalism," *Journal of Applied Physics*, vol. 107, no. 1, p. 013710, 2010.

[236] K.-H. Kao, A. S. Verhulst, M. Van de Put, W. G. Vandenberghe, B. Soree, W. Magnus, and K. De Meyer, "Tensile strained ge tunnel field-effect transistors: k· p material modeling and numerical device simulation," *Journal of Applied Physics*, vol. 115, no. 4, p. 044505, 2014.

[237] M. R. Bauer, J. Tolle, C. Bungay, A. V. Chizmeshya, D. J. Smith, J. Menéndez, and J. Kouvetakis, "Tunable band structure in diamond–cubic tin–germanium alloys grown on silicon substrates," *Solid State Communications*, vol. 127, no. 5, pp. 355–359, 2003.

[238] G.-E. Chang, S.-W. Chang, and S. L. Chuang, "Strain-balanced ge_zsn_{1-z} – $si_xge_ysn_{1-x-y}$ multiple-quantum-well lasers," *IEEE journal of Quantum Electronics*, vol. 46, no. 12, pp. 1813–1820, 2010.

[239] Y. P. Varshni, "Temperature dependence of the energy gap in semiconductors," *physica*, vol. 34, no. 1, pp. 149–154, 1967.

[240] J. Bardeen and W. Shockley, "Deformation potentials and mobilities in non-polar crystals," *Physical review*, vol. 80, no. 1, p. 72, 1950.

[241] C. Herring and E. Vogt, "Transport and deformation-potential theory for many-valley semiconductors with anisotropic scattering," *Physical review*, vol. 101, no. 3, p. 944, 1956.

[242] M. B. Clavel, F. Murphy-Armando, Y. Xie, K. Henry, M. Kuhn, R. J. Bodnar, G. Khodaparast, D. Smirnov, J. Heremans, and M. K. Hudait, "Multivalley electron conduction at the indirect-direct crossover point in highly tensile-strained germanium," *Physical Review Applied*, vol. 18, no. 6, p. 064083, 2022.

[243] R. Soref, J. Kouvetakis, and J. Menendez, "Advances in sigesn/ge technology," *MRS Online Proceedings Library (OPL)*, vol. 958, pp. 0958–L01, 2006.

[244] D. Saladukha, M. Clavel, F. Murphy-Armando, G. Greene-Diniz, M. Grüning, M. Hudait, and T. J. Ochalski, "Direct and indirect band gaps in ge under biaxial tensile strain investigated by photoluminescence and photoreflectance studies," *Physical Review B*, vol. 97, no. 19, p. 195304, 2018.

[245] N. Pavarelli, T. J. Ochalski, F. Murphy-Armando, Y. Huo, M. Schmidt, G. Huyet, and J. Harris, "Optical emission of a strained direct-band-gap ge quantum well embedded inside ingaas alloy layers," *Physical Review Letters*, vol. 110, no. 17, p. 177404, 2013.

[246] Z. Song, W. Fan, C. S. Tan, Q. Wang, D. Nam, D. H. Zhang, and G. Sun, "Band structure of ge1- xsnx alloy: a full-zone 30-band k· p model," *New Journal of Physics*, vol. 21, no. 7, p. 073037, 2019.

[247] J. W. Precker and M. A. da Silva, "Experimental estimation of the band gap in silicon and germanium from the temperature–voltage curve of diode thermometers," *American Journal of Physics*, vol. 70, no. 11, pp. 1150–1153, 2002.

[248] P. J. Collings, "Simple measurement of the band gap in silicon and germanium," *American Journal of Physics*, vol. 48, no. 3, pp. 197–199, 1980.

[249] M. El Kurdi, H. Bertin, E. Martincic, M. De Kersauson, G. Fishman, S. Sauvage, A. Bosseboeuf, and P. Boucaud, "Control of direct band gap emission of bulk germanium by mechanical tensile strain," *Applied Physics Letters*, vol. 96, no. 4, p. 041909, 2010.

[250] A. Goi, K. Syassen, and M. Cardona, "Direct-band-gap absorption in germanium under pressure," *Physical Review B*, vol. 39, no. 17, p. 12921, 1989.

[251] R. Dexter, H. Zeiger, and B. Lax, "Cyclotron resonance experiments in silicon and germanium," *Physical Review*, vol. 104, no. 3, p. 637, 1956.

[252] E. R. Johnson and S. M. Christian, "Some properties of germanium-silicon alloys," *Physical Review*, vol. 95, no. 2, p. 560, 1954.

[253] S. Tiwari, E. Kioupakis, J. Menendez, and F. Giustino, "Unified theory of optical absorption and luminescence including both direct and phonon-assisted processes," *Physical Review B*, vol. 109, no. 19, p. 195127, 2024.

[254] N. W. Ashcroft and N. D. Mermin, "Solid state physics, college edn," *Thomson Learning Inc*, 1976.

[255] F. Murphy-Armando and S. Fahy, "First-principles calculation of alloy scattering in ge x si 1- x," *Physical review letters*, vol. 97, no. 9, p. 096606, 2006.

[256] P. Güttinger, "Das verhalten von atomen im magnetischen drehfeld," *Zeitschrift für Physik*, vol. 73, no. 3, pp. 169–184, 1932.

[257] W. Pauli, "Principles of wave mechanics," *Handbuch der Physik*, vol. 24, no. 162, p. 43, 1933.

[258] H. Hellman, "Einführung in die quantenchemie," *Franz Deuticke, Leipzig*, vol. 285, p. 90, 1937.

[259] R. Elliott, J. Krumhansl, and P. Leath, "The theory and properties of randomly disordered crystals and related physical systems," *Reviews of modern physics*, vol. 46, no. 3, p. 465, 1974.

[260] J. Harrison and J. Hauser, "Alloy scattering in ternary iii-v compounds," *Physical Review B*, vol. 13, no. 12, p. 5347, 1976.

[261] C. Jacoboni and L. Reggiani, "The monte carlo method for the solution of charge transport in semiconductors with applications to covalent materials," *Reviews of modern Physics*, vol. 55, no. 3, p. 645, 1983.

[262] W. Van Roosbroeck and W. Shockley, "Photon-radiative recombination of electrons and holes in germanium," *Physical Review*, vol. 94, no. 6, p. 1558, 1954.

[263] H. B. Bebb and E. Williams, "Photoluminescence i: theory," in *Semiconductors and semimetals*, vol. 8, pp. 181–320, Elsevier, 1972.

[264] R. d. L. Kronig, "On the theory of dispersion of x-rays," *Josa*, vol. 12, no. 6, pp. 547–557, 1926.

[265] H. A. Kramers, "La diffusion de la lumiere par les atomes," in *Atti Cong. Intern. Fisica (Transactions of Volta Centenary Congress) Como*, vol. 2, pp. 545–557, 1927.

[266] S. Mukhopadhyay, B. Mukhopadhyay, G. Sen, and P. Basu, "Maximum theoretical electron mobility in n-type ge 1- x sn x due to minimum doping requirement set by intrinsic carrier density," *Journal of Computational Electronics*, vol. 20, pp. 274–279, 2021.

[267] S.-i. Takagi, A. Toriumi, M. Iwase, and H. Tango, "On the universality of inversion layer mobility in si mosfet's: Part i-effects of substrate impurity concentration," *IEEE Transactions on Electron Devices*, vol. 41, no. 12, pp. 2357–2362, 1994.

[268] W. Jiang, H. Yin, Y. Zhang, Y. Liu, W. Yu, J. Xu, and H. Zhu, "Study of electron mobility on silicon with different crystalline orientations," in *2012 IEEE 11th International Conference on Solid-State and Integrated Circuit Technology*, pp. 1–3, IEEE, 2012.

[269] S. Jin, M. V. Fischetti, and T.-W. Tang, "Modeling of surface-roughness scattering in ultrathin-body soi mosfets," *IEEE Transactions on Electron Devices*, vol. 54, no. 9, pp. 2191–2203, 2007.

[270] M. Liu, Y. Junk, Y. Han, D. Yang, J. H. Bae, M. Frauenrath, J.-M. Hartmann, Z. Ikonic, F. Bärwolf, A. Mai, *et al.*, "Vertical gesn nanowire mosfets for cmos beyond silicon," *Communications Engineering*, vol. 2, no. 1, p. 7, 2023.

[271] D. J. Paul, "8-band k. p modeling of the quantum confined stark effect in ge quantum wells on si substrates," *Physical Review B*, vol. 77, no. 15, p. 155323, 2008.

[272] C. Hartwigsen, S. Gœdecker, and J. Hutter, "Relativistic separable dual-space gaussian pseudopotentials from h to rn," *Physical Review B*, vol. 58, no. 7, p. 3641, 1998.

[273] A. H. Romero, D. C. Allan, B. Amadon, G. Antonius, T. Applencourt, L. Baguet, J. Bieder, F. Bottin, J. Bouchet, E. Bousquet, *et al.*, "Abinit: Overview and focus on selected capabilities," *The Journal of chemical physics*, vol. 152, no. 12, p. 124102, 2020.

[274] X. Gonze, B. Amadon, G. Antonius, F. Arnardi, L. Baguet, J.-M. Beuken, J. Bieder, F. Bottin, J. Bouchet, E. Bousquet, *et al.*, "The abinit project: Impact, environment and recent developments," *Computer Physics Communications*, vol. 248, p. 107042, 2020.

[275] F. Murphy-Armando, "Enhancement of the electronic thermoelectric properties of bulk strained silicon-germanium alloys using the scattering relaxation times from first-principles calculations," *Journal of Applied Physics*, vol. 126, no. 21, p. 215103, 2019.

[276] F. Murphy-Armando and S. Fahy, "First-principles calculation of carrier-phonon scattering in n-type si 1- x ge x alloys," *Physical Review B*, vol. 78, no. 3, p. 035202, 2008.

[277] F. Murphy-Armando and S. Fahy, "Giant enhancement of n-type carrier mobility in highly strained germanium nanostructures," *Journal of Applied Physics*, vol. 109, no. 11, p. 113703, 2011.

[278] F. Murphy-Armando, É. Murray, I. Savić, M. Trigo, D. Reis, and S. Fahy, "Electronic heat generation in semiconductors: Non-equilibrium excitation and evolution of zone-edge phonons via electron–phonon scattering in photo-excited germanium," *Applied Physics Letters*, vol. 122, no. 1, p. 012202, 2023.

[279] K.-Y. Tien, Y.-Y. Chen, C.-Y. Liu, H.-S. Kao, and J.-Y. Li, "Extremely high electron mobility in gesn epitaxial films by chemical vapor deposition," *Advanced Electronic Materials*, p. 2400925, 2025.

[280] Y. Song and H. Dery, "Analysis of phonon-induced spin relaxation processes in silicon," *Physical Review B—Condensed Matter and Materials Physics*, vol. 86, no. 8, p. 085201, 2012.

[281] G. F. Koster, "Solid state physics," *Academic Press, New York, 1957) Vol*, vol. 5, p. 173, 1957.

[282] P. Tamborenea, M. Kuroda, and F. Bottesi, "Spin relaxation in n-doped gaas due to impurity and electron-electron elliot-yafet scattering," *Physical Review B*, vol. 68, no. 24, p. 245205, 2003.

[283] J.-N. Chazalviel, "Spin relaxation of conduction electrons in n-type indium antimonide at low temperature," *Physical Review B*, vol. 11, no. 4, p. 1555, 1975.

[284] D. Johnson, "Measurement of low absorption coefficients in crystals," *Applied optics*, vol. 12, no. 9, pp. 2192–2197, 1973.

[285] L. Bychto and M. Maliński, "Determination of the optical absorption coefficient spectra of thin semiconductor layers from their photoacoustic spectra," *International Journal of Thermophysics*, vol. 39, pp. 1–11, 2018.

[286] H. Philipp and E. Taft, "Optical constants of germanium in the region 1 to 10 ev," *Physical Review*, vol. 113, no. 4, p. 1002, 1959.

[287] A. Mosleh, S. A. Ghetmiri, B. R. Conley, M. Hawkridge, M. Benamara, A. Nazzal, J. Tolle, S.-Q. Yu, and H. A. Naseem, "Material characterization of ge 1- x sn x alloys grown by a commercial cvd system for optoelectronic device applications," *Journal of electronic materials*, vol. 43, pp. 938–946, 2014.

[288] Y.-H. Hsieh, W.-Y. Hsieh, H.-H. Tseng, Y.-K. Liu, H. Cheng, and G.-E. Chang, "Enhanced infrared optical absorption in gesn alloys for full-telecommunication photodetection," in *Information Optoelectronics, Nanofabrication and Testing*, pp. ITh3B–3, Optica Publishing Group, 2012.

[289] I. Avdeev, A. Belolipetsky, N. Ha, M. Nestoklon, and I. Yassievich, "Absorption of si, ge, and sige alloy nanocrystals embedded in sio2 matrix," *Journal of Applied Physics*, vol. 127, no. 11, p. 114301, 2020.

[290] F. Murphy-Armando, M. Brehm, P. Steindl, M. Lusk, T. Fromherz, K. Schwarz, and P. Blaha, "Light emission from direct band gap germanium containing split-interstitial defects," *Physical Review B*, vol. 103, no. 8, p. 085310, 2021.

[291] T. Arguirov, M. Kittler, and N. Abrosimov, "Room temperature luminescence from germanium," in *Journal of Physics: Conference Series*, vol. 281, p. 012021, IOP Publishing, 2011.

[292] F. Pezzoli, A. Giorgioni, D. Patchett, and M. Myronov, "Temperature-dependent photoluminescence characteristics of gesn epitaxial layers," *Acs Photonics*, vol. 3, no. 11, pp. 2004–2009, 2016.

[293] V. Schlykow, P. Zaumseil, M. A. Schubert, O. Skibitzki, Y. Yamamoto, W. M. Klesse, Y. Hou, M. Virgilio, M. De Seta, L. Di Gaspare, *et al.*, "Photoluminescence from gesn nano-heterostructures," *Nanotechnology*, vol. 29, no. 41, p. 415702, 2018.

[294] S. Golovynskyi, I. Golovynska, L. I. Stepanova, O. I. Datsenko, L. Liu, J. Qu, and T. Y. Ohulchanskyy, "Optical windows for head tissues in near-infrared and short-wave infrared regions: approaching transcranial light applications," *Journal of biophotonics*, vol. 11, no. 12, p. e201800141, 2018.

[295] S. Rossi, V. Caprotti, A. Filippi, E. Bonera, J. Pedrini, R. Raimondi, M. Myronov, and F. Pezzoli, "Optical control of the spin-hall effect in a two-dimensional hole gas," *arXiv preprint arXiv:2503.05583*, 2025.